
Sede Amministrativa: Università degli Studi di Padova
Dipartimento di Fisica e Astronomia "G. Galilei"

Corso di Dottorato di Ricerca in Astronomia
Ciclo XXXI
Anno Accademico 2017/2018

# Calibrating the Thermally-Pulsing Asymptotic Giant Branch phase through resolved stellar populations in nearby galaxies

This Thesis has been done with the financial support of the ERC Consolidator Grant funding scheme *project STARKEY*, G.A. n. 615604

**Coordinatore:** Prof. Giampaolo Piotto
**Supervisore:** Prof.ssa Paola Marigo
**Co-Supervisore:** Dr. Léo Girardi

**Dottoranda:** Giada Pastorelli

**Valutatori:**
Prof. Achim Weiss
Prof. Daniel Weisz

# Abstract

Most of the physical processes driving the Thermally-Pulsing Asymptotic Giant Branch (TP-AGB) evolution are not yet fully understood and they need to be modelled with parametrised descriptions. The uncertainties of the models affect the interpretation of the spectrophotometric properties of galaxies up to high-redshift. In the framework of the ERC – STARKEY project, the aim of this Thesis is to constrain the uncertain parameters, i.e. third dredge-up and mass-loss, that still affect the TP-AGB models. To this purpose, I perform detailed simulations of AGB star populations in the Small Magellanic Cloud (SMC) based on robust measurements of the space-resolved star formation history as derived from the deep near-infrared photometry of the VISTA survey of the Magellanic Clouds. I compare the resulting synthetic catalogues with high-quality observations of resolved stellar populations in the infrared passbands of 2MASS and Spitzer. A large grid of TP-AGB evolutionary tracks is computed with several combinations of third dredge-up and mass-loss prescriptions. By requiring the models to reproduce the star counts and the luminosity functions of the observed Oxygen-, Carbon-rich and extreme-AGB stars, I put quantitative constraints on the efficiencies of the third dredge-up and mass-loss. The observed luminosity functions in all the available infrared photometric filters are successfully reproduced by two set of models, one with a relatively high mass-loss efficiency for Oxygen-rich stars and the second with a lower mass-loss efficiency and a lower efficiency of the third dredge-up for the more massive TP-AGB stars, i.e. initial masses larger than three solar masses. On the basis of the best-fitting model I present a complete characterisation of the AGB population in terms of stellar parameters, including the predicted mass-loss rates, initial masses, and Carbon-to-Oxygen ratio. I use the TP-AGB models calibrated in the SMC to model the population of Long Period Variables (LPVs) in the Large Magellanic Cloud as observed by Gaia. The remarkable agreement between models and observations allows us to guide the interpretation of a new observational diagram that is able to photometrically distinguish the evolutionary stages, the initial masses and the chemical type of these stars. In the context of the Large Synoptic Survey Telescope (LSST) science collaboration, I produce catalogues containing the synthetic photometry of the Magellanic Clouds in the Gaia and LSST filters. These catalogues, together with the all-sky simulations of the Milky Way will be made available to the community through the NOAO Data Lab to help defining the observing strategy of the LSST mini-surveys. In addition, I simulate samples of AGB stars in Local Group dwarf galaxies and find a general agreement with the data. However, to properly consider these objects in the TP-AGB models calibration, the simulations should be improved to take into account the crowding effects and the different areas used for the star formation histories derivation and the AGB stars identification. Finally, the products of this work, namely calibrated stellar isochrones and pulsation periods of LPVs, will be publicly available and ready to use for the interpretation of the data coming from present and future observing facilities. The calibrated TP-AGB models may be included in population synthesis models used to probe the integrated light of galaxies in the extragalactic Universe.

# Riassunto

La maggior parte dei processi fisici che controllano l'evoluzione delle stelle di ramo asintotico nella fase dei pulsi termici (TP-AGB) non sono ancora stati pienamente compresi e devono essere modellati con descrizioni parametriche. Le incertezze dei modelli hanno un impatto sull'interpretazione delle proprietà spettrofotometriche delle galassie fino ad alto redshift. Nel contesto del progetto ERC – STARKEY, lo scopo di questa Tesi è di vincolare i parametri incerti, ovvero il terzo dredge-up e la perdita di massa nei modelli stellari AGB. A tal fine, ho effettuato dettagliate simulazioni di popolazioni stellari della Piccola Nube di Magellano basate su robuste misure della storia di formazione stellare spazialmente risolta, derivata dalla fotometria infrarossa della survey VISTA delle Nubi di Magellano. Ho confrontato i risultati dei cataloghi sintetici con accurate osservazioni delle popolazioni stellari risolte nelle bande infrarosse di 2MASS e Spitzer. Un'estesa griglia di tracce evolutive TP-AGB è stata calcolata con diverse prescrizioni di perdita di massa e terzo dredge-up. Imponendo ai modelli di riprodurre i conteggi stellari e le funzioni di luminosità osservate delle stelle AGB e delle sottoclassi di AGB ricche di ossigeno, ricche di carbonio e delle stelle più arrossate, ho posto vincoli quantitativi sull'efficienza del terzo dredge-up e della perdita di massa. Le funzioni di luminosità osservate in tutti i filtri infrarossi disponibili sono riprodotte con successo da due set di modelli: il primo ha una perdita di massa con efficienza relativamente alta per le stelle ricche di ossigeno e il secondo ha un'efficienza di perdita di massa inferiore e una ridotta efficienza del terzo dredge-up per le stelle TP-AGB più massicce, ovvero con massa iniziale maggiore di circa tre masse solari. Sulla base di quest'ultimo set di modelli ho presentato una completa caratterizzazione della popolazione AGB della Piccola Nube di Magellano in termini di parametri stellari, inclusi i tassi di perdita di massa previsti, i valori di massa iniziale e rapporto carbonio ossigeno. Ho utilizzato i modelli TP-AGB calibrati nella Piccola Nube di Magellano per simulare le variabili a lungo periodo nella Grande Nube di Magellano osservate da Gaia. Il notevole accordo tra modelli e osservazioni ha permesso di guidare l'interpretazione di un nuovo diagramma osservativo capace di distinguere fotometricamente gli stadi evolutivi, le masse iniziali e il tipo chimico di queste stelle. Nel contesto della collaborazione scientifica Large Synoptic Survey Telescope (LSST), ho prodotto cataloghi contenenti la fotometria sintetica delle Nubi di Magellano nei filtri di Gaia e LSST. Questi cataloghi, assieme alle simulazioni della Galassia, saranno rese disponibili alla comunità scientifica tramite NOAO Data Lab per aiutare a definire la strategia osservativa dei programmi "mini-survey" di LSST. Inoltre, ho simulato alcuni campioni di stelle AGB in galassie locali e ho trovato un buon accordo tra dati e modelli. Tuttavia, per poter considerare questi oggetti nella calibrazione dei modelli TP-AGB è necessario migliorare le simulazioni per tenere conto degli effetti del crowding e delle diverse regioni utilizzate per la derivazione della storia di formazione stellare e l'identificazione delle stelle AGB. I prodotti di questo lavoro, ovvero isocrone stellari calibrate e periodi di pulsazione delle variabili a lungo periodo, saranno resi pubblicamente disponibili per interpretare dati osservativi già disponibili e dati che verranno rilasciati dai futuri telescopi. I modelli TP-

AGB calibrati potranno essere inclusi in modelli di sintesi di popolazione utilizzati per analizzare la luce integrata di galassie nell'Universo extragalattico.

# Contents

# List of Figures

# List of Tables

# Chapter 1

# Introduction

The present chapter is dedicated to a description of the evolution of low-and intermediate-mass stars, starting from the Main Sequence (MS). Special attention will be placed on the Thermally-Pulsing Asymptotic Giant Branch (TP-AGB) phase, the uncertainties that affect the current models and the need for a robust calibration of the key uncertain processes, i.e. mass-loss and third dredge-up.

## 1.1 The evolution prior to the AGB phase

The main parameter that determines the structure and the evolution of a star is its initial mass $M_{\rm i}$. The initial composition plays a minor role, but can be important especially in very-metal poor stars. According to their initial mass, stars in different evolutionary stages occupy specific locations in the so-called Hertzsprung-Russell diagram (HRD). Such diagram relates the effective temperature of a star and its luminosity and it is a fundamental tool to test stellar evolution theories. An illustrative HRD is shown in Figure 1.1. Stars are usually classified according to their initial mass in three main classes:

- Low-mass stars with $M_{\rm i} \approx 0.08 - 2\ M_{\odot}$ that develop a degenerate Helium core after the MS. They experience a relatively long-lived Red Giant Branch Phase (RGB) that ends when the He is ignited in the core producing the so-called *Helium Flash*. The upper mass limit of low-mass stars is usually denoted as $M_{\rm HeF}$.
- Intermediate-mass stars with $M_{\rm i} \approx M_{\rm HeF} - 8\ M_{\odot}$. Their He core is not degenerate and the ignition is stable, ultimately leading to the development of a degenerate Carbon-Oxygen (C-O) core.
- Massive stars with $M_{\rm i} \gtrsim 8\ M_{\odot}$. They develop a non-degenerate C-O core. The ignition of C is stable and if the initial mass is larger than $\approx 11\ M_{\odot}$the nuclear burning cycle can continue until an Iron core is formed. Such massive stars, as a consequence of the collapse of the Iron core explode as Supernovae.

Both low- and intermediate-mass stars evolve through the AGB phase. They experience strong mass-loss that causes the progressive removal of the whole envelope. The bare C-O core will eventually cool as a White Dwarf (WD). As the subject of this Thesis is the TP-AGB phase, I will briefly describe here the post-MS evolution of low- and intermediate-mass stars, whereas the TP-AGB phase will be described in more details in the next Section.

On the basis of initial mass and composition, the evolutionary path of a star starts from the Zero Age Main Sequence (ZAMS) locus of the HRD. From such location, stars

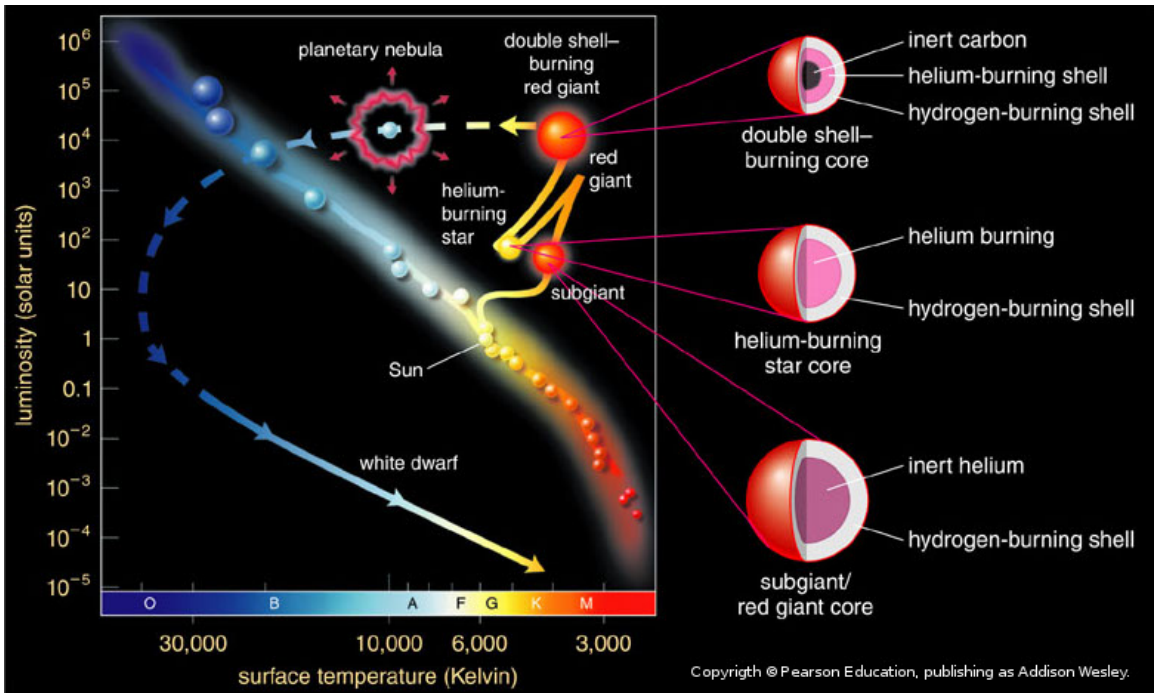


**Figure 1.1:** Illustration of the evolutionary path of a solar-like star in the HRD diagram. The zoomed pictures on the right side are schematic representations of the internal structure of the star in the subgiant branch phase, during the helium-burning and during the double-shell burning that takes place in the AGB phase.

evolve towards higher luminosities and larger radii. The conversion of Hydrogen into Helium takes place via two main series of nuclear reactions. The proton-proton (pp) chain which is the dominant reaction in stars with $M_{\rm i} \lesssim 1.3\ M_{\odot}$, and the CNO cycle that dominates in more massive stars. Once the Hydrogen is almost exhausted in the centre, the energy source moves outward and the H-burning continues in a shell around the He core. The H-shell burning in intermediate-mass stars is relatively slow at the beginning as they are in thermal equilibrium and the H-burning occurs in a thick shell. However, as soon as the mass of the He core exceeds the Schönberg-Chandrasekhar limit, the core contracts more rapidly. According to the "mirror principle", the envelope responds with en expansion. The temperature and density gradients between the core and the envelope become steeper and the H-burning continues in a thin shell. The evolution across the HRD occurs on the Kelvin-Helmholtz timescale resulting in the so-called *Hertzsprung gap*. As the envelope expands, the temperature decreases and the opacity increases making the envelope unstable to convection. The star now lies close to its Hayashi line and starts to ascend the RGB. Since low-mass stars can remain in hydrostatic and thermal equilibrium throughout the H-shell burning there is no gap in the HRD and this long-lived phase corresponds to the well populated Subgiant Branch (SGB) of old stellar populations in globular clusters.

During the RGB, the expansion continues in response to the core contraction and the luminosity (L) increases at almost constant effective temperature ($T_{\rm eff}$). The H-shell burning phase of intermediate-mass stars occurs on a thermal timescale, making the RGB a very-short lived phase, whereas low-mass stars evolve more slowly. Three main processes characterise the RGB evolution. The first dredge-up (FDU) occurs when the convective envelope penetrates in the deeper layers where H-burning products are present. As a consequence of the mixing, the He surface abundance increases, the H abundance decreases as well as the ratio between Carbon and Nitrogen (C/N). When

the H-shell reaches the discontinuity left by the convective envelope, the burning rate slows down leading to a slightly decrease in the luminosity, which increases again after the discontinuity is overcame. The resulting loop in the HRD produces the "bump" in the luminosity functions of old star clusters.

Low-mass stars experience significant mass losses at a rate up to $10^{-7} - 10^{-8} M_{\odot}/yr$ during the late, upper RGB phase. The process is not well understood and the effect of mass loss is usually included in stellar models by means of empirical or semi-empirical relations. One of the most popular choice is the use of the classical Reimers (1975) law, which contains an adjustable efficiency parameter $\eta_{\rm R}$. More recently, Schröder and Cuntz (2005) proposed a semi-empirical, modified version of the Reimers (1975) law, based on the assumption that the stellar wind originates from magneto-acoustic waves operating below the stellar chromosphere. This relation also contains a fitting parameter $\eta$. Low-mass stars can lose up to the 20% of their initial mass and a precise calibration of $\eta_{\rm R}$ or $\eta$ is necessary to account for the morphology of the Horizontal Branch in Galactic Globular clusters populated by low-mass stars during the helium-burning phase. The He core of intermediate-mass stars remains non-degenerate and the Helium ignition in the core occurs in a stable way. The He ignition corresponds to a local maximum in luminosity and radius and marks the end of the RGB.

Low-mass stars ignite helium in a degenerate core resulting in the *helium flash* and the helium burning starts with essentially the same core mass $M_{\rm c} \approx 0.45\ M_{\odot}$. After the thermonuclear runaway the condition of degeneracy is lifted when the temperature reaches about $3 \cdot 10^8$ K, the further nuclear burning of helium is thermally stable and proceeds in a convective core. The evolution through the helium flash is not usually calculated in evolutionary tracks. The models are evolved from a Zero Age Horizontal Branch sequence corresponding to the onset of the steady He burning in the centre. Luminosity and radius have decreased and the core has expanded while the envelope has contracted, with the H-shell acting as a "mirror". The position of the stars in the HRD does not change significantly. The luminosity is determined mainly by the core mass which is approximately the same for all masses, therefore the luminosity at which He burning occurs is almost independent of mass. At fixed composition, only the envelope mass varies from star to star and determines the radius and effective temperature of He burning stars. At solar metallicity, all stars are located in the Red Clump, observed in Colour Magnitude Diagrams (CMDs) of low-mass old stellar populations. However, stars with small envelope mass can be hotter than Red Clump stars and furthermore at low metallicity the critical envelope mass below which stars become small and hotter is larger. He burning stars then form the so called Horizontal Branch in the HRD.

In intermediate-mass stars the nuclear burning is thermally stable and since the He-burning reactions are very sensitive to the temperature the energy production is concentrated towards the centre, giving rise to a convective core with a mass growing with time. After He ignition at the Tip of the RGB (TRGB), the envelope contracts and the stellar radius decreases. The luminosity also decreases while the envelope is mostly convective and the star moves along an almost vertical line in the HR diagram, i.e. the Hayahi line, until the envelope becomes mostly radiative and the $T_{\rm eff}$ increases. The star moves away from the RGB and this is the beginning of the "blue loop" in the HRD of intermediate-mass stars. When the loop reaches its hottest point, the stellar radius has a minimum after which the envelope expands and the star moves again towards the RGB. At the end of the He core burning intermediate-mass stars find themselves very close to their Hayashi line. The blue extension of the loops increases with the stellar mass. Stars with $M_{\rm i} \lesssim 4\ M_{\odot}$ describe loops which remain very close to the RGB. The occurrence and the extension of blue loops depend on metallicity, ratio between He core mass and envelope

mass, shape of H abundance profile above the core, convective overshooting. At the end of the He burning phase, a central core composed of Carbon and Oxygen is formed. The subsequent evolution of low- and intermediate-mass star is qualitatively similar and is presented in the next section.

## 1.2 The evolution during the AGB phase

When the He is exhausted in the centre, the C-O core contracts and the He burning occurs in a shell around the C-O core. At this stage the star has two active burning shells, so that the core contraction is followed by the expansion of the He-rich layers above and the outer envelope contracts. However, the expansion of the He-rich zone decreases the temperature in the H-shell that quenches off. Thus, the entire envelope starts expanding and cooling down. The star moves towards lower $T_{\rm eff}$ and higher luminosities and evolve along the Asymptotic Giant Branch (AGB) in the HRD.

### 1.2.1 Early AGB phase

The initial phase during which the stellar luminosity is provided almost exclusively by the He-shell burning is the Early AGB (E-AGB) phase. The mass of the C-O core gradually increases until it becomes degenerate. Stars more massive than about 4 $M_{\odot}$ (the exact value depends on composition and overshooting) can experience a second dredge-up episode. As a consequence of expansion and cooling, the convective envelope can penetrate into the He-rich layers. The continuing expansion and cooling of these layers increase their opacity and the growing energy flux produced by the He-shell allows the deep penetration of the envelope. In lower-mass stars the H-shell remains active and the second dredge-up does not occur. The material which is dredged up and appears at the surface mainly consists of He and $^{14}$N. Compared to the RGB FDU it is qualitatively similar but the effect is more dramatic, in fact the dredged-up material can be as much as 1 $M_{\odot}$ in the most massive AGB stars. Furthermore, the occurrence of the second dredge-up reduced the mass of the H-exhausted core, limiting the mass of the WD that remains at the end of the AGB phase. During this phase the luminosity provided by neutrinos can balance the gravitational energy released by the C-O core contraction. Thus, the density increase becomes more significant than the temperature increase and the strong electron degeneracy stops the core contraction. The He-burning shell rapidly approaches the H-He discontinuity and its luminosity decreases due to the lack of fuel. The layers above respond with a contraction that heats up the extinguished H-burning shell which is finally re-ignited. This is the beginning of the double-shell burning phase. The He-shell burning occurs in a thin shell and becomes thermally unstable. This phase is characterised by periodic thermal pulses and it thus referred to as Thermally-Pulsing AGB.

### 1.2.2 The TP-AGB phase

The schematic evolution of the inner layers of a TP-AGB star during and between two consecutive thermal pulses is shown in Figure 1.2.

The He-shell burning remains inactive for most of the time, while the H-shell burning adds mass to the intershell region until a critical value is reached and the He is ignited in a thin shell. The He ignition is unstable and results in a thermonuclear runaway, called *helium shell flash* that produces a huge energy flux that drives convection in the whole intershell region, thus producing the intershell convection zone (ICZ). The ICZ mixes the elements produced by He burning, in particular $^{12}$C produced by 3$\alpha$ reactions throughout

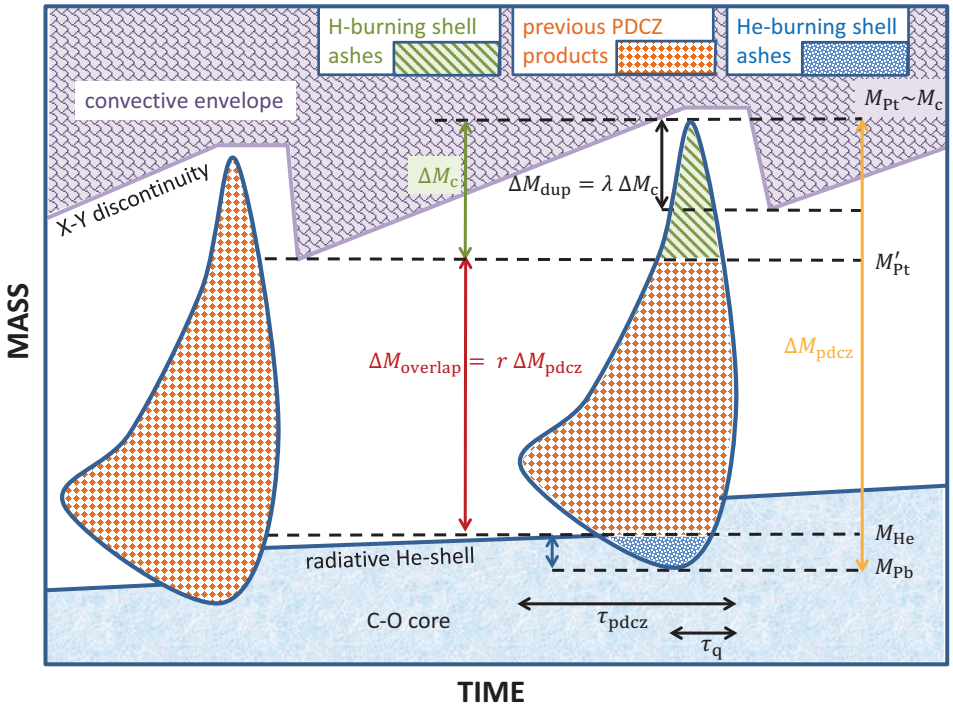


**Figure 1.2:** Schematic evolution of an AGB star through two consecutive thermal pulses from (Marigo et al., 2013).

the intershell region. The large energy release by the He-shell flash causes the expansion and the cooling of the intershell region leading to the quenching of the H-shell and allowing a deeper penetration of the outer convective envelope. The material of the intershell region (mainly He and C) is mixed and appears at the surface. This is the third dredge-up (3DU) and this term is used even for stars that do not experience the second dredge-up and for all the subsequent dredge-up events. After a 3DU episode, the H-shell is re-ignited while the He-shell is inactive again. During this interpulse period, H-burning adds mass to the intershell until the next thermal pulse. The pulse cycle repeats many times and the amplitude of the pulse increases at each cycle, facilitating the occurrence of the 3DU. An important consequence of the thermal pulses and third dredge-up is the limitation of the C-O core mass growth. A very efficient dredge-up implies that in the long-term the core mass does not increase significantly. The main effect of thermal pulses and the 3DU is the photospheric enrichment of carbon. The surface $^{12}$C abundance increases at each dredge-up episode until it eventually exceeds the $^{16}$O abundance. The ratio between the photospheric abundance of carbon and oxygen (C/O ratio) is a fundamental quantity that determines the spectral features of AGB stars. The low temperature of AGB star atmosphere causes the C and O atoms to be bound into CO molecules. When the C/O is below 1, the remaining Oxygen atoms form oxygen-rich molecules, such as Titanium Oxide (TiO) and water ($H_2O$), as well as dust particles, mainly silicate grains. The spectra of O-rich AGB stars are classified as type M. The repeated dredge-up events make the C/O ratio to increase, and eventually to exceed the unity, leading to the formation of carbon-rich molecules ($C_2$, CN) and carbonaceous grains like graphite. These more evolved stars are classified as Carbon-stars (spectral type C). Following the increase of the C/O ratio, AGB stars usually evolve along the spectral sequence M-S-C, where the spectral type S indicates stars with C/O ratio close to unity. The photospheric composition of S-stars is characterized by the presence of elements (e.g., Zr, Y, Sr, Ba, Tc) produced by the slow neutron-capture process (s-process). The typical spectral feature of S-stars is the

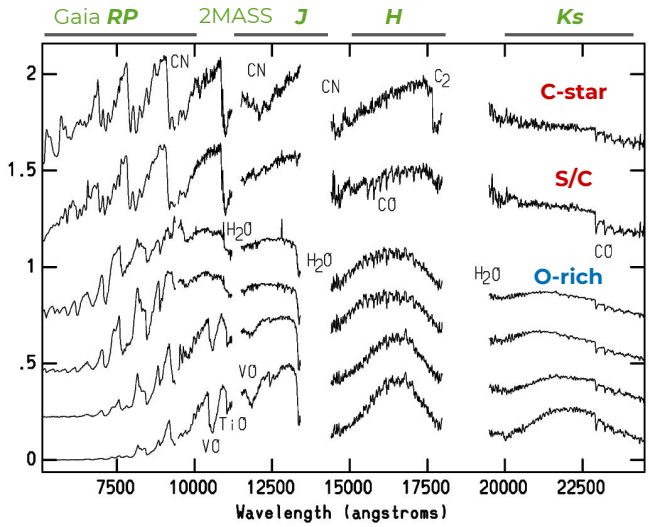


**Figure 1.3:** Optical/near-infrared spectra in which the distinct molecular features of C- and M-stars are indicated. The wavelength ranges of the Gaia *RP* and the 2MASS passbands are shown as reference. Adapted from Lançon and Wood (2000).

presence of the absorption bands of ZrO molecules. Typical optical/near-infrared spectra of AGB stars are shown in Figure 1.3. The spectra of C-rich and O-rich stars are clearly distinguishable by the distinct molecular features as indicated in the figure. By looking at mid-infrared wavelengths, the spectra are characterised by the dust spectral features as shown in Figure 1.4.

During the interpulse period in stars with $M \gtrsim 3-4\ M_{\odot}$, the temperature at the base of the convective envelope can become so high that H-burning through CNO cycle takes place. The main effects of this process, known as Hot-Bottom Burning (HBB), are an increase in the surface luminosity and the conversion of dredged-up $^{12}$C into $^{14}$N. HBB thus prevents massive AGB stars to become carbon stars and makes them efficient producers of nitrogen. If the HBB is very efficient, the activation of the ON cycle causes the conversion of $^{16}$O into $^{14}$N and the C/O can become larger than 1. The efficiency of third dredge-up and HBB depends on several factors, mainly stellar masses and metallicity, which will be discussed in the next section, as well as the complex interplay between the two processes. The stellar properties are mainly determined by the mass of the degenerate C-O core, thus similarly to the RGB, there is a relation between core mass and surface luminosity (CMLR; Wagenhuber and Groenewegen 1998):

$$L = (18160 + 3980 \cdot Z_{\rm i})(\mathrm{M}_c - 0.4468) + 10^{2.705+1.649 \cdot \mathrm{M}_c} \tag{1.1}$$

where $Z_{\rm i}$ is the initial metallicity. This approximate relation holds only during the quiescent interpulse period, while it is violated during the first sub-luminous thermal pulses, in stars with very efficient third dredge-up, and in massive stars experiencing HBB which may become significantly over-luminous compared to what expected for the same core mass.

More evolved TP-AGB stars experience strong mass-loss through stellar winds, as clearly demonstrated by their Spectral Energy Distributions (SEDs) which show large infrared excess. Furthermore many AGB stars, knows as OH/IR stars, are almost completely enshrouded in dusty circumstellar envelopes and are not visible at optical wavelengths.

Although the driving mechanism of mass-loss is not yet completely understood, recent theoretical works and empirical evidence point towards a two-phase scenario. In the

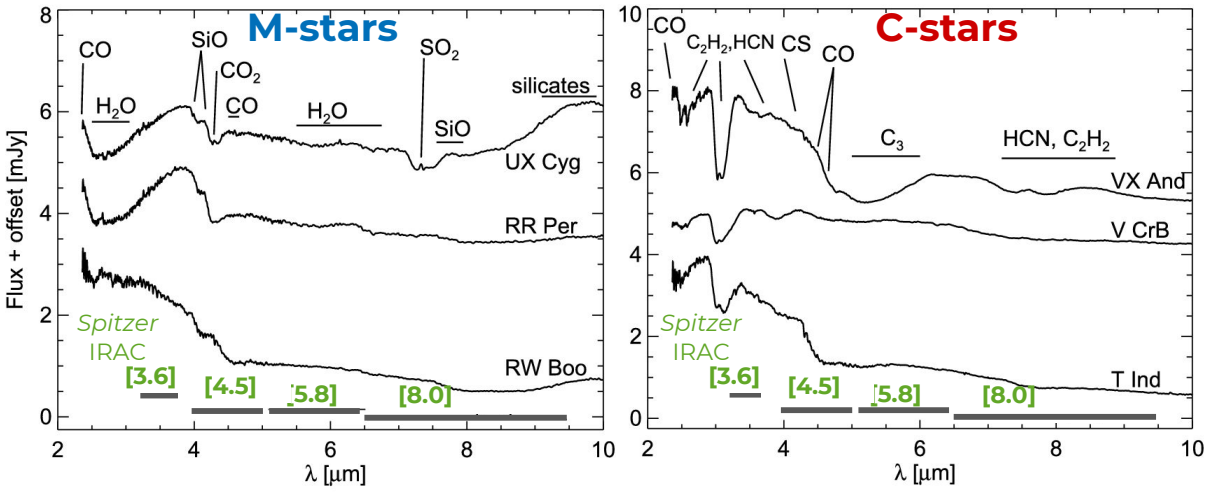


**Figure 1.4:** ISO SWS mid-Infrared spectra in which the distinct photosferic and dust features are visible as indicated. The wavelength ranges of the *Spitzer* IRAC passbands are shown as reference. Adapted from Reiter et al. (2015).

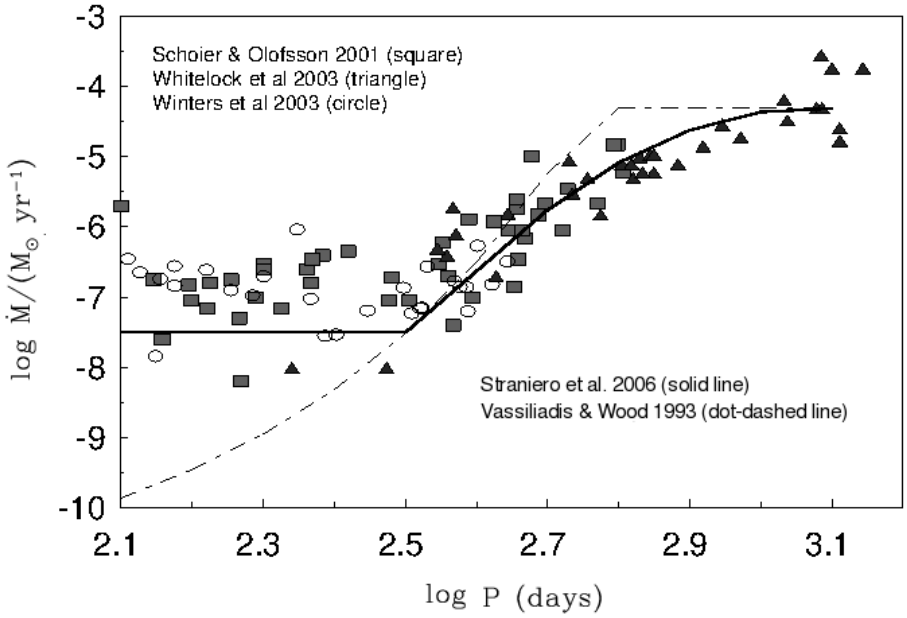


**Figure 1.5:** Comparison between mass-loss rates and pulsation periods, as measured by various authors, and prescriptions used in stellar evolution calculations. Mass-loss rates and periods for O-rich AGB stars (open circles) are measured by Winters et al. (2003), while C-rich AGB stars data (squares and triangles) are from Schöier and Olofsson (2001) and Whitelock et al. (2003), respectively. The dot-dashed line represents the prescription by Vassiliadis and Wood (1993) and the solid line the prescription by Straniero et al. (2006). Adapted from Straniero et al. (2006).

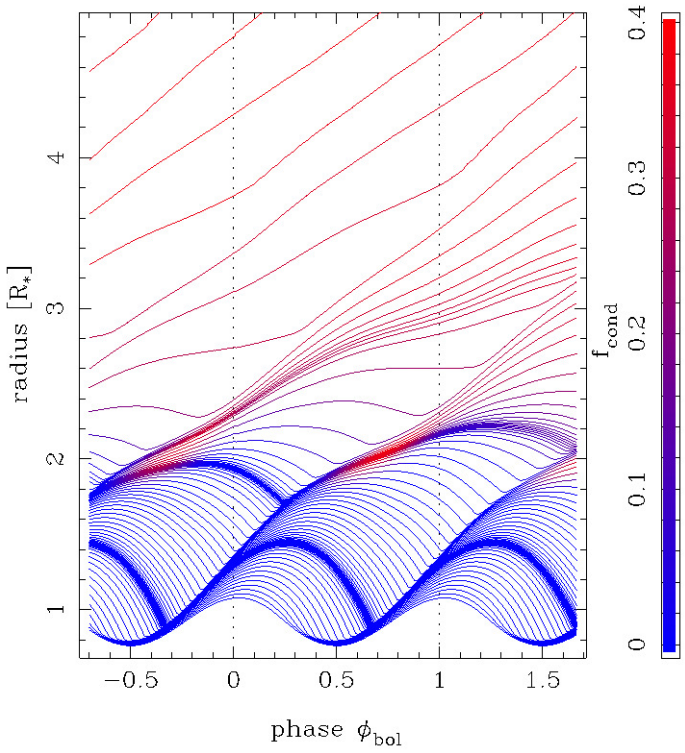


**Figure 1.6:** Scenario of a pulsation-enhanced dust-driven wind, from Nowotny et al. (2010). The plot illustrates the different regions within the atmosphere of a typical mass-losing AGB star. The innermost, dust-free layers below $\approx 2R_\star$ are subject to strictly regular motions caused by the pulsating interior (shock fronts). The dust-forming region (colour-coded is the degree of dust condensation $f_c$) at $\approx 2-3R_\star$ where the stellar wind is triggered represents dynamically a transition region with moderate velocities, not necessarily periodic. A continuous outflow is found from $\approx 4R_\star$ outwards, where the dust-driven wind is decisive from the dynamic point of view.

early stages of the AGB evolution when the amount of dust formed is not sufficient to drive a wind, a plausible driven mechanism is related to the flux of pressure waves i.e. Alfvén waves, (Schröder and Cuntz, 2005; Cranmer and Saar, 2011). Such mechanism is thought to be at work in the extended chromospheres of RGB stars as well. We refer to this first phase as "pre-dust" mass-loss. This first stage is followed by a "dust-driven" regime and it is likely caused by the combination of radial pulsations and radiation pressure on dust grains. The basic physical picture is illustrated in Figure 1.6. Radial pulsations induce shock waves in the stellar atmosphere, which bring gas out to larger radii, resulting in an increase of the gas density in the atmosphere. At about 1.5 - 2 stellar radii, the temperature is low enough that dust particles can condense. Optical properties of dust grains depend on their composition, in particular carbonaceous grains are more opaque than silicates, however they are sufficiently opaque to be easily accelerated by the radiation pressure resulting from the high stellar luminosity. Although the dust fraction is only about 1% of the gas in the atmosphere, the molecular gas is dragged along by the accelerated dust particles producing a large-scale outflow.

An observational correlation between pulsation period and mass-loss rate exists (see Fig. 1.5): the evolution proceeds with increasing pulsation periods and thus increasing mass-loss rates, from $\dot{M} \approx 10^{-8}\ M_\odot/yr$ for Mira variables up to $\dot{M} \approx 10^{-4}\ M_\odot/yr$, which is the value typically inferred for dust enshrouded OH/IR stars. At the latest stages of the evolution TP-AGB stars can reach a "super-wind" phase during which the H-envelope is rapidly removed by the strong stellar winds. An important consequence of mass-loss

is the reduction of the stellar lifetimes of the TP-AGB phase: the increasing mass-loss rate causes a rapidly increasing removal of the H-rich envelope. The high mass-loss rate experienced in the super-wind phase determines both the maximum luminosity and the final mass (i.e. the mass of the remaining WD) of AGB stars. AGB lifetimes are also affected by the third dredge-up and HBB efficiency, which modifies the surface chemical composition, mainly in terms of C/O. The chemical composition controls the atmospheric molecular opacity and the dust grains composition, which in turn influence the mass-loss rate. In general, the transition to carbon star makes the mass-loss rate increase, resulting in a shortening of stellar lifetimes. The second important consequence of mass-loss is the enrichment of Interstellar Medium (ISM) by AGB ejecta, the composition of which depends again on dredge-up and HBB efficiencies as well as dust formation efficiency. The detailed modelling of TP-AGB phase is thus fundamental for the understanding of several astrophysical aspects, including chemical evolution and SEDs of galaxies, multiple stellar populations in star clusters, interpretation of integrated colours of galaxies in both local and far Universe.

**Variability**

Variability due to stellar oscillations is a very common phenomenon among red giant stars (see, e.g., the discussion in Catelan and Smith, 2015, Chapter 8). AGB stars show stellar pulsation in multiple radial modes, with periods between a few tens of days up to a few years, and amplitudes ranging from a milli-magnitude level up to several magnitudes. Pulsation periods and amplitudes correlate with luminosity, so that both increase as stars evolve along the AGB.

These objects fall into the broad group of the Long-Period Variables (LPVs), further subdivided into a few variability types (Mira variables, semi-regular variables (SRVs) and irregular variables) mainly according to their amplitude of variability. Miras, characterised by visual amplitudes larger than 2.5 mag and regular light curves, are among the longest-studied variable stars, and have long been known to follow a period-luminosity (PL) relation that is most clear at infrared wavelengths. The same PL relation is followed by some SRVs as well. Studying a sample of LPVs in some LMC globular clusters, Wood and Sebo (1996) found evidence that SRVs can also follow a second PL relation, at shorter periods than the Miras one. Further evidence for the second PL relation came from a study of a sample of galactic LPVs by Bedding and Zijlstra (1998).

The most significant results in the study of LPVs, however, are associated with the advent of large, ground-based microlensing surveys, most notably MACHO (Alcock et al., 1992) and OGLE (Udalski et al., 1992). Using data from the MACHO program, Wood et al. (1999) (see also Wood, 2000) were able to investigate the variability of LPVs in the LMC, and found them to follow several distinct PL relations (later known as "Wood sequences", Figure 1.7). OGLE observations (Soszynski et al., 2007; Soszyński et al., 2009, 2011) added new pieces of information that led to the current picture of the PL diagram of LPVs (Figure 1.8), with six main sequences, labelled with letters[1] A′, A, B, C′, C, and D. Some of those sequences were found to split at magnitudes fainter than the RGB tip, which was interpreted as evidence that the brightest RGB stars can also show LPV-like variability (see, e.g., Ita et al., 2002, 2004; Kiss and Bedding, 2003; Soszyński et al., 2004). An additional degree of fine structure, especially in sequence A, was also identified in the form of closely spaced sub-ridges. Given the separation between such ridges being too small to be explained by adjacent radial modes, they are considered

[1] Note that a few different nomenclatures have been used to label the PL sequences of LPVs in the Magellanic Clouds. Here, we use the one employed by Wood (2015).

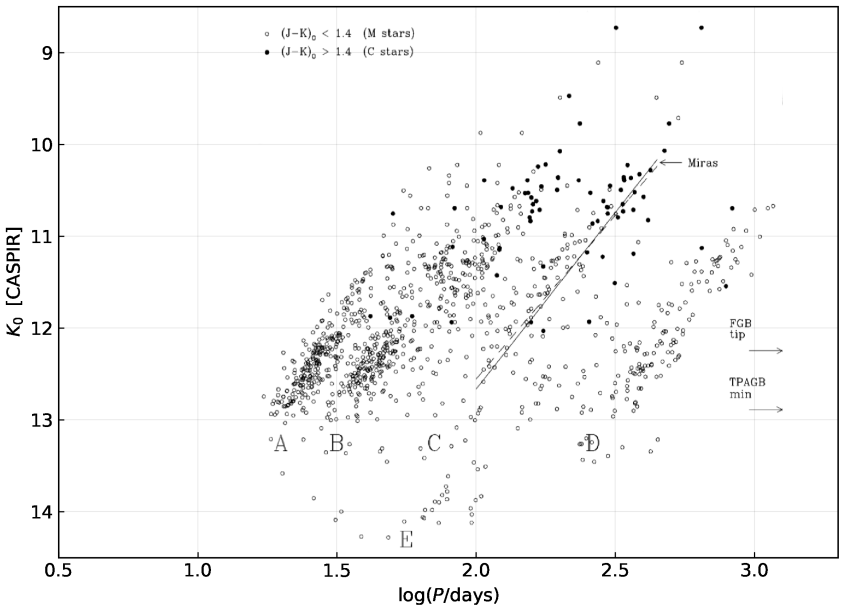


**Figure 1.7:** P-L sequences identified in the LMC with MACHO observations. M-stars ($J - K_0 < 1.4$) and C-stars ($J - K_0 > 1.4$) are shown as open and solid circles, respectively. Courtesy of M. Trabucchi, adapted from Wood et al. (1999)

evidence for non-radial oscillations (e.g. Soszyński et al., 2004).

The existence of multiple PL relations is due to the fact that LPVs can pulsate in modes of different radial orders, depending on their global properties and evolutionary status. Indeed, it is well known that, as a star evolves on the AGB, the radial order of its dominant pulsation mode (the one associated with the largest amplitude of variability) will shift towards lower radial orders of pulsation (e.g. Lattanzio and Wood, 2003, and references therein).

The exact identification of the modes responsible for each sequence has been a matter of debate (Wood, 2015). According to the most recent interpretation (Trabucchi et al., 2017), sequences A′ and A correspond to dominant pulsation in the third overtone and second overtone modes, respectively, while both sequences B and C′ are due to dominant pulsation in the first overtone mode, and sequence C (the PL relation of Miras) is due to dominant fundamental mode pulsation.

Sequence D, on the other hand, is associated with so-called Long Secondary Periods (LSPs, see, e.g., Nicholls et al., 2009). Having longer periods than the fundamental mode, they cannot be due to the same stellar pulsation process responsible for the variability associated with other sequences. At present, there is no accepted explanation for LSPs.

### 1.2.3 Post-AGB evolution

At the end of the TP-AGB evolution, once the H-rich envelope is almost completely removed, the envelope shrinks and the stellar radius decreases at almost constant luminosity because the stars follows the CMLR and evolves along a horizontal track in the HRD towards higher $T_{\rm eff}$. This is the post-AGB phase and has a typical timescale of about $10^4$ years. The mass of the envelope decreases as a consequence of the H-shell burning at the bottom and the continuing mass loss at the top of the envelope. When the $T_{\rm eff} \approx 3 \times 10^4$ K, a weak but fast wind develops driven by radiation pressure in UV absorption lines and dust grains are destroyed by the strong UV flux. Part of the circumstellar envelope becomes ionized and the stars appears as a planetary nebula, radiating in recombination

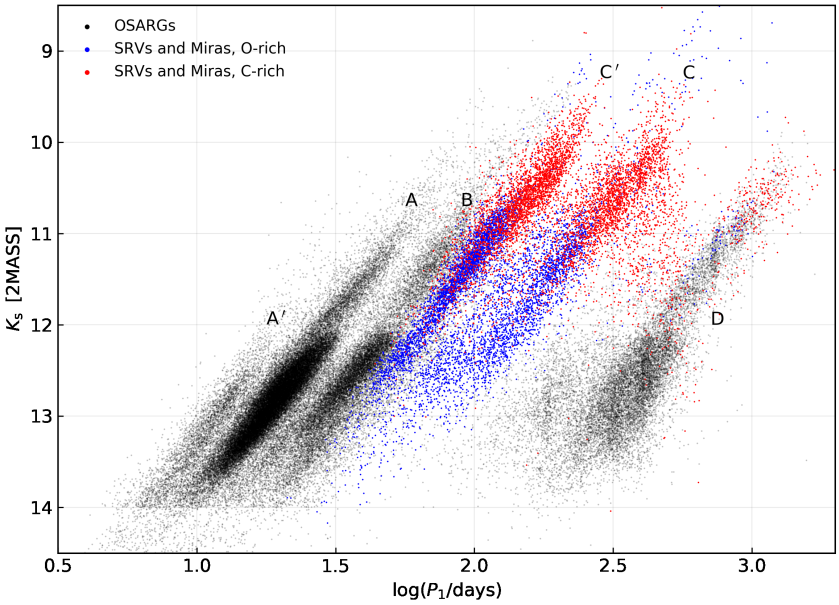


**Figure 1.8:** P-L sequences of the LMC from OGLE observations (Soszyński et al., 2009) with 2MASS photometry (Skrutskie et al., 2006). Miras and SRVs are shown as blue or red dots depending on whether they are M- or C-type stars, respectively (based on a photometric classification). Courtesy of M. Trabucchi.

lines. Finally, when the mass of the envelope has decreased enough, the H-burning shell is extinguished and the star cools down as a white dwarf.

## 1.3 The need of a robust calibration of the TP-AGB phase

TP-AGB stars contribute significantly to the total luminosity of a single stellar population, with a peak of about 40% at ages between $\approx 1$ and $\approx 3$ Gyr. Since their luminosities peak in the near-infrared and circumstellar dust emits at mid- to far-IR wavelengths, TP-AGB stars account for most of the infrared-bright objects in resolved galaxies, as demonstrated in the Magellanic Clouds (Boyer et al., 2011; Frogel et al., 1990).

Despite its importance in our understanding of galaxy evolution, the TP-AGB modelling is still affected by large uncertainties due to the presence of several and interconnected processes (third dredge-up, hot bottom burning, stellar winds, long period pulsations, reprocessing of radiation by circumstellar dust in mass-losing stars), for which a robust theory is still lacking, though promising steps have been made (Marigo et al., 2013; Herwig, 2005; Karakas and Lattanzio, 2014).

### 1.3.1 Population synthesis models and classical TP-AGB calibrators

The derivation and evolution of spectro-photometric properties of star clusters and galaxies is performed by means of Evolutionary Population Synthesis (EPS) models which are based on stellar evolution theory and predict the integrated properties of an object by adding up the contributions of the individual model stars after assuming an initial mass function (IMF) and a Star Formation History (SFH). There are basically two different techniques to include post-main sequence evolutionary phases, and in particular AGB stars, in EPS models, which are based on: (A) stellar tracks or isochrones and (B) the fuel consumption theorem (Renzini and Buzzoni, 1986). Method (A) relies on the adopted stellar models and hence is affected by stellar evolution uncertainties, but allowing a direct

comparison between predictions and observations it provides useful feedback of uncertain parameters. Method (B) makes use of empirical calibration of the nuclear fuel based on observed data and can account for the correct integrated light contribution of stellar populations, but cannot provide explicit feedback as model (A). Furthermore, while the resolution element of method (B) is the single stellar population, so that it can be used only for the derivation of integrated properties of unresolved AGB stars, for method (A) the resolution element is the single star and it can predict both resolved and unresolved properties of stellar populations.

The importance of including TP-AGB stars in stellar population synthesis model has been recognized after Maraston (2005) demonstrated that the mass-to-light ratios for old stellar populations (0.5 - 2 Gyrs) can be greatly altered by the presence of TP-AGB stars and this translates into discrepancies in the determination of stellar masses and ages of high-redshift galaxies by a factor of two or more.

Until recently, the calibration of TP-AGB evolutionary models was done mainly using observations of AGB stars in populous Magellanic Clouds' and Milky Way globular clusters (e.g. Girardi and Marigo, 2007), in which the observed numbers of the several sub-types of AGB stars could be compared to the predictions from single-age, single-metallicity models. This approach however is not completely satisfactory, and possibly fails, for a series of reasons. First, even in the most populous clusters the numbers of TP-AGB stars do not exceed two dozens, with typical numbers being much smaller, and close to unity. Second, due to the "AGB boosting" effect (Girardi et al., 2013), there is no guarantee that star counts in MC clusters of ages $\sim 1.6$ Gyr – the approximate age of the most populous ones – are proportional to the lifetime in the TP-AGB phase. Finally, the discovery of broad main sequence turn-offs in some of the most massive LMC and SMC clusters, i.e. those with the largest early escape velocity (Goudfrooij et al., 2014), and their possible connection with fast rotation (Brandt and Huang, 2015; Goudfrooij et al., 2017), opens the possibility that the clusters' population may not be representative of the stars found in galaxy fields. Due to this limitations, present-day TP-AGB models applied to external galaxies overestimate to various extents the TP-AGB contribution in integrated spectra of galaxies and star counts, hence the need of enhancing the classical calibration by the inclusion of other key properties of TP-AGB stars, such as pulsation periods and surface chemical abundances, and move beyond the MC clusters to extend the metallicity sampling.

In order to overcome these difficulties, the alternative is to use the AGB stars in galaxy regions for which the distributions of ages and metallicities are well constrained. This technique was pioneered by Groenewegen and de Jong (1993), who used the carbon star luminosity function in the Magellanic Clouds to calibrate the third dredge-up efficiency in synthetic AGB models. The same approach was later revised with increasingly more detailed models of the AGB evolution (e.g. Marigo et al., 2003, 2013, 2017), and extended to many dwarf galaxies with good determinations of their star formation histories through analysis of HST photometry (e.g. Girardi et al., 2010; Rosenfield et al., 2014, 2016).

Figure 1.9 shows the relevant area in the age-metallicity plane that needs to be covered for a reliable calibration of the TP-AGB phase. In addition to the MCs, it includes data of M31 from the Panchromatic Hubble Andromeda Treasury (PHAT) survey, dwarf galaxies from the ACS Nearby Galaxy Survey (ANGST) and the Galactic Bulge from both the OGLE and the Wide field Infrared Survey Explorer (WISE) surveys. Rosenfield et al. (2014, 2016) analyzed the star counts and the luminosity functions of TP-AGB stars in six quiescent, low metallicity ([Fe/H] $\leq$ - 0.86) galaxies taken from the ANGST sample. They confirmed the importance of pre-dust mass loss and that the third dredge-up has no significant effects on lifetimes of low-mass, low-metallicity TP-AGB stars.

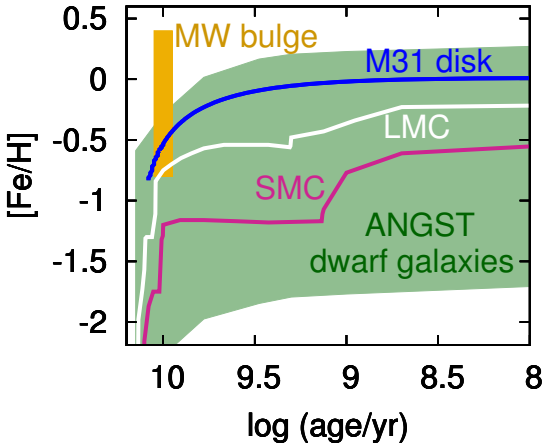


**Figure 1.9:** The relevant area in the age-metallicity plane that needs to be covered for a reliable TP-AGB calibration. In addition to the MCs, it includes M31 from PHAT data, ANGST dwarf galaxies and Galactic Bulge from OGLE and WISE data.

### 1.3.2 The STARKEY Project

My PhD Thesis work is part of the ERC project STARKEY[2]. The aim of the project is to provide calibrated and well-tested TP-AGB stellar tracks, isochrones in all photometric systems, chemical yields and variability information. These products will be eventually included in stellar population synthesis models of galaxies. The approach relies on the integration of theoretical tools able to account for the complex physics of AGB stars, i.e. evolution, nucleosynthesis, stellar pulsation and winds, dust formation and reprocessing of the radiation by circumstellar dust in mass-losing stars, and high-quality observations of resolved stellar populations in nearby galaxies with accurate identification and classification of AGB stars (C-, M-stars) and robust measurements of their Star Formation History. A global calibration method is adopted and the models are required to simultaneously reproduce a set of well-defined observational constraints, i.e. colours and luminosity distributions, star counts, pulsation periods. A scheme to illustrate the general calibration method is shown Figure 1.10.

Over the last decade, the quality of the Magellanic Cloud data necessary to perform this calibration work has improved significantly. First, catalogues of candidate TP-AGB stars were extended, from the initial near-infrared samples provided by DENIS (Cioni et al., 2000) and 2MASS (Nikolaev and Weinberg, 2000; Cutri et al., 2003), to include the mid-infrared data from *Spitzer* SAGE surveys (Boyer et al., 2011); moreover, a non-negligible fraction of the SMC field TP-AGB stars now have a spectroscopic classification. Second, a significantly better description of the space-resolved distribution of stellar ages, metallicities, distances, and mean extinctions across the SMC galaxy, is now available thanks to deep near infrared photometry of the VISTA survey of the Magellanic Clouds. Equally important are the significant improvements in the physical prescriptions adopted in TP-AGB evolutionary models, and the possibility of performing extremely fast calculations of extended model grids with the `COLIBRI` code. These better data and better models open the possibility of improving the calibration of the most uncertain processes in TP-AGB models. In this Thesis I used the population synthesis code `TRILEGAL` (Girardi et al., 2005) to produce synthetic samples of TP-AGB stars in the SMC. The predicted

[2]Solving the TP-AGB STAR Conundrum: a KEY to Galaxy Evolution - ERC Consolidator Grant funding scheme ( *project STARKEY*, G.A. n. 615604) , PI Prof. Paola Marigo

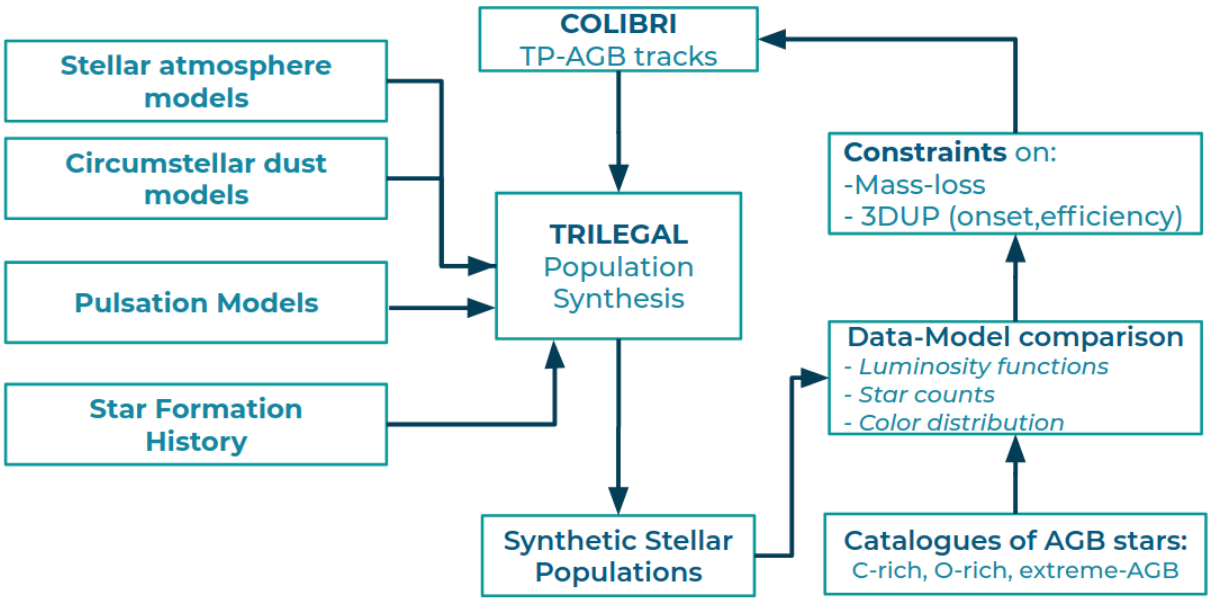


**Figure 1.10:** Scheme of the calibration method adopted in the STARKEY project. The inputs required to produce accurate simulations of AGB star populations include stellar atmosphere models and circumstellar dust models from which bolometric corrections are calculated. This is particularly important for mass-losing C-rich and O-rich stars. Fitting relations from linear pulsation models calculation are included in `TRILEGAL` to predicted the periods of LPVs. A reliable measurement of the SFH is fundamental to obtain a reliable synthetic population of AGB stars to be compared with observation of AGB stars accurately identified and classified. The flexibility and the computational agility of `COLIBRI` code allows the computation of extended grid of stellar evolutionary tracks with different input prescriptions for the mass-loss and the third dredge-up. The calibration of such uncertain processes is performed through an iterative approach: the simulations are compared to the data in terms of star counts, luminosity functions and colour distributions; the discrepancies between the data and the model are used to constrain the uncertain processes of mass-loss and third dredge-up; a complete set of TP-AGB tracks is computed in response to these discrepancies until a satisfactory reproduction of the observation is reached.

star counts, luminosity functions (LFs), and color distributions are compared to the observed ones from the AGB candidate list by Srinivasan et al. (2016, hereafter SR16). This allows to put quantitative constraints on lifetimes and efficiency of the critical processes of mass-loss and third dredge-up.

## 1.4 Outline of this Thesis

The main purpose of this Thesis is to provide a grid of models that simultaneously reproduce the observed luminosity functions of the AGB population and the sub-classes of C-rich, O-rich and dusty/extreme AGB stars in the Small Magellanic Cloud. In *Chapter 2* I will describe the stellar models used in this work, including the `PARSEC-COLIBRI` evolutionary tracks and the resulting stellar isochrones; the stellar atmosphere models from which bolometric corrections are calculated for the synthetic stars, and in particular for C-rich and O-rich giants; the bolometric corrections for mass-losing AGB stars derived from dust formation models and radiative transfer calculations. Given the importance of the Star Formation History in the calibration work, *Chapter 3* is dedicated to the derivation of the SFH of the SMC. The calibration of TP-AGB models in the SMC, which is the main part of this Thesis, is presented in *Chapter 4*. Here, the available observations of the AGB stars in the SMC are described; the calibration strategy is also presented in addition to the fundamental steps of the calibration that allows to reproduce the SMC photometry. The implications of the input 3DU and mass-loss prescriptions of best-fitting models are discussed and finally a full characterisation of the AGB population of the SMC in terms of stellar parameters is presented. *Chapter 5* includes the results of the modelling of AGB stellar populations in additional nearby objects. The first Section is dedicated to the modelling of the Long Period Variables (LPVs) in the Large Magellanic Clouds as observed by Gaia. The remarkable agreement between models and observations allows us to guide the interpretation of a new observational diagram that is able to photometrically distinguish the evolutionary stages, the initial masses and the chemical type of these stars. In the second Section, I present the simulations of the Magellanic Clouds that together with the all-sky simulations of the Milky Way will be made available to the community through the NOAO Data Lab to help to define the observing strategy of the Large Synoptic Survey Telescope mini-surveys. Finally, I present the preliminary results of the comparison between the best-fitting models calibrated in the SMC with the AGB populations of a sample of Local Dwarf Galaxies observed within the DUSTiNGs photometric survey program and a combination of narrow band filters of HST that allows to photometrically distinguish C-rich and O-rich stars. The conclusions and the future perspectives are presented in *Chapter 6*.

# Chapter 2

# Stellar Models

In order to take into account AGB stars in models of galaxies and in particular the contribution of carbon stars, three major ingredients are necessary. First, evolutionary tracks must be able to provide the distributions of luminosities, effective temperatures and surface compositions of red giants as a function of age, initial mass and metallicity. The stellar models used in this work will be described in Sections 2.1 and 2.2 . Secondly, synthetic spectra are necessary to allow the conversion of model quantities into observable properties of stars. In Section 2.3 the stellar atmosphere models in use will be presented. The last but equally important point is the modelling of the circumstellar reddening by dust, described in Section 2.4. The purpose of this work is the calibration of the TP-AGB phase but given the adopted approach of simulating the photometry of all stellar populations, the above mentioned ingredients are needed also for the phase preceding the TP-AGB evolution.

## 2.1 PARSEC evolutionary tracks

The evolution from the PMS up to the first thermal pulse is computed with the PARSEC code for which a detailed description is provided by Bressan et al. (2012, 2013, 2015). The grid of evolutionary tracks includes 15 values of initial metallicity, $Z_{\rm i}$, from 0.0001 to 0.06. The initial mass ranges from 0.1 to 350 $M_{\odot}$ (about 120 mass values for each metallicity). The set of PARSEC tracks used in this work are fully described in Bressan et al. (2012, 2013) and more recent updates can be found in Chen et al. (2014); Tang et al. (2014); Chen et al. (2015). Here we recall the main novelties and ingredients.

**Solar composition and heavy elements.** For each element heavier than $^4$Helium its fractional abundance is assigned relative to the total solar metallicity, i.e. $(X_{\rm i}/Z) = (X_{\rm i,\odot}/Z_{\odot})$. The helium initial content follows the relation $Y_{\rm i} = 1.78\,Z_{\rm i} + 0.2485$ that reproduces the primordial Helium content (Komatsu et al., 2011) and the chemical composition of the present Sun ($Z_{\odot}$= 0.01774, $Y_{\odot}$ = 0.28; see Bressan et al. (2013) for details). Finally, the reference solar-scaled composition is from Caffau et al. (2011).

**Opacities.** The opacity of the stellar matter has been evaluated by means of pre-computed Rosseland mean opacities $\kappa_R(\rho, T)$, thus it depends on temperature and density, but also on the gas chemical composition specified by the X and Y abundances and by the distribution of heavy elements. At high temperature, in the range $4.2 \leq \log(T/K) \leq 8.7$, the opacities are those provided by the Opacity Project At Livermore (OPAL) while at lower temperature ($3.2 \leq \log(T/K) \leq 4.1$), they have been computed through the ÆSOPUS code.

A linear interpolation between the opacities from OPAL and ÆSOPUS has been adopted for the temperature in the transition region $4.1 \leq \log(T/K) \leq 4.2$. Two distinct sets of opacity tables are generated: the H-rich one and the H-free one ($X = 0$) that describes the opacities for the He-burning regions.

**Convection and overshooting.** The overshoot across the border of core convective regions is described by the parameter $\Lambda_c$, which is the mean free-path of fluid elements (mixing length) and it is proportional to the local pressure scale height. The overshoot parameter $\Lambda_c$ in the convective H-core is chosen according to the stellar mass in order to describe the transition between radiative and convective cores: $\Lambda_c = 0$ for $M \leq M_{O1}$, $\Lambda_c$ increases linearly up to $\Lambda_{max} = 0.5$ between $M \leq M_{O1}$ and $M \leq M_{O2}$, $\Lambda_c = \Lambda_{max}$ for $M \geq M_{O2}$. The values of $M = M_{O1}$ and $M = M_{O2}$ depend on the initial chemical composition. The overshoot efficiency in the convective envelope is tratead as in Alongi et al. (1991) and Bressan et al. (1993), with $\Lambda_e = 0.05$ for $M \leq M_{O1}$ and $\Lambda_e = 0.7$ for $M \geq M_{O1}$, the transition between these two values is smooth. In the core helium burning stage, the value $\Lambda_c = 0.5$ is used for all stellar masses. Examples of stellar evolutionary tracks are shown in Figure 2.1 for three different values of the initial metallicity, Z=0.001, 0.004, 0.017.

## 2.2 COLIBRI evolutionary tracks

The COLIBRI code, fully described in Marigo et al. (2013), is used to compute stellar models starting from the first thermal pulse (or earlier during the early-AGB phase) until the almost complete loss of the envelope by stellar winds. The initial conditions for each stellar model with initial parameters ($M_i$,$Z_i$) at the first thermal pulse (core-mass, luminosity, effective temperature, envelope chemical composition) are taken from the PARSEC data base. The COLIBRI code represents a fundamental step forward in the development of envelope-based TP-AGB models (Marigo and Girardi, 2007) and the numerous improvements implemented make it perform much more like an "almost-full" model rather than an "improved synthetic" one. The robust numerical stability and the high computational speed of the code allow to perform a multiparametric and accurate calibration of the TP-AGB phase. With respect to purely-synthetic TP-AGB models, COLIBRI relaxes a significant part of the analytic formalism in favour of detailed physics applied to complete envelope models, integrated from the atmosphere down to the H-burning shell. A direct consequence of this approach is the possibility to follow the basic changes in the envelope and both the energetics and nucleosynthesis of the HBB with a level of accuracy than can even go beyond the accuracy of full models.

In the following, a brief summary of the COLIBRI features is presented, while the reader should refer to Marigo et al. (2013) for a detailed description of all input physics and the solutions method adopted, as well as the analytic relations of COLIBRI.

- **Opacities.** One of the most important feature is the accurate *on-the-fly* computation of the equation of state for roughly 800 atoms and molecular species, as well as the Rosseland mean opacities throughout the atmosphere and the deep envelope. This has been obtained by the inclusion of the ÆSOPUS code (Marigo and Aringer, 2009) for $3.2 \leq \log T \leq 4.2$ and the *Opacity Project* (OP) code (Badnell et al., 2005; Seaton, 2005) for $4.2 \leq \log T \leq 8$, as internal routines in COLIBRI. This technique allows in particular to follow in detail the evolution of the surface C/O ratio which is fundamental because of the dramatic impact on molecular chemistry, opacity, effective temperature resulting from the transition between C-rich and O-rich com-

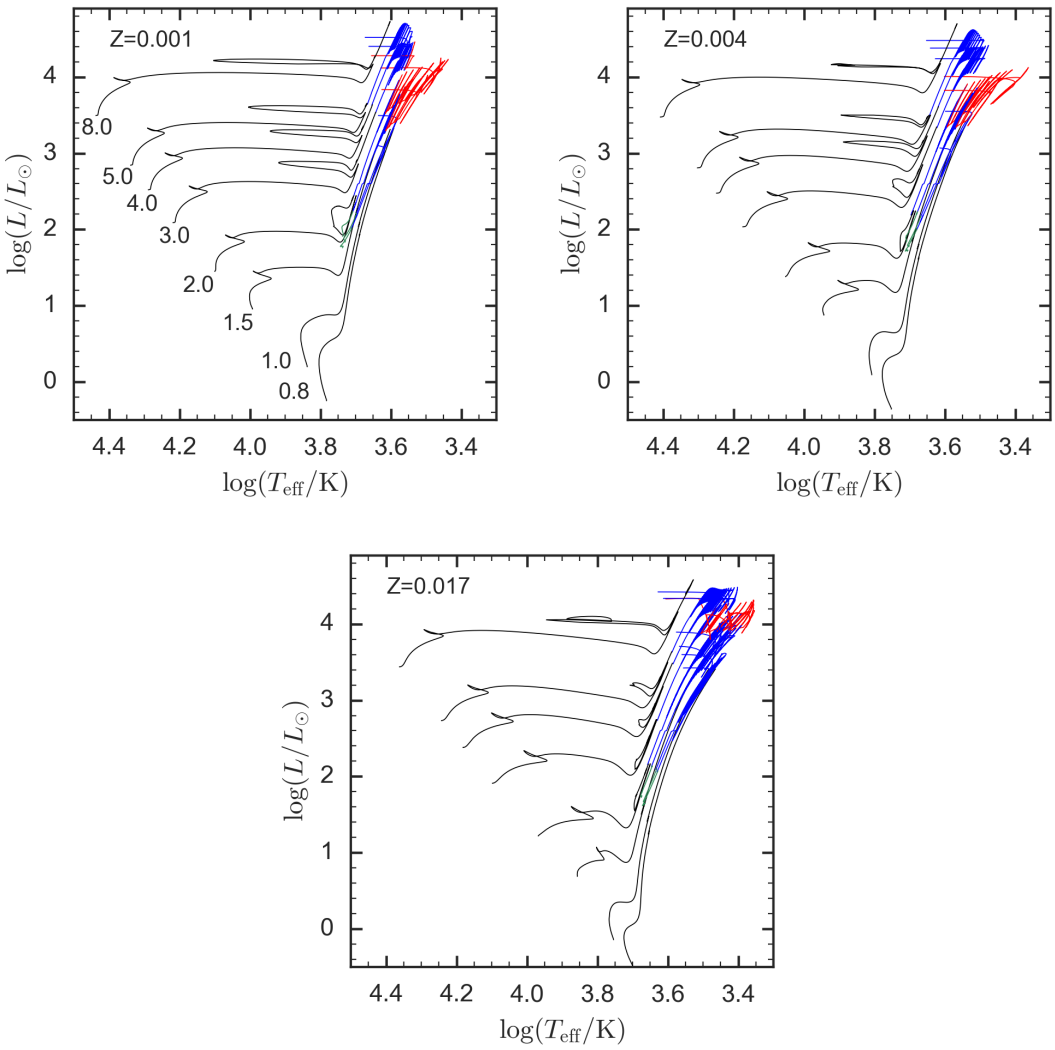


**Figure 2.1:** Evolutionary tracks for stars with Z=0.001 and masses of 1, 1.5, 2, 3, 4, 5 $M_{\odot}$. The blue lines correspond to thermal pulses developed when C/O $< 1$, red lines correspond to thermal pulses when C/O $> 1$. The He-burning phase of low-mass stars is plotted in green. The evolution prior to the TP-AGB phase is computed with `PARSEC` code, while the subsequent evolution, until the entire envelope is lost, by means of `COLIBRI` code.

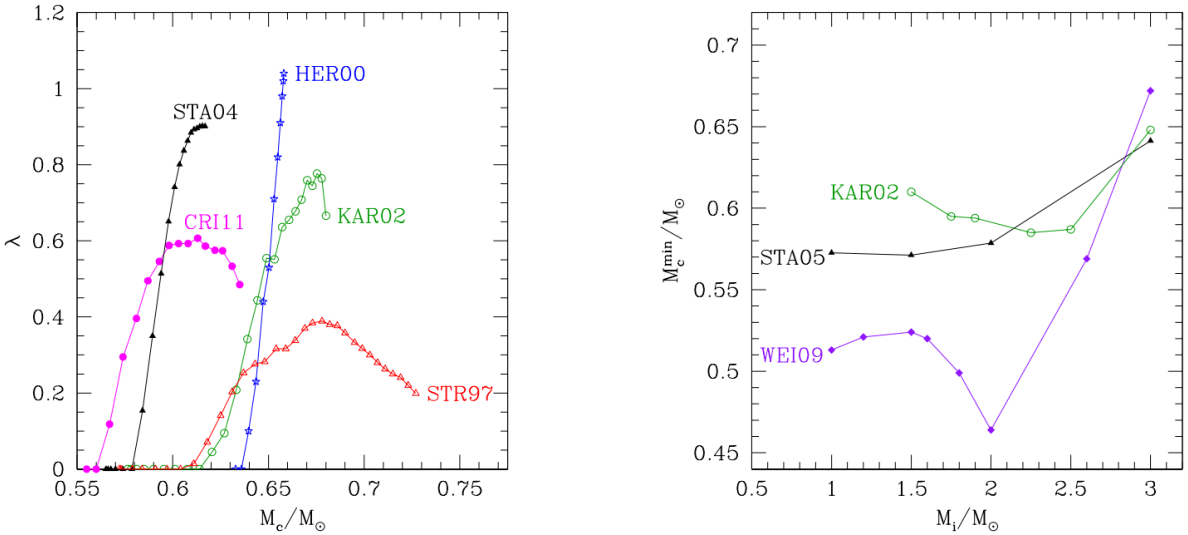


**Figure 2.2:** Comparison of various full TP-AGB models calculations (CRI11, Cristallo et al., 2011), (WEI09, Weiss and Ferguson, 2009), (STA05, Stancliffe et al., 2005), (STA04, Stancliffe et al., 2004), (KAR02, Karakas et al., 2002), (HER00, Herwig, 2000), (STR97, Straniero et al., 1997) for the efficiency $\lambda$ of the third dredge-up of 3 $M_{\odot}$ and $Z_{\rm i}$= 0.02 models (left panel) and the minimum core mass $M_{\rm c}^{\rm min}$ for the onset of the mixing events for $Z_{\rm i}$=0.008(right panel). Figure from Marigo et al. (2013).

position, as well as for the chemical and physical properties of the dust, as described in Section 2.4.

- **Hot Bottom Burning.** Another substantial improvement is related to the description of the HBB process which is described by coupling a complete nuclear network with a time-dependent diffusion scheme for convection. This approach allows to treat the lithium nucleosynthesis in intermediate-mass AGB stars with HBB. In the case of $^7$Li and $^7$Be nuclei, the usual approximation of *instantaneous mixing* in the whole convective envelope is no longer valid and $^7$Li nucleosynthesis follows the *Cameron-Fowler beryllium transport mechanism*: in the outermost layers $^7$Li is efficiently produced and sustained by electron captures on $^7$Be nuclei until the reservoir of $^3$He is exhausted or HBB is extinguished due to envelope ejection by stellar winds. In addition, COLIBRI allows to compute the nucleosynthesis of CNO, NeNa and MgAl cycles which is of particular interest in the context of multiple stellar populations in globular clusters. In the so-called self-enrichment scenario, the HBB nucleosynthesis in metal-poor AGB stars could explain the anticorrelations (CN, ONa, MgAl) observed in galactic globular clusters. COLIBRI gives the possibility to investigate the chemical yields of low metallicity AGB stars and put important constraints on the different scenarios of origin of multiple stellar populations.

- **Third dredge-up.**

  The convective mixing in full TP-AGB models is affected by large uncertainties and the predicted onset and efficiency of the third-dredge up vary from author to author. As shown in Figure 2.2, where the predictions of various full models are compared, there are substantial variations, especially for the maximum dredge-up efficiency. This justifies the parametric scheme adopted in our TP-AGB models as described in Marigo et al. (2013).

  In summary we need to specify three main characteristics of the third dredge-up: i) the onset, ii) the efficiency, and iii) the chemical composition of the intershell

material.

The occurrence of a mixing event is usually checked with a parameter, $T_{\rm b}^{\rm dred}$, that defines the minimum temperature that should be reached at the base of the convective envelope at the stage of the maximum post-flash luminosity. Typical values lie in the range $6.3 \leqslant \log(T_{\rm b}^{\rm dred}/{\rm K}) \leqslant 6.7$. At each thermal pulse the `COLIBRI` code performs complete envelope integrations to check whether the temperature criterion is satisfied or not.

Another choice, equivalent to $T_{\rm b}^{\rm dred}$, is the classical parameter $M_{\rm c}^{\rm min}$ that defines the minimum core mass for the onset of sequence of third dredge-up events. Typical values are usually within the range $0.54 M_{\odot} \leqslant M_{\rm c}^{\rm min} \leqslant 0.60 M_{\odot}$.

The efficiency of each mixing event is usually described by the parameter $\lambda = \Delta M_{\rm dred}/\Delta M_{\rm c}$, the fraction of the increment of the core mass during an inter-pulse period that is dredged-up at the next thermal pulse. Typical values are in the range between $\lambda = 0$ (no dredge-up) and $\lambda = 1$ (i.e. no net increase of the core mass), even though cases with $\lambda > 1$ are predicted in models that assume efficient convective overshoot (e.g., Herwig, 2004).

A detailed description of the parametrization of the third dredge-up is given in Section 4.3.4.

- **Intershell composition.** The chemical composition of the intershell just before the occurrence of a dredge-up episode consists mainly of $^{4}$He, primary $^{12}$C and $^{16}$O, $^{22}$Ne, and other less abundant species (such a $^{23}$Na, $^{25}$Mg, heavy nuclei produced by the slow-neutron capture reactions). Standard calculations of the thermal pulse nucleosynthesis predict typical abundances (in mass fraction) $^{4}{\rm He}/^{12}{\rm C}/^{16}{\rm O} \approx 0.70/0.26/0.01$, characterized by a low contribution of oxygen. The application of the convective overshoot at the formal Schwarzschild boundaries of the pulse-driven convection zone has the effect of increasing both carbon and oxygen abundances at the expense of helium, as first shown by Herwig et al. (1997), with typical proportions $^{4}{\rm He}/^{12}{\rm C}/^{16}{\rm O} \approx 0.23/0.50/0.25$ (depending on the assumed efficiency for convective overshoot). In the `COLIBRI` code the pulse-driven nucleosynthesis is computed coupling a synthetic description of the intershell with a complete nuclear network which includes the most important $\alpha$-capture reactions. In addition, we have the possibility to explore the impact of various efficiencies of the convective overshoot (refer to section 7.5.5 in Marigo et al., 2013). In the present work we limit to consider the standard case for the intershell composition (i.e. no overshoot, oxygen-poor case) and we plan to extend our investigation about the impact of an oxygen-rich intershell to a future study.

- **Mass-loss rates.** The treatment of mass loss in AGB models is critical since it controls the duration of the phase, which normally terminates when the whole envelope is ejected into the interstellar medium. The abundant literature on the topic proves that over the years substantial efforts have been devoted to understand the physical mechanisms responsible for mass loss in AGB stars, and more generally in red giants (see Höfner and Olofsson, 2018; Willson, 2000, for extensive reviews). While the key roles of stellar pulsation and dust growth are today universally acknowledged, a comprehensive theoretical framework is still missing. Likewise assumed in earlier studies (Girardi et al., 2010; Rosenfield et al., 2014, 2016), in this work we adopt a scheme that considers two regimes of mass loss, which we shortly refer to as "pre-dust mass loss" (with a rate $\dot{M}_{\rm pre-dust}$) and "dust-driven mass loss" (with a rate $\dot{M}_{\rm dust}$), respectively.

In our scheme the pre-dust mass loss corresponds to red giant stages, characterized by relatively low luminosities and high effective temperatures, which set unfavourable conditions for a stellar wind to be driven by radiation pressure on dust grains. During these phases mass loss should be produced by another, still not clearly identified, mechanism. Plausible candidates are the Alfvén waves and the turbulence that originate in cool extended chromospheres (e.g., Cranmer and Saar, 2011; Schröder and Cuntz, 2005). In this work we test two formalisms for $\dot{M}_{\rm pre-dust}$: the Schröder and Cuntz (2005) relation modified following Rosenfield et al. (2016), and the algorithm developed by Cranmer and Saar (2011). This latter, in particular, predicts $\dot{M}_{\rm pre-dust}$ that is driven by the pressure of Alfén waves, likely produced by stellar rotation.

At later stages along the AGB, we assume that the chromospheric mass loss is quenched and the outflow is accelerated by the radiation pressure on dust grains thanks to the dust–gas dynamical coupling. Several relations for $\dot{M}_{\rm dust}$, as a function of stellar parameters $(M, L, T_{\rm eff}, Z)$, are available in the literature. Here we investigate a few among the most popular ones, i.e. the Vassiliadis and Wood (1993) which relates the efficiency of mass loss with the pulsation period, and the Bloecker (1995) which is characterized by a significant dependence on the luminosity. In addition, we use the recent results of dynamical atmosphere models (Mattsson et al., 2010; Eriksson et al., 2014) to predict $\dot{M}_{\rm dust}$ as a function of the carbon excess, C − O, in carbon stars.

During the TP-AGB evolutionary calculations, if not otherwise specified, the current mass-loss rate is taken as:

$$\dot{M} = \max(\eta_{\rm pre-dust} \times \dot{M}_{\rm pre-dust},\, \eta_{\rm dust} \times \dot{M}_{\rm dust})\,, \tag{2.1}$$

where $\eta_{\rm pre-dust}$ and $\eta_{\rm dust}$ are adjustable efficiency parameters.

At each calibration step, for each selected combination of free parameters, to obtain a complete grid of stellar evolution models that cover a large range of metallicities, from very low to super-solar values, we need to compute ≈ 1000 TP-AGB tracks in the domain of low- and intermediate-mass stars. New grids of TP-AGB tracks need to be computed every time an input prescription is changed. The `COLIBRI` turns out to be suitable tool to carry out this kind of demanding procedure.

## 2.3 Stellar atmospheres models and bolometric corrections

In order to directly compare the predictions of stellar models with observations, one of the fundamental steps is the construction of an assembly of spectral fluxes, covering wide enough ranges of initial metallicities, effective temperatures and surface gravity values, which allow the conversion from model predicted quantities (luminosity, effective temperature) to observed quantities (magnitudes and colours). Evolutionary tracks obtained by stellar model calculations must be transformed into isochrones, which in turn must be converted to the photometric system of interest by means of the appropriate bolometric corrections. Given the spectral flux at the stellar surface, bolometric corrections for any set of filter transmission curves are calculated following the approach of Girardi et al. 2002. The library of stellar spectra is in constant updating, in particular synthetic spectra for cool evolved stars have been derived and included in the more recent version of the `TRILEGAL` code.

The sets of bolometric corrections adopted in this work are based on different library of stellar spectra according to the spectral type and surface temperature:

- **"Hot stars".** The term "hot stars" refers to stars with effective temperature larger than about 4000 K. In this case, the bolometric corrections are based on stellar atmospheres models computed with the ATLAS9 code and the new Opacity Distribution Functions (ODFNEW; Castelli & Kurucz 2003). The model grids cover a temperature range between $3500 - 50000$ K and are computed for metallicities [M/H] $= 0.0, -0.5, -1.0, -1.5, -2.0, -2.5,\ 0.5, 0.2$ and for gravity values from $\log g = 0.0$ to $\log g = +5.0$ in steps of $+0.5$.

- **Cool C-rich giants.** The library of C-star spectra is from Aringer et al. (2009, hereafter A09), which have produced hydrostatic atmosphere models with the COMARCS code, covering a range of $T_{\rm eff}$ between 2400 and 4000 K, surface gravities from $\log g = 0.0$ to $\log g = -1.0$, metallicities from $Z_\odot$ to 1/10 $Z_\odot$ and C/O ratios from 1.05 up to 5.0. The predicted $J-K_{\rm s}$ colours for a C-rich stars of 1 $M_\odot$ and $Z_{\rm i} \approx 0.005$ are shown in Figure 2.4.

- **Cool O-rich giants.** The library of stellar spectra has been derived from COMARCS atmosphere models (Aringer et al., 2016) covering the same ranges of effective temperature, metallicities, gravity and C/O ratio values as in A09. Figure 2.3 shows a comparison between the predicted $J-K_{\rm s}$ colours of O-rich giants adopting the version spectral libraries used in Marigo et al. (2008) an the present version that includes the Aringer et al. (2016) models.

All of the bolometric corrections for cool giants are derived from hydrostatic model atmospheres which do not take into account either the influence of dynamical processes, such as pulsation and mass-loss, nor the reddening due to circumstellar dusty envelopes. As a direct consequence, these models fail to reproduce the "tail" of extreme AGB stars in the Magellanic Clouds. This feature is instead reproduced when the bolometric corrections include the dust effect. However, C-star bolometric corrections based on A09 atmosphere model results to be one of the fundamental improvement since the work of Marigo et al. (2008).

## 2.4 Radiative transfer calculations across dusty envelopes

The general effect of dust is to shift part of the intrinsic emitted power of a source from the optical-ultraviolet to the mid- and far- infrared region of the spectrum. Moreover, the envelopes of AGB stars are considered to be one of the two main producers of interstellar grains together with supernoavae explosions. Taking into account the effects of the reprocessing of photospheric radiation by the dusty Circumstellar Envelopes (CSEs) of cool giants is fundamental to succeed in reproducing the photometric properties of redder and cooler AGB stars.

The determination of the optical properties of dust, i.e. the efficiency of absorption and scattering as a function of wavelengths, which basically depends on dust composition and grain size distribution, is a very complex issue for AGB envelopes. First of all, composition and grain size are expected to be very different from the ones present in the Interstellar Medium. Furthermore, the strong mass-loss experienced by AGB stars is also dependent on the dust composition. The overall picture is that despite the observational and theoretical progress, the dust formation and evolution in AGB stars is still affected by large uncertainties.

The effects of circumstellar dust in mass-losing AGB stars has been included in `TRILEGAL` since the work of Marigo et al. (2008). Tables of spectra are computed for a few dust mixtures (Groenewegen, 2006) and then interpolated to produce tables of bolometric

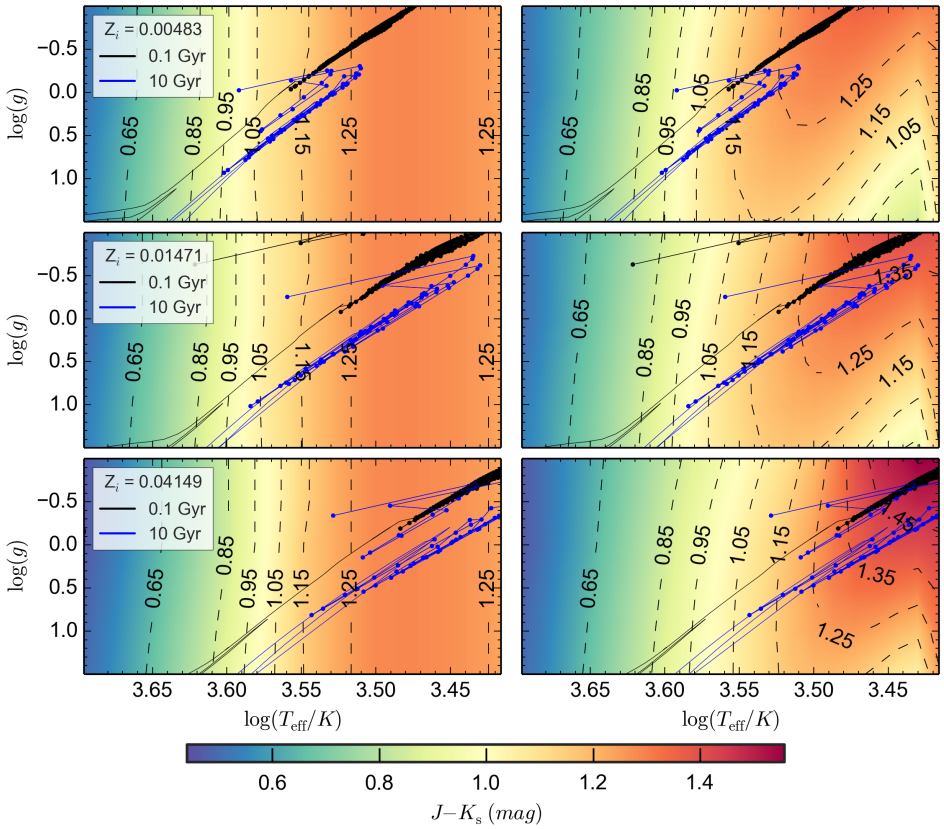


**Figure 2.3:** Map of the 2MASS $J-K_\mathrm{s}$ colours attributed to O-rich giants of metallicities [M/H] = −0.5, 0, and +0.5 (top, middle and bottom panels, respectively), as a function of $\log T_\mathrm{eff}$ and $\log g$, for two cases: the previous spectral library used in Marigo et al. (2008) (left panels), and the present one which incorporates the Aringer et al. (2016) results (right panels). A couple of isochrones with ages of 0.1 and 10 Gyr and initial $Z_\mathrm{i}$ = 0.00483 (top panels), $Z_\mathrm{i}$ = 0.01471 (middle panels) and $Z_\mathrm{i}$ = 0.04149 (bottom panels) are shown for comparison, displaying in particular the TP-AGB part – recognizable by the zig-zag during thermal-pulse cycles, at $\log g \lesssim 0.5$. Only the O-rich section of these isochrones is plotted. We note in particular that with the present prescriptions (right panels) the colours of the coolest giants depend on $\log g$ and [M/H], while with the former prescriptions (left panels), only the dependence with $T_\mathrm{eff}$ was being considered.

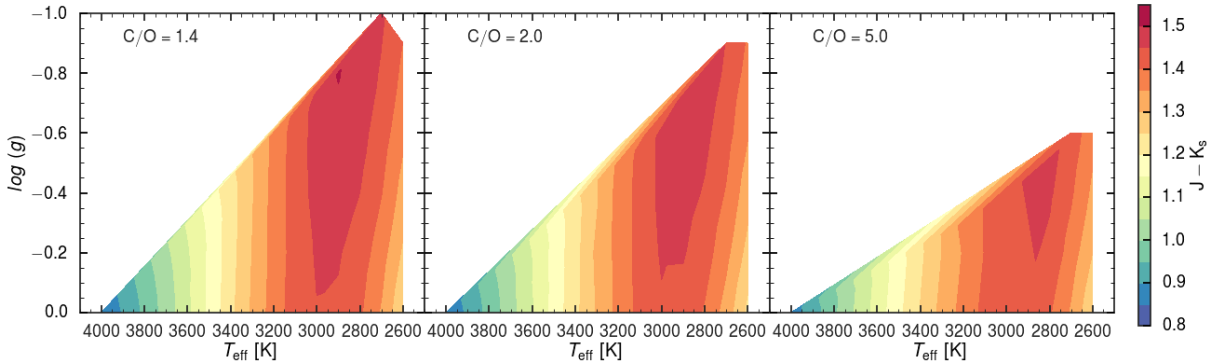


**Figure 2.4:** Same as Figure 2.3 but for C-rich stars Aringer et al. (2009). The three panels show the expected $J-K_\mathrm{s}$ colours for C-rich stars of 2 $M_\odot$ and metallicity 0.005.

corrections. The synthetic spectra are calculated with a 1-dimensional code that solves the radiative transfer equation and the thermal balance equation in a self-consistent way. The available dust mixtures for O-rich stars are (1) 100% Aluminium Oxide (AlOx) (2) a combination of 60% AlOx and 40% silicates (3) 100% silicates, and for C-rich stars (1) a combination of 85% Amorphous Carbon (AMC) and 15% Silicon Carbide (SiC) (2) 100% AMC. For a detailed description of the models, the reader can refer to the respective papers, while the detailed procedure to include the dust effect in the isochrones is described in Marigo et al. (2008). With respect to the original set of bolometric corrections used in Marigo et al. (2008), a few modifications have been implemented in the present work as explained in Section 4.2.1.

A second set of bolometric corrections is available since Marigo et al. (2017). These tables are based on a model for condensation and growth of dust grains developed by Nanni et al. (2013, 2016). These models include a formalism of dust growth coupled with a stationary wind for both O-rich and C-rich stars. The species for which the evolution is calculated are corundum ($Al_2O_3$), quartz ($SiO_2$), iron, olivine and pyroxene for O-rich stars, whereas for C-rich stars amorphous carbon (AMC), silicon carbide (SiC) and iron are considered. In this model, dust formation in CSEs of AGB stars is assumed to be a two-step process. First, the more stable compounds (seed nuclei) form from the starting molecules, then the accretion proceeds by adding other molecules on the surface of the seed nuclei. The process of dust growth can trigger a dust-driven wind if the radiation pressure of the photons onto the dust grains overcomes the gravitational pull of the star. This dust formation model requires as input the characteristic stellar parameters, such as the mass-loss rate, the luminosity, effective temperature, the actual stellar mass, and the atmospheric gas abundances, including the C/O ratio, or alternatively, the *carbon excess* defined as

$$\mathrm{C} - \mathrm{O} = \log(n_\mathrm{C} - n_\mathrm{O}) - \log(n_\mathrm{H}) + 12. \tag{2.2}$$

For each combination of these input quantities, the outcome of the model characterises the properties of the dust produced in the CSE in terms of chemistry, dust relative abundances, dust condensation fractions, grain sizes, condensation temperatures. Other relevant outputs concern the outflow dynamics, in particular the outflow expansion velocity.

Differently from the first set of models, some important quantities such as, the dust composition, its optical properties and so on, are self-consistently computed. It is worth noticing that the outcome of the dust formation model is dependent on the combination of the adopted stellar parameters. The dust formation model is coupled with the radiative transfer code MoD (More of Dusty) developed by Groenewegen (2012) which is based on DUSTY by Ivezic et al. (1999). In particular, some of the outputs of the dust formation code, such as a) the optical depth at a given wavelength , b) the dust condensation temperature, c) the dust optical properties (dependent of the dust composition) d) the stellar photospheric spectrum, are employed as input parameters for the radiative transfer calculation for each CSEs. A detailed description of the implementation of these models in the stellar isochrones is given in Marigo et al. (2017). In short, from a large set of synthetic spectra, grid of bolometric corrections are calculated. Such grids include all relevant combination of input stellar parameters and the resulting value of the dust extinction in the selected photometric passbands. Present models are calibrated to reproduce the colour-colour relations of carbon and extreme AGB stars in the SMC (Nanni et al., 2018). To apply these corrections, for each synthetic stars or for each isochrone point, a multi-dimensional interpolation over the pre-computed grids is performed to assign the dust extinction value to each star. The implementation of these new formalism, already available as an alternative option to the Marigo et al. (2008) approach has been subject of extensive tests that I carried out during my PhD project. Despite the improvements

in the treatment of the circumstellar dust with respect to Marigo et al. (2008), the grid of bolometric corrections based on Nanni et al. (2013, 2016) need to be further tested to ensure a proper and correct application to synthetic stellar populations and isochrones. The main issues are essentially related to technical details in the interpolation over the six-dimensional grid of models. Since the implementation of these models is presently under revision, the adopted set of bolometric corrections used in this work rely on the approach of Marigo et al. (2008).

## 2.5 PARSEC-COLIBRI stellar isochrones

COLIBRI usually starts from a stellar configuration with the same core mass and envelope composition as a PARSEC model just prior to its first significant thermal pulse. The subsequent pieces of tracks are then joined, inside TRILEGAL, to form continuous tracks spanning from the pre main-sequence to the end of the TP-AGB. As illustrated in Marigo et al. (2013), there is in general a quite good continuity in evolutionary properties as a given track is continued from PARSEC to COLIBRI. However, PARSEC tracks are computed at constant mass, whereas in this work we allow for the possibility that mass-loss occurs before the first thermal pulse. Therefore, we adopt an additional step before joining PARSEC and COLIBRI tracks: along the final sections of the PARSEC tracks (corresponding to Early-AGB stages), we compute the mass-loss rate according to the adopted mass-loss formalism. At each time step, the effective temperature along the PARSEC track is re-evaluated, using the envelope integration routines in the COLIBRI code, together with the corrected stellar mass. The entire procedure is justified by the fact that, as the TP-AGB is approached, the luminosity and the rate of brightening are mainly controlled by the core mass, and are much less sensitive to the envelope mass. The effect of accounting for mass loss during the Early-AGB is discussed in Sect. 4.3.3.

The evolutionary tracks are converted into isochrones that can be used in the populations synthesis simulations. I refer to Marigo et al. (2017) for a description of the method adopted in producing the isochrones. For the present work, it worth mentioning a few among the numerous improvements, specifically performed for the inclusion of the TP-AGB phase. The isochrones contain the information of the surface chemical abundance of H, He, C, N, O and current metallicity $Z$.

As shown in Figure 2.5, these values change along the isochrones as a result of the microscopic diffusion (especially during the MS of low-mass stars), of dredge-up events, and of HBB at the most massive TP-AGB stars. The metallicity variation due to second dredge-up in intermediate-mass stars and due to the first dredge-up along the RGB are also present in the isochrones. Furthermore, the variation in luminosity, effective temperature and chemical abundances along the thermal pulse cycles (TPCs) are recorded in the isochrones[1]. As an example, Figure 2.6 shows the luminosity and the effective temperatures as a function of the initial mass for two isochrones sections. In the left panel an intermediate-age isochrone is shown near the transition from the O- to the C-rich as a consequence of the 3DU. The right panel shows a younger isochrone in which the effect of HBB is weakened by the mass-loss resulting again in the transition O- to C-rich.

[1]The scheme adopted is intended to insert the TPC variations in the isochrones in a smooth, idealistic way, but at the same time with enough TPCs to provide a detailed probabilistic description of the expected distribution of the stellar parameters in a given stellar population.

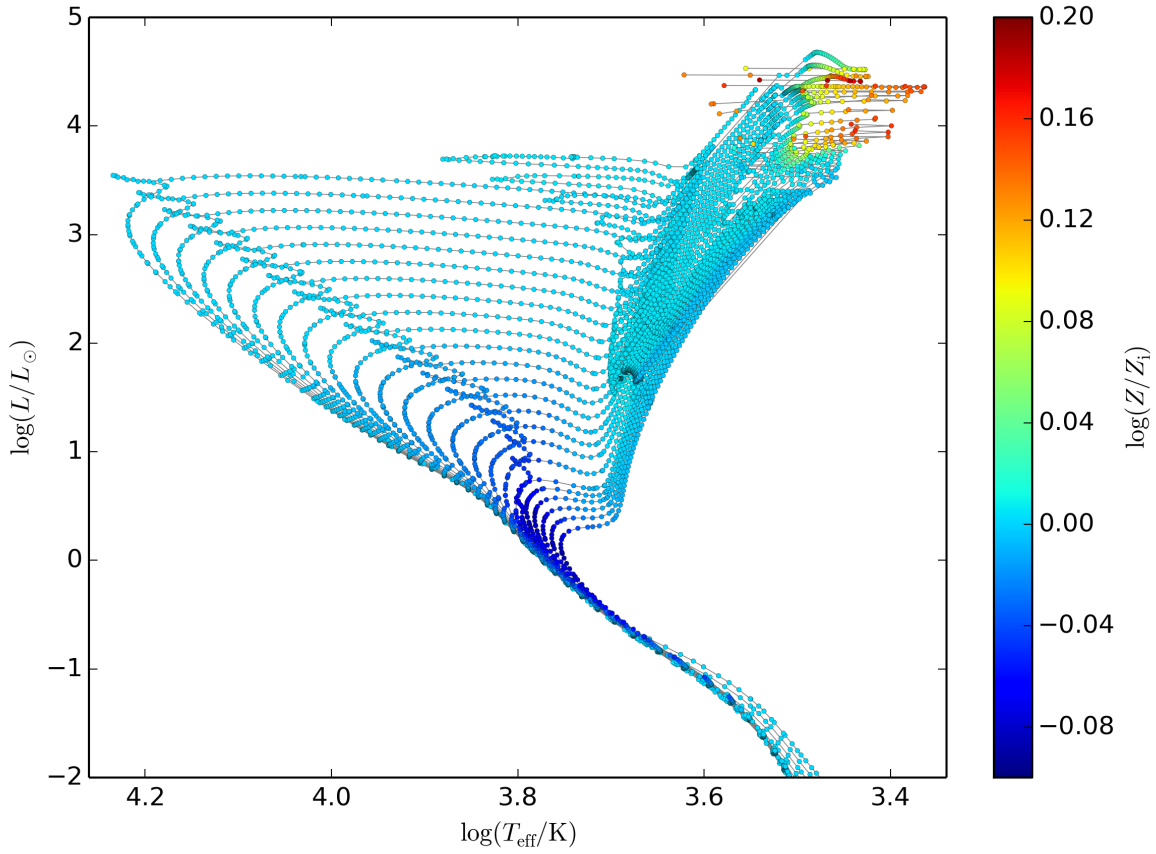


**Figure 2.5:** Variation in the current surface metallicity $Z$ for a set of isochrones of $Z_{\rm i}$=0.01471 in the age range log(t/yr) = 7.8–10.1 with step of 0.1 dex. This plot shows only quiescent points along the TP-AGB phase. Additional points can be added to describe the thermal pulse cycles, as shown in Fig. 2.6. Figure from Marigo et al. (2017)

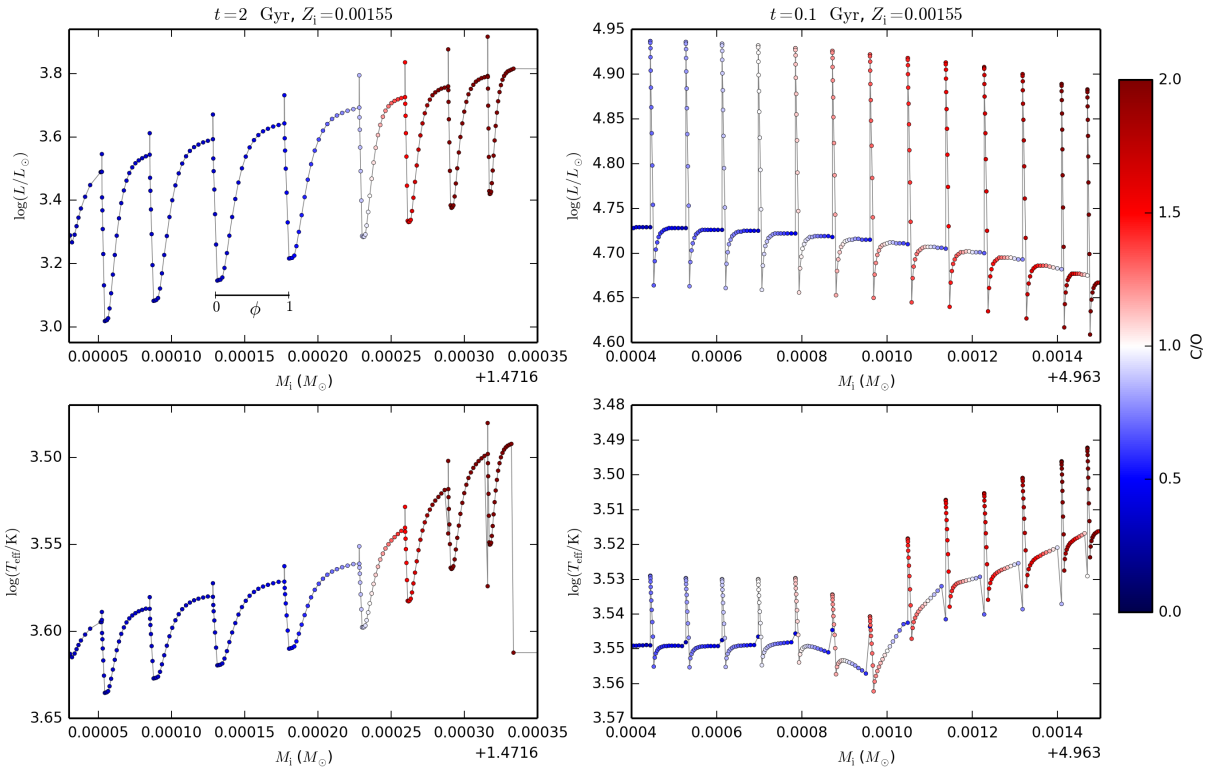


**Figure 2.6:** Variation of the luminosity and effective temperature as a function of initial mass for two isochrones sections. Left panel: section of a 2 Gyr isochrone in which the transition M- to C-star occurs due to the 3DU. Right panel: 0.1 Gyr isochrone undergoing HBB, the section represents a stage in which the mass-loss weakens the effect of the HBB by reducing the envelope mass and the transition from from M to C type occurs. The dots represent the points within a thermal pulsing cycle and they are colour-coded according to the predicted C/O ratio. Figure adapted from Marigo et al. (2017)

# Chapter 3

# The Star Formation History of the Small Magellanic Cloud

For many years, the most comprehensive study of the star formation history in the SMC was the spatially-resolved analysis performed by Harris and Zaritsky (2004) for an area of 18 deg$^2$, based on the optical photometry from the Magellanic Clouds Photometric Survey (MCPS). More recently, Rubele et al. (2015, hereafter R15) recovered the SFH of the SMC using data from the VISTA near-infrared survey of the Magellanic Clouds (VMC, Cioni et al., 2011). Both studies rely on CMD reconstruction methods to recover the Star Formation Rate (SFR), the Age-Metallicity Relation (AMR), the reddening and the distance of each analysed region. The main advantages of using VMC data are i) the lower extinction in the near-infrared passbands; ii) the photometry reaching the oldest main-sequence turn-off points, ensuring a robust estimate of the ages. In a very recent work, the derivation of the SFH of the SMC has been revised due to a number of discrepancies in the previous derivation, that were risking to affect the work on the calibration of the AGB models (Rubele et al., 2018). In this chapter I briefly mention the method used in R15, I present the discrepancies I have identified in the R15 SFH and the improved SFH as derived in Rubele et al. (2018, hereafter R18).

## 3.1 The CMD reconstruction method

The SFH recovery is based on the assumption that a Composite Stellar Population (CSP) can be considered as a linear combination of its constituent parts, which are Simple Stellar Populations (SSPs). Thus the recovery of the SFH of a CSP corresponds to the determination of the relative weight of each SSP. The technique is based on a statistical method that allows the recovery of non-parametrised SFH from the CMD of a CSP. The procedure of the SFH recovery is described with all details in Rubele et al. (2012). R15 applied this method to the deep images of the VMC in the $Y$,$J$,$K_\mathrm{s}$ filters for a SMC area of 14 deg$^2$ (10 tiles), divided into 120 subregions. The key steps for the recovery of the SFH of the SMC, as derived by R15, are summarised in the following:

(i) For every subregion of a tile, an absolute distance modulus $(\mathrm{m\text{-}M})_o$ and a V-band extinction $\mathrm{A}_V$ is assumed.

(ii) "Partial models" which represents synthetic SSP are computed for age and metallicity bins which are small enough so that the SSP properties do not change significantly inside that bin and large enough that the SFH recovery could be performed with reasonable CPU times. Age bins are defined as equally space intervals of $\Delta \log(t/yr) = 0.2$ dex, but for the youngest age bins for which wider interval are used due to the higher age resolution and the small number counts at very young ages. The metallicity bins

**Table 3.1:** Grid of partial models used in the SFH recovery. Table from Rubele et al. (2015).

| log(t/yr) | $[Fe/H]_1$ | $[Fe/H]_2$ | $[Fe/H]_3$ | $[Fe/H]_4$ | $[Fe/H]_5$ |
|---|---|---|---|---|---|
| 6.9 | −0.10 | −0.25 | −0.40 | −0.55 | −0.70 |
| 7.4 | −0.10 | −0.25 | −0.40 | −0.55 | −0.70 |
| 7.8 | −0.10 | −0.25 | −0.40 | −0.55 | −0.70 |
| 8.1 | −0.10 | −0.25 | −0.40 | −0.55 | −0.70 |
| 8.3 | −0.20 | −0.35 | −0.50 | −0.65 | −0.80 |
| 8.5 | −0.20 | −0.35 | −0.50 | −0.65 | −0.80 |
| 8.7 | −0.20 | −0.35 | −0.50 | −0.65 | −0.80 |
| 8.9 | −0.40 | −0.55 | −0.70 | −0.85 | −1.00 |
| 9.1 | −0.55 | −0.70 | −0.85 | −1.00 | −1.15 |
| 9.3 | −0.55 | −0.70 | −0.85 | −1.00 | −1.15 |
| 9.5 | −0.70 | −0.85 | −1.00 | −1.15 | −1.30 |
| 9.7 | −0.85 | −1.00 | −1.15 | −1.30 | −1.45 |
| 9.9 | −1.15 | −1.30 | −1.45 | −1.60 | −1.75 |
| 10.075 | −1.45 | −1.60 | −1.75 | −1.90 | −2.05 |

are separated by 0.15 dex from each other and a set of 5 partial models is calculated for each age bin covering an interval of ±0.3 dex with respect to the reference metallicity. Table 3.1 shows the grid of partial models used in the SFH recovery.

(iii) The partial models are "degraded" to the observational conditions by applying the results of the artificial star tests (ASTs), i.e. distribution of photometric errors and completeness. Then, they are translated into Hess diagrams, which are maps of stellar density across the $K_s$ vs. $Y-K_s$ and $K_s$ vs. $J-K_s$ CMDs.

(iv) By using the StarFISH optimisation code by Harris and Zaritsky (2002), adapted for this specific case, the linear combination of partial models the best-fit the observed Hess diagram is determined. The best-fitting solution is derived from the minimisation of a chi-squared ($\chi^2$) like statistics and characterised by the $\chi^2_{min}$ value, a measure of the residual between the best-fitting model and the data.

(v) The procedure is repeated over a range of different distance moduli and extinctions values spanning from 18.6 - 19.3 mag and 0 - 0.8 mag, respectively. In such a way, the value of the $\chi^2_{min}$ allows to determine the best-fit SFH, i.e. SFR and AMR, in addition to the distance and the extinction in the V-band for each subregion.

(vi) By using the same method, one hundred synthetic realisations of the best-fitting model are performed and analysed in order to derive the dispersion of the resulting coefficients which represents the confidence level of the SFH, $(m\text{-}M)_0$ and $A_V$.

## 3.2 Testing the SFH of the SMC

I started the work on the calibration of TP-AGB models by using the results of R15. Before proceeding with the TP-AGB population simulations and the comparison with the data, I performed extensive tests to check the consistency of the derivation of the SFH and the VMC photometry. This is a fundamental preliminary test to be sure to have a reliable description of the stellar populations below the RGB tip. Indeed, I find some discrepancies when I compared the result of `TRILEGAL` simulations based on the VMC SFH and the VMC photometry itself. More specifically, for each subregion I perform a `TRILEGAL` simulation using the same input used by R15, including the effect of the photometric errors and incompleteness by using the same set of Artificial Star Tests. I find two important discrepancies, the first one resulting in an overestimation of the best-fitting reddening values and the second one related to the AMR relation assumed for the young SMC population. The first one is illustrated in Figure 3.1, where I compare the

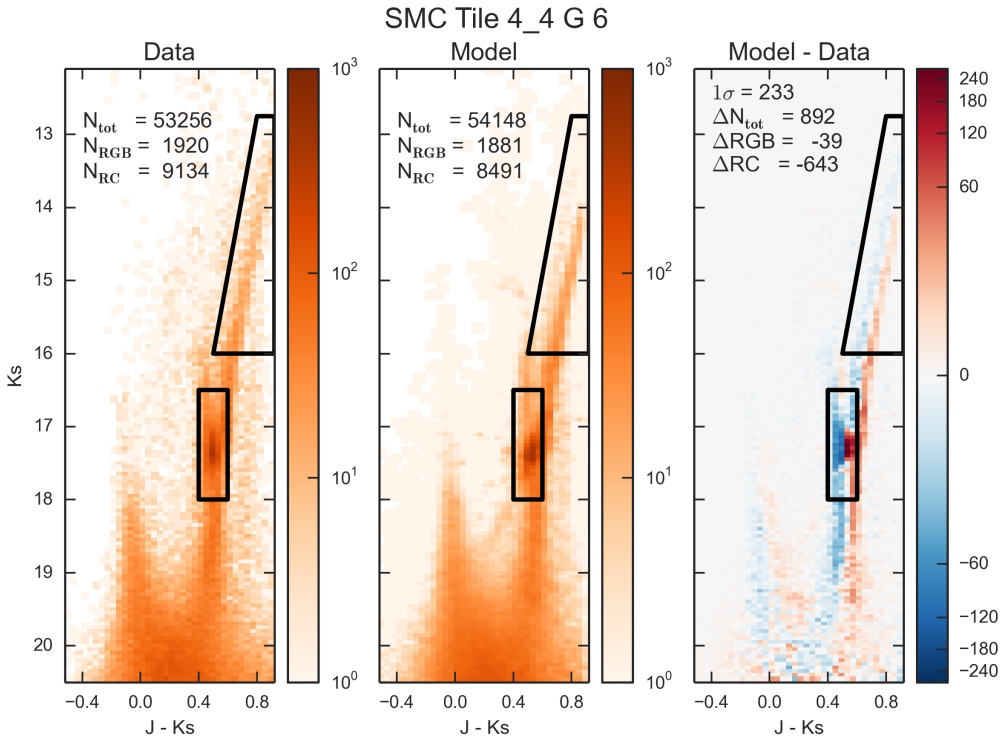


**Figure 3.1:** Hess diagrams of the VMC data (left panel) and the TRILEGAL simulation obtained from the best-fitting SFH of R15 (central panel) for the subregion G6 of tile 4_4. The black boxes show the CMD regions used to compare the observed and predicted number counts of RGB and red clump stars. The right panel shows the difference between the model and the data. There is an evident shift of the $J-K_s$ colour throughout the CMD plane.

$K_s$ vs. $J-K_s$ CMD of the SMC region 4_4 G 6 with the synthetic one calculated using as input the best-fitting value of the SFR, AMR, distance and reddening from R15. By looking at the third panel in which I show the difference between the model and the data, there is an evident shift in the $J-K_s$ colour. Since the shift affects the overall CMD the cause should be in some quantities that affect a CMD in a rigid way, i.e. the reddening.

I also tested if the same shift was present in the $Y-K_s$ colour and I find a shift in colour in the opposite direction (simulations bluer than observations). Since in the SFH recovery procedure the two CMDs are fitted at the same time, I checked if the value of the reddening derived from the two CMDs were consistent. I used the StarFish code to test this for a few representative subregions of the SMC and I find that indeed the best fitting values of the $A_V$ were not consistent with each other.

Figure 3.2 shows the values corresponding to the distance and reddening adopted in the partial models, colour coded according to the $\chi^2$ values as derived from the $J-K_s$ and $Y-K_s$ CMDs. The best-fitting values of the distance are consistent within 0.1 mag, whereas the reddening values are 0.5 and 0.2 mag for the $Y-K_s$ and the $J-K_s$ CMDs respectively. The most likely reason for such discrepancy is related to the small offsets in the VISTA photometry. In particular, the $Y$-band calibration is uncertain due to absence of a $Y$-band in the calibrating data from 2MASS. This has an important impact on the SFH solutions, especially on the reddening derivation in the R15 analysis. When using the two CMDs the derived value of the reddening lie in between the two reddening values derived independently from the $J-K_s$and $Y-K_s$CMDs. This results in an overestimation of the reddening in the $J-K$ and an underestimation in the $Y-K_s$. The solution to this problem is to decouple the two CMDs in the SFH recovery and to use the values of

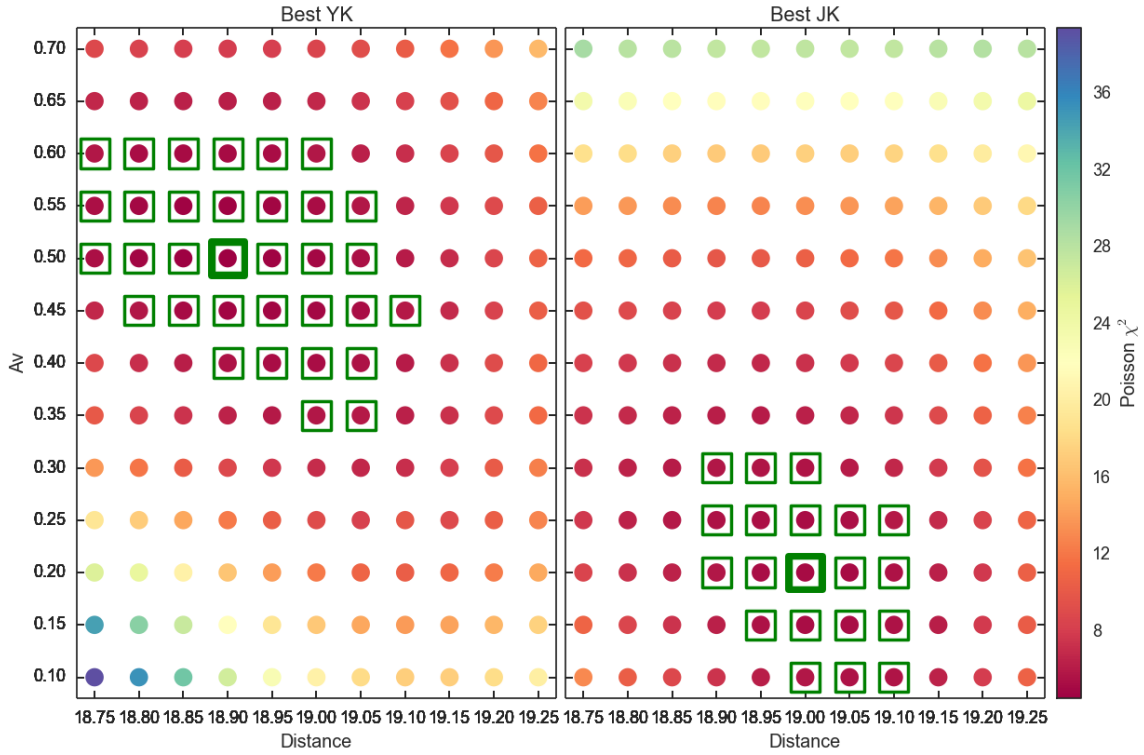


**Figure 3.2:** $\chi^2$distributions as derived through the CMD fitting technique applied separately to the $K_s$ vs. $Y-K_s$ (left panel) and $K_s$ vs. $J-K_s$. The best-fitting regions ($\chi^2 < 6$) in the distance–$A_V$ plane are represented with green squares and the best-fitting solution with the thick square. The two best-fitting distance values are consistent, whereas the $A_V$ solution from the $K_s$ vs. $Y-K_s$ CMD are 0.3 mag redder than the $K_s$ vs. $J-K_s$ solution.

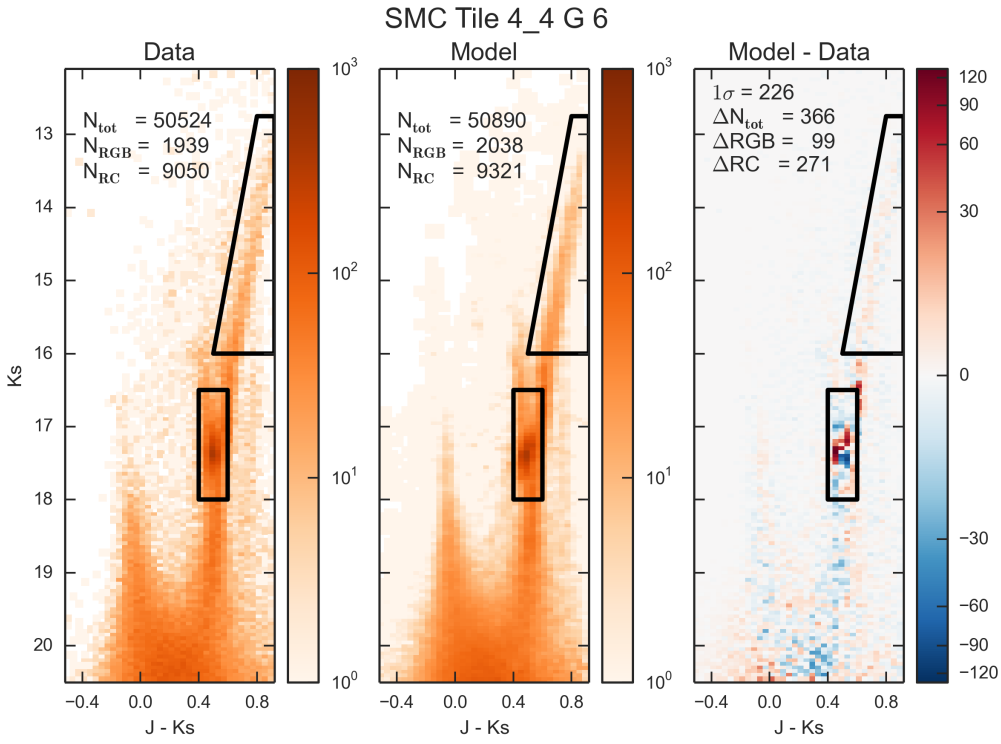


**Figure 3.3:** Same as in Fig. 3.1 but for the input SFH derived by R18. The residual differences do not show any systematic shift in colour.

reddening and distances obtained from the $JK_s$ solutions. Figure 3.3 shows the same SMC region as in Figure 3.3 for a `TRILEGAL` simulation calculated with the input SFH, distance and reddening derived in R18.

The residual difference between the models and the data does not shown any systematic shift, apart from a concentration in the Red Clump region, also visible in the $K_s$-band luminosity function shown in Figure 3.4. However, both the predicted luminosity function and the $J-K_s$ colour distribution are in agreement with the VMC data.

An additional discrepancy I found is related to the predicted number of RGB stars. By simulating all the regions analysed by R15, I found a significant overestimation in the number of simulated RGB stars, especially in the central regions where the models overestimate the RGB numbers more than 30 per cent. After performing additional consistency checks, I found that the most likely explanations are 1) updates and improvements in the `TRILEGAL` code with respect to the version used in R15 2) slightly different versions of the `PARSEC` tracks.

Finally, I checked the performance of the models in the upper part of the CMD, above the RGB tip. Since the saturation limit of the VMC photometry is around $K_s = 10$ mag, I used the 2MASS data to perform the comparison. I find that the sequence of Red Super Giants (RSG) in the simulations are systematically redder than the observations. This discrepancy has been already pointed out in other studies. For instance, McQuinn et al. (2011) compared the optical HST colours of a sample of 19 starburst dwarf galaxies with the one predicted by `PARSEC` based isochrones (Girardi et al., 2000), and found offsets of about 0.5 mag. Similarly, Melbourne et al. (2012) identified an offset of about 0.2 mag in the predicted HST near-infrared colours of a sample of 23 nearby dwarf an spiral galaxies (stellar isochrones from Girardi et al. (2010)).

The problem is illustrated in Figure 3.5. The mean colour of the RSG sequence is

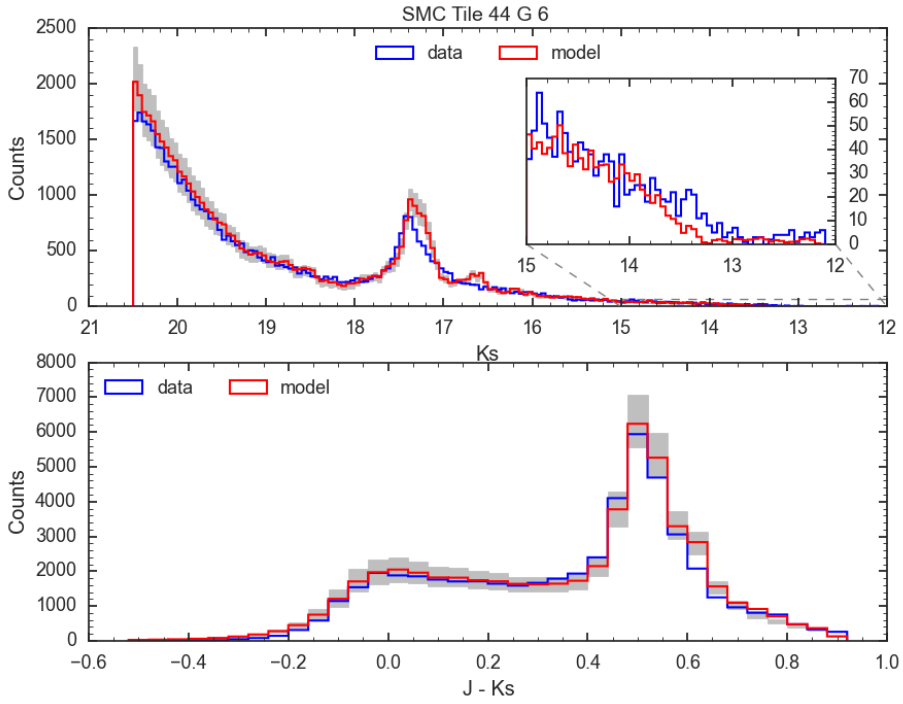


**Figure 3.4:** $K_s$ band luminosity function (top panel) and $J-K_s$ histogram (bottom panel) of the data and the simulation obtained from the best-fitting SFH for the subregion G6 of tile 4_4 (R18). The shaded grey region represents the upper and lower limits in the star counts obtained by simulating the same region with the upper and lower confidence intervals of the SFR(t).

redder than the observed one, in addition the slope of the sequence is not consistent with the 2MASS data. This sequence is populated by young stars, with a mean age younger than $10^8$ yr and the only constraints in the CMD fitting derivation comes from the sparsely populated upper part of the MS. It is possible that a small offset in the predicted colours of such young populations and their limited sensitivity to the metallicity in the near-infrared bands have biased the best-fitting AMR derivation. The predicted metallicity of the young populations is indeed quite high reaching solar and super-solar values. I then performed some tests by limiting the maximum metallicity as shown in Figure 3.5. I first tested the effect of lowering the metallicity for the younger populations ($\log(t/yr) < 8.4$) by 0.2 dex and 0.4 dex. The reproduction of the slope and the colour of the RSG is improved in the case of a 0.4 dex reduction in the metallicity. For this reason, the AMR used as input for the SFH recovery has been limited to a maximum value of [Fe/H] = -0.4 dex, i.e. $Z \approx 0.006$. The results of the simulation with the AMR derived by R18 are shown in the right-hand panel of Figure 3.5.

Constraining the AMR at younger ages is also motivated by the fact that observations of the SMC young population indicate even lower metallicities for the young SMC populations (Hill, 1999; Davies et al., 2015). These two problems, together with new updates in the stellar models and a larger data-set of the VMC photometry, motivated a revision of the SFH derivation as detailed in the next section.

## 3.3 The revised SFH of the SMC

The main changes in the derivation of the SFH performed by R18 are the following:

- First, there is a large increase in the area and depth covered by the VMC obser-

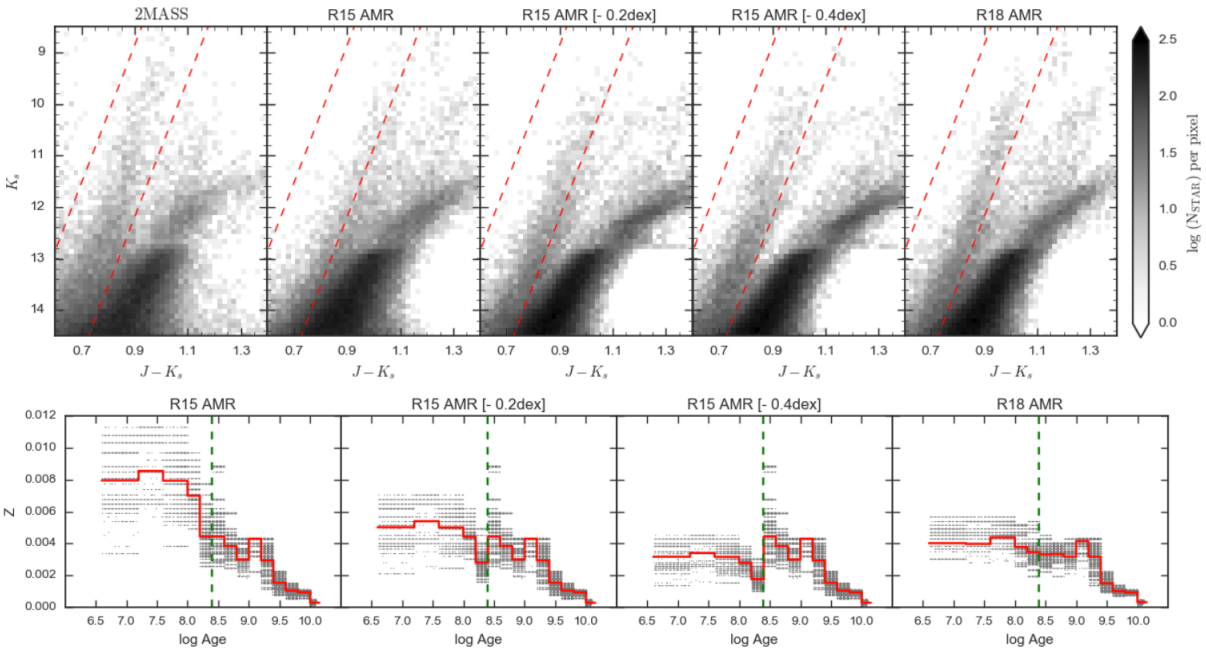


**Figure 3.5:** Comparison of the observed and simulated $K_s$ vs. $J-K_s$ Hess diagrams for the four central tiles (SMC 4_3, SMC 4_4, SMC 5_3, and SMC 5_4), at bright $K_s$magnitudes. Left-hand panel: 2MASS data. Middle panel: simulations computed with different AMR as indicated. The AMRs used for each simulation are shown in the bottom panels. The red dashed lines show the photometric criteria used by Boyer et al. (2011) to separate the RSG population of the SMC from the foreground and the TP-AGB stars. The use of the updated AMR R18 results in improvements of both the colour and the slope of the RSG sequence.

vations, compared to the R15 work. The completion is now of 100 per cent for a contiguous area of 23.57 deg$^2$, comprising the entire main body of the SMC as shown in Figure 3.6.

- We use the updated evolutionary tracks from PARSEC v1.2S (Bressan et al., 2012, 2015), which span a wider range of metallicities.
- Isochrones are generated with a revised algorithm (Marigo et al., 2017) that ensures a more reliable interpolation of all evolutionary features, as a function of both age (or initial mass) and metallicity.
- The partial models for $\log(t/yr) < 8.2$ were shifted by $-0.3$ dex, and those with $8.2 < log(t/yr) < 8.8$ by $-0.2$ dex, with respect to the values adopted in R18.
- The adoption of the IMF by Kroupa (2001), instead of the former Chabrier (2001) one.
- The decoupling of the two VMC CMDs, so as to compensate for the likely offsets in the photometric zeropoints.

The global SFR and AMR as derived by R18, together with the total stellar mass formed as a function of the lookback time are shown in Figure 3.7.

Similar results are available for 168 subregions across the SMC (see Fig. 3.6). For each SMC subregion, I checked the consistency between the VMC data and the best-fitting SFH derived by R18. The improvements in the analysis results in data–model differences in general smaller than $\approx$10 per cent. The largest differences are found in the immediate vicinity of the red clump (see Fig. 3.3). They probably reflect the small uncertainties

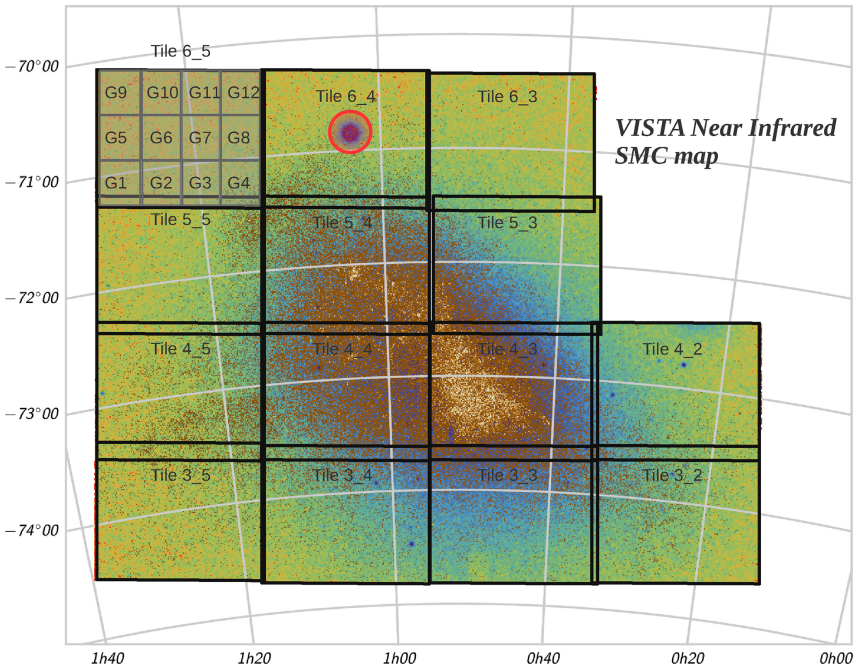


**Figure 3.6:** The stellar density distribution of the SMC as obtained from the VMC data. The deep tiles are shown as black rectangles and the 12 subregion are shown as grey rectangles on tile 6_5. The red circle illustrates the area around NGC 362 that was removed from the analysis. Figure from R18

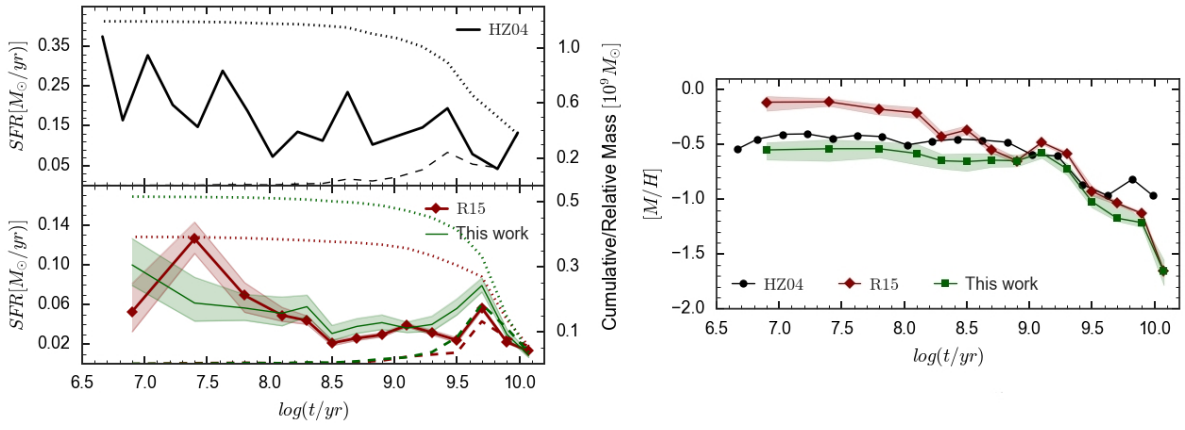


**Figure 3.7:** Left: SMC global SFR and total mass in stars formed as derived from Harris and Zaritsky (2004) (HZ04, upper panel) and R18 and R15 (lower panel). Right: AMR in the SMC as a function of the lookback time from HZ04, R15 and R18. The confidence intervals are shown as shaded regions. Adapted from R18.

in stellar evolutionary models for pre-AGB phases, together with the approximations adopted in the R18 analysis (e.g. the choice of a given resolution in CMD and age–metallicity space, the adoption of a single value of distance and extinction, etc.). Overall, such differences in star counts are negligible compared to the huge differences between the lifetimes of different TP-AGB models found in the literature; therefore, they represent a robust starting point for our analysis of TP-AGB models.

# Chapter 4

# Calibration of TP-AGB models in the Small Magellanic Cloud

This Chapter presents the work carried out as main project of my PhD, namely the calibration of TP-AGB models in the SMC. I will present the database that contains all information about the bulk of AGB stars in the SMC, based on the catalogue compiled by Srinivasan et al. (2016) using 2MASS and *Spitzer* observations, and I will give some additional details about the SFH derived by R18. I will discuss the calibration and the implications of the input prescriptions of the best-fitting models and present a full characterisation of the AGB population in the SMC in terms of stellar parameters.

## 4.1 Observations in the SMC

The calibration is based on the SMC population of evolved stars identified and classified by Srinivasan et al. (2016, hereafter SR16) using the observations from the *Spitzer Space Telescope* Legacy program entitled "Surveying the Agents of Galaxy Evolution in the Tidally Stripped, Low Metallicity Small Magellanic Cloud" (SAGE-SMC, Gordon et al., 2011). The SAGE-SMC catalogue includes optical to far-IR photometry, in particular $U$,$B$,$V$,$I$ photometry from the Magellanic Cloud Photometric Survey (MCPS), $J$, $H$, $K_{\rm s}$ photometry from 2MASS and the InfraRed Survey Facility (IRSF), 3.6, 4.5, 5.8, 8.0 $\mu$m mid-IR photometry from Spitzer's IRAC and far-IR photometry from MIPS, i.e 24 $\mu$m[1]. Figure 4.1 shows the VMC survey coverage superimposed on the density map of the AGB stars classified in SR16. As can be seen, a large fraction of the area studied by R18 (about 87 per cent) is also covered by the SR16 catalogue.

The first catalogue of evolved stars based on the SAGE-SMC survey was published by Boyer et al. (2011, hereafter B11), followed by the work of SR16 who reconstructed the candidate list using an updated version of the SAGE photometry and optical to mid-IR information from previous studies to refine the candidate selection. SMC stars are classified into Red Super-Giants (RSG), Carbon-rich AGB (C-AGB or C-rich), Oxygen-rich AGB (O-AGB or O-rich), anomalous-AGB (a-AGB) and extreme AGB (X-AGB). The a-AGB star sample hosts both C- and O-rich stars that are thought to be low-mass evolved AGB stars (Boyer et al., 2015a). The extreme-AGB sample contains the most dust enshrouded stars and the majority of them are C-rich stars. The classification is primarily based on the stellar position in the $K_{\rm s}$ vs. $J-K_{\rm s}$ CMD, where these stars draw distinct features. In addition, X-AGB and a-AGB stars are identified also with the help of mid-IR photometry. The details about the classification criteria used by SR16 are given

[1]IRAC and MIPS passbands will be also indicated with the following notation: [3.6], [4.5], [5.8], [8.0], [24]

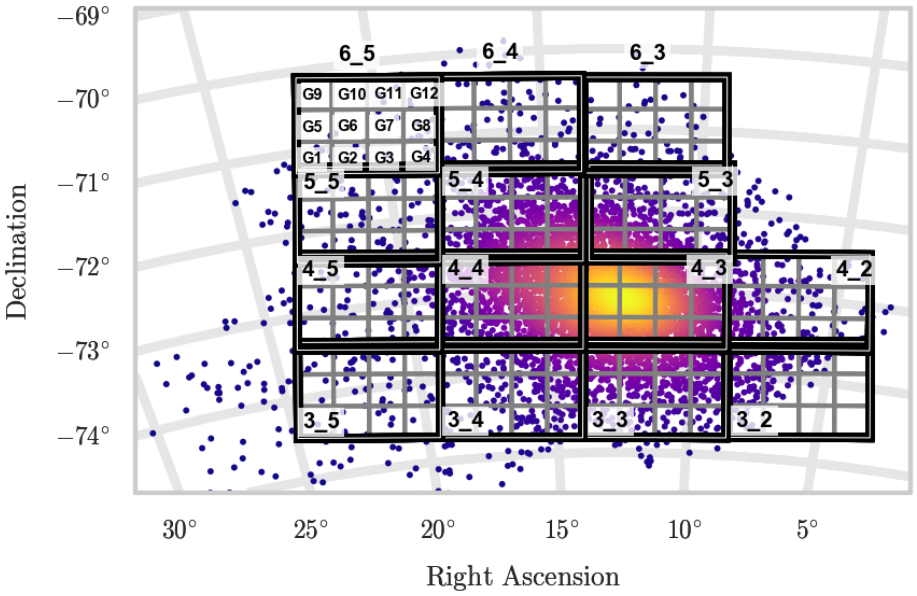


**Figure 4.1:** VMC tiles used in the SFH recovery by R18. The VMC tiles are in black and the sub-regions are shown in grey; the background image shows the density map of the AGB stars classified by Srinivasan et al. (2016).

in the next section.

### 4.1.1 Classification criteria

First, the samples of C-AGB and O-AGB stars are selected in the $J-K_s$ CMD, following Cioni et al. (2006). All C-AGB and O-AGB stars are brighter than the $K0$ line, defined as:

$$\mathrm{K0} = -0.48 \cdot (J-K_s) + 13.022 + 0.056 \cdot [\mathrm{M/H}] \tag{4.1}$$

where the value of the metallicity is $[\mathrm{M/H}] = \log(Z_{\mathrm{SMC}}/Z_{\odot})$. The adopted values of metallicity and distance of the SMC are $Z_{\mathrm{SMC}} = 0.2 \cdot Z_{\odot}$ and $d_{\mathrm{SMC}} = 61$ kpc. Two additional lines are used to separate C- and O-AGB stars:

$$\mathrm{K1} = -13.333 \cdot (J-K_s) + 25.293 + 1.568 \cdot [\mathrm{M/H}] \tag{4.2}$$

$$\mathrm{K2} = -13.333 \cdot (J-K_s) + 29.026 + 1.568 \cdot [\mathrm{M/H}] \tag{4.3}$$

C-AGB stars have $J-K_s$ colours redder than the $K2$ boundary while O-AGB stars lie between $K1$ and $K2$. To minimise the contamination from RGB stars, sources fainter than the RGB Tip (TRGB) in both $K_s$ and 3.6$\mu$m passbands – estimated to be at 12.7 mag and 12.6 mag, respectively – are excluded from the sample.

The class of the reddest AGB stars is denoted as extreme-AGB. The majority of them are probably in the "superwind" phase with high mass-loss rates. Since they are obscured at optical wavelengths by thick dusty envelopes, the selection also includes mid-IR photometry. The sources classified as X-AGB stars are brighter than the 3.6$\mu$m TRGB and redder than $J-[3.6] > 3.1$ mag, or redder than $[3.6]-[8.0] > 0.8$ mag if the $J$-band detection is not available. Two additional criteria are used to minimise the contamination from Young Stellar Objects (YSOs) and unresolved background galaxies (see 3.1.2 in Boyer et al., 2011).

The classification criteria adopted for selecting the RSGs are as follows: (i) they are bluer than the $K1$ line; in addition to minimise the contamination from O-AGB

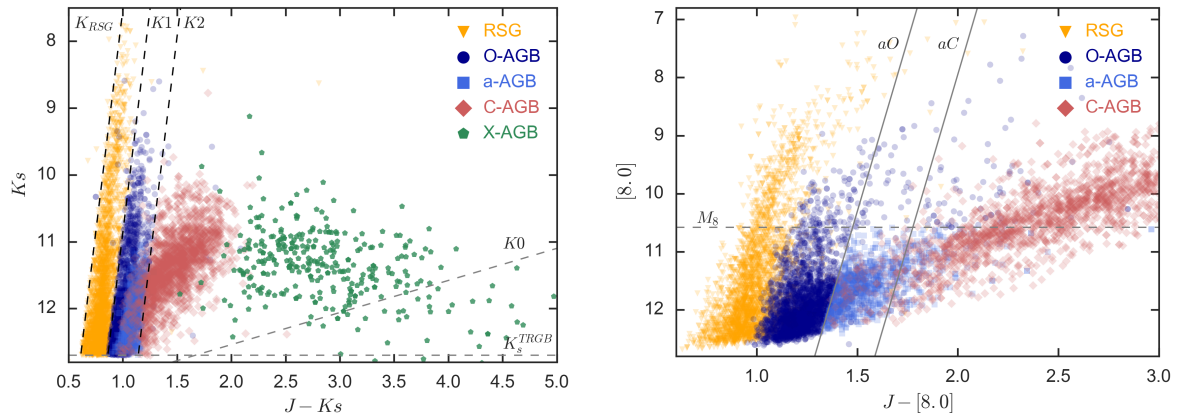


**Figure 4.2:** $K_s$ vs. $J-K_s$ (left panel) and [8.0] vs. $J-[8.0]$ (right panel) CMDs of the observed sample of evolved stars in the SMC. In the left panel, the dashed diagonal lines are the photometric criteria adopted to separate RSG from AGB stars and O-rich from C-rich stars ($K0$, $K1$ and $K2$, see text), the horizontal dashed line is the TRGB in the $K_s$ band. In the right panel, the three lines ($aO$, $aC$, $M_8$) are the photometric criteria used to select the a-AGB stars as explained in the text. Stars are colour-coded according to their class and plotted with different symbols as shown in the legend.

stars the RSG branch width is restricted to $\Delta(J-K_s) = 0.2$ mag; (ii) to minimise the contamination from foreground sources and RGB stars, RSGs have $K_s$ brighter than the TRGB.

B11 identified a new feature in the [8.0] vs. $J-[8.0]$ CMD suggesting the presence of a class of stars distinct from C- and O-AGB. They referred to these stars as anomalous Oxygen stars (aO-AGB), as they have been originally classified as O-rich by Cioni et al. (2006). These stars were selected from the original O-AGB sample if they are redder than the line ($aO$):

$$[8.0] = A - 11.76 \cdot (J-[8.0]), \tag{4.4}$$

with $A = 27.95$ mag, and with an $8\mu$m absolute magnitude fainter than $M_8 = -8.3$ mag. Stars in the original C-AGB sample fall in this population if they are bluer than the line ($aC$) defined by Eq. 4.4 with $A = 31.47$ mag. In a more recent work, Boyer et al. (2015a) carried out a detailed analysis of chemistry, pulsation properties, stellar parameters and dust production of these stars and concluded that they are low-mass dusty AGB stars at the very end of their evolution, with median current stellar masses of about 0.94 $M_\odot$ and initial masses $M < 1.25$ $M_\odot$. The spectral classification has been performed for a sample of 273 aO-AGB stars and resulted in 122 C-rich, 100 O-rich, 23 S-type and 28 unknown spectra. Since a high fraction ($\sim 50$ per cent) of the aO-AGB stars turned out to be C-rich, Boyer et al. (2015a) refer to aO-stars simply as a-AGB stars. Their results suggest that a-AGB stars should be photometrically selected using the $J-[8.0]$ colour, which is more reliable with respect to $J-K_s$ colour for the most evolved stars.

Figure 4.2 shows the $K_s$ vs. $J-K_s$ CMD of the observed sample of evolved stars in the SMC area used in this work and some of the adopted photometric criteria. The SR16 catalogue also includes the 81 IRS sources spectroscopically classified by Ruffle et al. (2015). In addition, I considered the spectroscopic classification of the 273 sources analysed by Boyer et al. (2015a). The star counts for the RSG/AGB populations are summarised in Table 4.1 and they refer to the area covered by the VMC regions shown in Figure 4.1

**Table 4.1:** Number counts of RSG/AGB populations classified by SR16. The star counts refer to the selected SMC area used in this work.

| Population | Number of stars |
|---|---|
| C-AGB | 1 854 |
| O-AGB | 2 623 |
| X-AGB | 343 |
| a-AGB | 972 |
| RSG | 3 150 |

## 4.2 Calibration Strategy

The adopted calibration strategy is schematically illustrated in Figure 4.3. Stellar models have been described in Section 2, together with the bolometric corrections and the circumstellar dust treatment. Further details will be given in the next section when necessary. Using the SFH of R18 as an input, the `TRILEGAL` code is used to simulate the population of every subregion, at magnitudes corresponding to the TP-AGB population. These simulations are performed for several sets of TP-AGB tracks calculated with the `COLIBRI` code with different combinations of input prescriptions for the mass-loss and the third-dredge up, until a good overall description of the observations is reached.

I will now describe the details of the `TRILEGAL` simulations and how the data-model comparison is performed. I then present the grid of TP-AGB models calculated, the steps of the calibration and finally discuss the results.

### 4.2.1 `TRILEGAL` simulations

In order to perform a one-to-one comparison between the predicted number counts of AGB stars and the SAGE-SMC observations, it is important to consider exactly the same sky areas. Therefore, given the coordinates of each VMC subregion, I assigned each star present in the SR16 catalogue to the correspondent subregion. I then compiled a catalogue in which each region has its SFH and the information about the AGB stars. This allows to preserve the details of the space-resolved SFH of R18 and to simulate the exactly same sky areas for which the information on the AGB stars are available. The VMC regions used in this work are listed in Table 4.2, together with the number of AGB stars in each tile according to the classification by SR16. I excluded all the subregions that are not completely covered by both the VMC and SR16 catalogue.

As already mentioned in the previous section, each subregion covered by both VMC and SAGE-SMC surveys is simulated according to its SFR($t$), AMR, $A_V$ and distance as derived from the SFH recovery procedure. Most of the assumptions are identical to those adopted by R18: (i) the adopted IMF for single stars is a Kroupa (2001) function; (ii) non-interacting binaries are simulated using a binary fraction of 30 per cent and an uniform distribution of mass ratios between the primary and secondary, between 0.7 and 1; (iii) moreover, our simulations use the same version of `PARSEC` tracks used to derive the SFH by R18, for all evolutionary phases previous to the TP-AGB. This ensures the maximum consistency between these works.

In the present work, however, a set of `COLIBRI` TP-AGB tracks is included in all simulations. The basic formalism for their inclusion in `TRILEGAL` is described in Marigo et al. (2017), with some improvements to be detailed in the next Section. Our starting point is the set of TP-AGB stellar models described in Rosenfield et al. (2016, 2014), in which the mass-loss prescription in `COLIBRI` was adjusted to reproduce the observed TP-AGB luminosity functions in a sample of nearby galaxies imaged in the optical via the Advanced Camera for Surveys Nearby Galaxy Survey Treasury (Dalcanton et al., 2009),

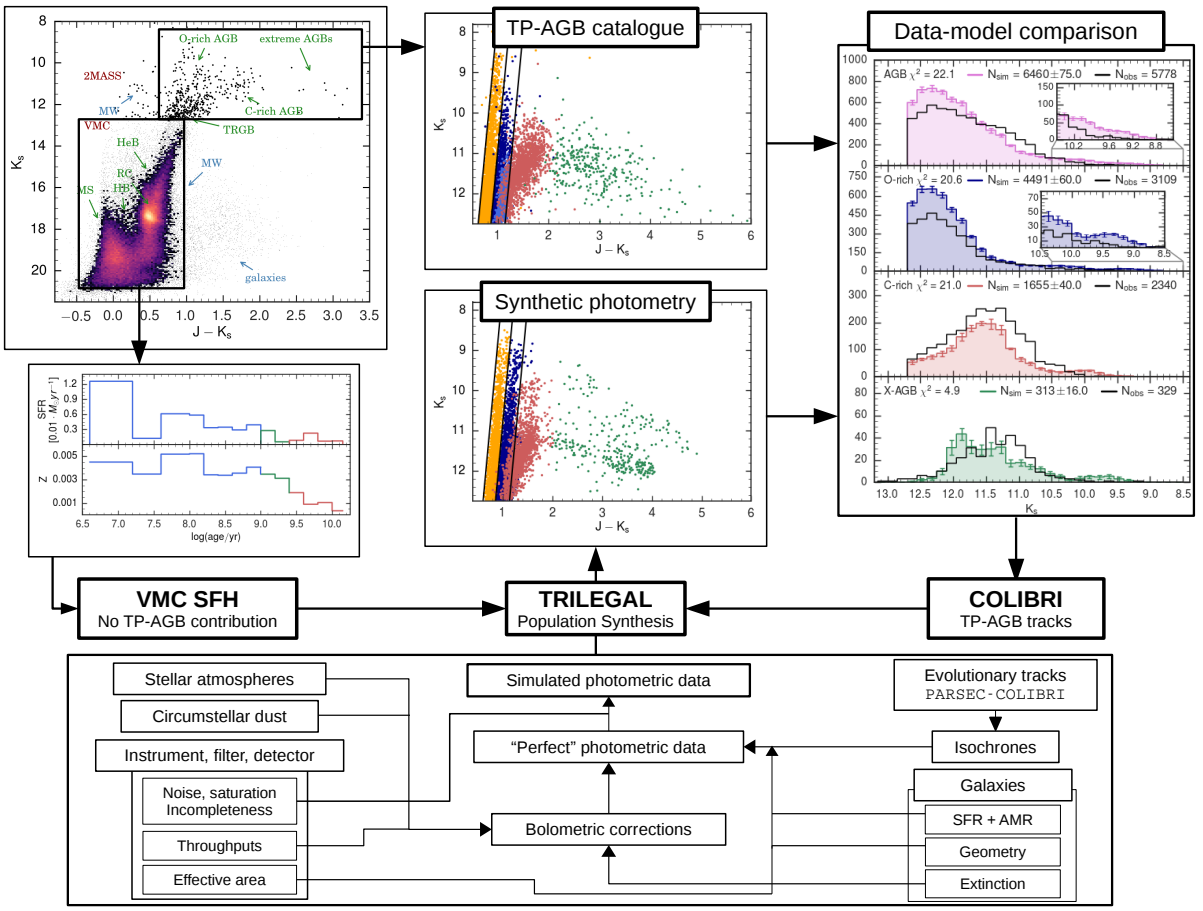


**Figure 4.3:** A scheme of the method and codes used in this work. The $K_s$ vs. $J-K_s$ CMD at the top-left corner shows the VMC plus 2MASS data for the same subregion of the SMC. It illustrates, schematically, the SMC data used in this work, namely: (a) the deep VMC data which has allowed the derivation of a detailed spatially-resolved SFH for the SMC by R18, at magnitudes not populated by TP-AGB stars, and (b) the catalogues of TP-AGB stars built from the combination of 2MASS with later surveys by Srinivasan et al. (2016). The central and right-hand panels illustrate the new steps performed in this work: the SFHs, together with TP-AGB evolutionary tracks from `COLIBRI`, are fed to the `TRILEGAL` code for the simulation of TP-AGB catalogues, for every subregion of the SMC. The simulations are then compared to the data (in terms of both star counts, and distributions in colour-magnitude space), and new TP-AGB tracks are computed in response to the observed discrepancies. Successive iterations are performed tuning the mass-loss and 3DU prescriptions until a satisfactory reproduction of the observations is reached. The lower part of the figure illustrates the general working scheme of the `TRILEGAL` code.

**Table 4.2:** Central coordinates of the VMC tiles used in this work and number of AGB stars identified by SR16 for each tile.

| Tile[1] | subregions used | R.A.$_{J2000}$ (deg) | Dec.$_{J2000}$[deg.] (deg.) | N. AGB |
|---|---|---|---|---|
| SMC 3_2 | 4 | 5.8981 | −74.1159 | 136 |
| SMC 3_3 | 11 | 11.2329 | −74.2117 | 578 |
| SMC 3_4 | 11 | 16.588 | −74.1774 | 272 |
| SMC 3_5 | 12 | 21.8784 | −74.0137 | 63 |
| SMC 4_2 | 11 | 6.3087 | −73.0299 | 205 |
| SMC 4_3 | 12 | 11.3112 | −73.1198 | 1888 |
| SMC 4_4 | 12 | 16.3303 | −73.0876 | 1146 |
| SMC 4_5 | 12 | 21.2959 | −72.9339 | 99 |
| SMC 5_3 | 12 | 11.2043 | −72.0267 | 484 |
| SMC 5_4 | 12 | 16.1088 | −71.9975 | 655 |
| SMC 5_5 | 12 | 20.7706 | −71.8633 | 84 |
| SMC 6_3 | 9 | 11.4532 | −70.9356 | 57 |
| SMC 6_4 | 10 | 15.9581 | −70.8929 | 96 |
| SMC 6_5 | 7 | 20.3437 | −70.7697 | 29 |
| | N. subregions | Total area | | $N_{TOT}$ AGB |
| | 147 | $\approx 21 deg^2$ | | 5792 |

**Notes.**
[1] Excluded subregions for each tile: SMC 3_2 G1, G2, G3, G4, G6, G7, G8, G12; SMC 3_3 G1, SMC 3_4 G4, SMC 4_2 G4, SMC 6_3 G8, G11, G12, SMC 6_4 G6, G7; SMC 6_5 G5, G6, G9, G10, G11.

and (for a subsample of them) on the near-IR via a HST/SNAP follow-up campaign (Dalcanton et al., 2012). These works concluded for the need of an efficient pre-dust mass loss, particularly for low-mass stars, in agreement with earlier findings (Girardi et al., 2010). Information about the third dredge-up could not be derived from those data, since the available HST photometry did not allow to discriminate between M- and C-stars.

For all our TP-AGB models, model quantities are converted into the relevant photometry by means of extensive tables of bolometric corrections, derived from the stellar spectral libraries from Aringer et al. (2009) for C-rich stars, and Castelli and Kurucz (2003) plus Aringer et al. (2016) for O-rich stars. As mentioned in Section 2.4, the effects of the circumstellar dust in mass-losing stars is taken into account following the approach described in Marigo et al. (2008). Here, such treatment has been improved by updating the sulphur, silicon and iron abundances according to Caffau et al. (2011) and by lowering the condensation degree for silicates to obtain a better reproduction of the colours of low-mass O-rich AGB stars and HBB stars in the SMC. In addition, the condensation degree of carbon dust is calculated with a fitting relation derived from Eriksson et al. (2014), which is also more consistent with the adoption of a mass-loss prescriptions based on the results from carbon stars dynamical models from (Mattsson et al., 2010; Eriksson et al., 2014). The spectra used here were computed by Groenewegen (2006) for a fixed dust mixture of 85% Amorphous Carbon and 15% Silicon Carbide for C-stars and 100% silicates for O-rich stars.

As described in Girardi et al. (2013), a pronounced peak in the production rate of AGB stars appears at ages $\sim$1.6 Gyr and for a timescale of about 0.1 Gyr. This is a real physical effect due to an abrupt change in the helium-burning lifetimes when low-mass stars develop electron-degenerate cores. Since the age of the more massive Magellanic Cloud clusters coincides with the AGB-boosting period, the inclusion in the EPS models

**Table 4.3:** Age resolution in TRILEGAL simulations.

| Period | log(age/yr) interval (dex) | Resolution (dex) |
|---|---|---|
| Pre-boosting | 6.600 - 9.000 | 0.020 |
| Boosting | 9.000 - 9.400 | 0.001 |
| Post-boosting | 9.400 - 10.170 | 0.020 |

of TP-AGB models calibrated to reproduce the lifetimes and the integrated fluxes of the Magellanic Cloud's clusters, are the more likely cause for the overestimation of the TP-AGB contribution in resolved star counts and integrated spectra of galaxies. The AGB-boosting effect is less dramatic when galaxy fields are considered, given their more continuous SFHs. However, after performing some tests for the SMC population I found that in in order to properly handle the AGB-boosting an increase in the age resolution of the TRILEGAL simulations is needed. In this work, each subregion is modelled by splitting the simulations into three age intervals (see Table 4.3). In the younger and older intervals, simulations are not affected by the boosting effect, therefore a resolution of 0.02 dex in log(age) suffices to represent the SFR($t$) for each subregion. During the boosting period, however, the log(age) resolution is reduced to 0.001 dex, in order to sample the fast variations that occur in the production rate of TP-AGB stars. This boosting interval is intentionally kept very wide (0.4 dex), in order to take into account the variation of its mean age with metallicity. This choice slightly increases the computational time of the simulations, but ensures a reliable TP-AGB calibration.

The simulations performed with TRILEGAL result in "perfect photometric catalogues" down to a specified magnitude, according to the input probability distributions, but for the Poisson noise. In order to take into account the photometric errors, I derive the mean photometric uncertainties as a function of the magnitude for each passband in the SR16 catalogue. The photometric errors are applied inside TRILEGAL according to these relations. A completeness of 100 is assumed down to the limiting magnitude of the catalogues. Even if the completeness assumption is not accurate for all the available filters, it does not impact the results of the calibration since the bulk of AGB stars have observed near-IR magnitudes for which the completeness can be safely assumed to be very close to 100 per cent.

### 4.2.2 SFH uncertainties

The degree of consistency between the present simulations and the SFH analysis of R18, has been verified as described in Section 3. The next step is to investigate how the uncertainties in the best-fitting SFR, AMR, distance and extinction impact the simulated luminosity functions (LFs) and the number counts. I compute two sets of 10 TRILEGAL simulations of the subregions 5, 8 and 9 of the tiles SMC 4_3 and 5_4, which can be considered as representative of most of the SMC regions. The first set is computed using the best-fitting values of the SFH and the second is computed using the values extracted from Gaussian distributions whose means are the best-fitting values of the SFH at each age bin, and the standard deviations are the associated uncertainties[2].

Figure 4.4 compares the mean $K_s$-band LFs for the two sets of simulations. The standard deviation and the Poisson error in each luminosity bin are equivalent, both in

[2]We use a single Gaussian to sample the symmetric uncertainties of distance and reddening values and a two Gaussian with the same mean but different standard deviations $\sigma_{up}$ and $\sigma_{low}$ to account for the asymmetric uncertainties in SFR($t$) and AMR.

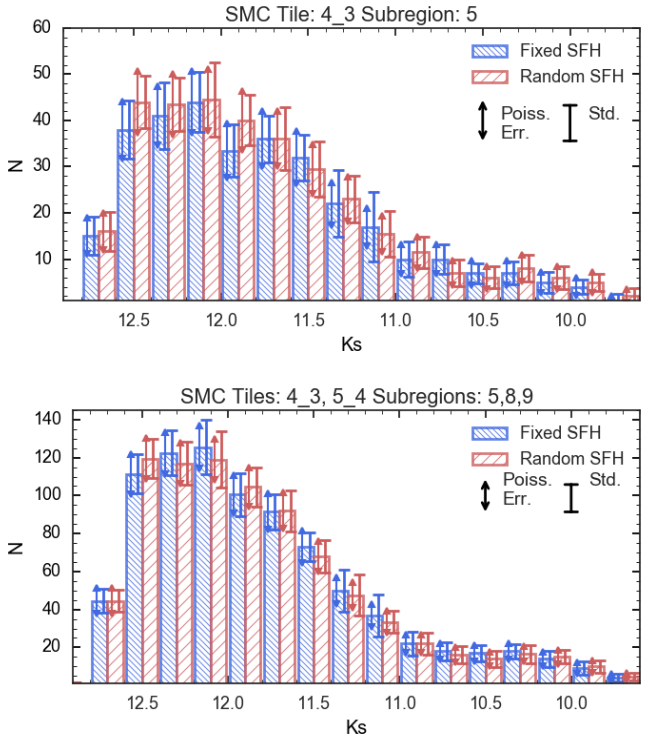


**Figure 4.4:** Comparison between the mean $K_s$-band LFs derived from two sets of simulations: those derived from the best fit SFH values (blue histograms), and those derived from randomly sampled SFH (red histograms). The two sets of error bars illustrate the standard deviations and the Poisson error, i.e. the square root of the number counts for each $K_s$ bin. The results for the region SMC 4_3 G5 are shown in the upper panel, while the bottom panel shows the result for the 6 subregions.

the case of a fixed SFH (as expected) and in the case with randomly extracted SFH. Furthermore, the difference in number counts between the two cases is within the Poisson error in each luminosity bin. Additionally, the uncertainties in the SFH produce variations in the total number of AGB stars smaller than 10 per cent. These results justify the use of a simplified approach, in which, for each SMC region, the LF and associated uncertainty in each luminosity bin are obtained as the mean value and standard deviation from 10 `TRILEGAL` simulations obtained with the best-fitting values of the SFH. Given the large number of TP-AGB sets tested in this work, this approach allows to significantly speed-up the calibration procedure.

### 4.2.3 Model selection criteria

In order to compare the results of the simulations with the SR16 catalogue, it is necessary to properly identify the different classes of stars in the synthetic catalogue. One possibility is to use the same photometric criteria as in SR16. In this case, however, small offsets in the model colours and magnitudes can significantly mix different kinds of stars, affecting the comparison with the observed star counts in the different AGB populations. On the other hand, the synthetic stars contain the surface chemical composition that allows a straightforward separation into different chemical types. For these reasons, I adopted an "hybrid" selection approach: whenever possible theoretical parameters – i.e. C/O, evolutionary stages – are used to distinguish different populations, and photometric criteria are only used to complement the selection when necessary.

The X-AGB stars can only be selected using photometric criteria, as they do not

correspond to a well defined set of intrinsic stellar parameters. Therefore, a star in the synthetic catalogue is identified as X-AGB following the same criteria as SR16: 1) $J-[3.6] > 3.1$ mag or $[3.6]-[8] > 0.8$ mag if $J > 19.69$; 2) $[3.6] < [3.6]_{\rm TRGB}$.

To separate the RSG sequence from the O-rich sequence, I used the same photometric criteria of SR16: i) $Ks < K_{\rm sTRGB}$, ii) $[3.6] < [3.6]_{\rm TRGB}$, and iii) $K1_{\rm RSG} \leq K_{\rm s} \leq K1$.

A simple comparison between models and observations suggests that the sequence of O-AGB stars is populated by both TP-AGB stars and early-AGB stars, which can be easily distinguished in the synthetic catalogues (looking at their evolutionary stages) but not in the data. To properly compare the synthetic and observed O-AGB sequences I first select them as in SR16: 1) $J-K_{\rm s}$ redder than $K1$; 2) $K_{\rm s} < K_{\rm sTRGB}$; 3) $[3.6] < [3.6]_{\rm TRGB}$ . I then considered the value of the C/O ratio and selected only stars with C/O $< 1$. The C-stars are selected according to the C/O ratio, i.e. if C/O $> 1$. I exclude from the C-AGB sequence the stars fainter than both $K_{\rm sTRGB}$ and $[3.6]_{\rm TRGB}$ and the already selected sample of X-AGB stars.

The observed class of a-AGB stars could be identified in the synthetic catalogues by using the photometric criteria, but this class hosts both C- and O-rich AGB stars that cannot be clearly separated using photometry. The only information about their chemical type is the spectral classification performed by Boyer et al. (2015a). They concluded that in the SMC the ratio between C-rich and O-rich a-AGB stars is $\approx 50$ per cent. When comparing the simulated and observed $K_{\rm s}$-band LFs, I take into account the contribution of the a-AGB stars by weighing the observed C- and O-AGB LFs with the a-AGB LF, according to the result of Boyer et al. (2015a). Thus, the total number counts of the C- and O-AGB stars are corrected to include the contribution of the aAGB stars. Therefore, the total number of observed C-AGB and O-AGB changes from 1854 to 2340 and 2623 to 3109 respectively.

In addition, I have identified a systematic colour shift between the models and observations, which is more marked for the more luminous O-rich stars (including RSGs and O-AGB stars). Since a slightly shift in colour can affect the number of O-rich stars due to the photometric criteria applied in the observations, to reconcile the differences in colours, I corrected the synthetic photometry a posteriori as fully discussed in Section 4.5.1.

### 4.2.4 Metrics for identifying the best-fitting model

I use as primary calibrators the star counts in the $K_{\rm s}$-band LFs and $K_{\rm s}$ vs. $J-K_{\rm s}$ CMD. The basic requirement is that the models simultaneously reproduce these quantities for the O-, C-, and X-AGB star samples identified by SR16. Among the many possible criteria to quantify this requirement, I choose two particular ones: The first is the $\chi^2$ of the LF distributions ($\chi^2_{\rm LF}$). The second criterion is the $\chi^2$ of the distributions in the $K_{\rm s}$ vs. $J-K_{\rm s}$ plane ($\chi^2_{\rm Hess}$). I compute both $\chi^2$ values separately for each class of AGB stars and for the entire sample. The value of the $\chi^2$ is computed following the $\chi^2$-like statistics defined by Dolphin (2002), i.e. assuming that the stars are distributed into the Hess diagram cells following a Poisson statistics:

$$\chi^2 = \frac{1}{N} \sum_{i=1}^{N} 2 \cdot \left[ m_i - n_i + n_i \cdot \ln \left( \frac{n_i}{m_i} \right) \right] \tag{4.5}$$

where $n$ and $m$ are the number of simulated and observed stars, respectively, in the $i$-th cell of the Hess diagram or the $i$-th bin of the LF, and $N$ is the number of cells or bins in which both $n$ and $m$ are different from zero. We note that the $\chi^2$ mentioned above do not have an absolute meaning, but they are used to compare the performance of each set of

models with respect to each other, i.e. lower $\chi^2$ values represent a better reproduction of the LF and colour distribution. Although they measure similar properties of the models, $\chi^2_{\rm Hess}$ is much more sensitive to the colour distributions of the model sequences.

For each of the three classes of AGB stars and for the entire sample, I compute the value of the $\chi^2_{\rm LF}$. The performance of each set of models is evaluated using a total $\overline{\chi^2_{\rm LF}}$, that is the average of the four $\chi^2_{\rm LF}$ values weighted by the respective number of observed stars. To identify the best-fitting model, I first select the sets that simultaneously reproduce the total number of observed AGB, O-, C- and X-AGB within 3-$\sigma$. The one with the lowest $\overline{\chi^2_{\rm LF}}$ value is considered as the best-fitting solution. This criterion is applied to the two series of models presented in Sections 4.3.3 and 4.3.4.

## 4.3 Calibration along the sequence of TP-AGB sets

In this section I first describe the results of the starting model. I then move to illustrate the calibration presenting the large grid of computed models and their performance in comparison with observations. A first series of models is computed to explore the effect of different mass-loss prescriptions for both O- and C-rich stars. Starting from the resulting best fitting-model of this series, a second series of models is calculated to constrain the 3DU parameters.

### 4.3.1 The starting set of TP-AGB models

The starting simulations of the SMC are based on the TP-AGB tracks described in Rosenfield et al. (2014, 2016) and presented in Marigo et al. (2017). I will refer to this set as S_00. The mass-loss prescription for the pre-dust driven wind is a modified version of the Schröder and Cuntz (2005, hereafter SC05) prescription (Rosenfield et al., 2016). The dust-driven phase is described with a mass-loss formalism similar to Bedijn (1988), for both O-rich and C-rich stars. As for the 3DU, the onset is controlled by a constant temperature parameter $\log(T_{\rm b}^{\rm dred}/{\rm K}) = 6.40$ and the efficiency parameter $\lambda$ follows the relations provided by Karakas et al. (2002, hereafter also K02).

Figure 4.5 compares the observed $K_{\rm s}$-band LFs for each class of AGB stars with the simulated ones based on the set S_00. The first panel of Figure 4.5 shows the LFs of the observed and synthetic AGB stars. The total number of AGB stars is reproduced to within 12 percent, in agreement with the calibration performed by Rosenfield et al. (2016). However, the model overpredicts the number of stars at magnitudes fainter than $K_{\rm s} \approx 12.6$ mag, and underpredicts the number of stars at brighter magnitudes. These discrepancies are due to an overestimation of O-rich AGB stars of about 40 per cent and an underestimation ($\approx$ 30 per cent) of C-rich stars as shown in the second and third panels of Figure 4.5. The O-rich overestimation is manly due to low-mass (1–1.5 $M_{\odot}$), low-metallicty ($Z_{\rm i} \approx 0.001$) stars populating the faint end of the $K_{\rm s}$-band LF. This is clearly shown in Figure 4.6, where I compare the observed and the synthetic $K_{\rm s}$-band LF of TP-AGB set S_00, decomposed in bins of initial mass. An excess of O-rich stars is also present at the bright end of the LF. Such stars are experiencing the HBB phase and have initial masses larger than about 3 $M_{\odot}$ and initial metallicity around $0.003 - 0.004$ (a small contribution is given by more metal rich stars with $Z_{\rm i} \approx 0.005$).

The total number of X-AGB stars is in agreement with the observations, but the shape of the LF is not consistent with the observed one. The peak in the X-AGB LF at $K_{\rm s} \approx 12.2$ mag corresponds to a $J-K_{\rm s}$ colour redder than 3 mag. The accumulation of stars is a consequence of the adopted mass-loss prescription. Following Vassiliadis and

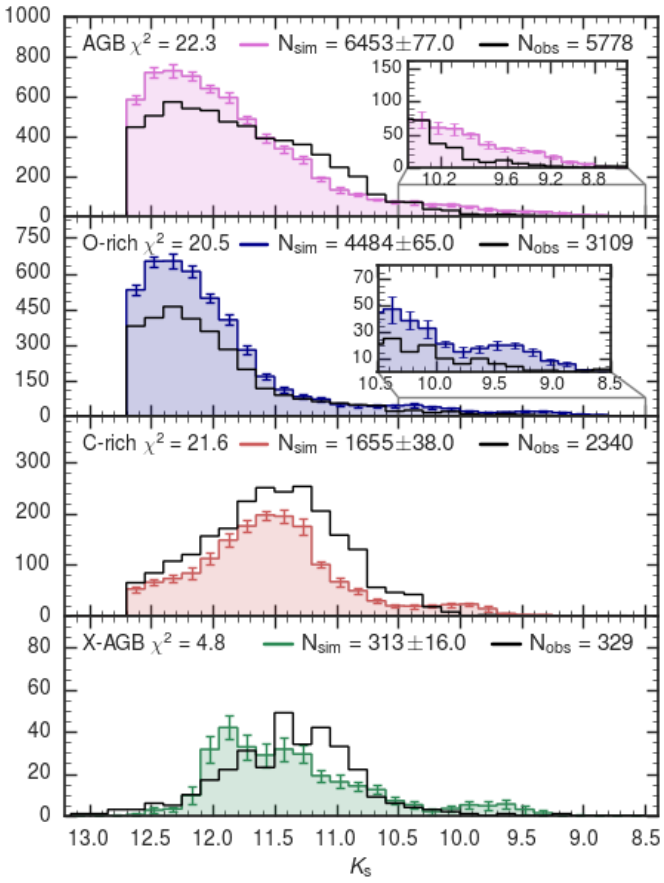


**Figure 4.5:** Mean $K_s$-band LFs from S_00 models (coloured histograms), as compared to the observations (dark-line histogram), both for the entire AGB sample (top panel) and for the three main classes of AGB stars (other panels). The error bars are the $1\sigma$ standard deviation of the 10 TRILEGAL realisations. The $\chi^2_{\rm LF}$ specific to each panel is also reported.

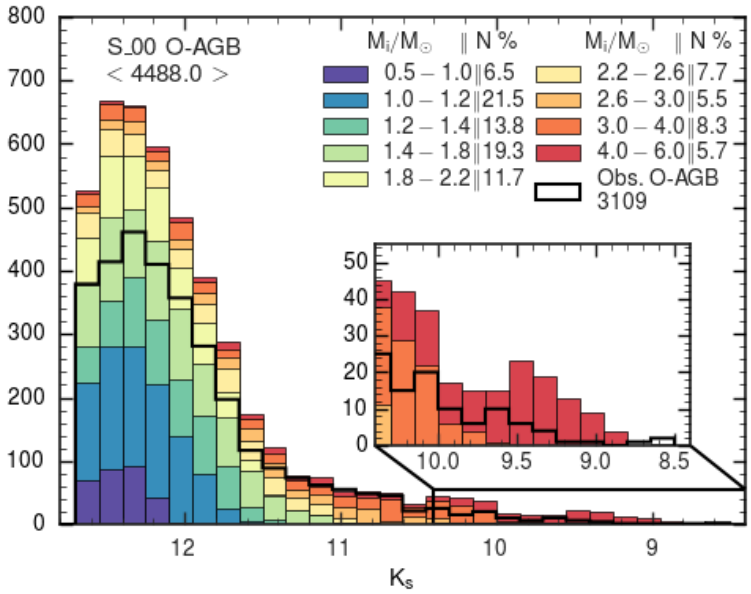


**Figure 4.6:** Synthetic $K_s$-band LF of the O-rich stars from TP-AGB set S_00, decomposed in bins of initial mass. The observed LF is shown as a black line. The legend shows the initial mass intervals and the percentage of stars in each bin. The inset is a zoom of the bright end of the LF, dominated by more massive AGB stars ($M_i \gtrsim 3\ M_\odot$).

Wood (1993), the radiation driven mass-loss reaches a maximum ($10^{-4}$–$10^{-5} M_{\odot}\mathrm{yr}^{-1}$) and then remains almost constant during the final thermal pulses.

The morphology of each class of stars can be appreciated in Figure 4.7 which shows the simulated Hess diagrams computed with the set S_00 for the O-AGB, the C-AGB and the X-AGB stars, as well as the observed ones. The $J-K_{\mathrm{s}}$ colour shift is immediately evident by looking at the residual differences between model and data in the first panel. The lack of C-rich stars for $K_{\mathrm{s}}$ fainter than 10 mag is also evident, as well as the overestimation at brighter magnitudes. These discrepancies are also present in the X-AGB distribution. The excess of X-AGB at brighter magnitude is due to massive C-rich stars.

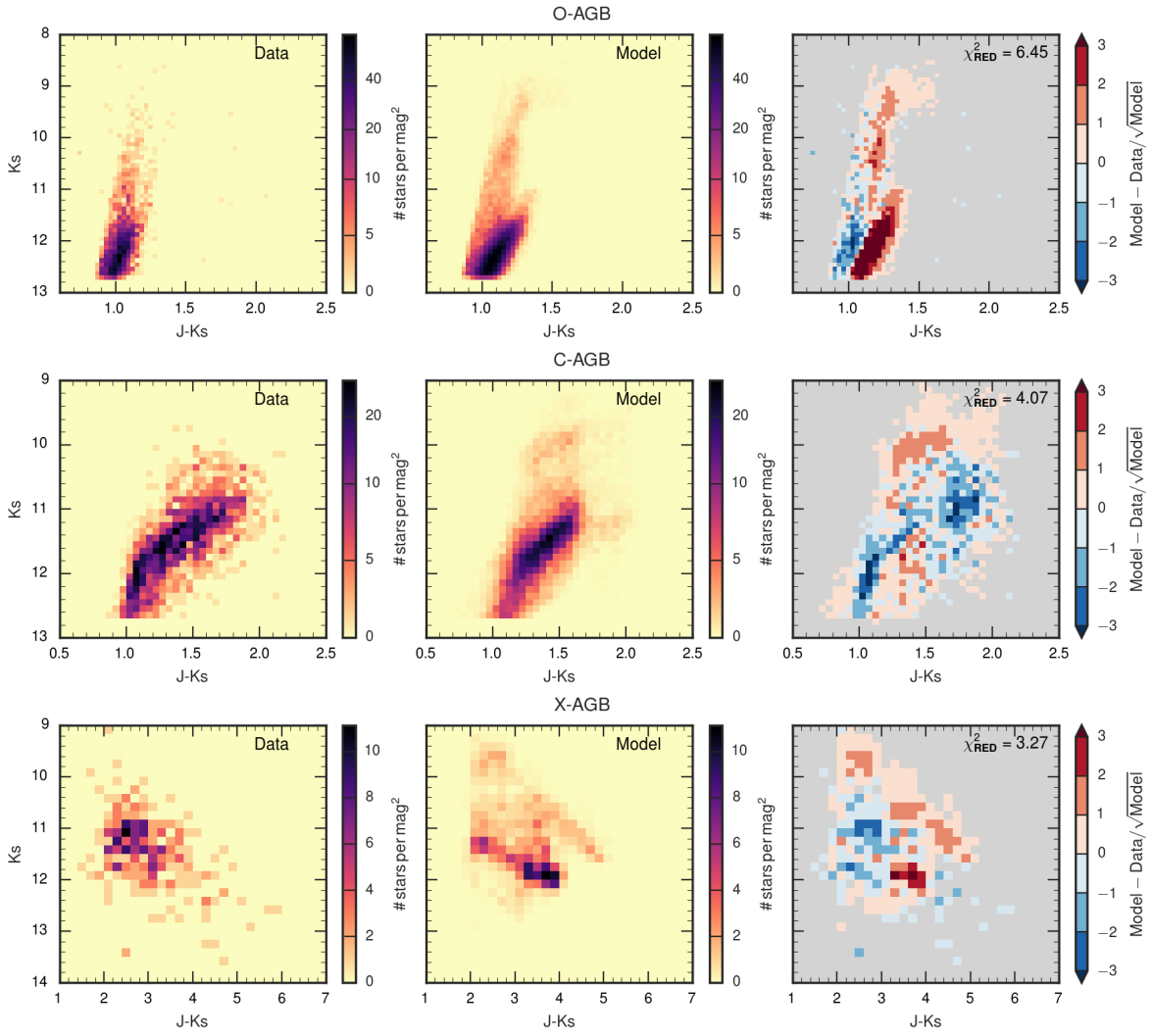


**Figure 4.7:** Observed (left panels) and simulated (middle panels) $K_{\mathrm{s}}$ vs. $J-K_{\mathrm{s}}$ Hess diagrams computed from S_00 models for the O-, C- and X-AGB samples separately. The right panels shows the residual difference between the models and the data. The value of the $\chi^2_{\mathrm{Hess}}$is also shown. The synthetic diagram is the average Hess diagram of the 10 `TRILEGAL` realisations.

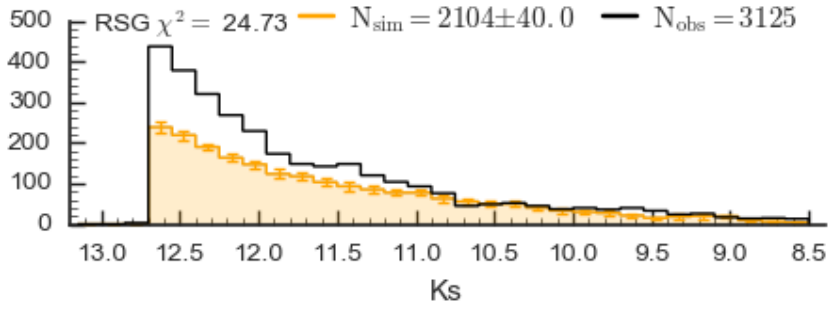


**Figure 4.8:** Similarly to Fig. 4.5, the $K_s$-band LFs for the RSGs.

Before leaving this section I consider it worth commenting on the sample of RSG present in the SMC data. The comparison between observed and simulated LFs is shown in Figure 4.8. The overall shape of the observed LF of the RSG stars is well reproduced by the starting models. However, there is an evident lack of stars at fainter magnitudes. Such discrepancies, which have been already pointed out by Melbourne et al. (2012), can be due to a number of reasons: i) a residual foreground contamination in the data up to $\approx$ 35 per cent (Boyer et al., 2011, their Sect. 2.2); ii) an underestimation of the SFR for these young populations; (3) an underestimation of predicted lifetimes for core-helium burning stars of intermediate and high initial mass. Since the present calibration does not rely on this class of stars, I will focus the analysis on AGB stars, postponing the investigation of the RSGs to a future work. The same issue was also reported by Melbourne et al. (2012).

### 4.3.2 Grid of TP-AGB tracks

The calibration procedure relies on extended grids of TP-AGB tracks computed with `COLIBRI`, adopting different descriptions for the third dredge-up and mass loss. Each combination of the adopted parameters corresponds to a set of tracks. Each set covers a range of masses (at the first TP) from about 0.5 $M_\odot$ to 5–6 $M_\odot$ (typically 70 values) and spans a wide metallicity interval, from $Z = 0.0005$ to $Z = 0.02$ (typically 10 values). Therefore, each set includes roughly 700 TP-AGB tracks, computed up to the complete ejection of the envelope. For the purposes of this work we computed a large grid of evolutionary models that consists of more than 30 sets (about 24500 TP-AGB tracks). Such a demanding computational effort can only be achieved with a flexible and fast code such as `COLIBRI`. The full grid of TP-AGB tracks is summarised in Table 4.4. Each set (from S_00 to S_35) is characterized by different choices of mass loss and/or third dredge-up. In Figure 4.9 I show a summary of the performance of the calculated models. The observed and simulated number counts for each class of AGB stars, the corresponding $\chi^2_{\rm LF}$ and the C/M ratios are shown in Table 4.5. I will refer to Figure 4.9 and Table 4.5 discussion of the fundamental steps of the calibration presented in the next Section.

To facilitate the presentation of the calibration it is convenient to split the TP-AGB sets into two groups, depending on the assumptions adopted for the two key processes under examination, namely mass loss (see Sect. 4.3.3) and 3DU (see Sect. 4.3.4).

**Table 4.4:** Grid of TP-AGB sets

| | **Mass Loss** | | | | | | | **Third Dredge-Up** | | | |
|---|---|---|---|---|---|---|---|---|---|---|---|
| | **Pre-Dust** | | **Dust - driven** | | | | | **Activation** | **Efficiency** | | |
| | | | **M-stars** | | **C-stars** | | | | | | |
| **SET** | **Id** | $\eta$ | **Id** | $\eta$ | **Id** | $\eta$ | $\dot{M}^{(1)}$ | $\log(T_{\rm b}^{\rm dred}/[{\rm K}])^{(2)}$ | $\lambda$ | | |
| S_00 | SC05 | – | BE88 | – | BE88 | – | (a) | 6.40 | K02 | | |
| S_01 | CS11 | 2 | BL95 | 0.05 | BL95 | 0.05 | (a) | 6.40 | K02 | | |
| S_02 | CS11 | 2 | BL95 | 0.02 | CDYN | 1 | (a) | 6.40 | K02 | | |
| S_03 | CS11 | 2 | BL95 | 0.03 | CDYN | 1 | (a) | 6.40 | K02 | | |
| S_04 | CS11 | 2 | BL95 | 0.05 | CDYN | 1 | (a) | 6.40 | K02 | | |
| S_05 | CS11 | 2 | BL95 | 0.06 | CDYN | 1 | (a) | 6.40 | K02 | | |
| S_06 | CS11 | 3 | BL95 | 0.06 | CDYN | 1 | (a) | 6.40 | K02 | | |
| S_07 | CS11 | 3 | BL95 | 0.06 | CDYN | 1 | (a) | $f_1(Z_{\rm i})$ | K02 | | |
| S_19 | CS11 | 3 | VW93 | – | CDYN | 1 | (a) | $f_1(Z_{\rm i})$ | K02 | | |
| S_12 | CS11 | 3 | BL95 | 0.01 | CDYN | 1 | (b) | $f_1(Z_{\rm i})$ | K02 | | |
| S_08 | CS11 | 3 | BL95 | 0.06 | CDYN | 1 | (a) | $f_1(Z_{\rm i})$ | $\lambda_{\rm max}$= 0.5 | | |
| S_09 | CS11 | 3 | BL95 | 0.02 | BL95 | 0.02 | (a) | $f_1(Z_{\rm i})$ | $\lambda_{\rm max}$= 0.5 | | |
| S_10 | CS11 | 3 | BL95 | 0.01 | BL95 | 0.01 | (a) | $f_1(Z_{\rm i})$ | $\lambda_{\rm max}$= 0.5 | | |
| S_11 | CS11 | 3 | BL95 | 0.01 | CDYN | 1 | (b) | $f_1(Z_{\rm i})$ | $\lambda_{\rm max}$= 0.5 | | |
| S_31 | CS11 | 3 | BL95 | 0.01 | CDYN | 1 | (b) | $f_1(Z_{\rm i})$ | $\lambda_{\rm max}$= 0.4 | | |
| | | | | | | | | | $\widetilde{\lambda}_{\rm max}$ | $\widetilde{\rm M}_{\rm c}[M_\odot]$ | ${\rm M}_{{\rm c},\lambda=0}[M_\odot]$ |
| S_13 | CS11 | 3 | BL95 | 0.01 | CDYN | 1 | (b) | $f_1(Z_{\rm i})$ | 0.5 | 0.65 | 0.95 |
| S_14 | CS11 | 3 | BL95 | 0.01 | CDYN | 1 | (b) | $f_1(Z_{\rm i})$ | 0.5 | 0.65 | 0.85 |
| S_15 | CS11 | 3 | BL95 | 0.01 | CDYN | 1 | (b) | $f_1(Z_{\rm i})$ | 0.6 | 0.60 | 0.85 |
| S_16 | CS11 | 3 | BL95 | 0.01 | CDYN | 1 | (b) | $f_2(Z_{\rm i})$ | 0.6 | 0.60 | 0.85 |
| S_17 | CS11 | 3 | BL95 | 0.01 | CDYN | 1 | (c) | $f_2(Z_{\rm i})$ | 0.6 | 0.60 | 0.85 |
| S_18 | CS11 | 3 | BL95 | 0.02 | CDYN | 1 | (c) | $f_2(Z_{\rm i})$ | 0.6 | 0.60 | 0.85 |
| S_20 | CS11 | 3 | BL95 | 0.02 | CDYN | 1 | (a) | $f_2(Z_{\rm i})$ | 0.6 | 0.60 | 0.85 |
| S_22 | CS11 | 3 | BL95 | 0.02 | CDYN | 1 | (c) | $f_2(Z_{\rm i})$ | 0.7 | 0.70 | 0.85 |
| S_23 | CS11 | 3 | BL95 | 0.02 | CDYN | 1 | (c) | $f_2(Z_{\rm i})$ | 0.8 | 0.60 | 0.85 |
| S_24 | CS11 | 3 | BL95 | 0.02 | CDYN | 1 | (c) | $f_2(Z_{\rm i})$ | 0.8 | 0.60 | 1.30 |
| S_25 | CS11 | 3 | BL95 | 0.02 | CDYN | 1 | (c) | $f_2(Z_{\rm i})$ | 0.8 | 0.60 | 1.00 |
| S_26 | CS11 | 3 | BL95 | 0.02 | CDYN | 1 | (c) | $f_2(Z_{\rm i})$ | 0.7 | 0.60 | 0.85 |
| S_27 | CS11 | 3 | BL95 | 0.02 | CDYN | 1 | (c) | $f_2(Z_{\rm i})$ | 0.7 | 0.60 | 1.00 |
| S_28 | CS11 | 3 | BL95 | 0.02 | CDYN | 1 | (b) | $f_2(Z_{\rm i})$ | 0.7 | 0.60 | 1.00 |
| S_29 | CS11 | 3 | BL95 | 0.02 | CDYN | 1 | (c) | $f_2(Z_{\rm i})$ | 0.7 | 0.625 | 1.00 |
| S_30 | CS11 | 3 | BL95 | 0.02 | CDYN | 1 | (c) | $f_2(Z_{\rm i})$ | 0.5 | 0.6 | 1.00 |
| S_32 | CS11 | 3 | BL95 | 0.02 | CDYN | 1 | (c) | $f_2(Z_{\rm i})$ | 0.5 | 0.5 | 1.00 |
| S_33 | CS11 | 3 | BL95 | 0.02 | CDYN | 1 | (c) | $f_2(Z_{\rm i})$ | 0.5 | 0.5 | 1.00 |
| S_34 | CS11 | 3 | BL95 | 0.02 | CDYN | 1 | (c) | $f_2(Z_{\rm i})$ | 0.6 | 0.6 | 1.00 |
| S_35 | CS11 | 3 | BL95 | 0.03 | CDYN | 1 | (c) | $f_2(Z_{\rm i})$ | 0.7 | 0.60 | 1.00 |

**Notes:**

(1) Current mass-loss value:
(a) $\max(\dot{\rm M}_{\rm pre-dust},\dot{\rm M}_{\rm dust})$
(b) $\max(\dot{\rm M}_{\rm pre-dust},\dot{\rm M}_{\rm dust})$, for C/O > 1 if $\dot{\rm M}_{\rm dust}$is not active, we assume $\dot{\rm M}_{\rm dust} = \dot{\rm M}_{\rm dust}({\rm C/O} < 1)$
(c) $\max(\dot{\rm M}_{\rm pre-dust},\dot{\rm M}_{\rm dust})$ for C/O < 1; for C/O > 1 $\max(\dot{\rm M}_{\rm dust}({\rm C/O} < 1), \dot{\rm M}_{\rm dust}({\rm C/O} > 1)$ )

(2) 3DU activation temperature as a function of $Z_{\rm i}$:
$f_1(Z_{\rm i})$: $\log T_{\rm b}^{\rm dred} = \max[6.3, T_1 + (T_2 - T_1)(Z - Z_1)/(Z_2 - Z_1)]$ with $T_1 = 6.3$, $T_1 = 6.60$, $Z_1 = 0.001$, $Z_2 = 0.02$.
$f_2(Z_{\rm i})$: $\log T_{\rm b}^{\rm dred} = \max[6.2, T_1 + (T_2 - T_1)(Z - Z_1)/(Z_2 - Z_1)]$ with $T_1 = 6.1$, $T_1 = 6.75$, $Z_1 = 0.001$, $Z_2 = 0.02$.

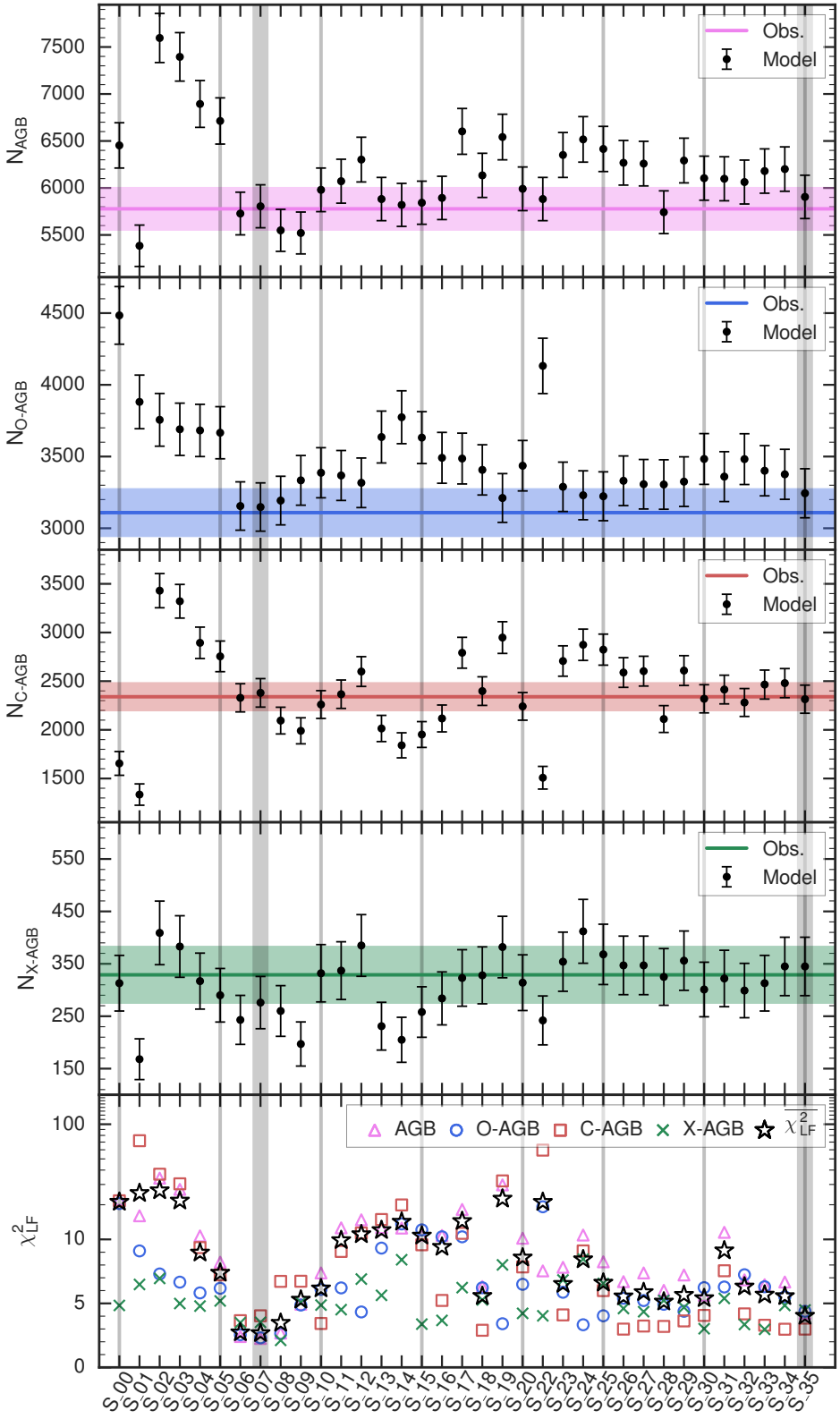


**Figure 4.9:** Summary of the results obtained from the calculated models. In the first four panels, we show the number of simulated stars and the $3\sigma$ error bars for each set of models. The horizontal lines represent the number of observed stars and the relative $3\sigma$ error bars (estimated as the square root of the number counts). The bottom panel shows the resulting $\chi^2_{\rm LF}$ values for the AGB, O-, C- and X-AGB samples. The average value of the four $\chi^2_{\rm LF}$ is shown with the star symbols. The two well defied minima, highlighted with the vertical grey strips, correspond to the two best-fitting models (S_07 and S_35). The vertical thin grey lines marked sets S_00, S_05, S_10, S_15, S_20, S_25, S_30 and S_35.

**Table 4.5:** Comparison of observed star counts with `COLIBRI` models.

| | AGB | | | O-AGB | | | C-AGB | | | X-AGB | | | C/M |
|---|---|---|---|---|---|---|---|---|---|---|---|---|---|
| | $N_{\rm TOT}$ | $\Delta N\%^1$ | $\chi^2_{\rm LF}$ | $N_{\rm TOT}$ | $\Delta N\%^1$ | $\chi^2_{\rm LF}$ | $N_{\rm TOT}$ | $\Delta N\%^1$ | $\chi^2_{\rm LF}$ | $N_{\rm TOT}$ | $\Delta N\%^1$ | $\chi^2_{\rm LF}$ | |
| OBS | 5778 | | | 3109 | | | 2340 | | | 329 | | | 0.86 |
| S_00 | 6453 | 11.7 | 22.3 | 4484 | 44.2 | 20.5 | 1655 | -29.3 | 21.6 | 313 | -4.9 | 4.8 | 0.44 |
| S_01 | 5385 | -6.8 | 16.0 | 3881 | 24.8 | 9.1 | 1335 | -42.9 | 71.9 | 168 | -48.9 | 6.5 | 0.39 |
| S_02 | 7596 | 31.5 | 34.0 | 3756 | 20.8 | 7.3 | 3430 | 46.6 | 36.8 | 409 | 24.3 | 7.0 | 1.02 |
| S_03 | 7395 | 28.0 | 27.2 | 3690 | 18.7 | 6.7 | 3321 | 41.9 | 30.4 | 383 | 16.4 | 5.0 | 1.0 |
| S_04 | 6894 | 19.3 | 10.7 | 3682 | 18.4 | 5.8 | 2894 | 23.7 | 9.4 | 317 | -3.6 | 4.8 | 0.87 |
| S_05 | 6713 | 16.2 | 8.2 | 3666 | 17.9 | 6.2 | 2755 | 17.7 | 7.2 | 290 | -11.9 | 5.2 | 0.83 |
| S_06 | 5728 | -0.9 | 2.4 | 3155 | 1.5 | 2.6 | 2329 | -0.5 | 3.6 | 243 | -26.1 | 3.5 | 0.82 |
| S_07 | 5805 | 0.5 | 2.3 | 3148 | 1.3 | 2.3 | 2380 | 1.7 | 4.0 | 276 | -16.1 | 3.5 | 0.84 |
| S_08 | 5549 | -4.0 | 2.7 | 3193 | 2.7 | 2.6 | 2095 | -10.5 | 6.7 | 260 | -21.0 | 2.1 | 0.74 |
| S_09 | 5521 | -4.4 | 4.9 | 3334 | 7.2 | 4.9 | 1990 | -15.0 | 6.7 | 197 | -40.1 | 5.1 | 0.66 |
| S_10 | 5980 | 3.5 | 7.4 | 3387 | 8.9 | 6.1 | 2260 | -3.4 | 3.4 | 332 | 0.9 | 4.9 | 0.76 |
| S_11 | 6072 | 5.1 | 12.6 | 3368 | 8.3 | 6.2 | 2366 | 1.1 | 9.1 | 337 | 2.4 | 4.5 | 0.8 |
| S_12 | 6302 | 9.1 | 14.8 | 3317 | 6.7 | 4.3 | 2599 | 11.1 | 11.4 | 385 | 17.0 | 6.9 | 0.9 |
| S_13 | 5882 | 1.8 | 12.7 | 3636 | 17.0 | 9.3 | 2014 | -13.9 | 14.9 | 231 | -29.8 | 5.6 | 0.62 |
| S_14 | 5820 | 0.7 | 12.5 | 3774 | 21.4 | 13.6 | 1841 | -21.3 | 19.9 | 205 | -37.7 | 8.4 | 0.54 |
| S_15 | 5843 | 1.1 | 10.9 | 3632 | 16.8 | 12.1 | 1952 | -16.6 | 9.6 | 258 | -21.6 | 3.4 | 0.61 |
| S_16 | 5894 | 2.0 | 10.8 | 3491 | 12.3 | 10.5 | 2117 | -9.5 | 5.2 | 284 | -13.7 | 3.7 | 0.69 |
| S_17 | 6602 | 14.3 | 18.2 | 3486 | 12.1 | 10.5 | 2792 | 19.3 | 11.3 | 323 | -1.8 | 6.2 | 0.89 |
| S_18 | 6134 | 6.2 | 6.3 | 3407 | 9.6 | 6.2 | 2398 | 2.5 | 2.9 | 328 | -0.3 | 5.3 | 0.8 |
| S_19 | 6542 | 13.2 | 29.7 | 3211 | 3.3 | 3.4 | 2948 | 26.0 | 32.2 | 382 | 16.1 | 8.0 | 1.04 |
| S_20 | 5991 | 3.7 | 10.2 | 3436 | 10.5 | 6.5 | 2241 | -4.2 | 7.8 | 314 | -4.6 | 4.2 | 0.74 |
| S_22 | 5882 | 1.8 | 7.5 | 4132 | 32.9 | 19.2 | 1508 | -35.6 | 59.6 | 242 | -26.4 | 4.0 | 0.42 |
| S_23 | 6351 | 9.9 | 7.8 | 3289 | 5.8 | 5.9 | 2707 | 15.7 | 4.1 | 354 | 7.6 | 6.8 | 0.93 |
| S_24 | 6517 | 12.8 | 10.9 | 3230 | 3.9 | 3.3 | 2874 | 22.8 | 9.1 | 412 | 25.2 | 8.5 | 1.02 |
| S_25 | 6415 | 11.0 | 8.2 | 3223 | 3.7 | 4.0 | 2824 | 20.7 | 6.0 | 368 | 11.9 | 6.6 | 0.99 |
| S_26 | 6268 | 8.5 | 6.7 | 3331 | 7.1 | 5.4 | 2589 | 10.6 | 3.0 | 347 | 5.5 | 4.6 | 0.88 |
| S_27 | 6259 | 8.3 | 7.4 | 3307 | 6.4 | 5.2 | 2603 | 11.2 | 3.2 | 347 | 5.5 | 4.4 | 0.89 |
| S_28 | 5742 | -0.6 | 6.0 | 3305 | 6.3 | 4.9 | 2111 | -9.8 | 3.2 | 325 | -1.2 | 5.2 | 0.74 |
| S_29 | 6292 | 8.9 | 7.2 | 3325 | 6.9 | 4.4 | 2609 | 11.5 | 3.6 | 356 | 8.2 | 4.7 | 0.89 |
| S_30 | 6104 | 5.6 | 5.6 | 3483 | 12.0 | 6.2 | 2319 | -0.9 | 4.1 | 301 | -8.5 | 3.0 | 0.75 |
| S_31 | 6098 | 5.5 | 11.5 | 3360 | 8.1 | 6.3 | 2414 | 3.2 | 7.6 | 322 | -2.1 | 5.4 | 0.81 |
| S_32 | 6063 | 4.9 | 6.8 | 3482 | 12.0 | 7.2 | 2281 | -2.5 | 4.2 | 299 | -9.1 | 3.4 | 0.74 |
| S_33 | 6180 | 7.0 | 6.5 | 3401 | 9.4 | 6.3 | 2465 | 5.3 | 3.3 | 313 | -4.9 | 3.0 | 0.82 |
| S_34 | 6201 | 7.3 | 6.7 | 3376 | 8.6 | 5.5 | 2480 | 6.0 | 3.0 | 345 | 4.9 | 4.8 | 0.84 |
| S_35 | 5905 | 2.2 | 4.2 | 3244 | 4.3 | 4.4 | 2315 | -1.1 | 3.0 | 345 | 4.9 | 4.5 | 0.82 |

**Notes:**
(1) Percentage of the difference between model and observations with respect to the observations: $100 \times (N_{\rm model} - N_{\rm obs.})/N_{\rm obs.}$

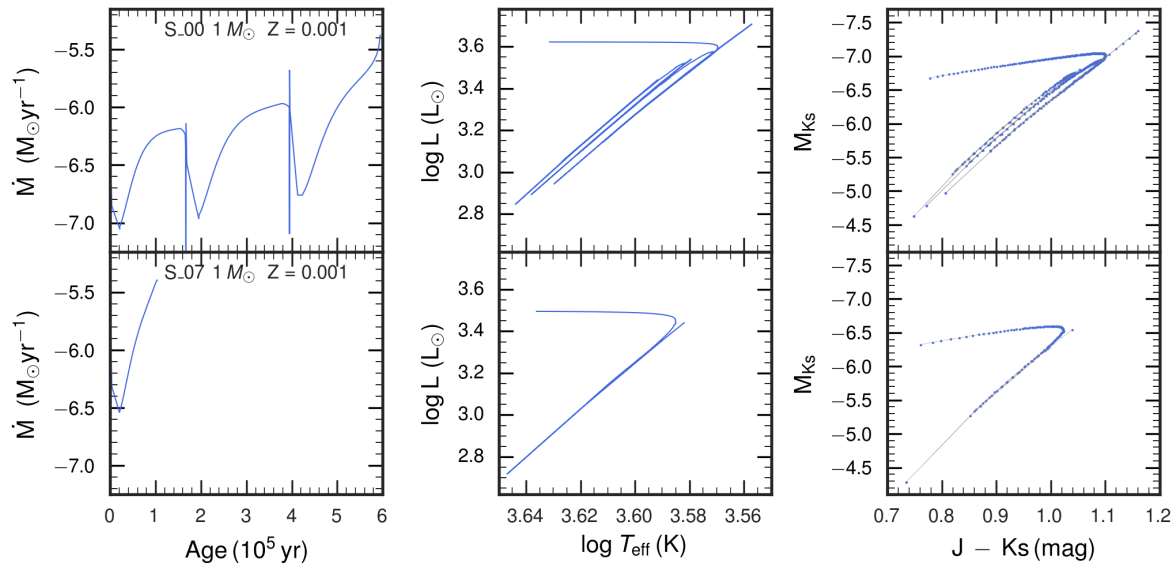


**Figure 4.10:** Evolutionary tracks of $1M_{\odot}$ and $Z_{\rm i}$=0.001 from models S_00 and S_07. Left panels: mass-loss rate as a function of the TP-AGB lifetime; middle panels: luminosity vs. effective temperature; right panels: $J-K_{\rm s}$ vs. $K_{\rm s}$-bolometric magnitude.

### 4.3.3 Changing mass loss

The first series of models (S_01 – S_07) shares the same prescriptions for the 3DU. In particular, the efficiency $\lambda$ follows the formalism introduced by K02, which assigns quite high values ($\lambda \simeq 1$) to stars with initial masses larger than $\simeq 3\ M_{\odot}$.

The initial step is to reduce the excess of O-rich stars present in the starting set S_00. This goal requires increasing the efficiency of mass loss both during the pre-dust and the dust-driven regimes. This is partly achieved with the adoption of the CS11 formalism to describe the cool chromospheric mass loss during the early stages when dust is expected not to be the main driver of stellar winds. In fact, the pre-dust mass loss is already active prior to the 1TP, i.e. during the brightest part of the early-AGB. For instance, in the case of a 1 $M_{\odot}$ model with $Z_{\rm i} = 0.001$ the current mass at the beginning of the TP-AGB phase is reduced by $\approx 15$ per cent. The net effect is the shortening of the the duration of the TP-AGB phase, mostly for low-mass O-rich stars, thus reducing their numbers. All S_01 – S_07 sets exhibit a reduction in the number of O-rich stars compared to the set S_00, improving the comparison with observations.

The effects on the evolutionary tracks are shown in Figure 4.10 for the $1M_{\odot}$ track with $Z_{\rm i}$=0.001 from models S_00 and S_07. The latter models have a higher mass-loss rate already at the beginning of the TP-AGB phase and the evolution of such stars quickly terminates within 0.1 Myr, whereas the lifetime of model S_00 is about 6 Myr. In addition, the evolutionary track of model S_07 reaches a lower luminosity, hence a lower bolometric magnitude.

To explore the impact of mass loss in the dust-driven regime, the set S_01 assumes a very efficient mass loss, adopting BL95 with $\eta_{\rm dust} = 0.05$ for all models. However, the reduction of O-rich stars is accompanied by a further deficit in the predicted number of C-rich stars, which worsens the comparison with observations compared to S_00.

In all sets from S_02 – S_07 the adopted mass loss during the dust-driven depends on the surface C/O ratio: the relation proposed by BL95 is used for C/O $< 1$ , while a routine based on the recent results of dynamical atmosphere models (Eriksson et al.,

2014; Mattsson et al., 2010, hereinafter CDYN) is used for C/O > 1 .

In contrast with S_00 and S_01, the results of S_02 show an overestimation of C-rich stars (see Fig. 4.9), especially at brighter magnitudes, i.e. $M_{\rm i} \gtrsim 2.5 M_{\odot}$. The reason is that the activation of the CDYN $\dot{\rm M}_{\rm dust}$ occurs later during the evolution with respect to the previously adopted formalism, because of its dependence on the values of the carbon excess (C − O) and the luminosity. For instance, in a 2 $M_{\odot}$ model with $Z_{\rm i} = 0.004$, the CDYN $\dot{\rm M}_{\rm dust}$ is fully active after 7 thermal pulses when the C − O is larger than about 8.2.

All these models from S_02 to S_07 adopt the same CDYN prescription for $\dot{\rm M}_{\rm dust}$ when C/O > 1, while the efficiency of the BL95 relation, active for C/O < 1, is increased from $\eta_{\rm dust} = 0.02$ (for S_02) to $\eta_{\rm dust} = 0.06$ (for S_07). Interestingly, this variation results in a relatively modest effect on the total number of O-rich stars, but has a significant impact on the predicted C-rich LF (see Figs. 4.34, 4.34, 4.34, 4.34). This effect can be appreciated in Fig. 4.9 which shows that the total number of O-rich stars do not vary significantly along the sequence from S_02 to S_05, whereas the total number of C-rich (and X-AGB) stars progressively decreases.

The reason of the small effect on the number of O-rich stars is that the bulk of them have low-mass progenitors, i.e. $M_{\rm i} \lesssim 2\ M_{\odot}$, for which the duration of the AGB phase is mainly controlled by the cool chromospheric mass loss active before the TP-AGB phase, as shown in Figure 4.11. Due to its high luminosity dependence, the BL95 relation mainly affects the evolution of more massive (and brighter) AGB stars that experience HBB. These represent a small contribution to the total number of O-rich stars. On the other hand, the sizeable impact on the number of C-rich stars can be explained as follows. The activation of the CDYN $\dot{\rm M}_{\rm dust}$ takes place once specific physical thresholds are met, i.e. sufficiently low effective temperatures, enough carbon excess to be condensed into dust grains, and suitably large L/M ratios. In general, increasing the efficiency of mass loss during the O-rich phase tends to favour larger mass-loss rates also during the stages with C/O > 1, since TP-AGB stars will enter the C-rich phase with lower current masses and lower effective temperatures. However, the extremely efficient mass loss during the O-rich stages may even inhibit the formation of C-stars by either anticipating the termination of the TP-AGB phase, or preventing the star from attaining the minimum temperature, $T_{\rm b}^{\rm dred}$ for the onset of the 3DU if the envelope mass has been significantly reduced. Indeed, this circumstance is met in the evolutionary models of the set S_07, so that the maximum initial mass for the formation of C-stars at $Z_{\rm i} = 0.004$ is found to be around 2.6 $M_{\odot}$ (see Sect. 4.4.2).

The LFs computed with S_05 show a good agreement with the observations and produces number counts that are within 15 per cent for each class. However, S_05 has a residual overestimation of the low-mass O-rich and the C-rich stars, which leads us to increase the $\eta_{\rm pre-dust}$ in the CS11 prescription (S_06 and S_07). The models S_06 and S_07 are both computed with $\eta_{\rm pre-dust} = 3$ but they differ for the $T_{\rm b}^{\rm dred}$ parameter, which increases linearly with the initial $Z_{\rm i}$ in the case of S_07 (see notes of Table 4.4). This assumption is equivalent to reducing the formation of C-stars at higher metallicity, as indicated by observations of the C/M ratio in galaxies (e.g. Boyer et al., 2013; Cioni and Habing, 2003; Groenewegen, 2002), and by earlier population synthesis studies (Marigo and Girardi, 2007; Marigo et al., 1999). However, since the metallicity of the SMC is lower than 0.02, the effects on the resulting star counts and LFs are not significant. In addition, the simulations computed with S_07 are in agreement with the observations of the more metal-rich galaxy M31 (Chen et al. in prep.).

In addition to the BL95 relation for mass-loss, we run a set of models (S_19) in which we adopt the formalism of VW93 for the efficiency of dust-driven winds during the O-

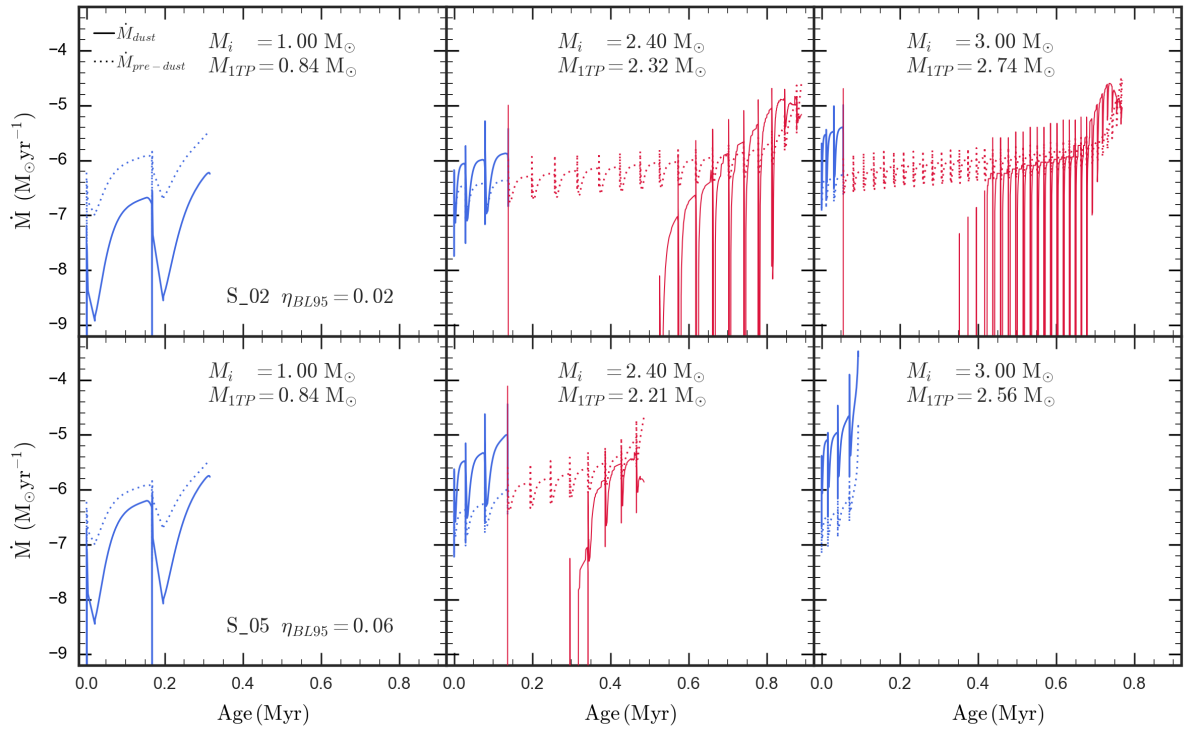


**Figure 4.11:** Mass-loss rate as a function of time for selected TP-AGB tracks from models S_02 (upper panels) and S_05 (bottom panels) with initial mass and metallicity as indicated. The tracks are color-coded according to the C/O ratio (blue for the M-star phase and red for the C-star phase) and the predicted $\dot{M}_{\rm pre-dust}$ and $\dot{M}_{\rm dust}$ are shown with dashed and solid lines respectively. The current mass at the first thermal pulse $M_{\rm 1TP}$ is also shown. Increasing $\eta_{\rm dust}$ from 0.02 to 0.06 does not affect the lifetime of low-mass mass stars for which the cromospheric mass-loss rate is always larger than the BL95. The BL95 law mainly affects the lifetimes of more massive AGB stars (middle and right panels). As a consequence of the high mass-loss rates attained with $\eta_{\rm dust}$=0.06 the quick termination of the TP-AGB phase prevents the formation of C-stars in models with $M_{\rm i}$ larger than $2.8 M_\odot$.

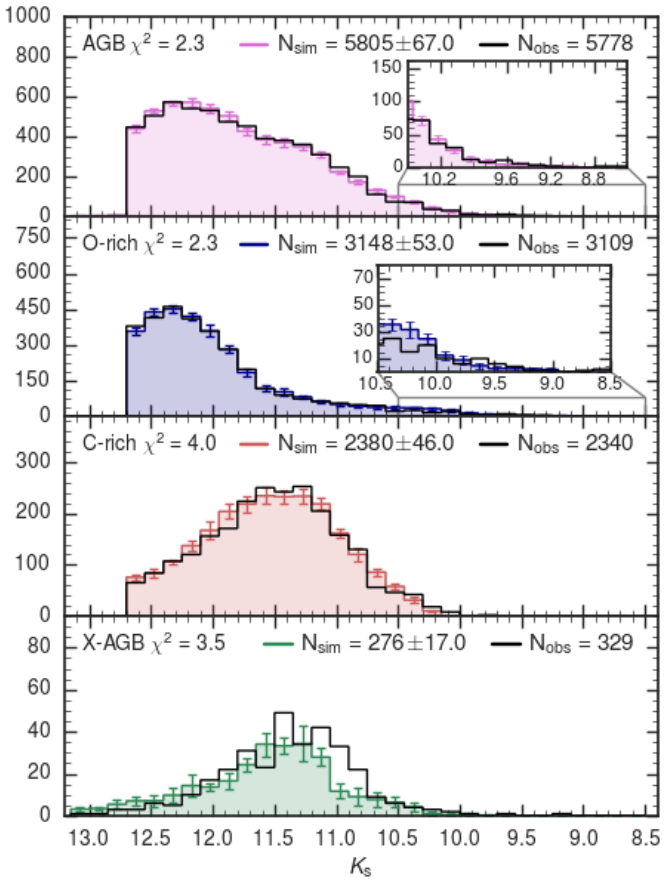


**Figure 4.12:** Same as Fig. 4.5 but for set S_07.

rich stages, while keeping the CDYN prescription for C-stars. The LF of O-rich stars is recovered very well, with a relative difference in the number counts within $\sim 3$ per cent. However, the same model leads to an excess of C-stars (in the brighter bins, $K_s \lesssim 10.5$ mag) of about 25 per cent.

Among all the sets of this first series we identify the best-fitting model as the set S_07, for which we obtain the lowest $\chi^2_{LF}$ values. The LFs and the Hess diagrams resulting from S_07 are shown in Figures 4.12 and 4.13. The predicted number counts for all the AGB classes are in excellent agreement with the observed ones. There is also a remarkable agreement in the shape of the LFs, as demonstrated also by the lower $\chi^2_{LF}$ values. This set recovers quite well both the LFs of all classes of AGB stars and the number counts. The optimal combination of parameters includes: CS11 pre-dust mass loss with efficiency $\eta_{pre-dust} = 3$, dusty regime with BL95 and $\eta_{dust} = 0.06$ for C/O $\leq 1$ and the CDYN for C/O $> 1$; 3DU efficiency described following K02 (see Table 4.4).

As for the distribution in the $J-K_s$ vs. $K_s$ plane, even if the number counts of O-rich AGB stars are in agreement with the observations, the value of $\chi^2_{Hess}$ is similar to the model S_00 because of the systematic colour-shift described in Sect. 4.5.1. A significant improvement can be seen in the C- and X-AGB distributions. The value of the $\chi^2_{Hess}$ are somewhat lower with respect to S_00 and the residual difference are within 1 $\sigma$ for most of the Hess diagram cells. The predicted tail of X-AGB stars does not show the same spread as in the observations. The most likely reason is that the variability is not taken into account in the simulations, whereas these stars are known to exhibit magnitude variations up to 3 mag in the $K_s$-band (Habing and Olofsson, 2004).

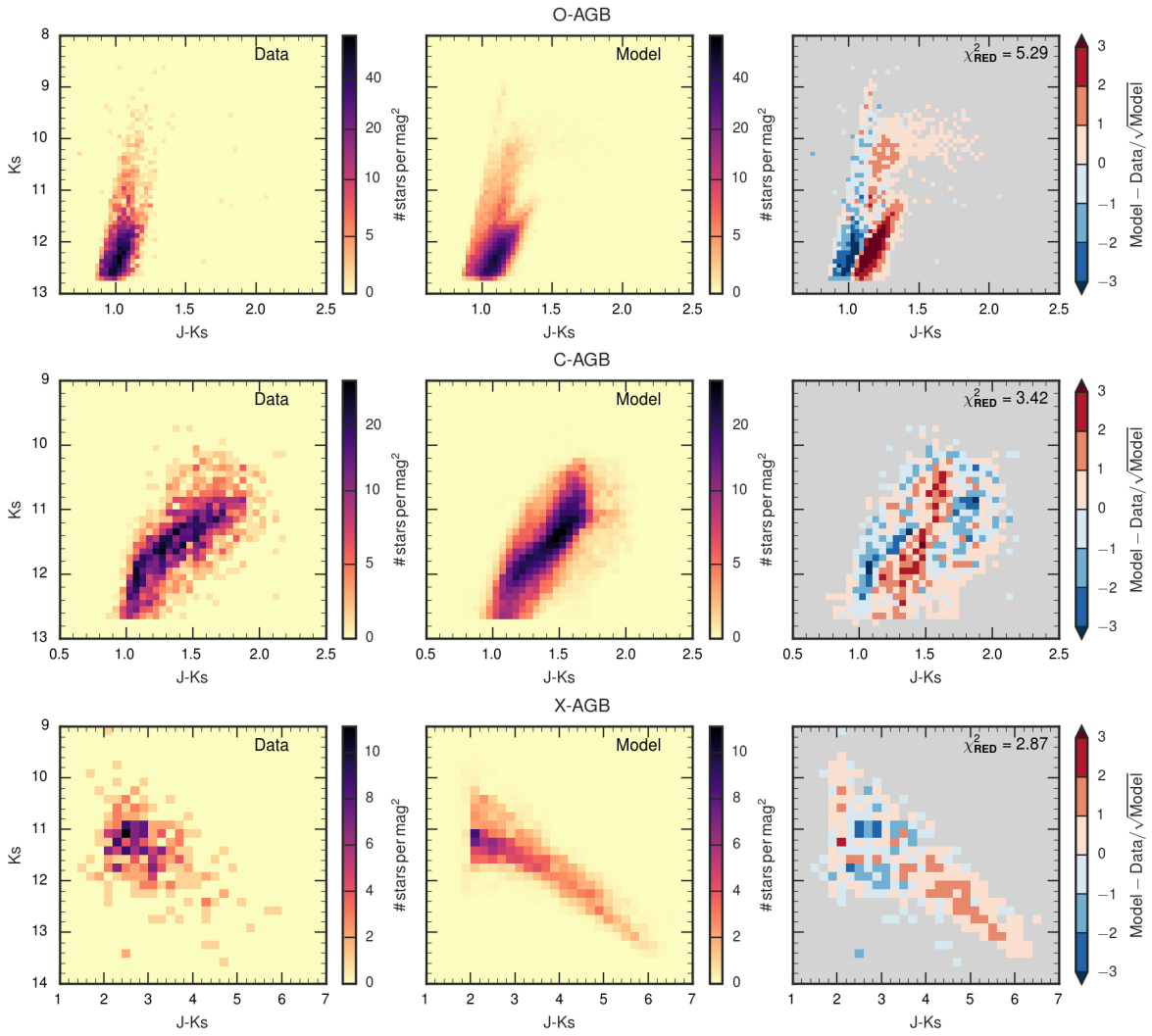


**Figure 4.13:** Same as Fig. 4.7 but for set S_07.

The main conclusions that can be drawn from these first results are:

- As already found by Rosenfield et al. (2016), the pre-dust mass-loss is very important for the low-mass, low-metallicity O-rich stars.
- The number counts of the brightest O-rich stars experiencing HBB can be reproduced by invoking a very efficient mass-loss during the dust-driven regime.
- The combination of large values of the mass-loss rate of the O-rich stars and the adoption of the results from dynamical models for C-stars (CDYN) allows to reproduce the number counts of the C-rich and the X-AGB stars.
- An important consequence of these prescriptions is that the maximum mass for which a star becomes a C-star is 2.6 $M_{\odot}$ at $Z_{\rm i} = 0.004$.

A discussion about the implications of these findings is given in Section 4.4.

### 4.3.4 Changing the third-dredge up

The first part of this work shows that adopting the standard prescriptions for the 3DU, based on Karakas et al. (2002) models, the AGB star population in the SMC can be well reproduced with suitable choices for the mass-loss regimes. However, at this stage the calibration cannot be considered completed. Given the lack of a robust treatment of stellar convection and mixing in stellar evolution codes it is not sufficient to limit the investigation to a single 3DU prescription. I describe a new formalism for the 3DU parametrisation in Section 4.3.4 and I then present a second series of models calculated to explore the effects of different 3DU prescriptions ( see Sect. 4.3.4).

#### A new parametrisation for the 3DUP

As mentioned in Section 2.2, the efficiency of each mixing event is described by the parameter $\lambda$, i.e. the fraction of the increment of the core mass during an inter-pulse period dredged up during the next thermal pulse. I recall that typical values range from $\lambda = 0$, i.e. no dredge-up, up to $\lambda = 1$, i.e. no net increase of the core mass. Values of $\lambda > 1$ are predicted by models that assume efficient convective overshoot (e.g. Herwig, 2004).

Figure 4.14 provides an example of the 3DU efficiency predicted by full TP-AGB models from a few different authors. During the TP-AGB evolution of a given star, $\lambda$ first increases following the strengthening of thermal pulses, reaches a maximum value $\lambda_{\rm max}$, and then decreases as the envelope mass is reduced by stellar winds, until the 3DU is eventually quenched. The peak value $\lambda_{\rm max}$ is not fixed, but varies from star to star depending on the initial stellar mass. Hoever, this behaviour is not homogeneously described by existing models. For instance, the models of Karakas et al. (2002), and, in general, all TP-AGB models computed with the Mount Stromlo Evolutionary code (e.g. Karakas et al., 2002; Karakas, 2010; Fishlock et al., 2014, and references therein), reach a high 3DU efficiency ($\lambda \simeq 1$) for $M_{\rm i} \gtrsim 3\,{\rm M}_{\odot}$, regardless of metallicity. In contrast, TP-AGB models by Cristallo et al. (2011, 2015, the FRUITY database) and by Ventura and D'Antona (2009) are characterized by lower values of $\lambda$, and by a decreasing trend of $\lambda_{\rm max}$ with the initial stellar mass.

The new parametric description of $\lambda$ is designed to a) qualitatively reproduce the results of full TP-AGB models calculations, and b) to keep the necessary flexibility, through the adoption of free parameters, in order to perform a physically-sound calibration based on observations.

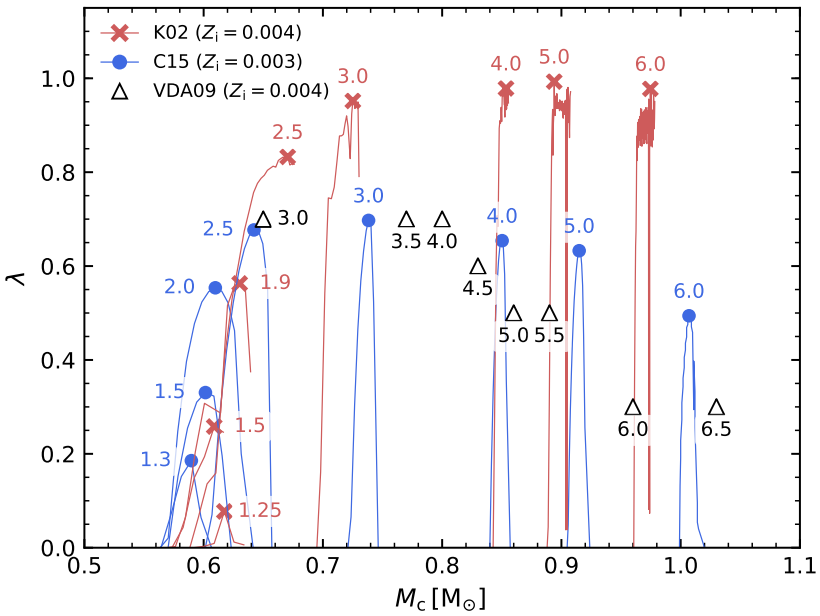


**Figure 4.14:** Predictions of the maximum 3DU efficiency $\lambda_{\rm max}$ as a function of the core mass from a few complete TP-AGB models with initial metallicity $Z_{\rm i} = 0.003, 0.004$ and initial mass as indicated. The predicted values of $\lambda_{\rm max}$ from Karakas et al. (2002, K02) and Cristallo et al. (2015, C15) are shown with red crosses and blue filled circles, respectively. The predicted values of $\lambda_{\rm max}$ as a function of the core mass at the first thermal pulse from the models of Ventura and D'Antona (2009, VDA09) are shown with empty triangles.

To account for the behaviour of the 3DU efficiency, $\lambda$ is expressed as a function of the ratio between the current total mass and the current core mass, $\xi = M/M_{\rm c}$, a dimensionless parameter that is expected to decrease during the TP-AGB evolution as a consequence of mass loss and core mass growth. A scheme of the new parametric formalism is shown in Fig. 4.15. $\xi$ is assumed to have a parabolic dependence, that allows to capture the bell-shaped evolution of $\lambda$. The controlling parameters for this relation are the centre $\widetilde{\xi}$ of the parabola, the value $\xi_{\lambda=0}$ at which $\lambda$ drops to zero, and the peak value $\lambda_{\rm max}$. The latter is not treated as a free parameter, but rather expressed as a parabolic function $\lambda_{\rm max}(M_{\rm c})$ of the core mass, to reflect the increase in 3DU efficiency with initial stellar mass, while also allowing for a decrease towards the high-mass range. The controlling parameters, equivalent to the previous case, are $\widetilde{M}_{\rm c}$, $M_{{\rm c},\lambda=0}$, and $\lambda^*_{\rm max}$.

The explicit form of the new parameterisation is:

$$\lambda = \lambda^*_{\rm max} \left[ \left( \frac{\xi - \widetilde{\xi}}{\widetilde{\xi} - \xi_{\lambda=0}} \right)^2 - 1 \right] \left[ \left( \frac{M_{\rm c} - \widetilde{M}_{\rm c}}{\widetilde{M}_{\rm c} - M_{{\rm c},\lambda=0}} \right)^2 - 1 \right] , \tag{4.6}$$

that is used to assign the 3DU efficiency at each thermal pulse as a function of $M$ and $M_{\rm c}$, provided the $T^{\rm dred}_{\rm b}$ criterion for the occurrence of the 3DU is fulfilled. The physical interpretation of the parameters is the following.

1. For a given star, $\widetilde{\xi}$ is the value of $M/M_{\rm c}$ at which the maximum $\lambda$ is reached, while $\xi_{\lambda=0}$ is the value at which the 3DU is quenched due the decrease of the envelope mass caused by mass loss. The adopted ranges for these parameters ($\widetilde{\xi} \simeq 3 - 4$, $\xi_{\lambda=0} \simeq 1.5 - 2$) are based on full evolutionary calculations available in the FRUITY database (Cristallo et al., 2015).

2. $\lambda^*_{\rm max}$ is the maximum efficiency of the 3DU among all TP-AGB stars, that is attained at $M_{\rm c} = \widetilde{M}_{\rm c}$, while $M_{{\rm c},\lambda=0}$ is the value of core mass beyond which the 3DU does not occur. These are the key parameters that we aim at constraining with the aid of the observed AGB stars in the SMC.

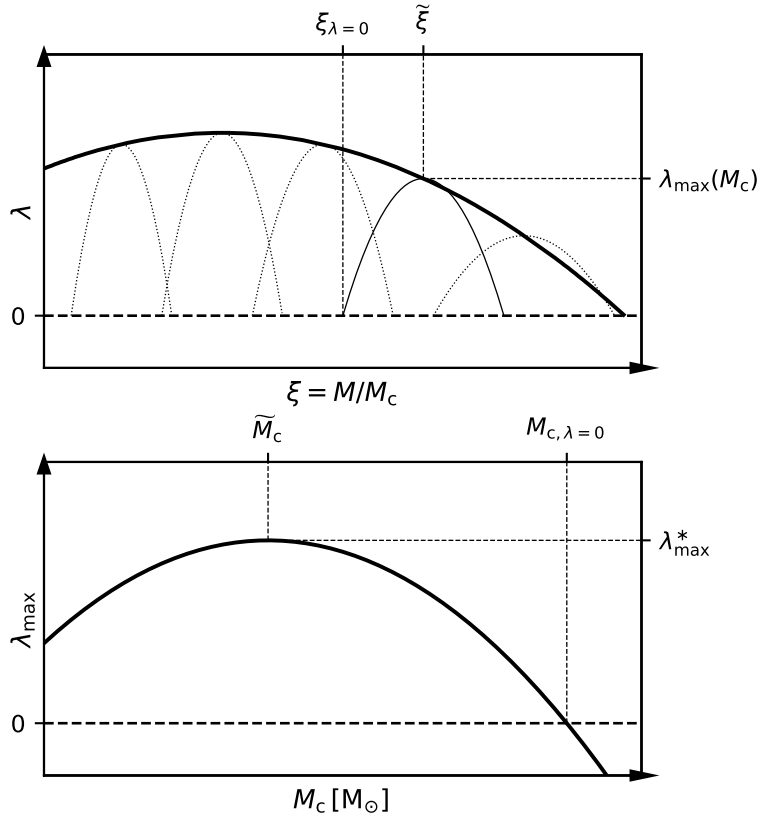


**Figure 4.15:** Schematic depiction of the meaning of the free parameters in our new formalism for the 3DU efficiency. Top panel: evolution of $\lambda$ as a function of $\xi$ for individual models having different values of the core mass (thin lines). For each model, $\lambda$ reaches a maximum $\lambda_{\rm max}$ at $\widetilde{\xi}$ and drops to zero at $\xi = \xi_{\lambda=0}$, representing the quenching of the 3DU when the envelope mass is substantially reduced by mass loss. The maximum value of $\lambda$ for each model is assumed to be a function of the core mass (thick line). Bottom panel: $\lambda_{\rm max}$ increases with core mass to a peak $\lambda^*_{\rm max}$, the maximum 3DU efficiency among all TP-AGB models, met at $M_{\rm c} = \widetilde{M}_{\rm c}$, then decreases until $\lambda_{\rm max} = 0$ at $M_{{\rm c},\lambda=0}$, beyond which the 3DU does not occur.

### Constraining the third dredge-up

As mentioned in Sect. 2.2 and shown in Fig. 4.14, the predicted properties of the 3DU are quite heterogeneous in the literature. The largest differences show up at larger stellar masses, typically for $M_{\rm i} \gtrsim 3M_\odot$. In this mass range the K02 formalism predicts a very efficient 3DU, $\lambda \simeq 1$, for all models with $M > 3M_\odot$, irrespective of metallicity. TP-AGB evolutionary calculations by other authors predict lower efficiencies of the 3DU, with typical values $\lambda \lesssim 0.5$ for $M_{\rm c} > 0.8\ M_\odot$ (Cristallo et al., 2015; Ventura and D'Antona, 2009). It is worth noticing that that hints for a reduced efficiency of the 3DU in intermediate-mass AGB stars ($\lambda < 1$ for $M_{\rm i} > 3 - 4\,M_\odot$) come also from studies on the initial-to-final mass relation (IFMR) derived from white dwarfs (WD) data in Galactic open clusters (see Fig. 4.19). As already pointed out by Kalirai et al. (2014), current TP-AGB models tend to predict WD masses that are too low for initial masses $\gtrsim 3\ M_\odot$. A significant improvement is obtained by reducing the efficiency of the third dredge-up during the TP-AGB

phase of progenitor stars. In fact the 3DU has a direct impact on the evolution of the core mass reducing its net growth (e.g. Kalirai et al., 2014; Marigo et al., 2013; Herwig, 2004). Therefore, lowering the 3DU in intermediate-mass stars may help to obtain more massive WDs.

In the following I will focus the discussion on those sets that share the same description for the dusty regime. This relies on two alternatives depending on the C/O ratio, namely: the BL95 relation for O-rich stars and the CDYN option for C-rich stars. This latter represents our preferred option as it is based on well-tested and state-of-the-art dynamical atmosphere models for C-stars (Eriksson et al., 2014; Mattsson et al., 2010).

As an initial step, the 3DU is described following K02, but lowering $\lambda_{\rm max}$ down to a fixed value of 0.4-0.5 (S_08, S_11, S_31), i.e. the 3DU efficiency does not exceed the selected $\lambda_{\rm max}$in all models. By analysing the C-rich and X-AGB LFs I find that, unless a very efficient mass loss ($\eta_{\rm dust} = 0.06$ as in S_08) is assumed during the O-rich dusty regime, the models predict an excess of bright C-rich stars ($K_{\rm s} < 10$ mag), most evident in S_11 and S_31.

To carry out a more systematic exploration on the effects of varying the 3DU efficiency, the standard choice, based on K02, was relaxed and the the new formalism, introduced in Sect. 4.3.4 was used in sets from S_13 to S_35. The parametric formulation allows to investigate various choices of the 3DU law, including also the possibility that the efficiency of the mixing episodes become lower at larger stellar masses. Since the cases of extremely efficient mass loss for O-rich stars (first series of models in Sect. 4.3.3) has already been explored, the value of $\eta_{\rm dust}$ is now reduced down to 0.01-0.03, values that are also adopted in other widely used AGB models (e.g. Karakas et al., 2018; Ventura and D'Antona, 2009).

In Figure 4.16 I show the resulting carbon star luminosity functions (CSLFs) for a few sets, together with the evolution of $\lambda$ as a function of the core mass $M_{\rm c}$ for some selected TP-AGB evolutionary tracks at $Z_{\rm i} = 0.004$ (representative of the initial metallicity of C-rich stars in the SMC). The emerging picture is quite complex due to the interplay of the 3DU with mass loss, still we can extract a few key general indications that help the interpretation of the results.

(i) *The faint tail* contains information about the lowest-mass stars that become C-stars. This limit is controlled by the temperature parameter $T_{\rm b}^{\rm dred}$, as well as by $\widetilde{M}_{\rm c}$. As illustrated in panel (a) of Fig. 4.16, lowering $T_{\rm b}^{\rm dred}$, i.e. moving from set S_15 to set S_16, favours an earlier formation (i.e. at lower $M_{\rm c}$ and $L$) of C-stars with low masses and therefore increases the predicted number of C-stars in the faintest bins of the CSLF. Decreasing $\widetilde{M}_{\rm c}$ has a similar effect on the faint tail, as shown in panel (b) of Fig. 4.16.

(ii) *The position of the peak* is mainly affected by the choice of $\widetilde{M}_{\rm c}$ as shown in panel (b) of Fig. 4.16. At lower $\widetilde{M}_{\rm c}$, i.e. moving from set S_22 to set S_26, the CSLF peak shifts towards fainter magnitudes. At the same time, lowering the value of $\widetilde{M}_{\rm c}$ results in an increase of the total number of C-stars, in particular those that populate the faint tail of the CSLF.

(iii) *The amplitude of the peak* is mainly controlled by the choice of $\lambda^*_{\rm max}$. As shown in panel (c) of Fig. 4.16 increasing the maximum 3DU efficiency, i.e. moving from set S_18 to set S_23, produces a higher peak in the CSLF.

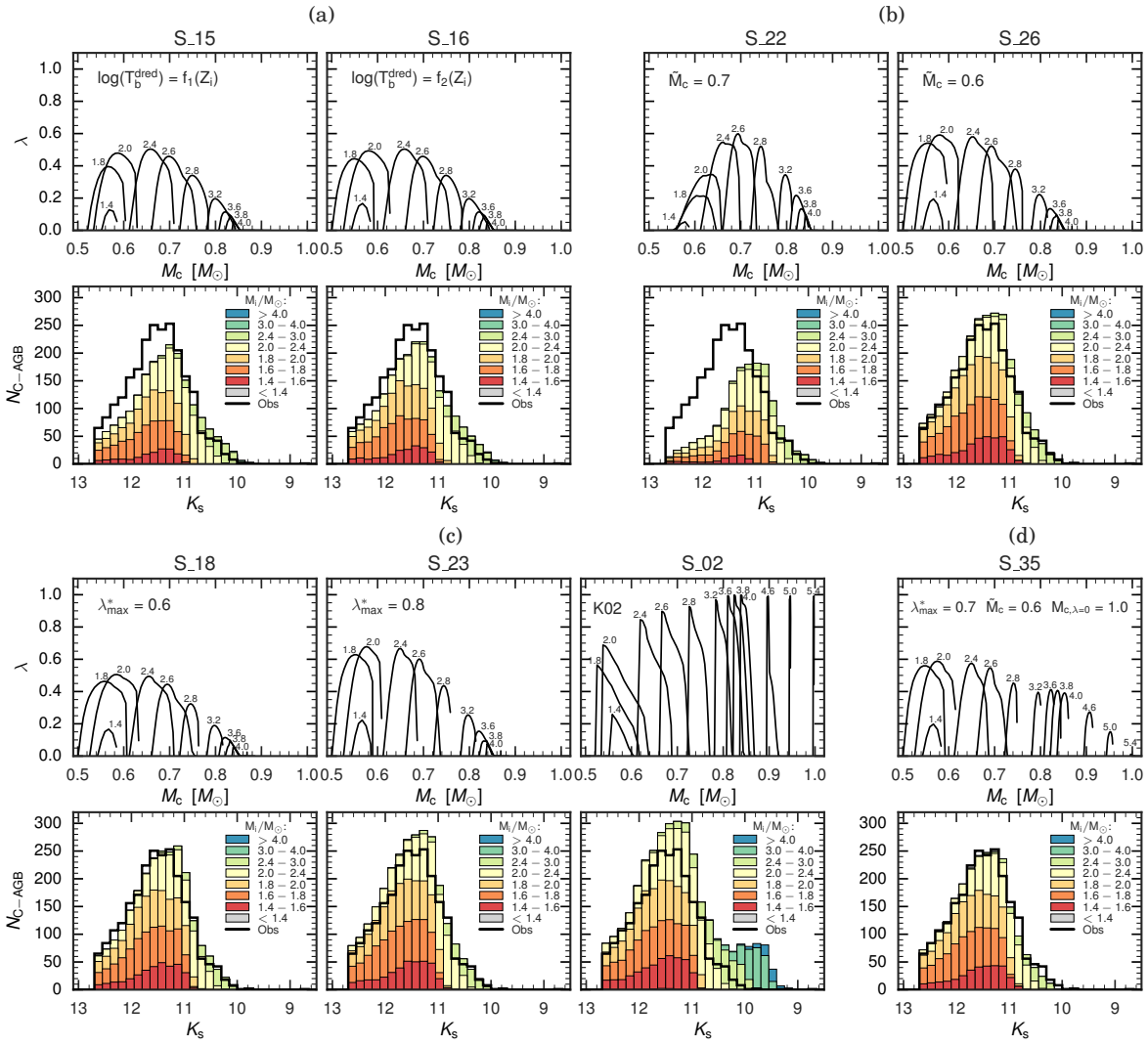


**Figure 4.16:** Top rows of each panel: efficiency of the 3DU ($\lambda$) as a function of the core mass $M_{\rm c}$ of a few selected evolutionary tracks with $Z_{\rm i} = 0.004$ and initial mass as labelled in the figure. Bottom rows of each panel: observed (black histograms) and simulated CSLFs as derived from the corresponding above sets of models. The synthetic LFs are shown as stacked histograms to highlight the contribution of each initial mass bin to the LF as indicated in the legend. Panel (a): these models (S_15 and S_16) share the same input prescriptions but for the temperature parameter (as indicated) that controls the onset of the 3DU. Panel (b): models S_22 and S_26, which differ by the core mass, $\widetilde{M}_{\rm c}$, that corresponds to the maximum 3DU efficiency. Panel (c): moving rightward the former two sets (S_18 and S_23) differ in $\lambda^*_{\rm max}$, while the latter two sets (S_23 an S_02) mainly differ by the efficiency of the 3DU in TP-AGB stars of higher initial mass, i.e. $M_{\rm i} \gtrsim 3\,M_\odot$. Panel (d): best-fitting model of this series (S_35) which has the same input prescriptions of S_26 but for the $M_{\rm c,\lambda=0}$ and the BL95 efficiency ($\eta = 0.03$).

(iv) *The bright end* contains information about the highest-mass stars that become C-stars, and is controlled by $M_{c,\lambda=0}$ together with the efficiency of mass loss. As illustrated in panel (c) of Fig. 4.16, increasing the value of $M_{c,\lambda=0}$ , i.e. moving from set S_23 to set S_02, causes the appearance of C-stars at brighter magnitudes. This essentially reflects the larger $\lambda$ attained by stars with $M_i \gtrsim 2.5 M_\odot$ in the present models. One conclusion is that with a very efficient 3DU in more massive AGB stars ($\lambda \approx 1$, as in K02) models tend to largely over-predict the number of bright C-stars (rightmost plot of Fig.4.16, panel (c), for the set S_02). As already discussed in Sect. 4.3.3, such excess can be removed only by invoking a powerful mass loss during the preceding O-rich stages (e.g. as for S_07 in the first series of sets).

Among all sets of the second series, the best-fit is provided by S_35. Its $K_s$-band LFs and the Hess diagrams are illustrated in Figures 4.17 and 4.18. Despite a residual discrepancy in the X-AGB LF and in the bright end of the O-rich LF, S_35 reproduce well all LFs and the corresponding number counts within 5 per cent. The optimal combination of parameters includes: CS11 pre-dust mass loss with efficiency $\eta_{\rm pre-dust} = 3$, dusty regime with BL95 and $\eta_{\rm dust} = 0.03$ for C/O $\leq 1$ and the CDYN for C/O $> 1$; $\lambda^*_{\rm max} = 0.7$, $\widetilde{M}_c = 0.6$, (see Table 4.4 and panel (d) of Fig. 4.16).

In the next section, I discuss the results of the two best-fitting models S_07 and S_35 and the main differences with respect to the starting set S_00.

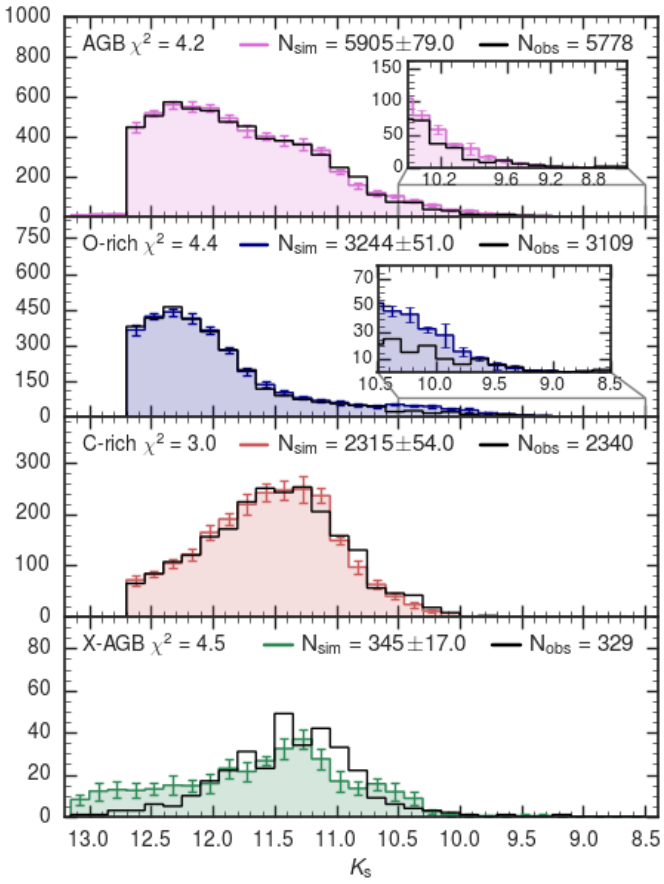


**Figure 4.17:** Same as Fig. 4.5 but for set S_35.

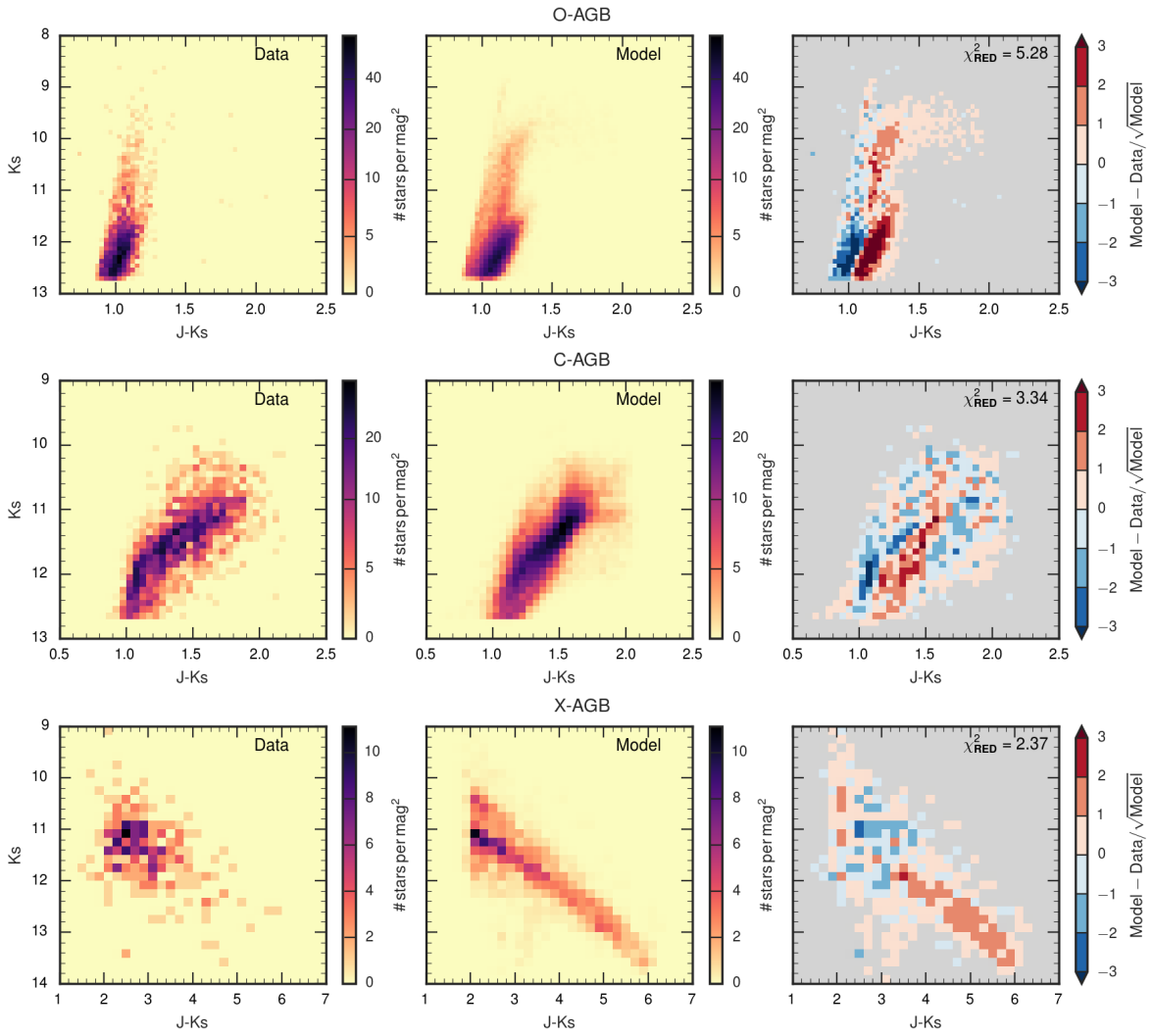


**Figure 4.18:** Same as Fig. 4.13 but for set S_35.

## 4.4 The best-fitting models

The final results are summarised in Table 4.5 and Figure 4.9. Models S_07 and S_35 stand out clearly by their smaller $\chi^2_{\rm LF}$ and indeed provide an excellent description of the observed CMDs (see Fig. 4.22) and LFs (see Figs. 4.12 and 4.17). In the following, the main implications that can be derived from the analysis of the results are discussed. The main differences between the two sets deal with the chemical composition of the ejecta and the final core masses. While a proper analysis on the predicted chemical yields is postponed to a follow-up work (Marigo et al., in prep.), I briefly discuss the IFMR in the next Section 4.4.1.

### 4.4.1 The IFMR relation

Two recent semi-empirical IFMR together with model predictions from the two best-fitting sets are shown in Fig. 4.19.

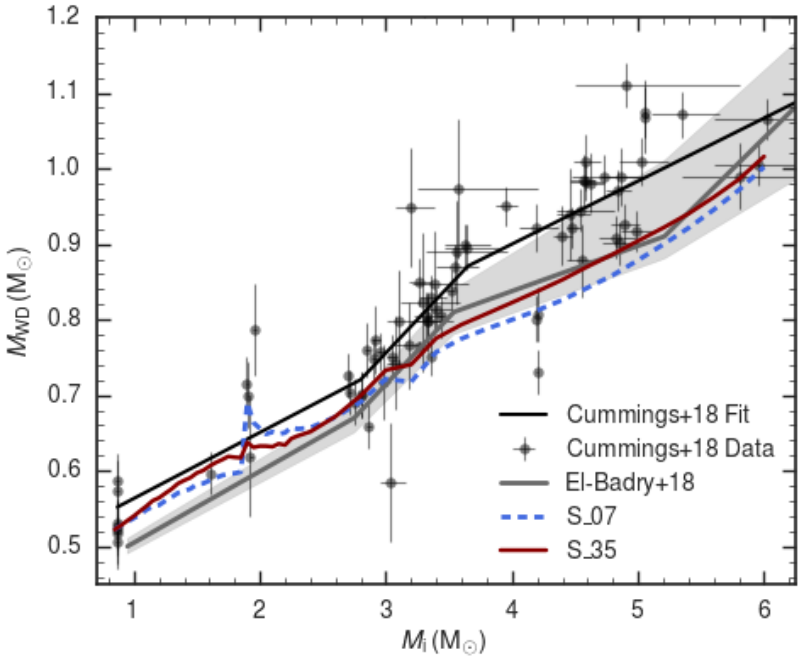


**Figure 4.19:** Initial-final mass relation for white dwarfs in the solar neighbourhood. The grey line and the shaded region show the best-fitting IFMR and its 95 per cent probability, respectively, derived from *Gaia* data (El-Badry et al., 2018). The `PARSEC` based semi-empirical data and the 3-pieces fit derived by Cummings et al. (2018) are shown as grey points with relative error bars and a solid black line, respectively. The IFMRs for $Z_{\rm i} = 0.014$ (the solar metallicity) derived from S_07 and S_35 are shown as blue dashed and red solid lines, respectively.

While the general trend is satisfactory for both sets S_07 and S_35, at larger initial masses, $M > 3M_\odot$, the S_07 models are only marginally consistent with the semi-empirical IFMRs. The WD masses for intermediate-mass stars ($M_{\rm i} > 3\,M_\odot$) appear to be underestimated by the models, in comparison with both relations presented by Cummings et al. (2018) and El-Badry et al. (2018). The predicted IFMR based on the set S_35 improves the comparison, mostly with respect to the initial masses larger than about 3 $M_\odot$. The larger WD masses predicted by these models, compared to those of the set S_07, result from reducing the efficiency of both the third dredge-up and mass loss during the TP-AGB phase of the progenitors. In addition the agreement becomes quite good with the semi-empirical relation based on *Gaia* DR2 data (El-Badry et al., 2018), whereas a

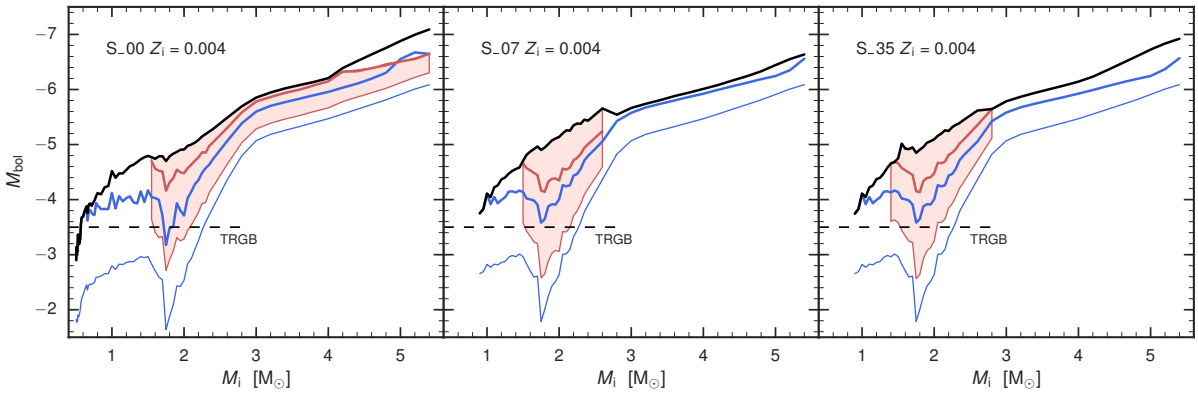


**Figure 4.20:** Bolometric magnitudes as a function of $M_i$ for a few relevant transition stages: the first TP (blue), the transition from the O-rich to the C-rich domain (red), and the AGB tip (black). In the first two cases, thick solid lines correspond to the luminosities at the quiescent stages that precede TPs, while thin solid lines correspond to the faintest luminosities reached during the post-TP low-luminosity dips. Results are shown for the TP-AGB sets S_00, S_07, and S_35 with $Z_i = 0.004$.

substantial discrepancy still affects the comparison with the IFMR from Cummings et al. (2018). This latter runs systematically above the mean relation from *Gaia* data. The reason for such a large difference between the two semi-empirical relations is not known at present. More work is required to clear up this point, given its importance for the calibration of the AGB stellar evolution models.

### 4.4.2 The initial masses of C-stars

Figure 4.20 shows the predicted ranges of initial masses and bolometric magnitudes of C-stars for the starting set S_00 and the two best fitting sets S_07 and S_35.

First, it is striking that in both S_07 and S_35 models, C-stars are expected to form only in a limited interval of initial masses, between 1.4 and 2.8 $M_\odot$, at SMC-like metallicities, i.e. $Z_i = 0.004$. In particular, the upper limit for C-stars formation at around 3 $M_\odot$ is mainly constrained by the observed deficit of C-rich stars for magnitudes brighter than $K_s \simeq 10$ mag. The present calibration indicates that C-stars with initial masses $> 3M_\odot$ would form a bright red tail that is not actually observed in the 2MASS CMD.

The two best-fitting sets converge to the same threshold mass following somewhat different paths. In the case of S_07, the formation of massive C-stars is prevented because of a high mass-loss efficiency that drastically shorten the lifetimes, despite the efficient 3DU based on K02 formalism. In the case of S_35, the reduced 3DU efficiency – assumed for TP-AGB models of higher masses – contributes to confining the formation region of C-stars to lower initial masses. In both sets of models the upper mass limit for C-stars formation is controlled by the efficiency of mass loss and 3DU, rather than by the onset of HBB.

The results of the calibration need to be compared with the predictions available in the literature. Past works that try to reproduce the CSLF in the SMC present much wider ranges of masses for the formation of C-stars. For instance, Groenewegen and de Jong (1993) and Marigo and Girardi (2007) find C-stars still forming at initial masses as high as 4 $M_\odot$. Also, recent AGB models, more focused on the chemical yields, predict that the maximum initial mass for C-star formation at SMC-like metallicity lies between between 4.0 and 4.5 $M_\odot$ (Karakas et al., 2018, $Z_i = 0.028$), or up to 6 $M_\odot$ (Cristallo et al., 2015, $Z_i = 0.003$). On the other hand, AGB models presented by Ventura and D'Antona

(2009) and Dell'Agli et al. (2015) form carbon stars with initial masses up to $\simeq 3\,M_{\odot}$ at $Z_{\rm i} = 0.004$, a value that is in close agreement with our calibration.

It is also interesting to compare these predictions with the cluster data in the Magellanic Clouds. According to the classical compilation by Frogel et al. (1990), 'the youngest clusters in which C-stars are found have an age of about 100 Myr implying a maximum initial mass for these stars of 3–5 $M_{\odot}$'. This conclusion appears in contradiction with our results; however, it was based on quite crude age estimates for the clusters, and uncertain memberships for the C-stars. According to the revised compilation by Girardi and Marigo (2007), the youngest LMC cluster to contain a C-star in its central region is NGC 1850, which has isochrone ages of $\sim$60–90 Myr (Correnti et al., 2017) and hence turn-off masses $\gtrsim 5.5\ M_{\odot}$. This high turn-off mass appears compatible with AGB stars that experience efficient HBB, a process that usually prevents the formation of C-stars; therefore the C-star in NGC 1850 is usually regarded as a chance alignment of a field LMC star. The second youngest LMC clusters to contain C-stars are NGC 1987 and NGC 2209, with one and two C-stars, respectively. NGC 1987 has estimated ages between $\sim$1 (Goudfrooij et al., 2017) and 1.3–1.5 Gyr (Milone et al., 2009), while NGC 2209 has ages of $\sim$1.15 Gyr (Correnti et al., 2014). Both clusters therefore have turn-off masses slightly below 2 $M_{\odot}$. We remark that NGC 2209 was regarded as a much younger cluster (ages between 120 and 370 Myr, hence turn-off masses between 4 and 2.7 $M_{\odot}$) in the work by Frogel et al. (1990). In the SMC, the revised cluster ages by Glatt et al. (2008) indicate that the youngest such cluster is the $\sim$1.5-Gyr old NGC 419, with its impressive population of ten C-stars. The presence of a double red clump in this cluster (Girardi et al., 2009) firmly points to turn-off masses of $\sim$1.75 $M_{\odot}$ (Girardi et al., 2013). Overall, the revised cluster data do not appear to indicate the presence of C-stars with progenitors more massive than about 2 $M_{\odot}$. On the other hand, Magellanic Clouds star clusters with turn-off masses between 2 and 3 $M_{\odot}$ are rare and more scarcely populated than older clusters, so that the maximum turn-off mass giving origin to C-stars cannot be identified with confidence from these data alone.

Figure 4.20 shows other aspects that are worth note. The faintest transition to the C-star domain happens at $M_{\rm i} \simeq 1.8\ M_{\odot}$. This value coincides (at $Z_{\rm i}$=0.004) with the initial mass boundary between stars that develop degenerate He-cores after the main sequences and the more massive ones that skip electron degeneracy. As discussed by Lebzelter et al. (2018), the presence of a well-defined minimum in the M-to-C transition luminosity at increasing stellar mass explains the splitting of the data along two branches (labelled (a) and (c) in fig. 3 of Lebzelter et al., 2018) in the diagram that combines 2MASS and *Gaia* photometry for long period variables.

Some fraction of TP-AGB stars are expected to appear below the RGB-tip (at $M_{\rm bol} \approx -3.5$ mag), mostly during the relatively long-lived low-luminosity dip that follows the occurrence of a thermal pulse (see e.g., Boothroyd and Sackmann, 1988). These faint stars may be either O-rich or C-rich. The O-rich stars below the RGB-tip span a range of initial masses $1.0\ M_{\odot} \gtrsim M_{\rm i} \lesssim 2.2\ M_{\odot}$ and cover a fraction of $\approx$ 26-27 per cent of the entire O-rich TP-AGB population, for both sets S_07 and S_35. The C-rich stars below the RGB-tip should correspond to initial masses in the range $1.5\ M_{\odot} \lesssim M_{\rm i} \lesssim 2.0\ M_{\odot}$. Our simulations indicate these faint C-stars represent $\approx$ 7 per cent of the entire C-rich population, for both sets S_07 and S_35.

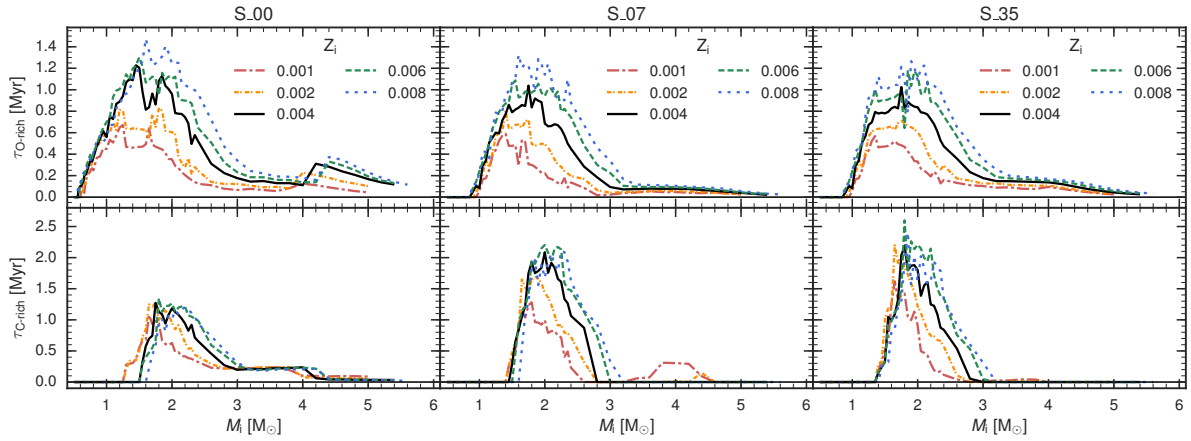


**Figure 4.21:** TP-AGB lifetimes of O- and C-rich stars for selected values of initial metallicities as predicted by the initial set S_00 (left panels) and the two best-fitting sets S_07 (middle panels) and S_35 (right panels).

### 4.4.3 Lifetimes

TP-AGB lifetimes are relevant to quantify the contribution of low- and intermediate-mass stars to i) the chemical enrichment of the interstellar medium, and ii) the integrated light of galaxies (Marigo, 2015). In fact, the duration of the TP-AGB phase, $\tau_{\rm TP-AGB}$, determines the level of chemical enrichment of the ejecta, which is set through the number of thermal pulses and 3DU episodes experienced by a star and/or the period in which HBB is operating. At the same time $\tau_{\rm TP-AGB}$ controls the energy emitted during the phase through the relation $E_{\rm TP-AGB} = \int_{\tau_{\rm TP-AGB}} L(t)dt$, where $L(t)$ is the stellar luminosity at time $t$.

In Figure 4.21, I present the comparison between the predicted lifetimes of O- and C-rich stars as derived from the starting set of TP-AGB models S_00 and the two best-fitting models S_07 and S_35. I consider only models with luminosity higher than $\log(L/L_{\odot}) = 3.3$, i.e. brighter than the RGB tip. As in other models in the literature (e.g. Weiss and Ferguson, 2009; Karakas, 2010), the predicted TP-AGB lifetimes peak at $M_{\rm i} \simeq 2\ M_{\odot}$, close to the value below which stars develop a degenerate helium core after the main sequence, the exact value depending on the initial metallicity and other model details. The general trends of the lifetimes for O-rich stars are similar in the three set of models, yet some differences are present for $M_{\rm i} \gtrsim 3\ M_{\odot}$. Compared to set S_00, the best-fitting models S_07 and S_35 predict shorter lifetimes by a factor of $\approx 2$. As to C-stars, we note an increase of the lifetimes in the new models compared to set S_00, reaching a factor of 2 near the peak at $M_{\rm i} \sim 2\ M_{\odot}$.

Within the metallicity range covered by the calibration ($0.001 \lesssim Z_{\rm i} \lesssim 0.004$), we expect shorter O-rich stages at decreasing $Z_{\rm i}$. This is the consequence of the earlier transition to the C-rich regime. The lifetimes for C-rich stars also follow a decreasing trend with lower $Z_{\rm i}$, particularly evident for initial masses close to the peak and larger than $\approx 2\ M_{\odot}$. The reason is linked to the fact that, at a given initial mass, a TP-AGB star of lower metallicity is characterised by a larger core mass. As a consequence, the TP-AGB phase proceeds at higher luminosities and with shorter inter-pulse periods, i.e. thermal pulses and 3DU episodes take place more frequently with consequent quicker increase of the carbon excess during the C-star stages. Both factors (related to luminosity and carbon excess) tend to favour an earlier onset of the dust-driven wind in C-stars of lower metallicity, in the range under consideration.

### 4.4.4 Characterisation of AGB star population

Given our detailed population synthesis simulations it is possible to provide a full characterisation of the AGB population in the SMC in terms of stellar parameters. A comparison between the best-fitting models S_07 and S_35 and the observations in the $K_s$ vs. $J-K_s$ CMD is shown in Figure 4.22. Both sets of models give essentially the same results in terms of the predicted stellar photometry. Most of the stars classified as X-AGB are C-rich (in agreement with the results from the SED fitting by SR16), with a small contamination of O-rich stars undergoing HBB. The stars populating the upper part of the CMD, with $K_s$ magnitudes brighter than 10 mag, are exclusively O-rich and most of them are experiencing HBB. The inset of Figure 4.22 clearly shows that C-rich and O-rich stars cannot be accurately separated by using classical $J-K_s$ criteria, in agreement with Boyer et al. (2015a).

A more quantitative analysis can be performed with the help of the $K_s$-band LFs decomposed in bins of selected stellar parameters. In Figure 4.23, we show some of the most relevant ones for the O-rich and the C- and X-AGB populations (i.e. C/O, C − O, $\dot{M}$ and $M_i$) as predicted by the best-fitting set S_35. The bulk of O-rich stars contains low-mass stars with $M_i \lesssim 2\ M_\odot$ and $K_s$ magnitudes fainter than $\approx 11$ mag. Most massive TP-AGB stars mainly populate the bright-end of the LF (see panel (a) of Fig. 4.23). As shown in panel (b) of Figure 4.23, the predicted values of the C/O ratios are between 0.2 and 0.6 for the $\approx 80$ per cent of the stars. The contribution of stars that have a lower surface abundance of carbon as a consequence of the HBB is visible at $K_s \approx 9.5$ mag. As for the mass-loss rates attained by O-rich stars, the models predict a rate around $10^{-7}\ M_\odot/yr$ for a half of them, and the higher mass-loss rates, i.e. $\dot{M} \gtrsim 10^{-5}\ M_\odot/yr$, are predicted for the most massive and luminous stars (see panel (c) of Fig. 4.23). A fundamental parameter for the C-rich stars is the C − O as it is the main parameter that determines the activation of the CDYN $\dot{M}_{dust}$, the minimum C − O value being $\approx 8.2$. The bulk of C-stars has C − O $\gtrsim 8$ and values larger than 9 are attained by the X-AGB stars, as can be appreciated in panel (d) of Figure 4.23. The predicted values of the C/O ratio are also shown in panel (e) of Figure 4.23 and they essentially reflect the distribution of C − O values. Finally, the predicted mass-loss rates for the C-rich stars are similar to those of the O-rich, with the X-AGB stars reaching the higher mass-loss rates (see panel (f) of Fig. 4.23).

The distributions of the predicted mass-loss rates for the C-, X- and O-AGB synthetic population are shown Figure 4.24. The predicted mass-loss rates for both O-rich and C-rich stars are in agreement with the mass-loss rates estimates derived from the spectral energy distribution (SED) fitting performed by Nanni et al. (2018) for the same sample of C- and X-AGB stars used in this work. In particular, the separation between C- and X-AGB stars at $J-K_s \approx 2$ occurs when the mass-loss rate reaches $\approx 10^{-6}\ M_\odot/yr$ (see Fig. 4.22), in agreement with the value found by Nanni et al. (2018). The predicted ranges of mass-loss rates are also in agreement with the results of three additional SED fitting studies of AGB stars in the SMC by SR16, Groenewegen and Sloan (2018b) and Goldman et al. (2018).

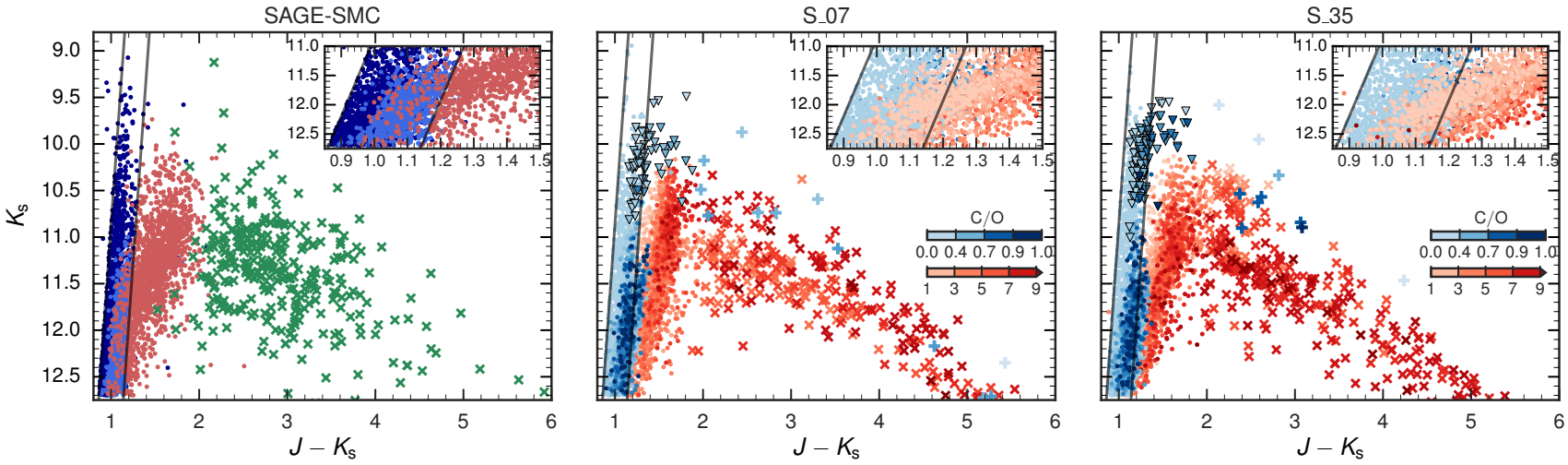


**Figure 4.22:** Left panel: observed $K_s$ vs. $J-K_s$ CMD with stars colour-coded according to the B11 and SR16 classification (O-rich in blue, a-AGB in light blue, C-rich in red and X-AGB stars are shown with green crosses). Middle and right panels: simulated CMDs from the best-fitting set S_07 and S_35 with stars colour-coded according to the predicted C/O ratio (O-rich stars are overplotted to C-rich stars). HBB stars are shown with triangles and with plus symbols when they fall in the X-AGB classification criteria. The insets show the CMD region where the O-rich and C-rich stars cannot be clearly separated using the classical photometric criteria shown as solid lines (Cioni et al., 2006; Boyer et al., 2011, 2015a) (C-rich stars are overplotted to O-rich stars).

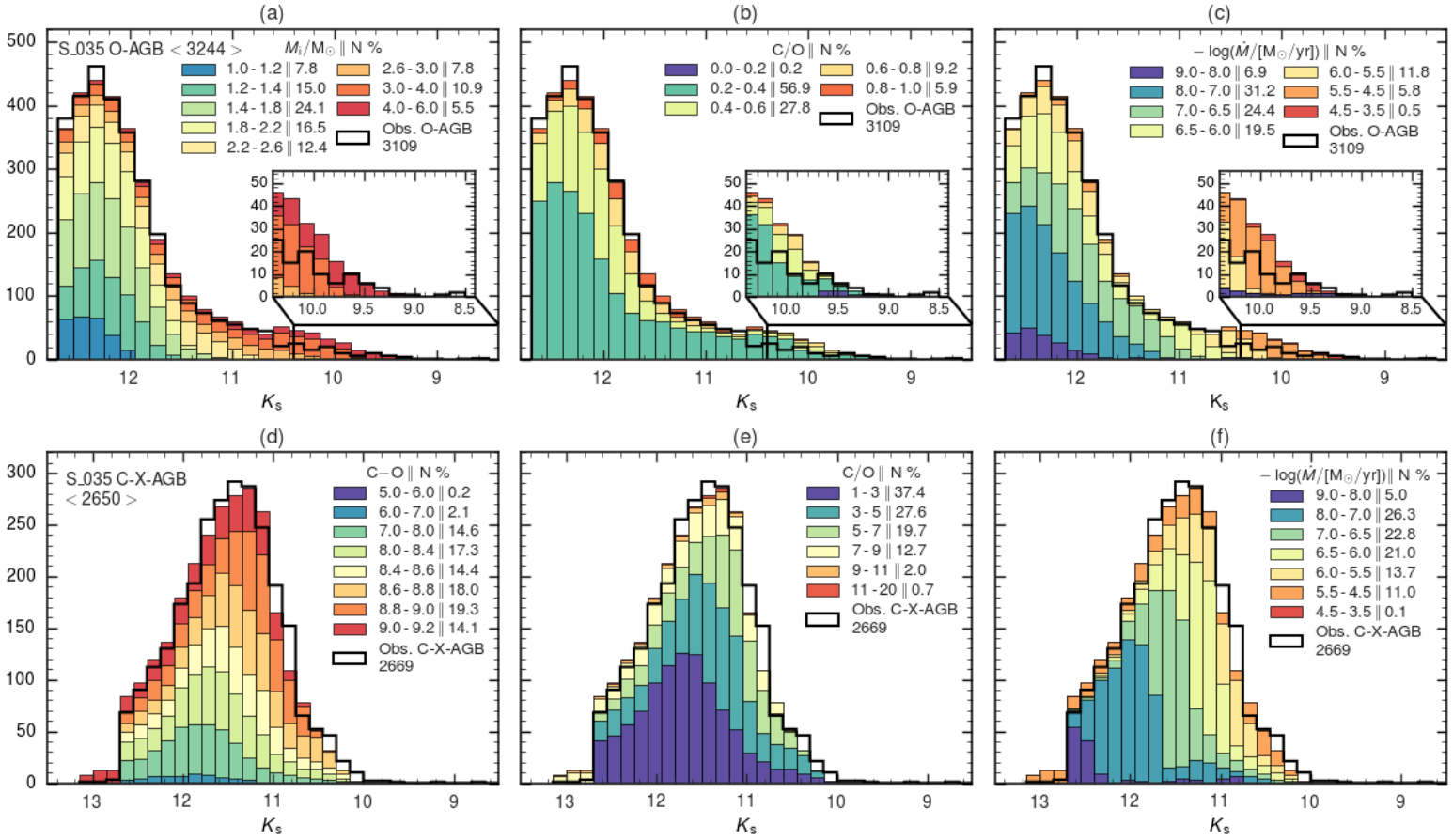


**Figure 4.23:** $K_s$-band LFs from the best-fitting set S_35 decomposed in bins of selected stellar parameters ($M_i$, C − O, C/O, and $\dot{M}$) as indicated in each panel. The O-rich LFs are shown in the three upper panels, whereas the lower panels shows the LFs of the C- plus X-AGB. The observed LFs are shown as solid black lines. The legend of each panel shows the selected bins and the corresponding percentage of synthetic stars. The synthetic LFs are constructed as the average of the 10 TRILEGAL realisations.

It is also interesting to compare the distributions of the bolometric magnitudes ($M_{\rm bol}$) as predicted by the best-fitting model S_35 with the results of SR16, B11 and Nanni et al. (2018). SR16 estimated the luminosities of the observed AGB stars in the SMC using the results of their best-fitting SED models, whereas B11 performed a trapezoidal integration from the observed optical $U$-flux through the mid-infrared 24 $\mu$m-flux. Nanni et al. (2018) performed a similar study on the sample of C-rich and X-AGB stars identified by SR16. The predicted $M_{\rm bol}$-LFs as derived from the average LFs of the 10 `TRILEGAL` simulations with the TP-AGB set S_35 are shown in Figure 4.25. The predicted peaks of the $M_{\rm bol}$ distributions, i.e. the median values, of the O-rich, C-rich and X-AGB LFs are $-4.11$, $-4.49$ and $-4.86$ mag, respectively. The combined C- and X-AGB LF peaks at $-4.54$ mag. The values reported by B11 are $-4.59$ mag for the C-AGB and $-4.63$ mag for the C- and X-AGB samples combined, and the values estimated by SR16 are $-4.2$ mag for the O-rich and $-4.5$ mag for the C-rich stars (including the stars classified as X-AGB). The bolometric luminosity distribution of the C-rich and X-AGB stars estimated by Nanni et al. (2018) are very similar and are well reproduced by our best-fitting model. The predicted bolometric luminosities are in excellent agreement with both the results of B11 and SR16, given that small discrepancies can be due to the fact that both authors adopted a fixed distance modulus across the SMC.

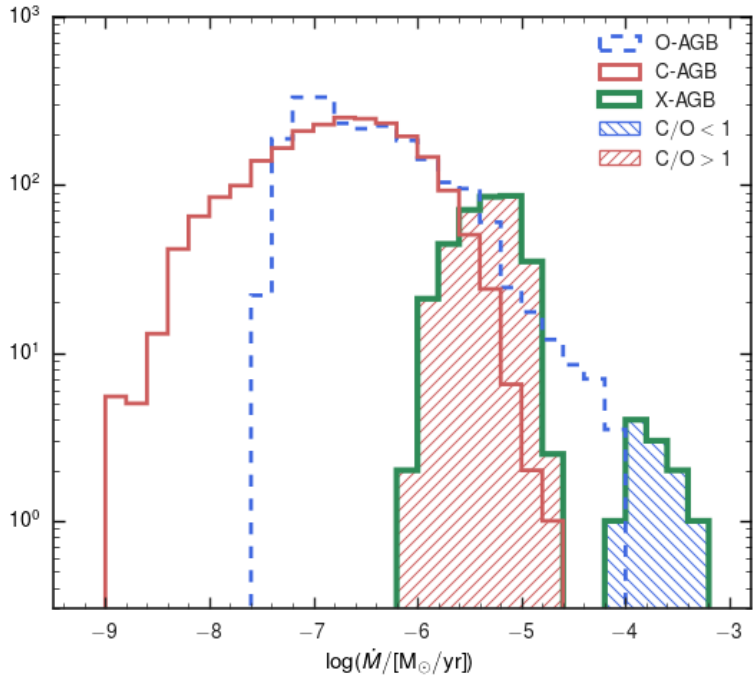


**Figure 4.24:** Distributions of the predicted mass-loss rates for the C-, X- and O-AGB synthetic populations from the best-fitting model S_35. Only stars in the TP-AGB phase are included. The X-AGB stars with C/O $> 1$ and those with C/O $< 1$ are shown as red and blue hatched regions, respectively, as indicated in the legend.

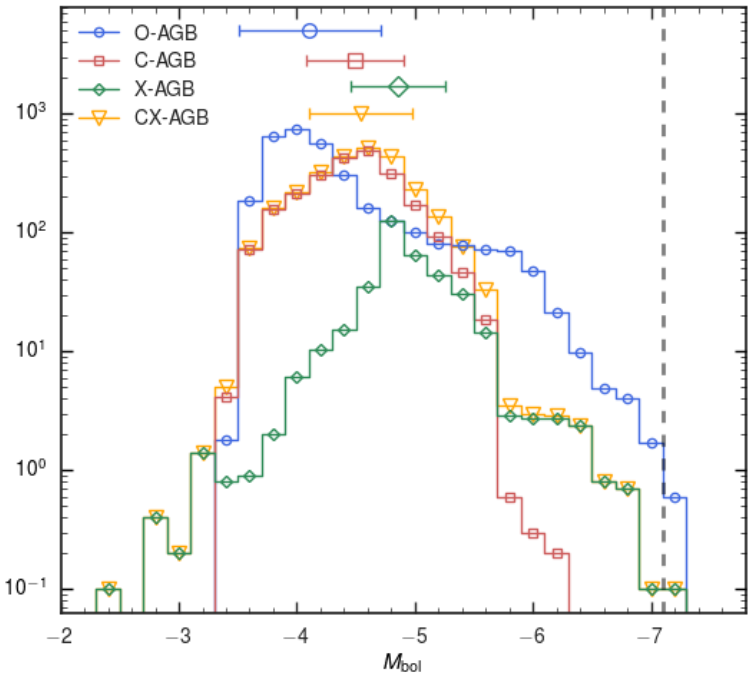


**Figure 4.25:** Bolometric magnitude distributions of the synthetic populations of O-, C and X-AGB stars as predicted by the best-fitting set S_35. The distribution for the combined C- and X-AGB populations is also shown. The median values and the $1\sigma$ dispersion of the bolometric magnitude distributions are $-4.11 \pm 0.60$, $-4.49 \pm 0.43$, $-4.86 \pm 0.40$ and $-4.54 \pm 0.44$ mag for the O-, C, X-AGB and C- and X-AGB combined respectively, as also shown in the upper part of the figure. The vertical dashed line is the "classical" AGB limit at $M_{\rm bol}$= -7.1 mag. The distributions are calculated as the median of the 10 `TRILEGAL` simulations.

### 4.4.5 2MASS and Spitzer LFs

Figure 4.26 shows the comparison between our best-fitting model S_35 and the LFs in the 2MASS and *Spitzer* bands. There is a general satisfactory agreement between the best-fitting model S_35 and the observed LFs, which supports the validity of the adopted treatment of the circumstellar dust based on an improved version of Marigo et al. (2008). A few discrepancies exist, in particular affecting the LFs of X-AGB class in some photometric bands. This is the case of the *Spitzer* filters [4.5], [5.8] and [8.0]; the predicted X-AGB LFs are shifted to brighter magnitudes with respect to the observed ones. At the same time, the predicted C-AGB LFs in the *Spitzer* filters [5.8] and [8.0] appear slightly shifted towards magnitudes fainter than observed. Overall, these differences are of small entity, and more importantly, I expect they do not impact on the results of the TP-AGB calibration, since the X-AGB sample includes less than 6 per cent of the total number of AGB stars. The most likely cause is the treatment of the circumstellar dust and the resulting bolometric corrections. I plan to improve this aspect of the models by investigating the effects of different carbon dust mixtures and eventually new synthetic spectra based on additional dust compositions will be computed.

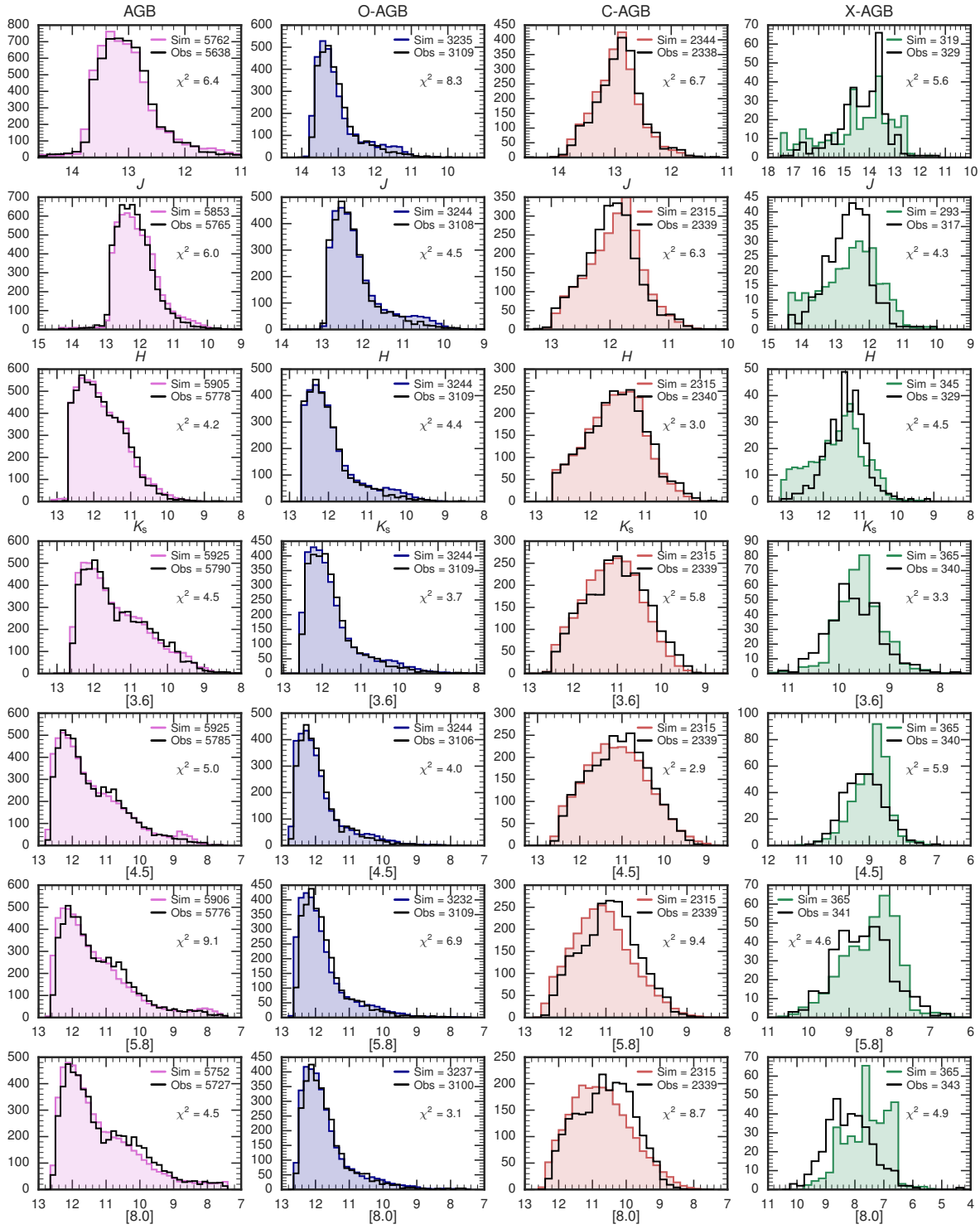


**Figure 4.26:** Synthetic LFs obtained from the best-fitting model S_35 and the observed LFs in the 2MASS and Spitzer filters, going from shorter (top panels) to longer wavelengths (bottom panels).

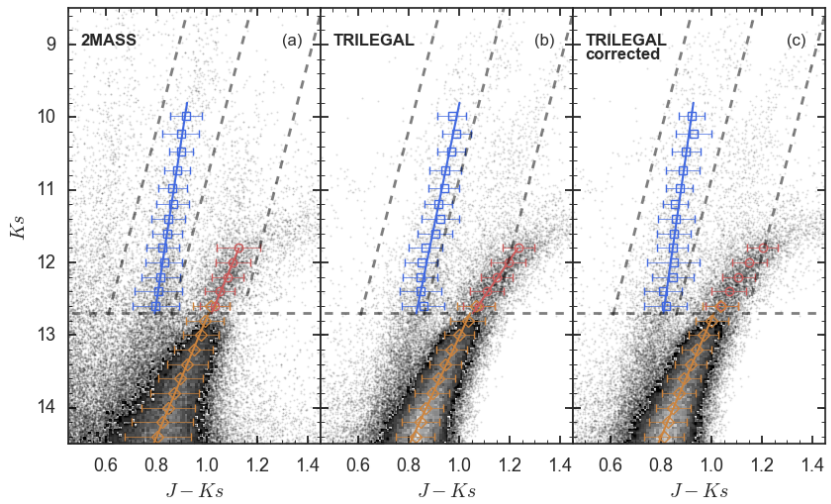


**Figure 4.27:** Panel (a) $K_s$ vs. $J-K_s$ CMD of the SMC from 2MASS data. Panel (b) synthetic CMD (c) same as in panel (b) but with the correction applied to the synthetic photometry as explained in the text. The 2MASS data and the simulation cover the same SMC areas. The fiducial lines are shown as solid lines and the centers of the magnitude bins are marked with different empty symbols for the RGB (diamonds), the AGB (circles) and the RSG (squares) sequences. The error bars represents the $1-\sigma$ standard deviations of the fitted gaussian distributions. The dashed horizontal line marks the $K_s$-band TRGB, while the diagonal dashed lines correspond to the photometric cuts used by B11 and S11 to separate the RSG sequence from the Milky Way foreground and the sequence of O-rich AGBs from the RSGs.

## 4.5 Additional tests

### 4.5.1 The colour shift of giants and supergiants

By comparing the observed and simulated $K_s$ vs. $J-K_s$ CMD we found an evident discrepancy in the colour and slope of the RSG and O-rich TP-AGB sequences. To analyse the population above the Tip of the RGB, the VMC photometry is not suitable due to the saturation limit of the instrument that is around $K_s \approx 10$ mag. However, it possible to take advantage of the 2MASS data Cutri et al. (2003). These data may suffer of incompleteness at magnitude fainter than $K_s \approx 15$, but they can be safely used above the Tip of the RGB. As for the AGB catalogues of SR16, according to each VMC subregion of the SMC, I first selected all the 2MASS sources in that region. Then, for each 2MASS-VMC region I perform a `TRILEGAL` simulation using the R18 SFH, reddening and distance. Since artificial star tests are not available, I take into account the photometric errors using the results of Bonatto et al. (2005) that provides the photometric errors for a given 2MASS passband as a function of the magnitude. The left panels of Fig. 4.27 show the CMD of the SMC from the 2MASS data and the `TRILEGAL` simulation performed with the TP-AGB set S_00, i.e. the starting TP-AGB set. The Milky Way foreground is not included in the `TRILEGAL` simulation, but I verified that the contamination of the RSG and AGB samples is very low and it does not impact the results. The dashed horizontal line marks the $K_s$-band TRGB, while the diagonal dashed lines correspond to the photometric cuts used by B11 and S16 to separate the RSG sequence from the Milky Way foreground and the sequence of O-rich AGBs from the RSGs. By visual inspection it is immediately evident that the simulated RSG and O-rich AGB sequences are redder than the observed ones.

To quantify such a shift in color, I calculate the fiducial lines of both the observed and simulated RSG, O-rich and RGB sequences. The fiducial lines are obtained by fitting a

Gaussian distribution in the case of the RGB and a double Gaussian for the RSG and AGB to the distributions of the $J-K_s$ colours in different magnitude bins. In the left panels of Fig. 4.27, the centres of the magnitude bins are marked with coloured symbols and the error bars represents the $1-\sigma$ standard deviations of the fitted Gaussian distributions. I used a linear fit to infer the value of the shift as a function of the $K_s$magnitude, for the RGB stars ($K_s > 12.7$), for the AGB stars ( $11.8 < K_s < 12.7$) and for the RSG stars ( $K_s < 12.7$). The linear fits are shown as solid lines with empty markers in panels a), b) and c) of Fig. 4.27.

Panel d) of Figure 4.28 shows the $J-K_s$ colour difference between the observed and simulated sequences as a function of the $K_s$-band. The horizontal lines represent a zero difference in colour and a difference of $\pm 0.05$ mag. The colour of the RGB sequence is reproduced within 0.025 mag, while the RSG and the AGB are shifted toward redder colours, with a difference larger than 0.05 mag. The colour shift has a dependence on the $K_s$ magnitude, hence on the luminosity. It worth noticing that the colour shift of the RGB and RSG sequences seem to follow the same relation as a function of the luminosity, whereas the AGB sequence colour difference seems to follow a different and more steep relation. These different behaviours can be due to the effect of the circumstellar dust even if the low-mass AGB stars are not expected to be largely affect by dust. Further tests are currently being performed and will be addressed in a future dedicated work.

For the purpose of this work, it is important to have the right slope and colours for the different evolutionary sequences because of the photometric selections that have been performed on the data. This is particularly important for the selection of RSG and O-AGB stars for which the the photometric criteria of SR16 have been used. To reconcile the differences in colours, I correct the synthetic photometry a posteriori by assuming that the $J-K_s$ colour difference is due to an extinction-term correction $dA_\lambda$. I first derived the $dA_J$ correction from the $J-K_s$ colour difference as a function of the $K_s$magnitude for the RGB, RSG and AGB sequences, by assuming a zero correction for the $K_s$-band. The value of $dA_\lambda$ as a function of $K_s$ magnitude is computed using the extinction coefficient of each photometric band (see, Girardi et al., 2010). Such corrections are applied to all the photometric bands bluer than $K_s$, as shown in panel e) of Figure 4.28. The corrections for the $J$-band $dA_J$ are the following:

$$dA_J^{RGB} = 0.012 \cdot K_s - 0.191 \quad \text{if } K_s > 12.7 \tag{4.7}$$

$$dA_J^{RSG} = 0.016 \cdot K_s - 0.236 \quad \text{if } K_s < 12.7 \tag{4.8}$$

$$dA_J^{AGB} = 0.077 \cdot K_s - 1.020 \quad \text{if } 12.7 < K_s < 11.8 \tag{4.9}$$

Panel c) of Figure 4.28 shows the simulated CMD after correcting the sequences and the resulting $J-K_s$ colour differences are shown in panel d) with filled markers as indicated in the legend. The differences for the RGB and RSG sequences are reduced within 0.01 mag, whereas a slightly larger difference (up to 0.05 mag) is still present in the AGB sequence. Such residual difference is due to the fact that in the synthetic catalogues the photometry has been corrected using the relation found for the RSG sequence for stars brighter than $K_s$= 12.7 mag and the correction derived for the RGB sequence for the stars fainter than $K_s$= 12.7 mag. This choice is firstly motivated by the difficulty of applying the $dA_V{}^{AGB}$ correction to the simulated stars, since this would require a selection based on stellar parameters. Secondly, RSG and RGB models are computed with the `PARSEC` code and they are not subject of the calibration. In addition, the reason of the different slope of the AGB colour shift has not been identified. For this reasons, the photometric corrections applied to the synthetic SMC photometry only include the correction derived

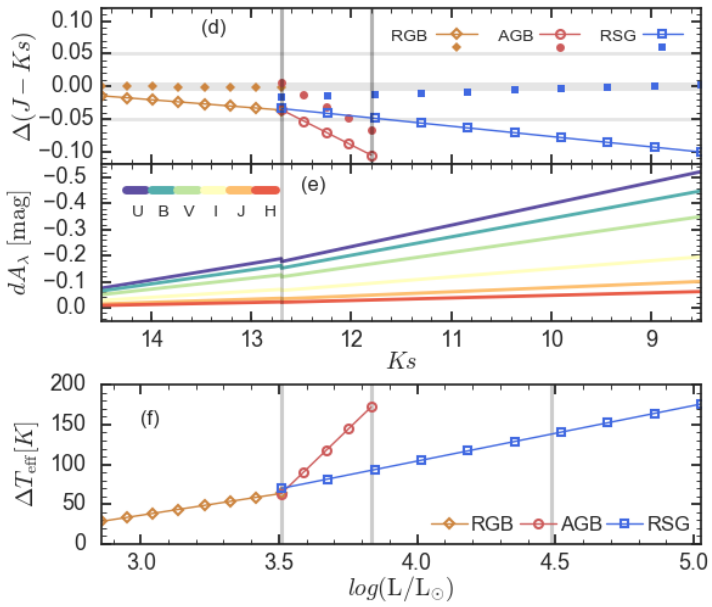


**Figure 4.28:** Top panel d): $J-K_s$ difference between the observed and simulated sequences as a function of $K_s$ for the RGB, AGB and RSG sequences. The differences corresponding to the uncorrected simulation are shown as solid lines with empty markers, while the differences after the correction applied to the photometry are shown as smaller filled symbols. The horizontal lines represent a zero difference in color and a difference of $\pm 0.05$ mag. Middle panel e): $dA_\lambda$ correction applied to the photometry for the magnitudes bluer than $K_s$. Bottom panel f) Correction to effective temperature $\Delta T_{\rm eff}$ as a function of the luminosity for the RGB, AGB and RSG sequences.

from the RSG sequence. Furthermore, since the separation of synthetic O-AGB and C-AGB is based on the predicted C/O ratio, a mismatch in the $J-K_s$ colour does not affect the star counts.

However, I decided to investigate further this issue and I present some interesting findings in the next Section.

### 4.5.2 Further test on the colour-shift

The possible explanations for such redder colours could be an overestimation of the reddening or the metallicity as derived from the SFH recovery. However, since the RGB slope and colour do not show these discrepancies, it is more likely that the cause of this discrepancy is due to some effects related to the colours of the more evolved giants as a function of the luminosity.

A likely explanation for this shift in colour which is luminosity dependant could be related to the mixing-length parameter. Several studies have shown how a fixed value of the mixing length is not suitable for all stars (see e.g. Ludwig et al., 1999; Trampedach et al., 2014; Magic et al., 2015; Tayar et al., 2017). They suggest an increase in the mixing length parameter as a function of the luminosity, which has the main effect of increasing the effective temperature of such stars. The too red colours of our synthetic RSG and AGB sequences can be interpreted as a too rapid cooling as a function of luminosity, hence as an underestimation of the mixing length parameter.

To properly test this hypotheses, it is necessary to compute complete sets of PARSEC evolutionary tracks with different mixing length values. These calculations are time consuming and I refer to a forthcoming paper in which this issue will be addressed. this issue. However, given the flexibility and the computational agility of the `COLIBRI` code, some

tests on the TP-AGB population can be performed. Here I describe the results of one test based on the assumption that the mixing length parameter should increase as a function of the luminosity. In practice, I derived a correction to the effective temperature as a function of the luminosity, which is translated in a relation between the difference in effective temperature required to match the observed sequences and the mixing length parameter as described below. First, I used a simple fitting relation derived from the synthetic populations to translate the observed colours and magnitudes in effective temperature and luminosity and I derived an approximate correction to the effective temperature as a function of the luminosity, which is shown in the lower panel f) of Figure 4.28.

The estimated correction to the effective temperature for the RGB, AGB and RSG sequences are the following.

$$\Delta {T_{\rm eff}}^{\rm RGB} = 53.9 \cdot \log L - 125.6 \quad (4.10)$$

$$\Delta {T_{\rm eff}}^{\rm RSG} = 69.8 \cdot \log L - 174.8 \quad (4.11)$$

$$\Delta {T_{\rm eff}}^{\rm AGB} = 334.7 \cdot \log L - 1110.9 \quad (4.12)$$

The relation that provides the correction to the effective temperature is translated into a relation involving the mixing-length parameter with the aid of complete envelope integrations carried out with the `COLIBRI` code (Marigo et al., 2013). In brief, large grids of envelope structures are calculated varying the main stellar parameters (mass, luminosity, metallicity) over the relevant ranges, together with the mixing-length that is made sample the interval from $\alpha_{ML} = 1.4$ to $\alpha_{ML} = 2.7$. For each combination of the input parameters $(M, L, Z, \alpha_{ML})$ the envelope integration yields the corresponding effective temperature.

At any time step during the evolutionary calculations with `COLIBRI` we single out the suitable value of the mixing length that provides the correction to the effective temperature by simply interpolating on the above grid. On the base of those calculations, in the present work we derive a fitting relation that expresses the correction to the mixing-length parameter as a function of global stellar parameters, namely:

$$\Delta\alpha_{ML} = f(M, L, Z)\,, \quad (4.13)$$

where $\Delta\alpha_{ML} = \alpha_{ML} - \alpha_{ML,0}$ is the difference between the corrected mixing-length parameter (that gives the seeked effective temperature shift at that $L$) and the constant mixing-length parameter ($\alpha_{ML,0} = 1.74$) used in all standard `PARSEC` and `COLIBRI` models.

A complete set of TP-AGB tracks (S_21) has been computed using such relation. S_021 has the same prescriptions for the mass-loss and the 3DUP as in models S_20. In the simulations computed with S_021 only the RSG colours have been corrected to account for the colour shift.

The $K_{\rm s}$-band LFs are shown in Figure 4.34. The resulting $\chi^2_{\rm LF}$ values are not as low as S_07 and S_018 but the models show a fairly good agreement with the observations. A significant improvement in the colour distributions of the simulated stars is demonstrated in Fig. 4.29. This set results in the lowest $\chi^2_{\rm Hess}$ values and in the lowest residual differences (right panels of Fig. 4.29 ), especially for the O-rich stars. As for the C-rich and X-AGB stars the most significant discrepancy is the overproduction of bright C-stars, but their colour distributions satisfactorily match the observed ones.

Pulsation periods and growth rates corresponding to the 5 lowest-order radial modes have been computed for two population models following Trabucchi et al. (2018, submitted) and the results are compared with the observed primary periods from the OGLE-3 Catalog of LPVs in the SMC (Soszyński et al., 2011). The simulated pulsations periods are selected as primary periods according to the growth rates, i.e. the largest growth

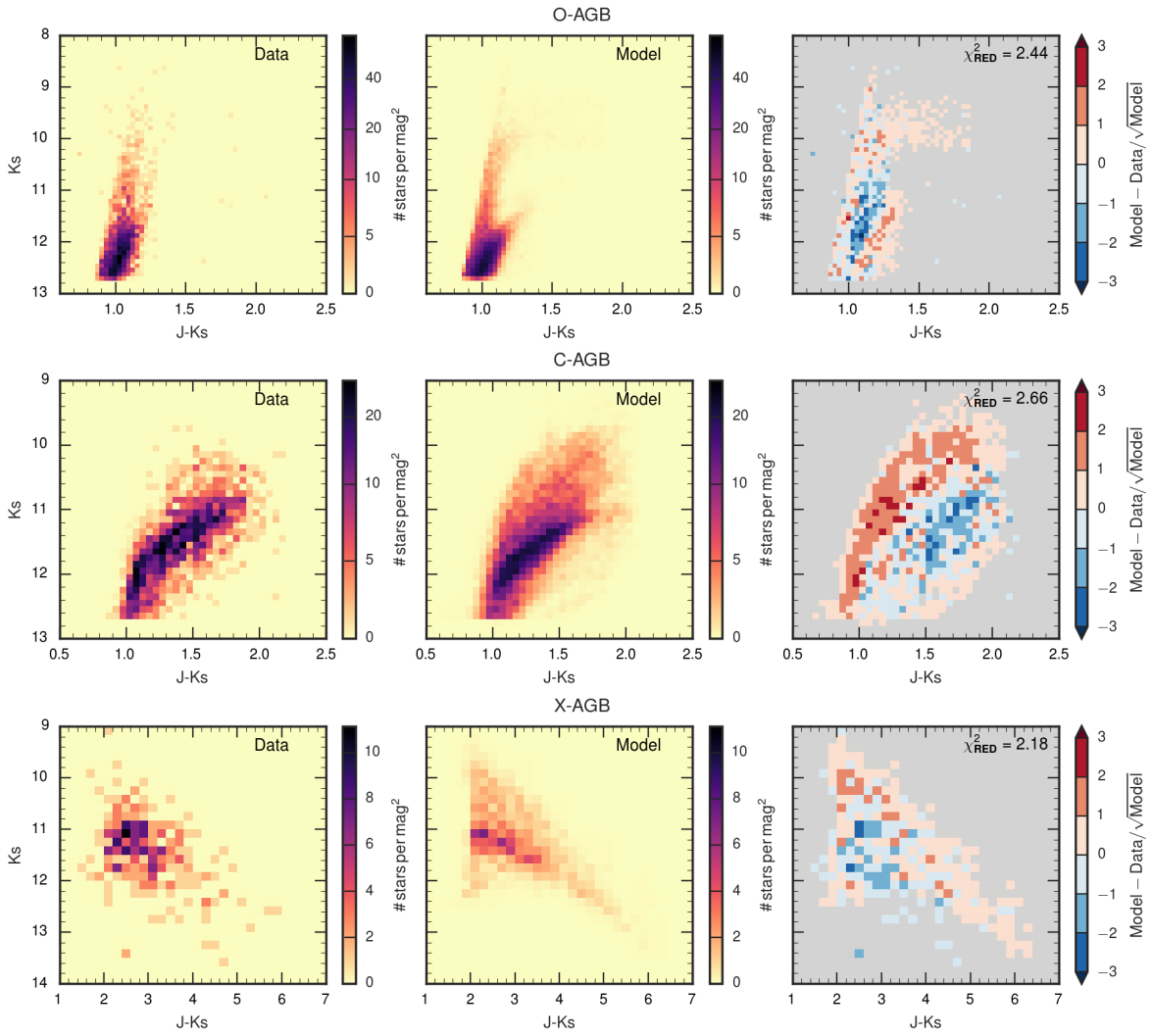


**Figure 4.29:** Same as Fig. 4.7 but for set S_21.

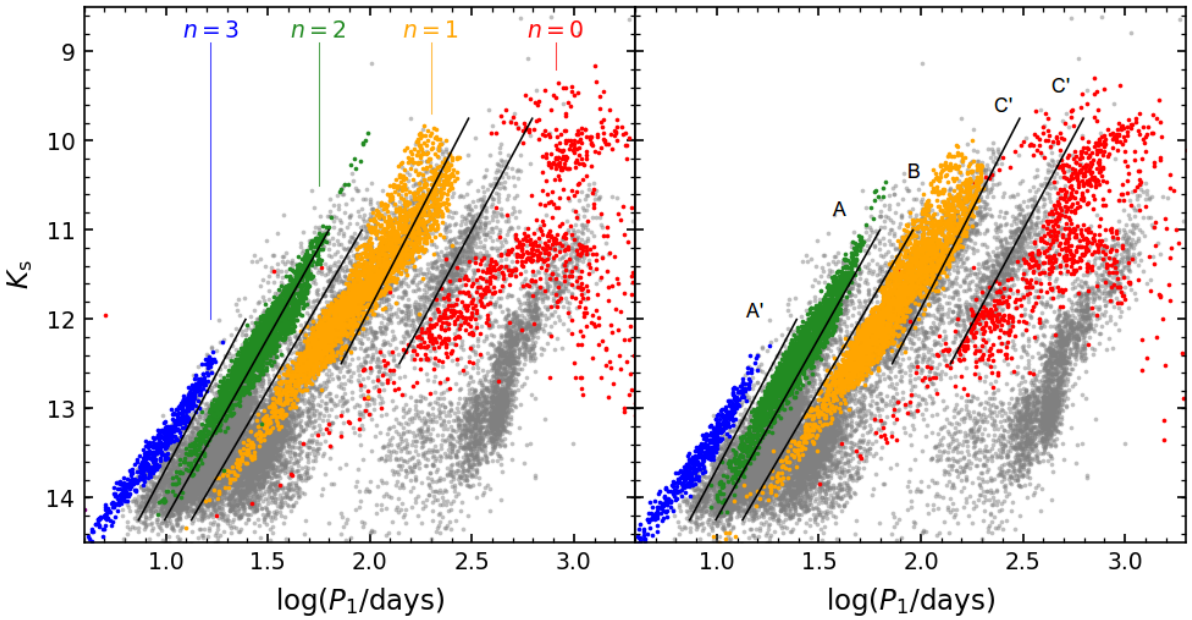


**Figure 4.30:** Distributions of periods of the dominant modes in AGB stars from simulations S_20 (left panel) and S_21 (right panel). Points are coloured according to the radial order of the dominant mode. Grey points in the background are primary periods from the OGLE-3 catalog of LPVs in the SMC (Soszyński et al., 2011). Solid lines are the best fit PL relations (Soszynski et al., 2007) corresponding to sequences A′, A, B, C′, and C (from left to right).

rates identify the dominant modes (Trabucchi et al., 2017). As shown in Figure 4.30, the periods of simulated stars form four distinct distributions, corresponding to the fundamental mode, first overtone (1O) mode, second overtone (2O) mode, and third overtone (3O) mode (i.e., radial orders $n = 0$ to 3). The distributions of theoretical 3O and 2O mode periods reproduce the observed sequences A′ and A, while the distribution of 1O mode periods from the models is able to reproduce both sequences B and C′. Sequence C, due to pulsation in the fundamental mode and harboring Mira variables, is not well reproduced by models (cf. Trabucchi et al., 2017).

When the mixing length parameter is assumed to increase as a function of luminosity, the effective temperature at a given luminosity is higher, and the stellar radius is smaller. Such a change impacts the pulsation properties of the models in two main ways. First, the decrease in radius results in shorter periods. Since the effect is stronger for higher luminosities, the result is that of increasing the slope of the theoretical PL sequences. The effect is stronger for the longer-period sequences (C′ and C), since they host the cooler stars. A second effect is related to the fact that the fundamental mode's growth rates increase with the effective temperature, so that in the population model obtained from set S_21 the fundamental mode periods are more unstable than in set S_20. The growth rates of the 1O mode show a similar, but weaker, dependence upon the effective temperature. The net result is that a larger number of simulated stars show a dominant fundamental mode in the region of the PL diagram near sequence C, at the expenses of the 1O mode. The shortening of periods and the increase of the growth rates of the fundamental mode help to improve the agreement with observations for both sequences C′ and C.

### 4.5.3 Tentative comparison with Harris & Zaritsky SFH

Harris and Zaritsky (2004) and Harris and Zaritsky (2009) are still the classical references

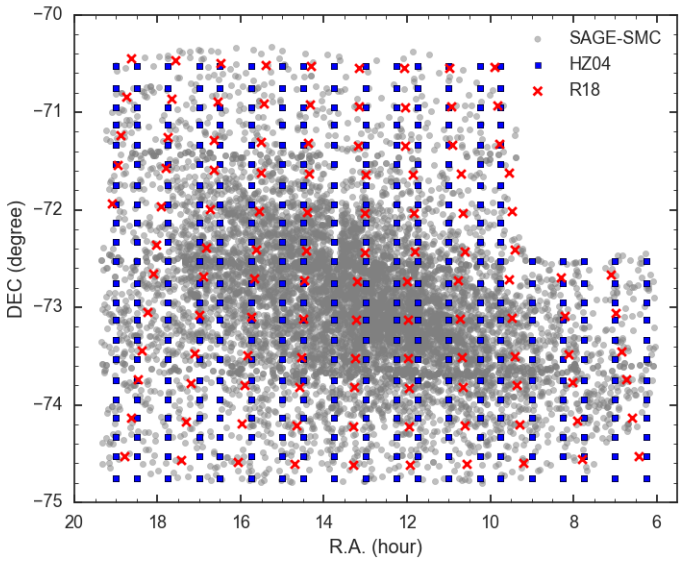


**Figure 4.31:** Common area between the regions analysed by R18 and HZ. The coordinate of the centers of the regions are shown as blue squares for HZ04 and with red crosses for R18. The AGB stars identified by SR16 are shown as grey dots

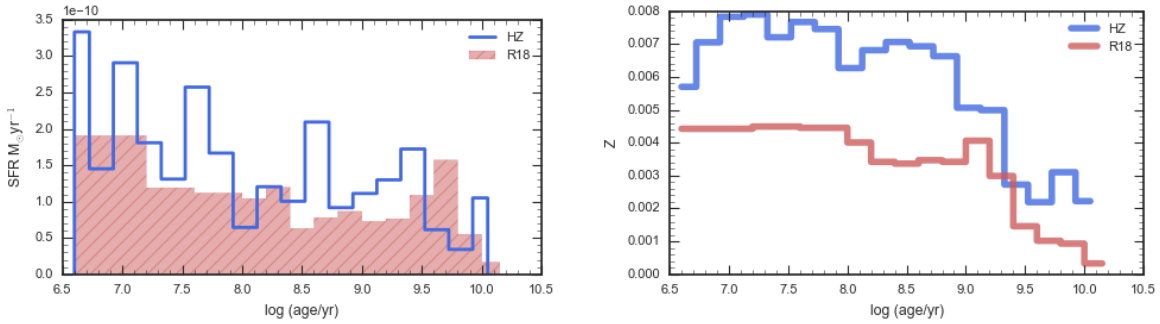


**Figure 4.32:** Global SFR(t) and AMR for the selected SMC area.

for the space-resolved SFHs of the Small and Large Magellanic Cloud, because they include the complete main bodies of these galaxies. It is therefore interesting to compare our results, with those which would have been obtained with their SFHs. To perform such comparison, starting from the space-resolved SFHs of both Rubele et al. (2018) and Harris and Zaritsky (2004), we compute the global SFH selecting only the regions in common between the two analysis and with the observed AGB catalogue. Figure 4.31 shows the coordinates of centres of the regions employed and the AGB stars from the SR16 catalogue.

It worth noticing that in the work of Harris and Zaritsky (2004) the adopted IMF is a Salpeter and the stellar isochrones used in the CMD-fitting were calculated by Girardi et al. 2000. Thus, the comparison with the R18 SFH is not straightforward. The global SFR(t) and the AMR for the selected SMC area are shown in Figure 4.32.

In the population synthesis simulations I adopted the mean values of reddening and distance found by Rubele et al. (2018) and the same IMF (Kroupa, 2001) . Furthermore, in these tests I did not increase the age resolution during the boosting period. This results in an overestimation of AGB stars that it is not visible in the detailed simulations presented in the previous section. However, this does not impact the comparison between the two SFHs. The simulations are normalized to the same total stellar mass in stars as derived by R18. The resulting LFs of the AGB populations are shown in Figure 4.33

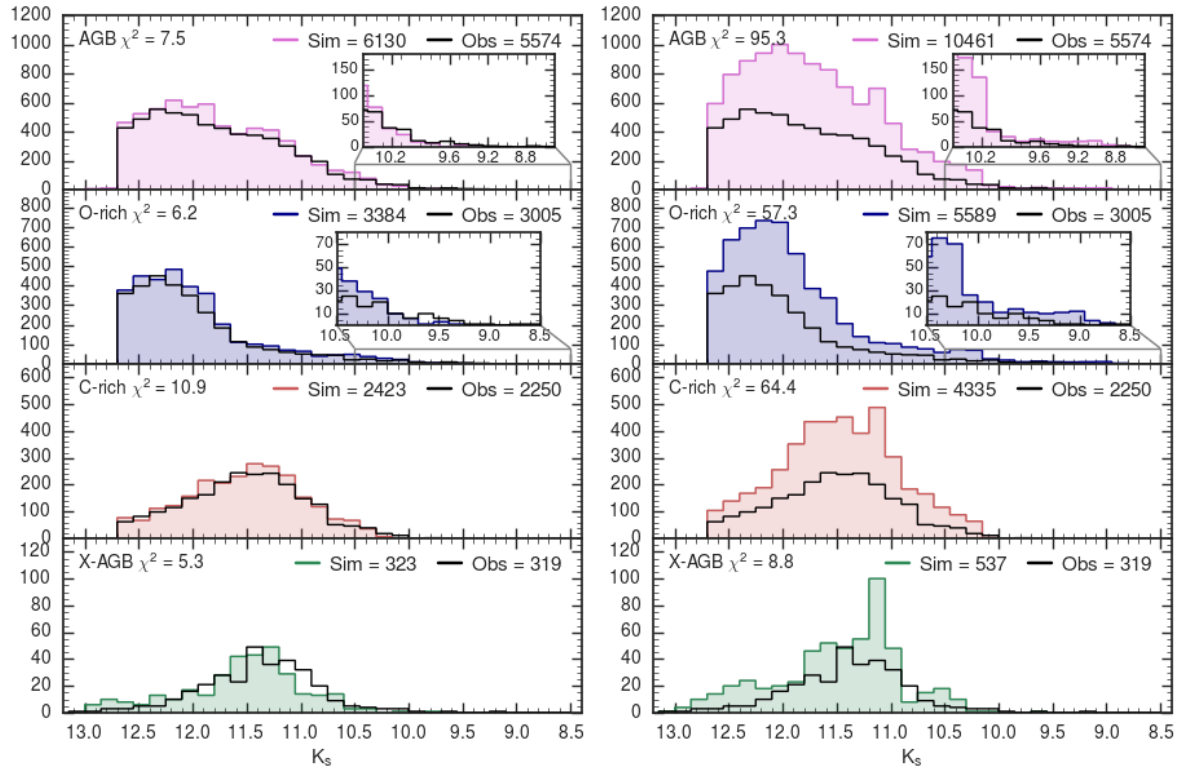


**Figure 4.33:** LFs of the AGB populations of the SMC as derived from the SFH of R18 (left panel) and HZ04 (right panel). The set of TP-AGB tracks is S_035.

By using the global SFH from R18, the synthetic LFs are in agreement with the observed ones, as expected. The result obtained with the SFH of HZ04 do not show the same agreement. Even if the total stellar mass in stars is the same in both simulations, the total number of AGB stars is overpredicted by a factor of $\approx 2$. This overproduction is reflected in the subclasses of AGB stars. This is also interesting to comment about the peaks in the LFs of C- and X-AGB at $K_s \approx 11$ mag. They are caused by the adopted age resolution of 0.02 dex that is not suitable to handle the TP-AGB boosting effect. Such effect is not visible in the LFs calculated from the SFH of R18 since the age intervals of the two SFHs are slightly different, as well as the rate of Star Formation corresponding to age bins around $\log t = 9.2$ (see left panel of Fig. 4.32). As already mentioned in Chapter 3, the input models and the VMC photometry allows a more accurate derivation of the SFH with respect to HZ04. In addition, in the case of R18 it has been possible to perform a series of tests using the same VMC photometry from which the SFH has been derived, ensuring the maximum consistency between that work and the present calibration. The same kind of investigation is not possible in the case of HZ04, mainly because they used very different set of isochrones and different assumptions, i.e. the IMF, that cannot be reproduced in a straightforward way.

## 4.6 Conclusions

With the aim of providing quantitative constraints on the mass-loss efficiency and the onset and efficiency of the 3DU, the approach presented in this work extends the quantitative fit of star counts from the lower, main parts of the CMD (main sequence, RGB, red clump, etc., as in R18), to the upper part populated by TP-AGB stars. The most updated stellar spectra library of O-rich and C-rich stars, together with an improved treatment of

the circumstellar dust in mass-losing AGB stars are included in the population synthesis code TRILEGAL. In particular, the C-rich stars dust bolometric corrections include fitting relations derived from the result of dynamical models (Mattsson et al., 2010; Eriksson et al., 2014) to determine the carbon-dust condensation factor. TP-AGB evolutionary tracks are calculated with the COLIBRI code and then converted into stellar isochrones inside TRILEGAL. This allows us to account for the complex physics of these stars and to produce detailed synthetic catalogues that are directly comparable with AGB observations. The catalogues of AGB stars identified and classified by Boyer et al. (2011); Srinivasan et al. (2016) offered the possibility to compare our models with the observed luminosity functions in the 2MASS and *Spitzer* passbands. The observed AGB stars have been classified in O-rich, C-rich and extreme-AGB stars, allowing us to retrieve information not only on the total lifetimes, hence the mass-loss rate but also on the third-dredge up. A large grid of TP-AGB models has been calculated to explore the effects of the mass-loss prescriptions and their efficiency. Since, the work of Rosenfield et al. (2016) our models assumed a stage of "pre-dust" mass-loss described following the formalism of CS11. At a later stage, when the radiation pressure on dust grains is sufficient to drive a stellar wind, distinct prescriptions for the O-rich and C-rich stars are assumed. As for the C-rich stars the results of dynamical models of C-stars have been implemented. The mass-loss in O-rich stars is mainly modelled using the BL95 prescription. The role of the mass-loss has been investigated in the first series of models. The comparison with the observed star counts and luminosity functions confirmed the importance of the pre-dust mass-loss for low-mass, low-metallicity O-rich stars. We identified a first best-fitting model that reproduces the photometry of the SMC. The 3DU prescription follow the K02 formalism and the pre-dust mass loss from CS11 has an efficiency $\eta_{\rm pre-dust} = 3$. The BL95 efficiency for O-rich stars is relatively high with $\eta_{\rm dust} = 0.06$. A second series of models has been computed with the aim of exploring the effect of different 3DU prescriptions. In these models, the mass-loss efficiency of O-rich stars is kept lower ($\eta_{\rm dust} = 0.01 - 0.03$) and the free parameters that describe the 3DU have been tuned to reproduced the observed number counts and luminosity functions. With this respect, a new parametrisation has been introduced to account for the behaviour of $\lambda$ as a function of the core mass during the TP-AGB evolution. The qualitative behaviour is supported by full models calculations and the formalism is flexible enough to allow an accurate calibration of the onset and efficiency of the 3DU. The best-fitting model of this second series gave essentially the same results as the first one in terms of photometric properties, but the input prescriptions are very different. First of all the mass-loss efficiency has been lowered down to $\eta_{\rm dust} = 0.03$. Secondly, the efficiency of the 3DU for the more massive TP-AGB stars ($M_{\rm i} \gtrsim 3$) is lower. The predicted IFMR is in better agreement with the semi-empirical data. The best-fitting models strongly favour a somewhat limited mass interval for the formation of C-rich stars with a maximum initial mass for a star to become C-rich around 2.8 $M_{\odot}$. These models are shown to fit fairly well not only the $JHK_{\rm s}$ CMDs, but also the LFs in several mid-infrared passbands.

The main conclusions drawn from the results of the present work can be outlined as follows:

- We confirm the importance of the pre-dust mass loss for the low-mass (with initial masses around 1 $M_{\odot}$), low-metallicity O-rich stars, as already found by earlier works (Girardi et al., 2010; Rosenfield et al., 2014, 2016).

- The inclusion of a mass-loss prescription based on detailed dynamical models for C-stars (Eriksson et al., 2014; Mattsson et al., 2010) is of key importance to correctly describe the population of this class of TP-AGB stars, given its dependence on stellar

parameters, in particular the carbon excess.

- The minimum and maximum initial masses for the formation of C-stars are around 1.4 $M_\odot$ and 3 $M_\odot$ respectively, at SMC-like metallicity (i.e. $Z_\mathrm{i} = 0.004$) that is representative for the bulk of C-stars. The lack of C-stars for $K_\mathrm{s} < 10$ mag clearly indicates that the third dredge-up in TP-AGB stars with $M_\mathrm{i} \gtrsim 3\ M_\odot$ should not take over many thermal pulses nor with extreme efficiency. The minimum mass threshold is found to increase with the initial metallicity, in agreement with previous studies (e.g. Marigo and Girardi, 2007). The maximum mass threshold also shows a positive correlation with metallicity, though less pronounced. In general, these trends would lead the C/M ratio to decrease in host systems of increasing metallicity (depending also on their SFH), a well-known fact in the literature (e.g. Boyer et al., 2013).

- The number counts of the brightest O-rich stars experiencing HBB can be reproduced by invoking a mass loss with a significant luminosity dependence (Bloecker, 1995, with $\eta_\mathrm{dust} = 0.02 - 0.03$ for a shallow 3DU, or with $\eta_\mathrm{dust} = 0.06 - 0.07$ for an extremely deep 3DU). We find that a good reproduction of the O-rich LF is also attained with the empirical relation between mass-loss rate and pulsation period proposed by Vassiliadis and Wood (1993).

- A direct outcome of our calibration, based on resolved stellar populations, is the full characterisation of the AGB population in the SMC in terms of stellar parameters (i.e. initial mass, mass-loss rate, C/O, carbon excess, luminosity). The distribution of mass-loss rates for C-rich and extreme-AGB stars agree well with the one derived by Nanni et al. (2018) through the technique of SED fitting applied to the same observed catalogue adopted in this work. We also find a good agreement with the mass-loss rate estimates derived by Groenewegen and Sloan (2018b) and Goldman et al. (2018). The main features (the position of the peak and the width) of the predicted distributions in bolometric magnitude for the O-rich, C-rich and extreme-AGB star classes are in line with studies based on the SED-fitting methodology (Srinivasan et al., 2016), as well as with the work of Boyer et al. (2011).

- Finally, the $J-K_\mathrm{s}$ colours of the synthetic RSG and AGB sequences are found to be shifted to redder colours with respect to the observations. The synthetic photometry has been corrected to reduce such discrepancies that could have been affect the calibration. Further investigation of such discrepancies revealed a possible connection with the mixing length parameter that should be varied as a function of the luminosity as suggested by 3D-models computations. A slower increase of the mixing length parameter seems to be required to reproduce the slope of the fundamental mode period-luminosity sequence of LPVs in the Magellanic Clouds.

**Data retrieval**

Complete set of TP-AGB tracks have been computed for all metallicities present in the original `PARSEC` v1.2S database, spanning the range $0.0001 < Z < 0.06$ ($-2.2 <$ [Fe/H] $< +0.7$) for the best-fitting sets S_07 and S_35. `PARSEC+COLIBRI` isochrones derived from these tracks will be available from our web interfaces `http://starkey.astro.unipd.it/cmd` and `http://stev.oapd.inaf.it/cmd_3.1`, for over 50 different photometric systems including major photometric surveys and instruments (e.g. 2MASS, SDSS, Spitzer, AKARI, HST/ACS, HST/WFC3, WISE, VISTA, Gaia, TESS), and future datasets (e.g. JWST, LSST, Euclid). A general description of the isochrone characteristics and data format is provided in Marigo et al. (2017).

## 4.7 $K_s$-band luminosity functions

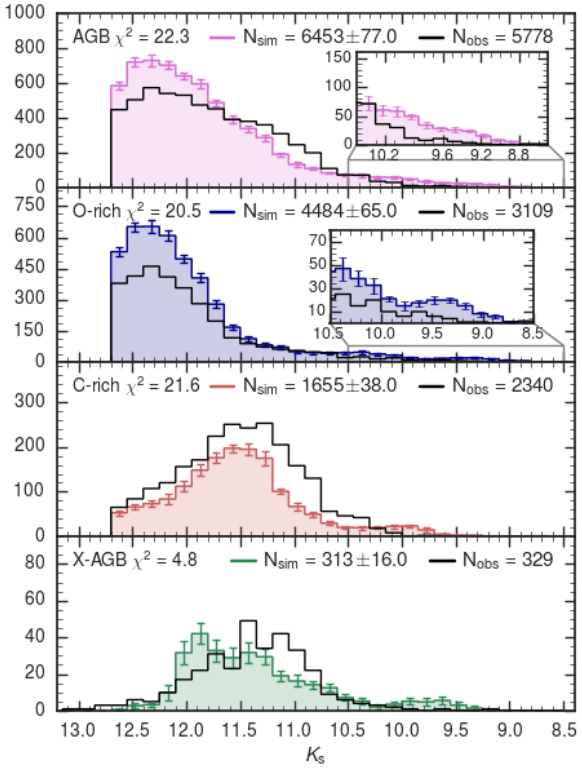


**Figure 4.34:** $K_s$-band LFs from S_00

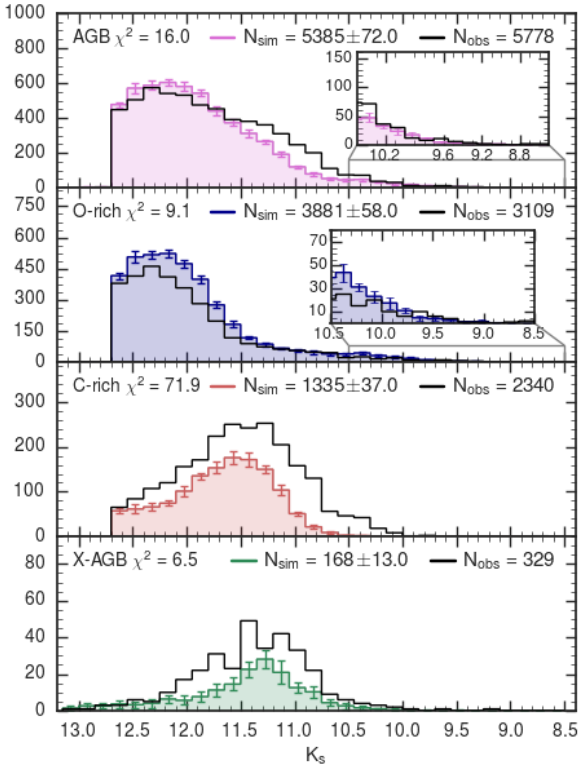


**Figure 4.34** (cont.)**:** $K_s$-band LFs from S_01

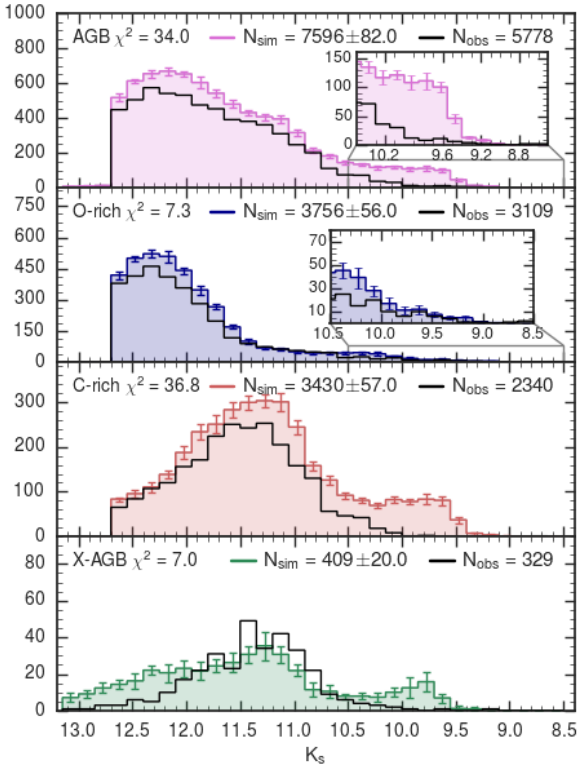


**Figure 4.34** (cont.)**:** $K_s$-band LFs from S_02

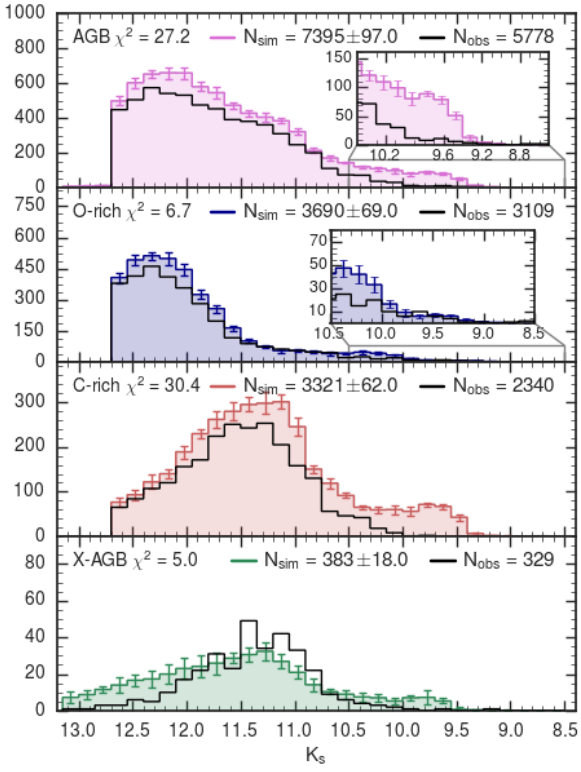


**Figure 4.34** (cont.)**:** $K_s$-band LFs from S_03

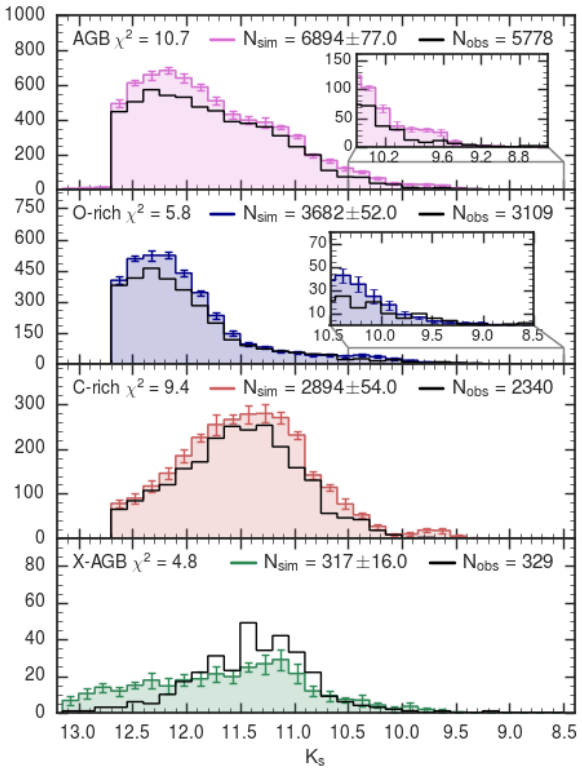


**Figure 4.34** (cont.)**:** $K_s$-band LFs from S_04

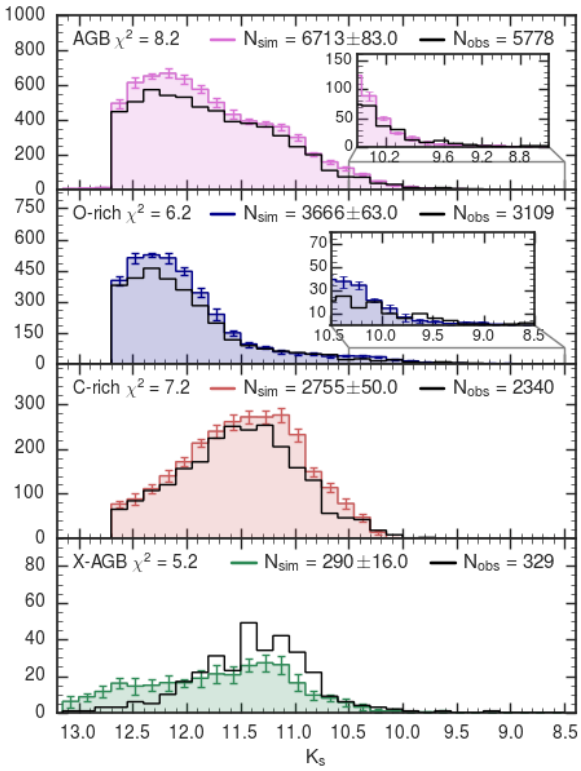


**Figure 4.34** (cont.)**:** $K_s$-band LFs from S_05

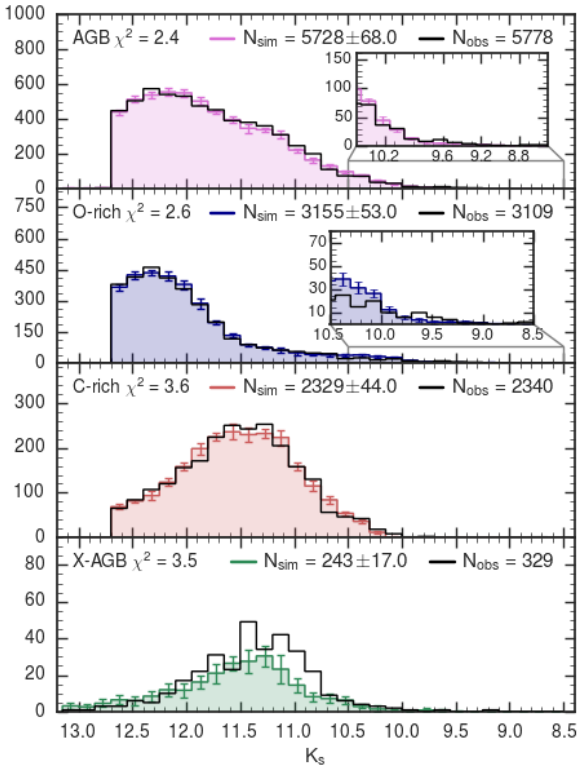


**Figure 4.34** (cont.)**:** $K_s$-band LFs from S_06

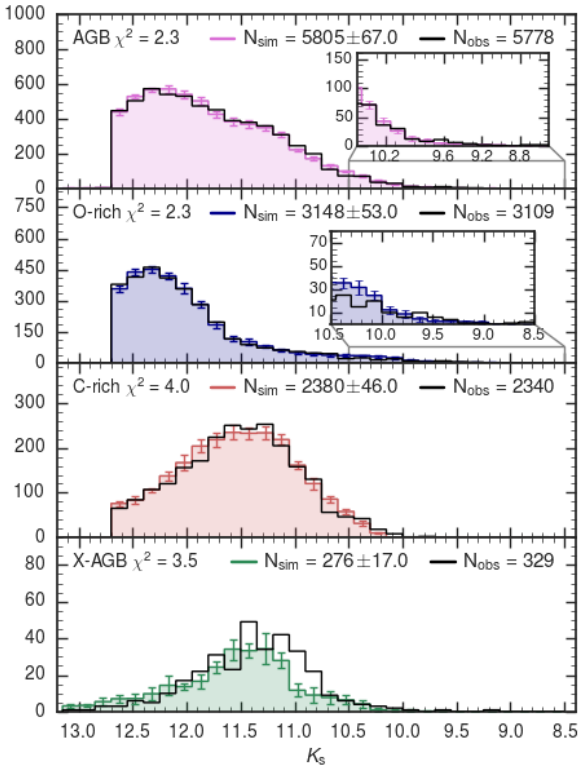


**Figure 4.34** (cont.)**:** $K_s$-band LFs from S_07

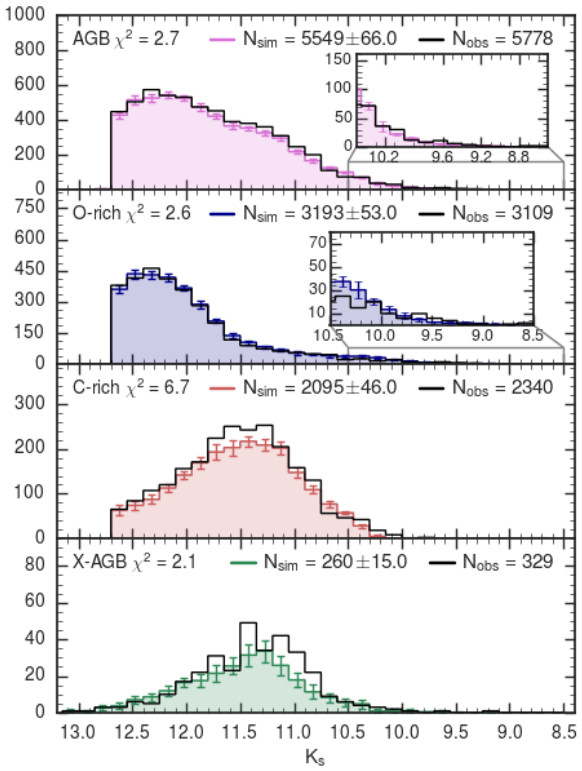


**Figure 4.34** (cont.)**:** $K_s$-band LFs from S_08

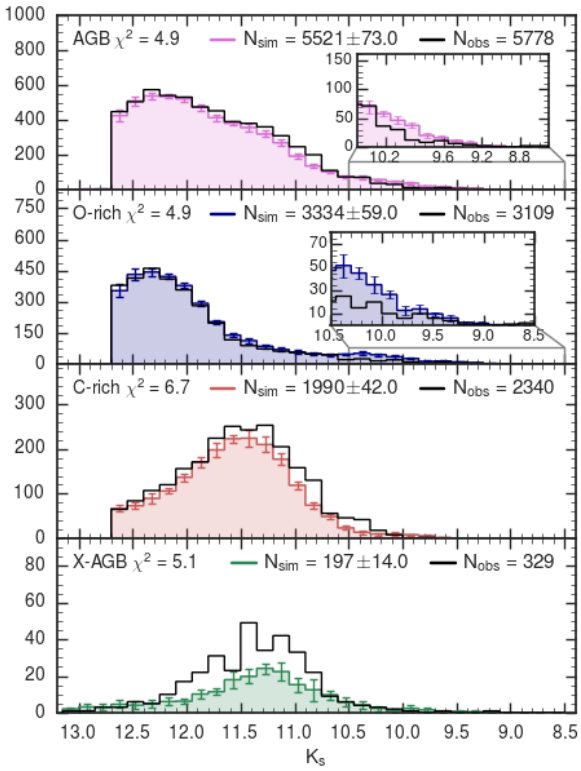


**Figure 4.34** (cont.)**:** $K_s$-band LFs from S_09

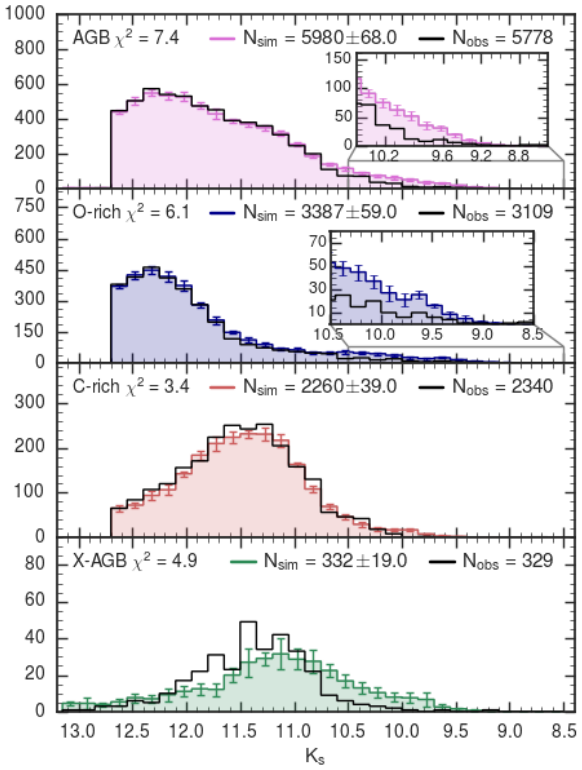


**Figure 4.34** (cont.)**:** $K_s$-band LFs from S_10

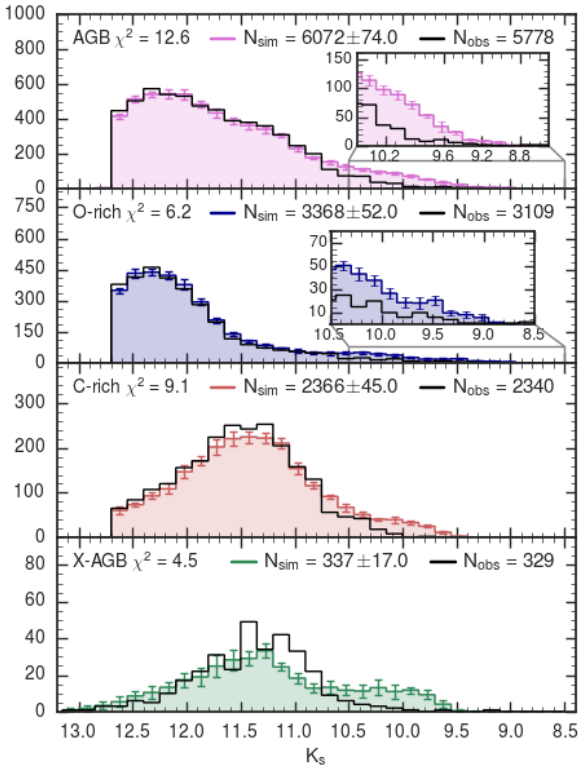


**Figure 4.34** (cont.)**:** $K_s$-band LFs from S_11

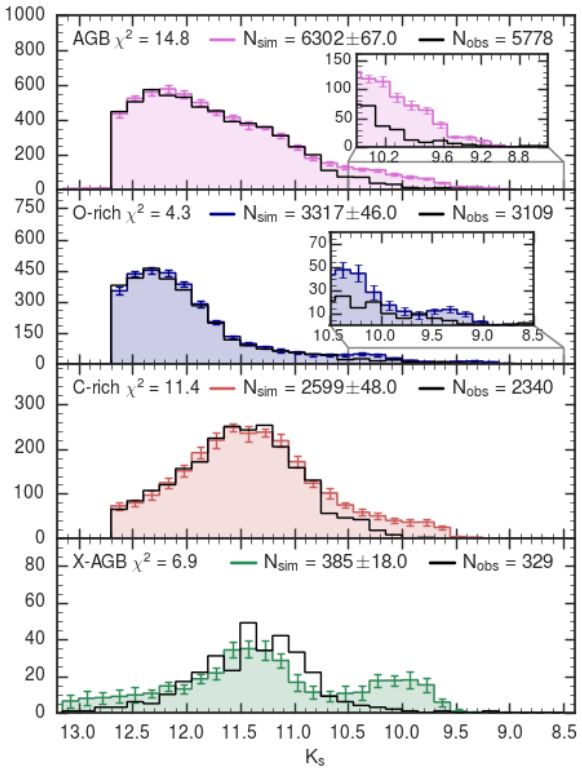


**Figure 4.34** (cont.)**:** $K_s$-band LFs from S_12

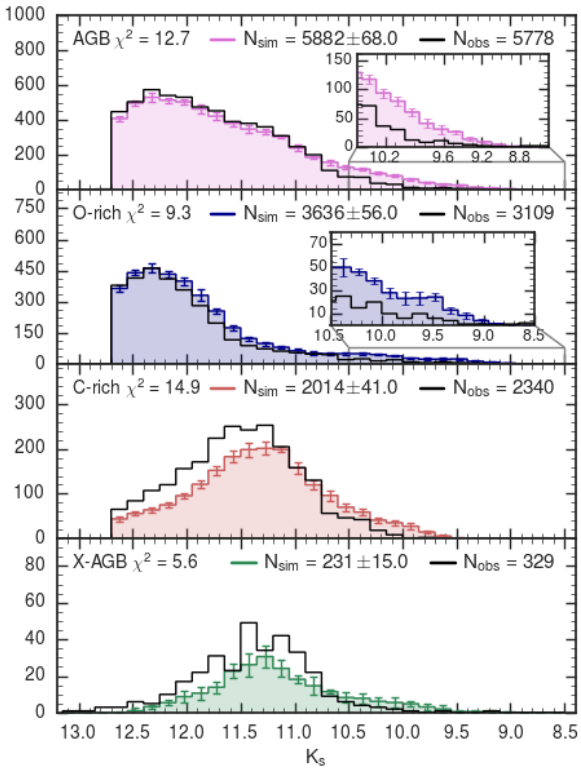


**Figure 4.34** (cont.)**:** $K_s$-band LFs from S_13

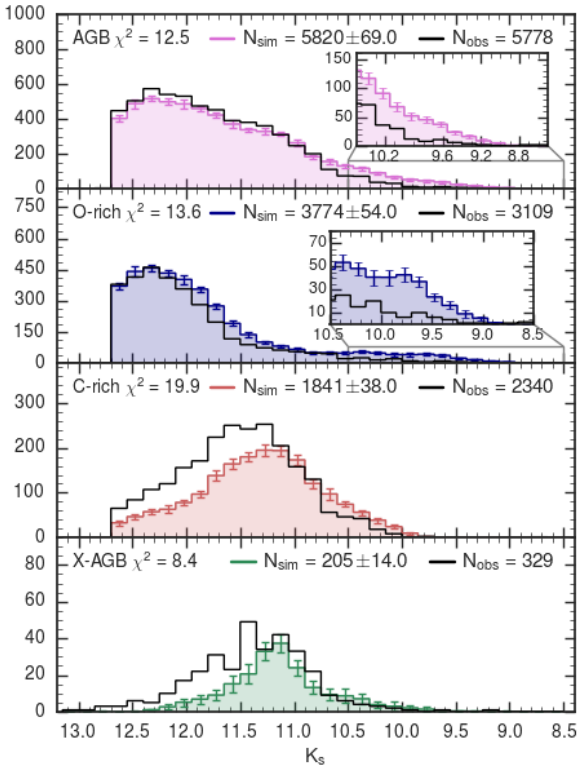


**Figure 4.34** (cont.)**:** $K_s$-band LFs from S_14

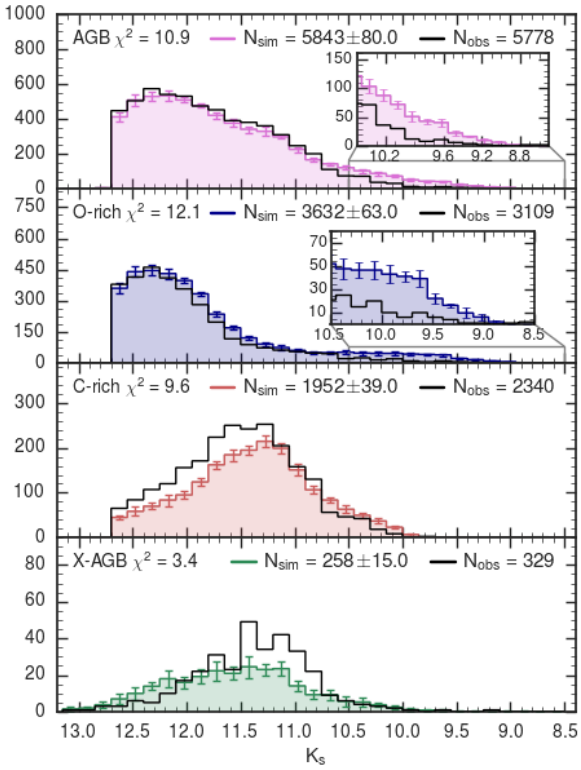


**Figure 4.34** (cont.)**:** $K_s$-band LFs from S_15

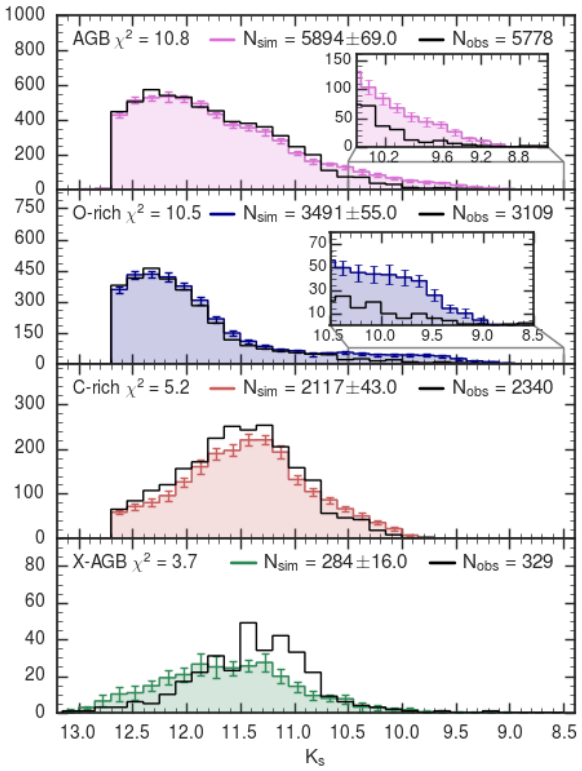


**Figure 4.34** (cont.)**:** $K_s$-band LFs from S_16

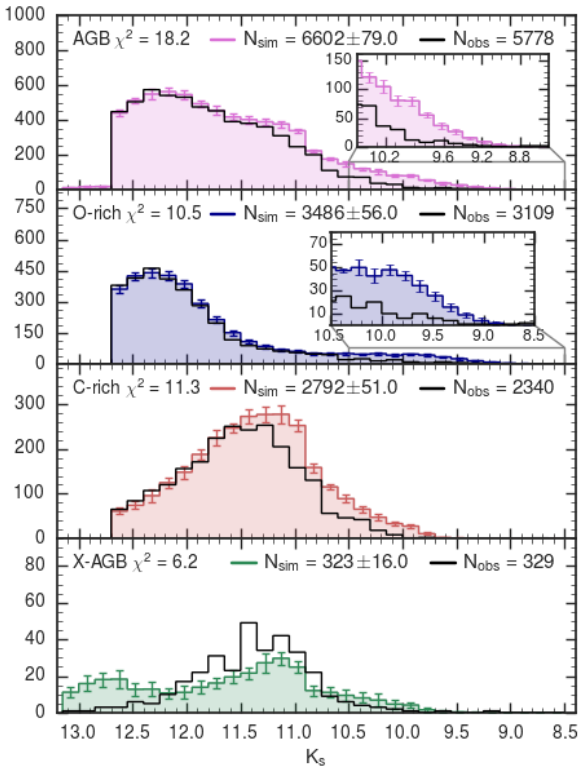


**Figure 4.34** (cont.)**:** $K_s$-band LFs from S_17

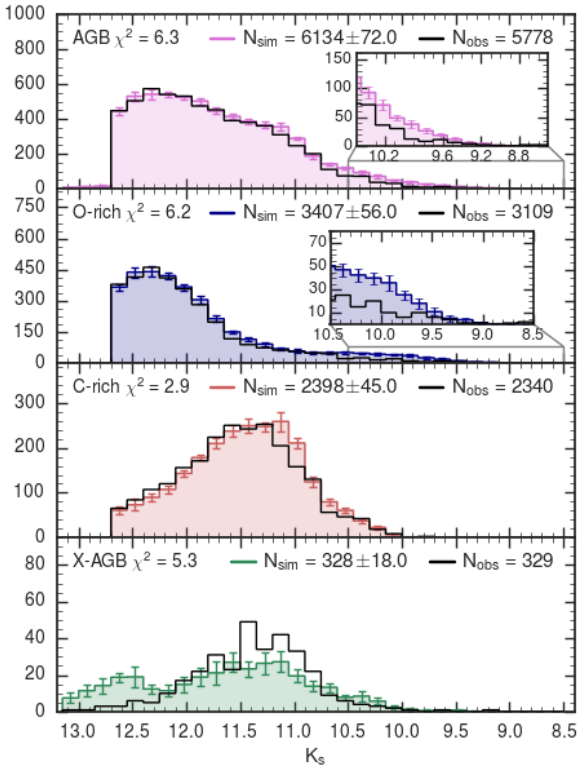


**Figure 4.34** (cont.)**:** $K_s$-band LFs from S_18

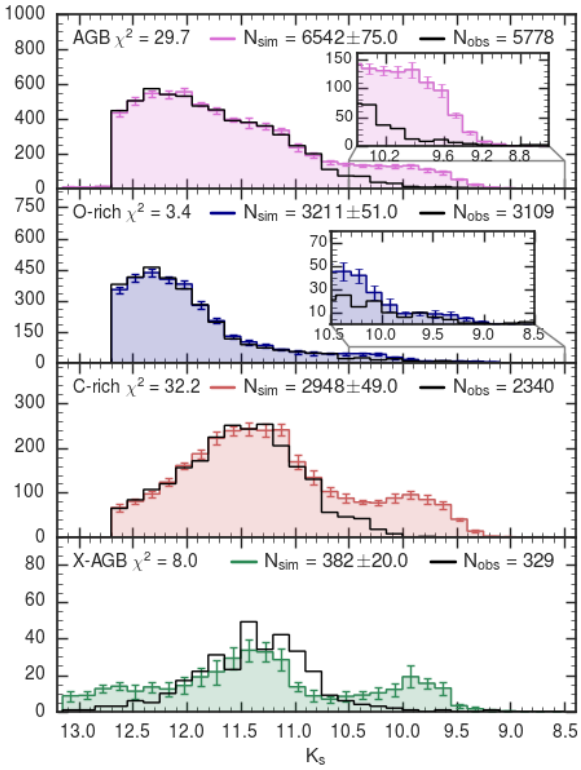


**Figure 4.34** (cont.)**:** $K_s$-band LFs from S_19

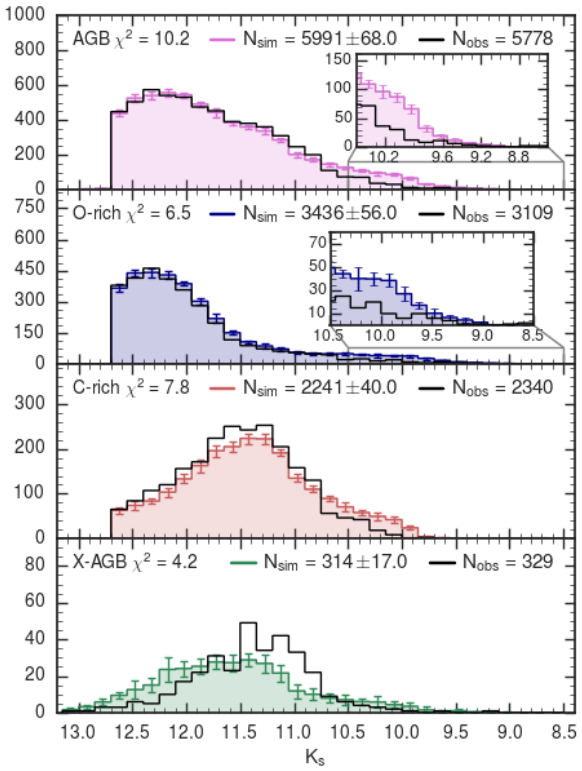


**Figure 4.34** (cont.)**:** $K_s$-band LFs from S_20

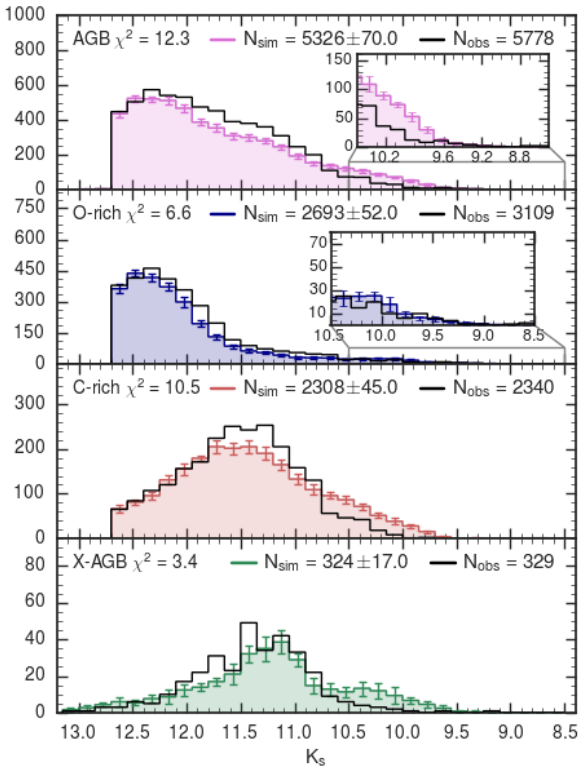


**Figure 4.34** (cont.)**:** $K_s$-band LFs from S_21

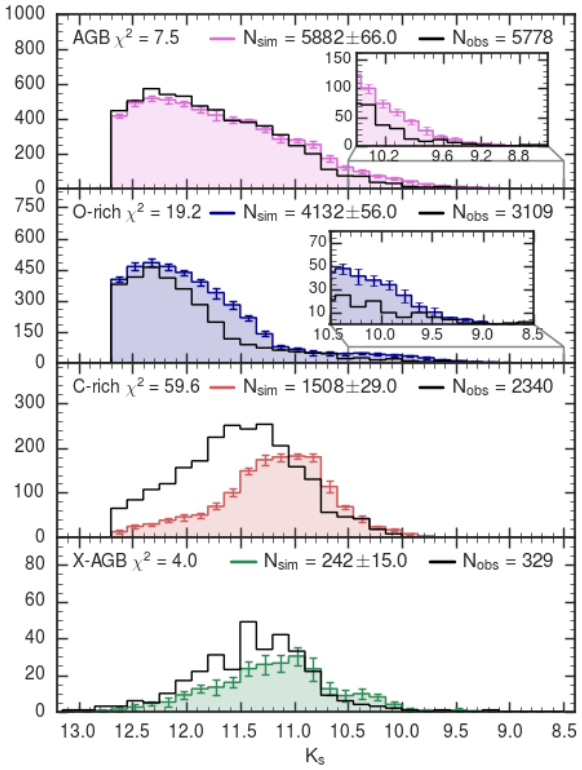


**Figure 4.34** (cont.)**:** $K_s$-band LFs from S_22

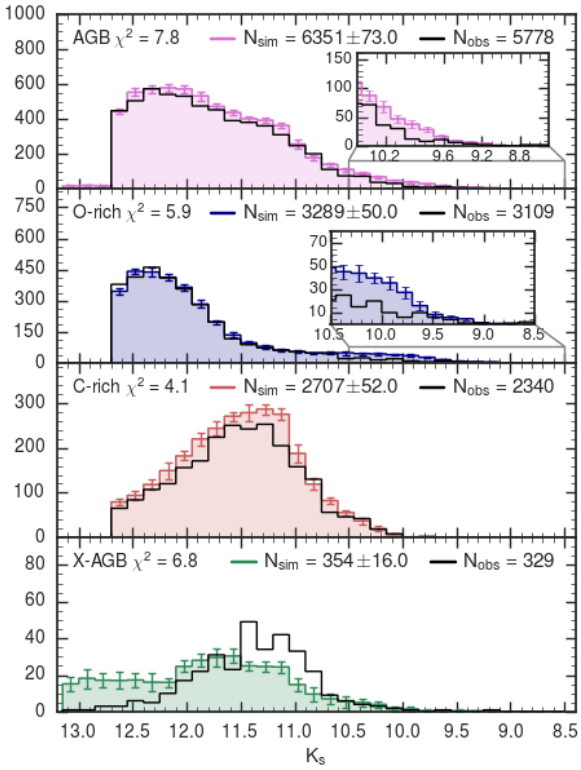


**Figure 4.34** (cont.)**:** $K_s$-band LFs from S_23

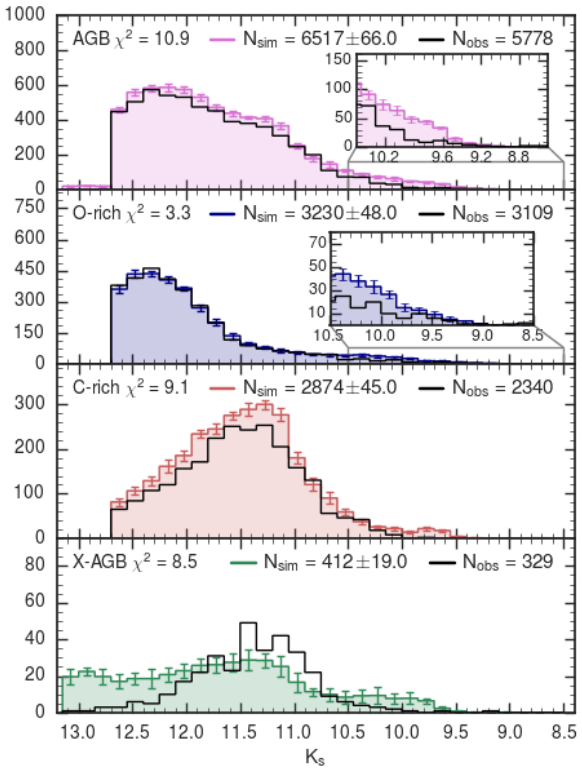


**Figure 4.34** (cont.)**:** $K_s$-band LFs from S_24

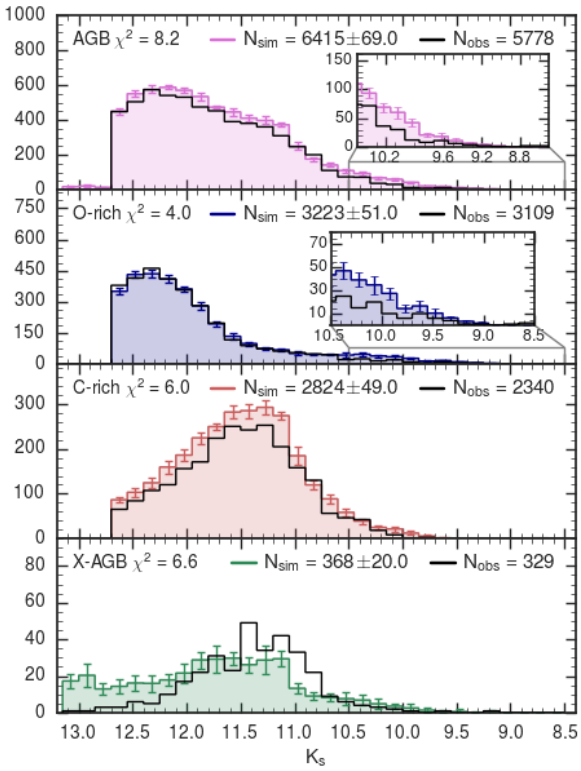


**Figure 4.34** (cont.)**:** $K_s$-band LFs from S_25

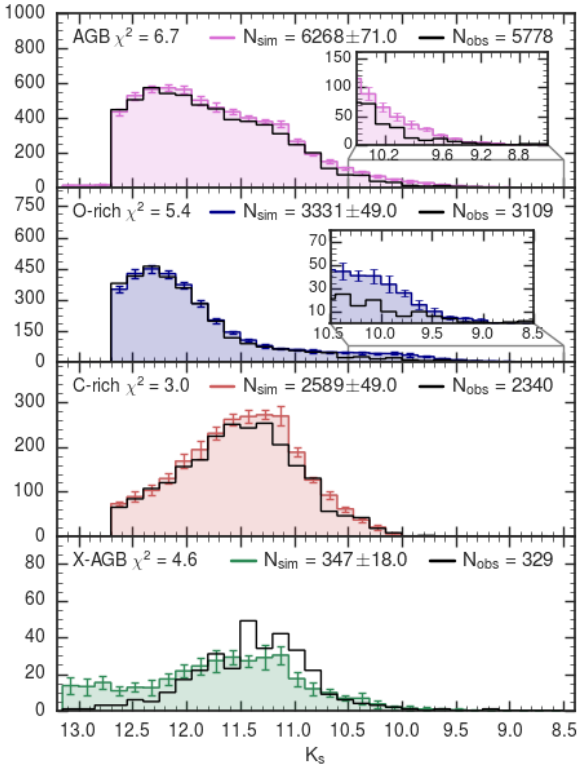


**Figure 4.34** (cont.)**:** $K_s$-band LFs from S_26

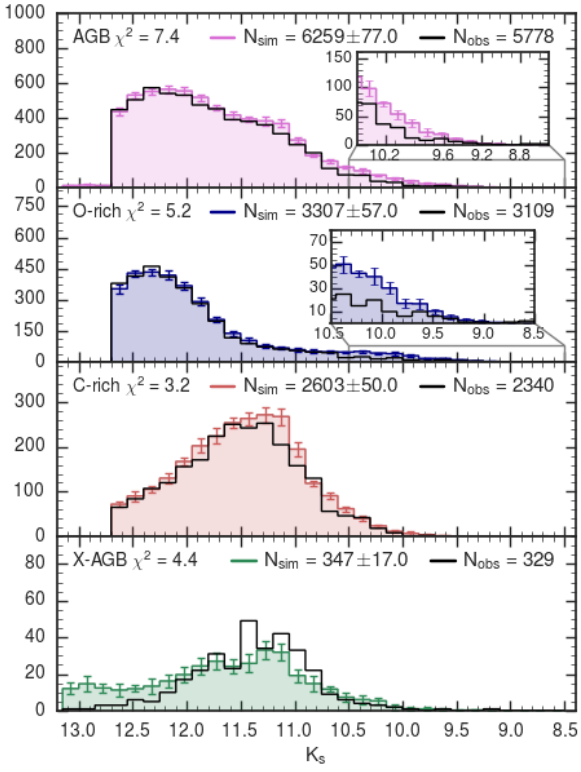


**Figure 4.34** (cont.)**:** $K_s$-band LFs from S_27

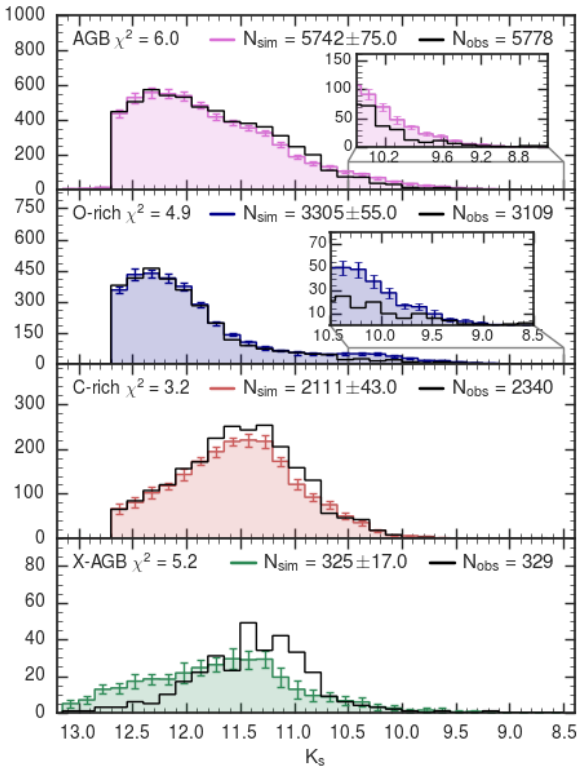


**Figure 4.34** (cont.)**:** $K_s$-band LFs from S_28

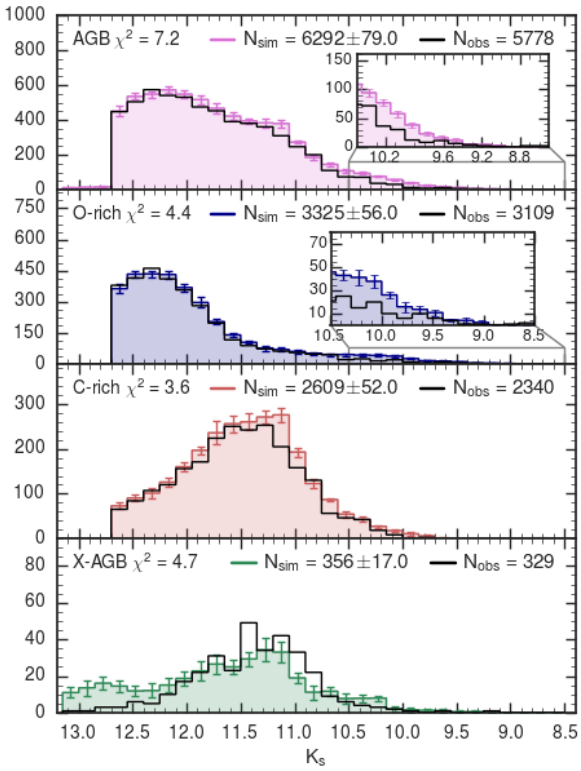


**Figure 4.34** (cont.)**:** $K_s$-band LFs from S_29

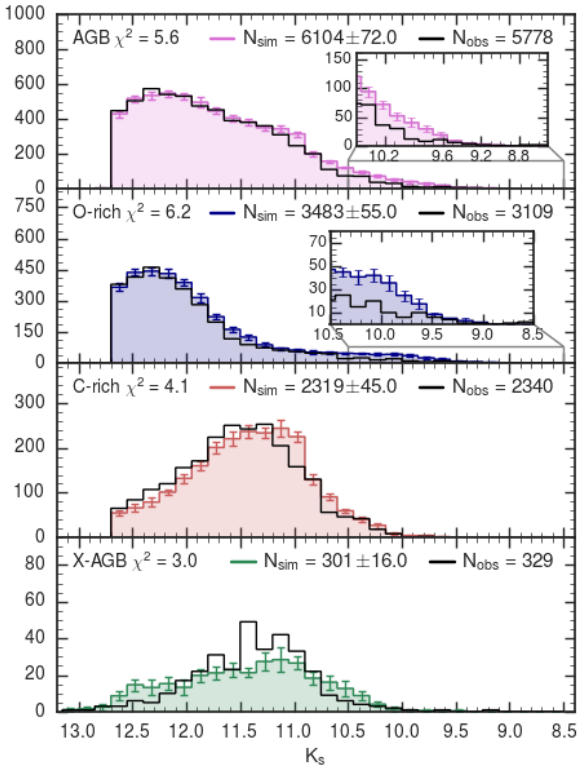


**Figure 4.34** (cont.)**:** $K_s$-band LFs from S_30

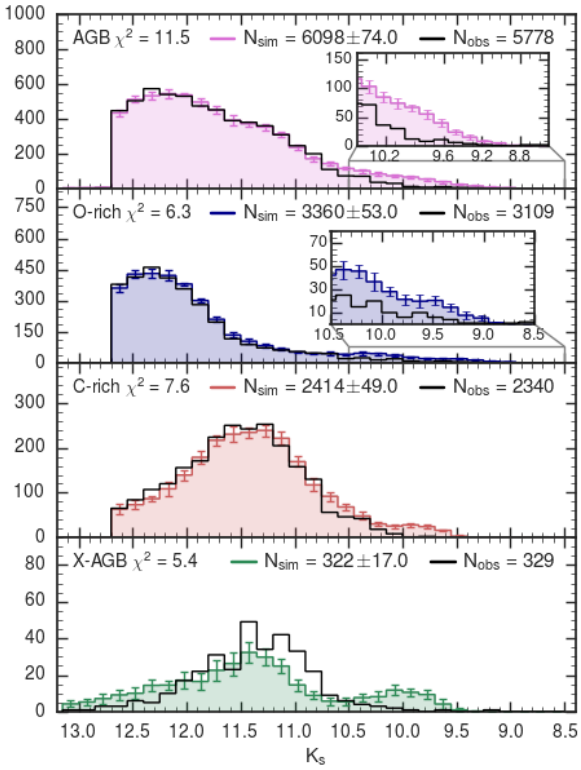


**Figure 4.34** (cont.)**:** $K_s$-band LFs from S_31

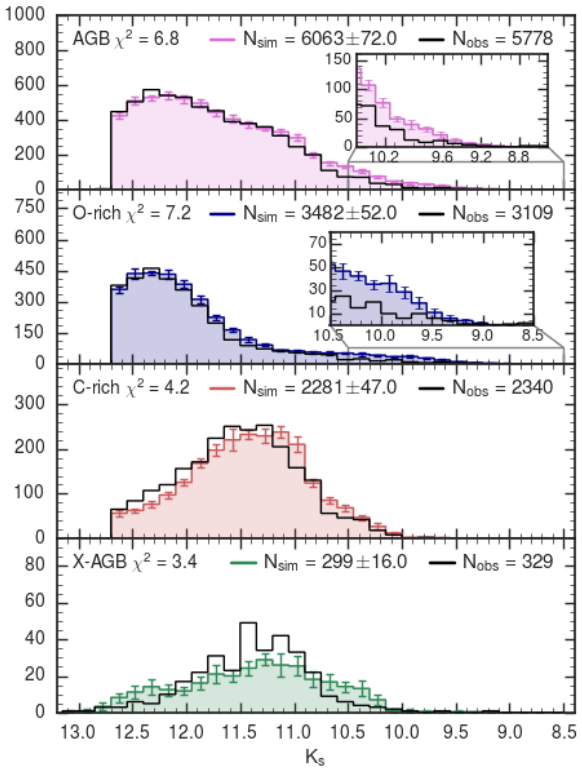


**Figure 4.34** (cont.)**:** $K_s$-band LFs from S_32

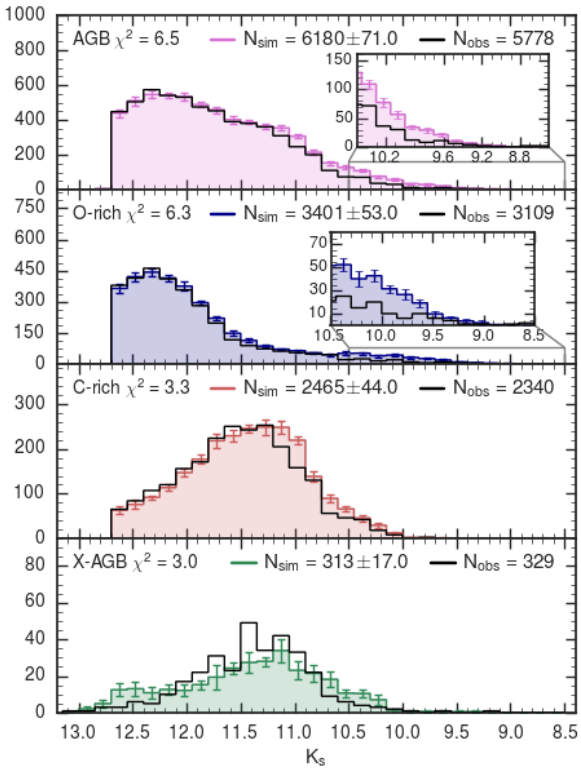


**Figure 4.34** (cont.)**:** $K_s$-band LFs from S_33

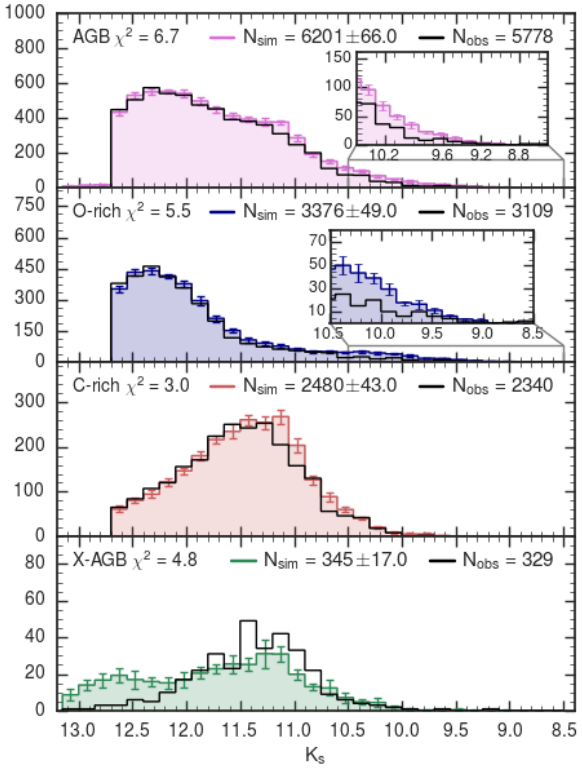


**Figure 4.34** (cont.)**:** $K_s$-band LFs from S_34

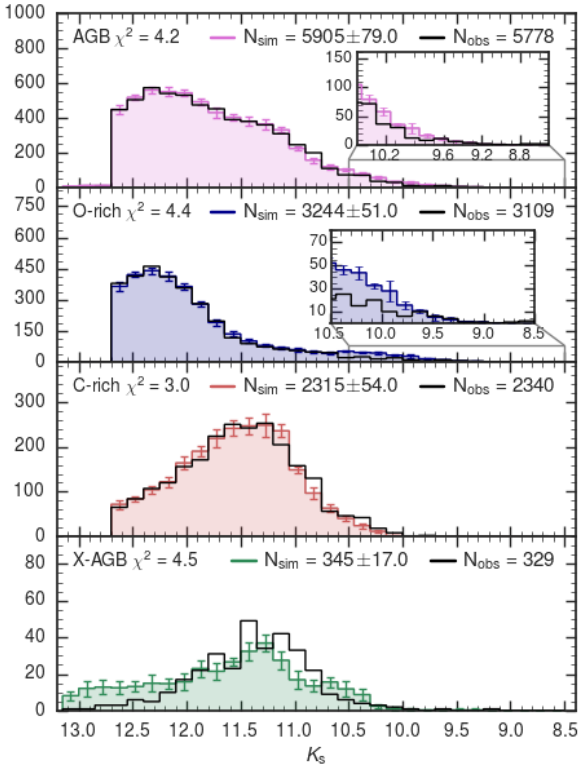


**Figure 4.34** (cont.)**:** $K_s$-band LFs from S_35

# Chapter 5

# Modelling AGB stars in other galaxies

This chapter is dedicated to the simulations of the stellar populations of nearby systems in the context of additional projects carried out during my PhD. I will first describe how I modelled the LMC stellar populations by adopting the SFH derived by Harris and Zaritsky (2009). The simulations of the LMC have been employed to study the population of Long Period Variables in the Gaia DR2 and the results have been included in a recent A&A Letter (Lebzelter et al., 2018). As a further application, I present the Magellanic Clouds simulations in the Large Synoptic Survey Telescope (LSST) survey filters. Finally, I discuss some preliminary results about the AGB population of Local Group dwarf galaxies observed within the *Spitzer* DUSTiNGS program and the relative HST follow-up.

## 5.1 The Star Formation of the LMC

As already discussed in Chapter 3, we have a very good description of the SMC populations thanks to the space-resolved SFH derived by Rubele et al. (2018) with the deep VMC photometry. As for the LMC, the derivation of the SFH using the same data is currently on-going, thus we need to rely on the space-resolved SFH by Harris and Zaritsky (hereafter HZ09, 2009). Both studies rely on CMD fitting technique but there are a number of reasons for which the adoption of the SFH by Harris and Zaritsky (2009) has to be carefully considered, mainly due to the fact that the work of HZ09 relies on optical data of the MCPS photometric survey (Zaritsky et al., 1997):

- The extinction is very low in the near-infrared VMC photometry, whereas the MCPS data can be severely affected by the extinction.
- The VMC photometry reaches the the oldest main-sequence turn-off points in each SMC region analysed, but this is not the case for HZ09. Therefore, the estimate of the ages cannot be considered as robust as in R18.
- They used the set of isochrones published by Girardi et al. (2002), whereas R18 employed the latest version of PARSEC tracks.
- The IMF used by HZ09 is a Salpeter-like (with a power-low index of $-1.35$), whereas R18 used Kroupa (2001)
- HZ09 used a set of 3 initial metallicities to produce their "partial models", whereas in R18 we have a more extended grid of models.

Furthermore, we had the possibility to perform several consistency checks for the SFH of R18. This is not possible for the work of HZ09. In the following I describe how

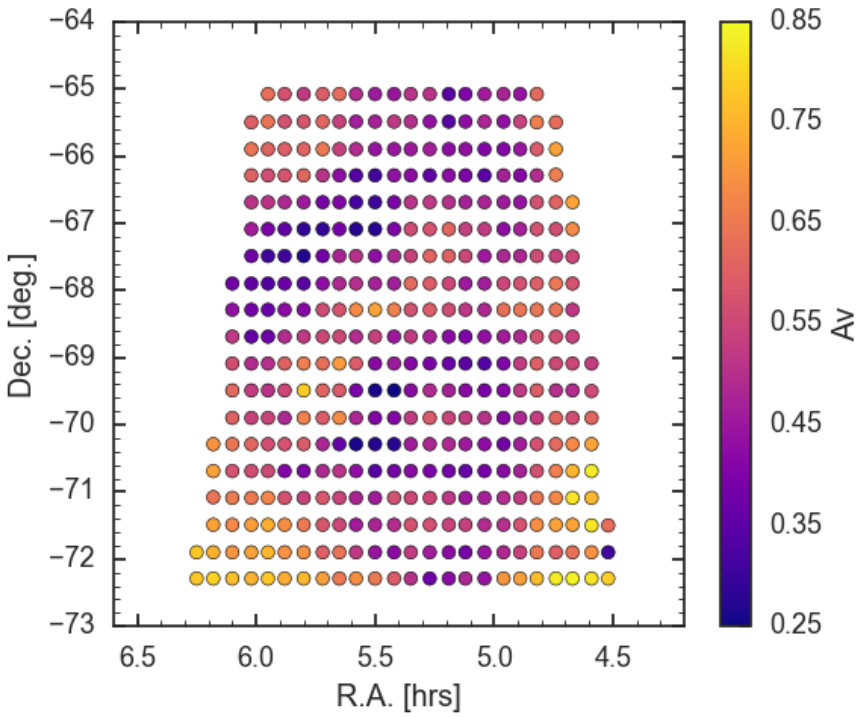


**Figure 5.1:** Centres of the LMC regions colour-coded according to the reddening values ($A_V$) adopted in the `TRILEGAL` simulations.

I implement the results of HZ09 and the main caveats to be taken into account when comparing number counts of the LMC simulation with data.

HZ09 divided the MCPS region in a uniform grid of 24′ x 24′ and further divided the original region in a 2x2 grid according to a minimum number of stars per region. The SFH solutions are given for each of these regions. As in R18, the SFR and AMR are given for a number of age intervals (16 bins with $\log(Age/yr) = [6.8 - 10.20]$), whereas the reddening is provided in a slightly different way. They provide the interstellar extinction for each star used in the SFH analysis, differentiating between younger hot stars and older cool stars.

Starting from the LMC grid of HZ09, I produce a uniform grid taking into account the regions that were further divided. Such grid consists of 386 regions of $\sim 0.16$ deg$^2$, each having its own SFR and AMR. In order to have a value of the reddening for each region, I start from the two reddening maps of hot and cool stars derived by HZ09, and I derive the corresponding mean reddening values ${A_V}_i^{Hot}$ and ${A_V}_i^{Cool}$ for each LMC region $i$. The reddening value $A_{Vi}$ adopted in the simulations is the mean value between ${A_V}_i^{Hot}$ and ${A_V}_i^{Cool}$. Figure 5.1 shows the resulting $A_V$ values for each LMC region.

Before performing the SFH analysis HZ09 deprojected the MCPS photometry to a common true distance modulus of 18.50 mag, by using the LMC disk geometry described in van der Marel and Cioni (2001). The latter showed that the LMC stellar populations are distributed in a disk with an inclination of 34.7 deg with the respect to the plane of the sky. As such inclination results in distance modulus variations larger than ±0.1 mag, it is important to take into account the disk geometry. Following the approach of HZ09, I projected the common distance modulus to obtain the distance modulus of each region according to disk geometry of van der Marel and Cioni (2001). In practice, I transform the sky coordinates of each subregion centre to a polar coordinate system ($R$,$\Theta$) centred on the LMC (5.483333 h, -69.5 deg). Then, I assigned to each LMC region a distance $D$

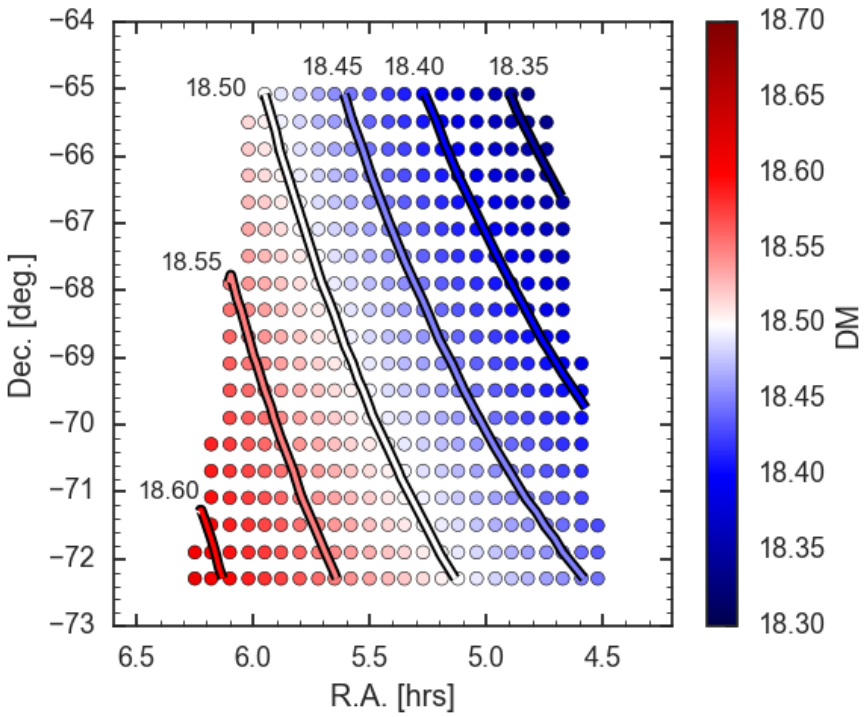


**Figure 5.2:** Centres of the LMC regions colour-coded according to the distance modulus (DM) values adopted in the `TRILEGAL` simulations.

according to the following formula (see HZ09, their Sect. 3.4):

$$D(kpc) = 50 + 0.873 \cdot R \cdot \tan(i) \cdot \sin(\Theta - \Theta_0), \tag{5.1}$$

where $R$ is the angular separation of the centre of each region from the LMC centre (in degrees), $\Theta$ is the azimuthal angle, $i$ is the inclination angle and $\Theta_0$ is the position angle (van der Marel and Cioni, 2001). The value 0.873 is the linear separation (in kpc) that corresponds to an angular separation of one degree at a distance of 50 kpc. The resulting distance modulus values obtained for each region are shown in Figure 5.2. As for the SMC, we now have a complete catalogue of the LMC SFH with SFR, AMR, distance and $A_V$ for each region.

Given the discrepancies found in the derivation of R15, where the input models were even more consistent that those used by HZ09, I checked the predicted number counts obtained with the HZ09 SFH by using the 2MASS photometry. I divided the 2MASS photometry, according to the sky coordinates of each LMC region and I produced a `TRILEGAL` simulation for each single region and checked if the star counts in the RGB were reproduced. An example is shown in Figure 5.3 where the simulated and observed $K_s$ vs. $J-K_s$ CMDs are plotted for one LMC region. The results of such test are shown in Figure 5.4 , where the number of predicted RGB stars are plotted against the observed ones for each region. Apart for a few outliers, the predicted numbers of RGB stars match the observed ones within a $3\sigma$ difference. It is important to notice that this result is obtained when a Kroupa IMF is used in place of the Salpeter IMF originally used by HZ09 in their analysis.

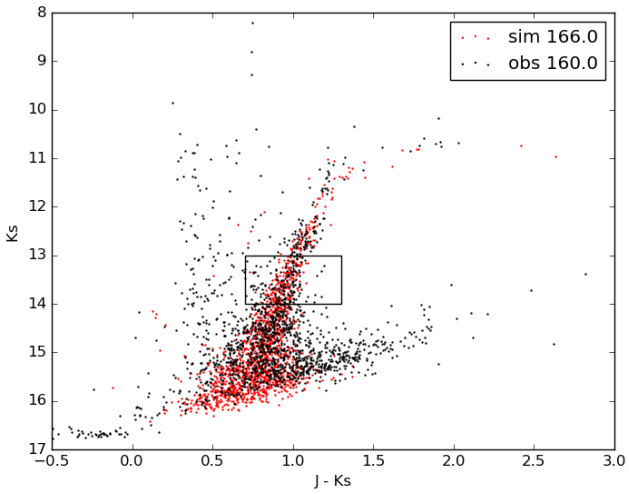


**Figure 5.3:** Simulated (red) and observed (black) $K_s$ vs. $J-K_s$ CMDs for one LMC region. The black rectangle indicates the RGB region used to compare the number counts reported in the legend.

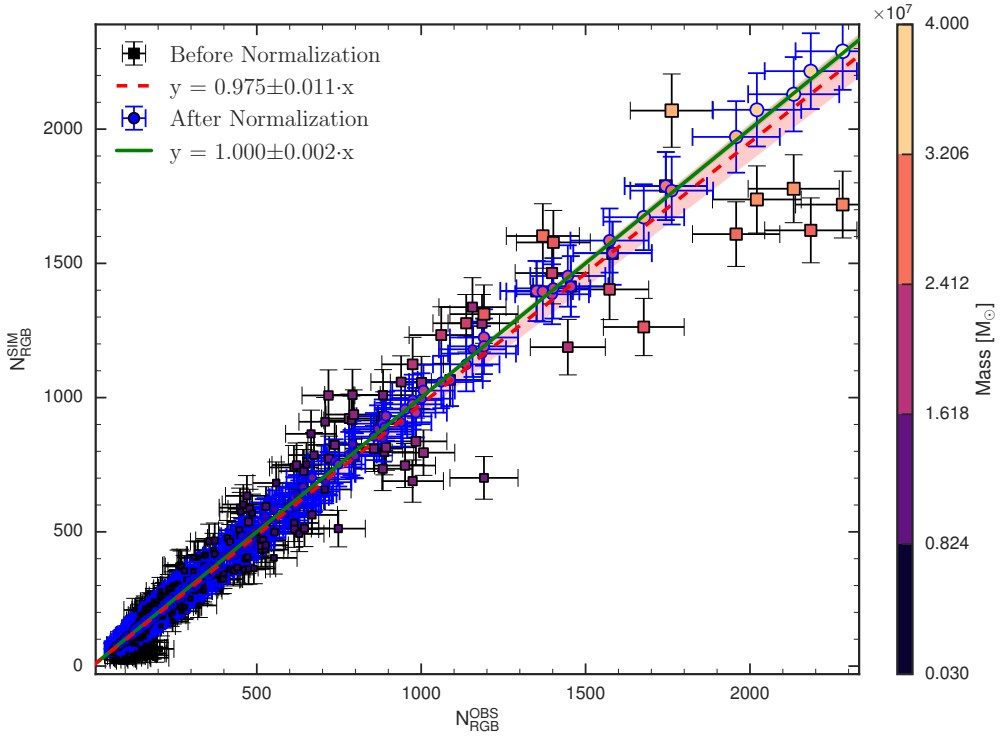


**Figure 5.4:** Number of observed and simulated RGB stars for each LMC region with $3\sigma$ error bars. The number counts obtained using the total stellar mass from HZ09 are shown as squares, the number counts obtained after normalising the total stellar mass to the number of RGB stars are shown as circle. Both are colour-coded according to the total stellar mass. The red dashed line and the solid green line are the linear fits to the number counts before and after the normalisation respectively.

## 5.2 Long Period Variables in Gaia DR2

In a recent work, we exploit the high-quality data of the Gaia data release 2 (Gaia Collaboration et al., 2018) to study the Long-Period Variables (LPVs) observed in the LMC.

The first catalogue of LPVs published by Mowlavi et al. (2018) contains 151 761 candidates. By applying a selection criteria based on proper motions, we find 11 022 candidates in the LMC, that have been cross-matched with the 2MASS photometry.

LPVs are usually studied in the Period-Luminosity diagram. In order to construct an observational diagram it is of common use to employ as representative of the luminosity the Wesenheit function defined as:

$$\mathrm{W}_{JK} = K_\mathrm{s} - 0.686 \cdot (J - K_\mathrm{s}) \tag{5.2}$$

Since the Wesenheit function can correct for the interstellar reddening, with the exception of very high reddening values due to the circumstellar dust in mass-losing stars, we refer to this function as "reddening-free" magnitude. In the optical range, the situation is complicated by the fact that the effective temperature affects in a non negligible way the colour of red giants. However, it is possible to construct the equivalent Wesenheit function for the Gaia passbands. In this work we used the following function:

$$\mathrm{W}_\mathrm{RP} = \mathrm{G}_\mathrm{RP} - 1.3 \cdot (\mathrm{G}_\mathrm{BP} - \mathrm{G}_\mathrm{RP}) \tag{5.3}$$

The main difference between the $\mathrm{W}_\mathrm{JK}$ and the $\mathrm{W}_\mathrm{RP}$ is in the sensitivity to the effective temperature of the stars, hence to the chemistry of AGB stars.

We find that by combining $\mathrm{W}_\mathrm{JK}$ and $\mathrm{W}_\mathrm{RP}$, it is possible to distinguish between evolutionary stages and initial masses of LPVs, in addition to their chemical type.

Figure 5.5 shows the $\mathrm{W}_\mathrm{RP} - \mathrm{W}_\mathrm{JK}$ vs. $K_\mathrm{s}$ diagram of the Gaia LPV candidates in the LMC. The identification of their evolutionary stages and chemical types has been guided by evolutionary tracks and a population synthesis simulation I performed as described below.

To perform the population synthesis simulation of the LPVs candidates, I used the SFH of HZ09 as described in details in the previous section. The total mass in stars of the simulation is $\approx 2.3 \cdot 10^9 M_\odot$. The evolutionary tracks are from the PARSEC database and the TP-AGB tracks computed with the `COLIBRI` code have the input prescriptions of S_18 models (the best-fitting models at the time of the publication of the work). The effects of the circumstellar dust in mass-losing AGB stars is taken into account with the same tables of bolometric corrections used for the SMC calibration, i.e. the revised Marigo et al. (2008) tables. I simulated the Gaia photometry considering a completeness of 100 per cent down to G = 20 mag and photometric errors of the order of 0.01 mag. The LPVs candidates have magnitudes brighter than $K_\mathrm{s} = 13.7$ mag and $\mathrm{G}_\mathrm{RP} = 17.5$ mag. Adopting these magnitudes limits, the LMC simulation predicts a much higher number of stars, that is, about $1.69 \cdot 10^5$ with respect to the 11 022 observed LPVs. The reason is that not all variable stars have a sufficiently large amplitude to be detected in Gaia DR2. To have a comparable number of stars, following the results of Trabucchi et al. (2017, and in prep.), we apply a set of selection criteria based on the result of linear pulsation models. Trabucchi et al. (2017) showed that growth rates are a good proxy for the observed amplitudes of LPVs and they depend on the ratio between the dynamical frequency and the acoustic cut-off frequency of the star, the latter being proportional to the radius, the effective temperature and the mass of the star. By using these selection criteria, the total number of synthetic stars is reduced to 18 700 in good agreement with the observations.

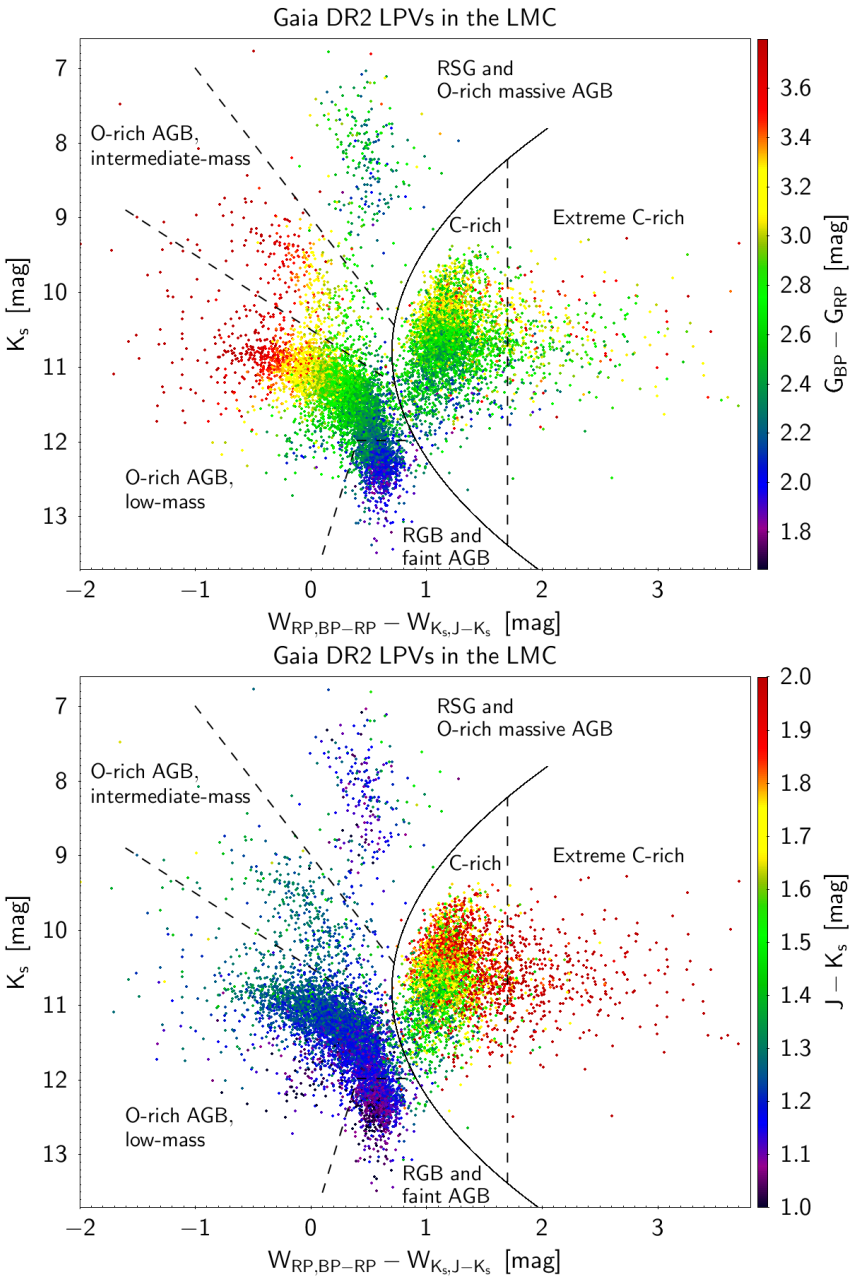


**Figure 5.5:** $W_{RP} - W_{JK}$ vs. $K_s$ diagram of the Gaia LPV candidates in the LMC, colour-coded according to their Gaia $G_{BP} - G_{RP}$ colour (top panel) and their 2MASS $J - K_s$ colour (bottom panel). The solid line separates O-rich and C-rich stars, whereas dashed lines distinguish the sub-groups as indicated (see discussion in the text). Adapted from Lebzelter et al. (2018).

The synthetic simulations in the $W_{RP} - W_{JK}$ vs. $K_s$ diagram are shown in Figure 5.6. In the left panel I show the stars colour-coded according to the predicted initial mass, whereas in the right-panel they are colour-coded according to the predicted C/O ratio.

The remarkable agreement between the simulation and the observations allows us to guide the interpretation of this new diagram and to prove its ability to distinguish between the initial mass of the stars that are located in the different branches. Branch a) is populated by low-mass O-rich stars with initial masses between $\approx 0.9$ and $\approx 1.4 M_\odot$ that do not become C-stars. Stars with a slightly larger initial mass ($M_i \gtrsim 1.4 M_\odot$) instead become C-stars and they are visible in branch (b). The branch b) mainly contains C-rich stars with initial masses in the range 1.4 – 3.2 $M_\odot$. Branch c) is populated by intermediate-mass O-rich stars. Such stars have initial masses larger than $\approx 2$ $M_\odot$ and the most brighter are undergoing HBB. The O-rich stars in the initial mass range 1.8 – 2 $M_\odot$ will move to the branch b) at later stages of their evolution once they become C-stars. A very interesting features of this diagram is the gap between branches a) and c). We interpret the absence of stars in this region as the result of the evolution prior to AGB phase. As can be appreciated in the inset of Figure 5.6, where we show the location of stars with initial mass in the range 1.4 to 3 $M_\odot$, the curves mark the brighter edge of branch a) and the fainter edge of branch c) in correspondence of the gap. The stars in the fainter curve are low-mass stars ($M_i \approx 1.4 - 1.8 M_\odot$) that developed an electron degenerate He-core after the main sequence. Stars with $M_i \approx 1.8 M_\odot$ ignite He when the core mass is the smallest possible, hence they are the fainter ones. They are at the transition between low- and intermediate-mass stars. The latter have a non degenerate He core and corresponds to the brighter curve. Finally, branch d) hosts RSG ($M_i > 8 M_\odot$) and massive O-rich AGB ($M_i > 5 M_\odot$) stars. A small fraction of these stars, specifically those in the initial mass range 5-6 $M_\odot$, can include super-AGB stars.

The importance of this new diagram is also evident by looking at the right panel of Figure 5.6. The separation between C-rich and O-rich stars predicted by the simulation is very clear. The only exception is a narrow region around $W_{RP} - W_{JK} = 0.9$, in addition to a few C-stars visible in branch a). These C-stars are the ones expected to be in the luminosity dip of a pulse cycle.

The picture drawn so far is also confirmed by the location of some representative TP-AGB evolutionary tracks of initial masses 1.3, 1.6, 2.6, and 4.4 $M_\odot$, and more massive tracks with 12 and 20 $M_\odot$, as shown in Figure 5.7.

Finally, I perform some test to investigate if and how the morphology of this diagram depends on the adopted SFH (see Figure 5.8). In general, the location of the branches and the morphology of the diagram do not change significantly because these properties mainly depend on the intrinsic evolution of the stars. The use of a constant SFH and a constant metallicity has an effect on the relative number counts in the different branches, but the main features remain the same. It is also interesting to see the effect of not including the circumstellar reddening by dust. As shown in the bottom panel of Figure 5.8, the reddening caused by the dust around the mass-losing C-rich stars is responsible for the rightward tail of the extreme C-rich stars. It also worth noticing that the leftward excursion of branches populated by O-rich stars is due the lower effective temperatures.

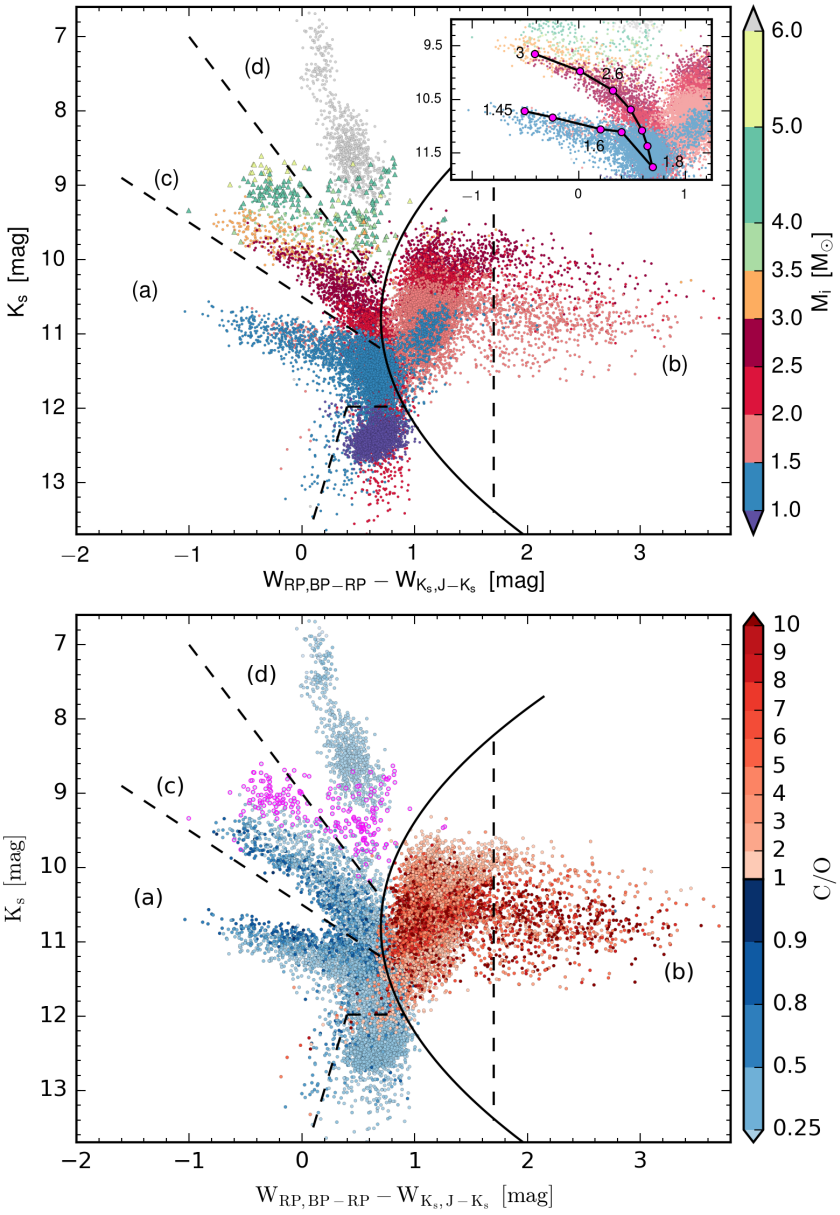


**Figure 5.6:** Synthetic $W_{RP} - W_{JK}$ vs. $K_s$ diagrams of the LMC `TRILEGAL` simulation. The simulated stars are colour-coded according to their predicted initial masses (top panel) and their C/O ratio (bottom panel). In the inset, the curve connects the stages immediately before stars turn to C-stars at varying initial mass in the range from 1.45 to 3 $M_\odot$ for $Z_i$=0.006. AGB stars with HBB are marked with triangles in the left panel and with magenta circles in the right panel. Adapted from Lebzelter et al. (2018).

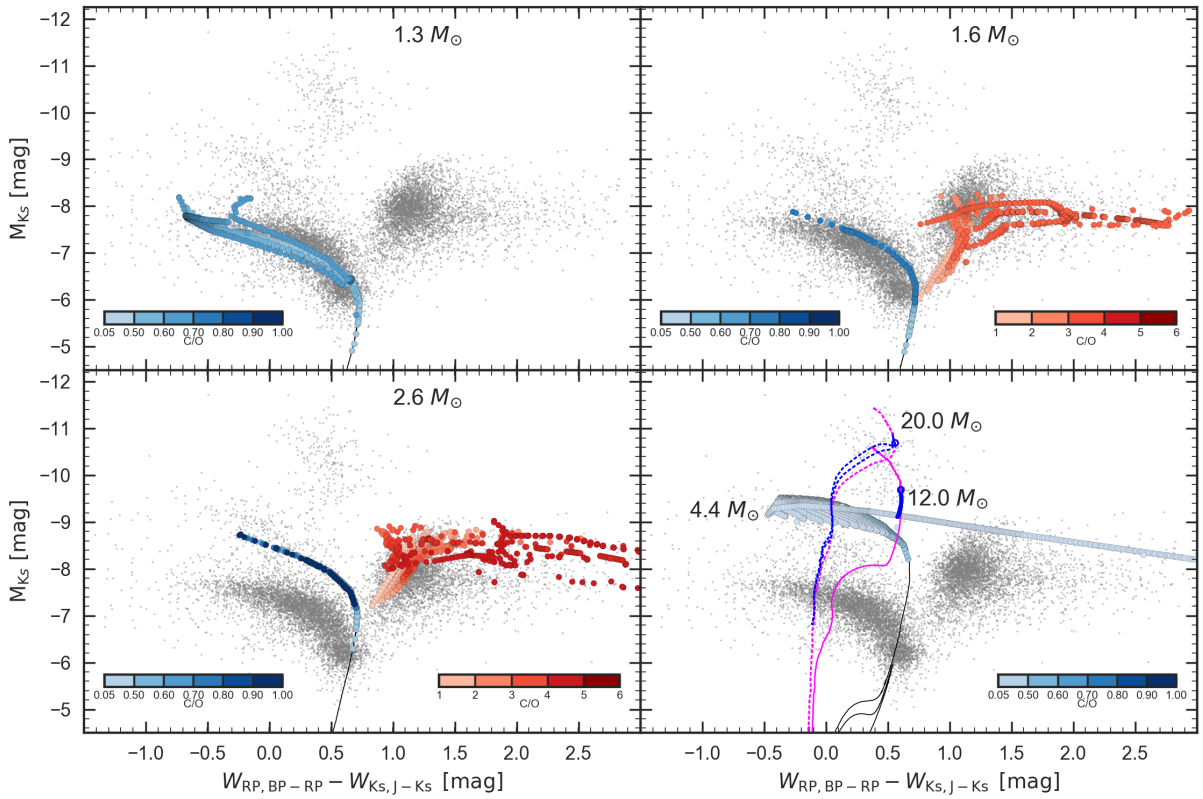


**Figure 5.7:** $W_{RP} - W_{JK}$ vs. $K_s$ diagram of the Gaia data with evolutionary tracks of initial masses 1.3, 1.6, 2.6, and 4.4 $M_\odot$and $Z_i$=0.006, and 12 and 20 $M_\odot$with $Z_i$=0.008. TP-AGB tracks are color-coded according to the C/O ratio. The massive stars tracks include part of the H-shell burning phase, the core-helium burning phase in blue (the blue loop is visible for the 20 $M_\odot$models), and the stages before the carbon ignition in the core. Adapted from Lebzelter et al. (2018).

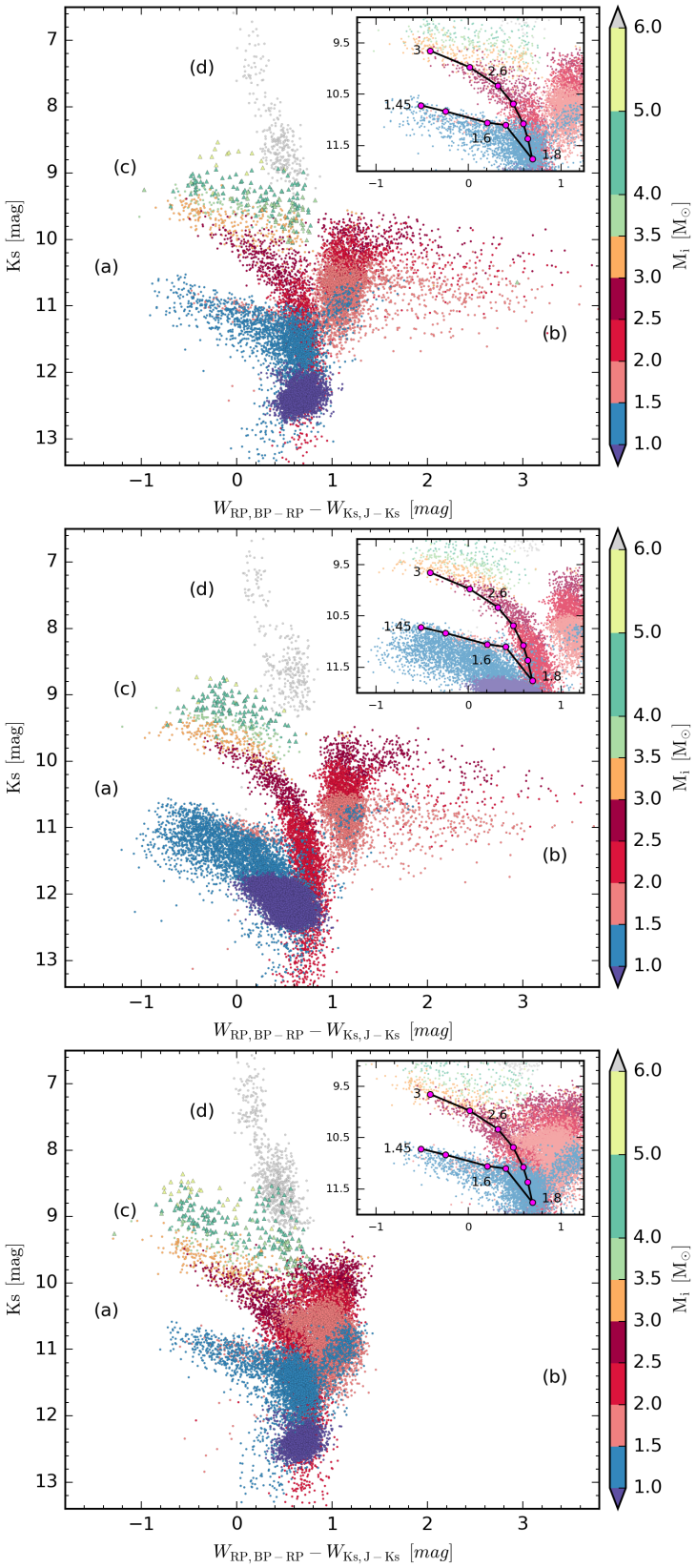


**Figure 5.8:** Same as left panel of Fig. 5.6 but for a constant SFH and the HZ09 AMR (top panel), a constant SFH and a constant metallicity of 0.006 (middle panel), SFH as in HZ09 but not taking into account the effect of circumstellar reddening by dust (bottom panel).

## 5.3 LSST simulation

The Large Synoptic Survey Telescope is a wide-field survey facility that will be operational starting from January 2022 for ten years. LSST main survey will cover the southern sky ($\approx$ 18000 deg$^2$) in 6 filters (*ugrizy*). The 90 per cent of the telescope time has already been allocated for the main survey, while the remaining 10 per cent will be used for special focused surveys (mini-surveys and Deep-Drilling Fields).

As a Junior member of the LSST team headed by L. Girardi (PI), and member of the LSST "Stars, Milky Way and Local Volume Science Collaboration", I am currently producing stellar population synthesis simulations of the Magellanic Clouds. These simulations, together with all-sky simulations of the Milky Way will be available to the community with the aim of helping to define the observing strategy for the mini-surveys.

We recently performed a first run of the complete Milky Way simulations, including the Magellanic Clouds. The MW simulations are performed using the Hierarchical Equal Area Iso Latitude pixelisation of the sphere (HEALPix) nesting scheme with a resolution of about 0.21 deg$^2$. For the MCs simulations I adopted the spatial resolution given by the respectively space-resolved SFH. I then add random sky coordinates within each simulated region. Finally, according to the same HEALPix resolution adopted for the MW, I assign the corresponding HEALPix index to all simulated stars of the MCs. All simulations are complete down to r=27.5 mag. The LMC is modelled according to the HZ09 SFH as already explained in previous sections. As for the SMC, I use the results of R18 for the available regions. Since there is a portion of the SMC that has not been analysed by R18, I used the SFH solutions to obtain the SFH of such regions by extrapolation. Figure 5.9 shows the density stellar maps of the MCs as obtained for a test shallow simulation.

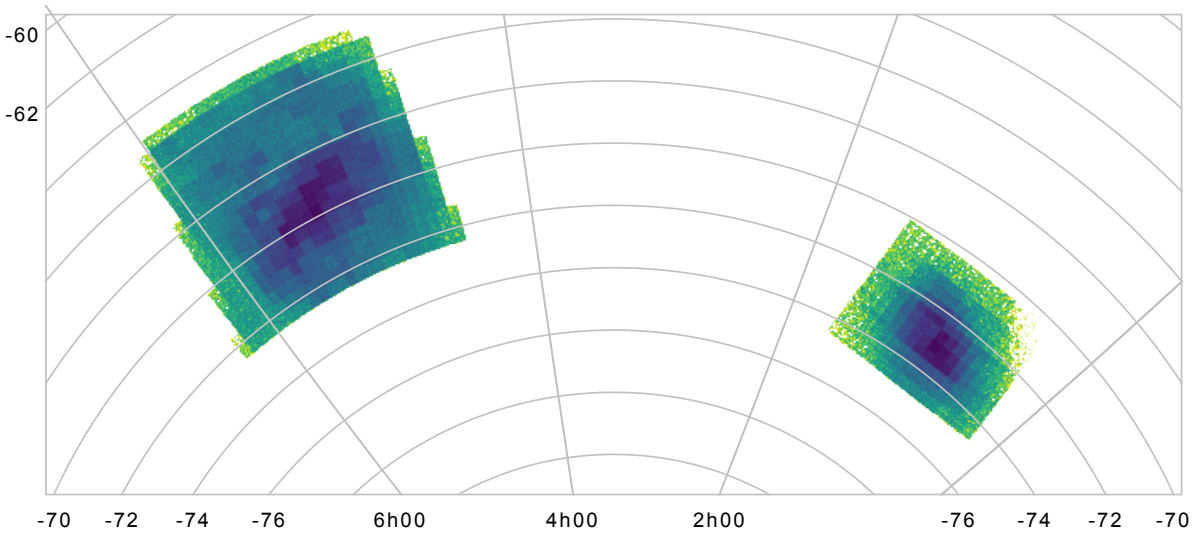


**Figure 5.9:** Stellar density maps of the LMC (left) and (SMC) obtained with a shallow simulation (only stars brighter than 16 in the $K_s$-band). The map is in equatorial coordinates with the Right Ascension and the declination expressed in hours and degrees respectively.

As a result of the first run, we found that the total number of stars in the sky region accessible to LSST is of about 19 billions stars, down to the $r < 27.5$ mag limit of co-added images from the main survey. $1.6 \cdot 10^8$ and $6 \cdot 10^8$ stars are expected for the SMC and LMC, respectively. However, these estimates do not take into account the crowding limit, that is, the fact that in some regions of the sky the stellar density is so high that the PSF photometry becomes unreliable for all stars fainter than a given brightness. To estimate this limit, we follow the formalism by Olsen et al. (2003), which uses the

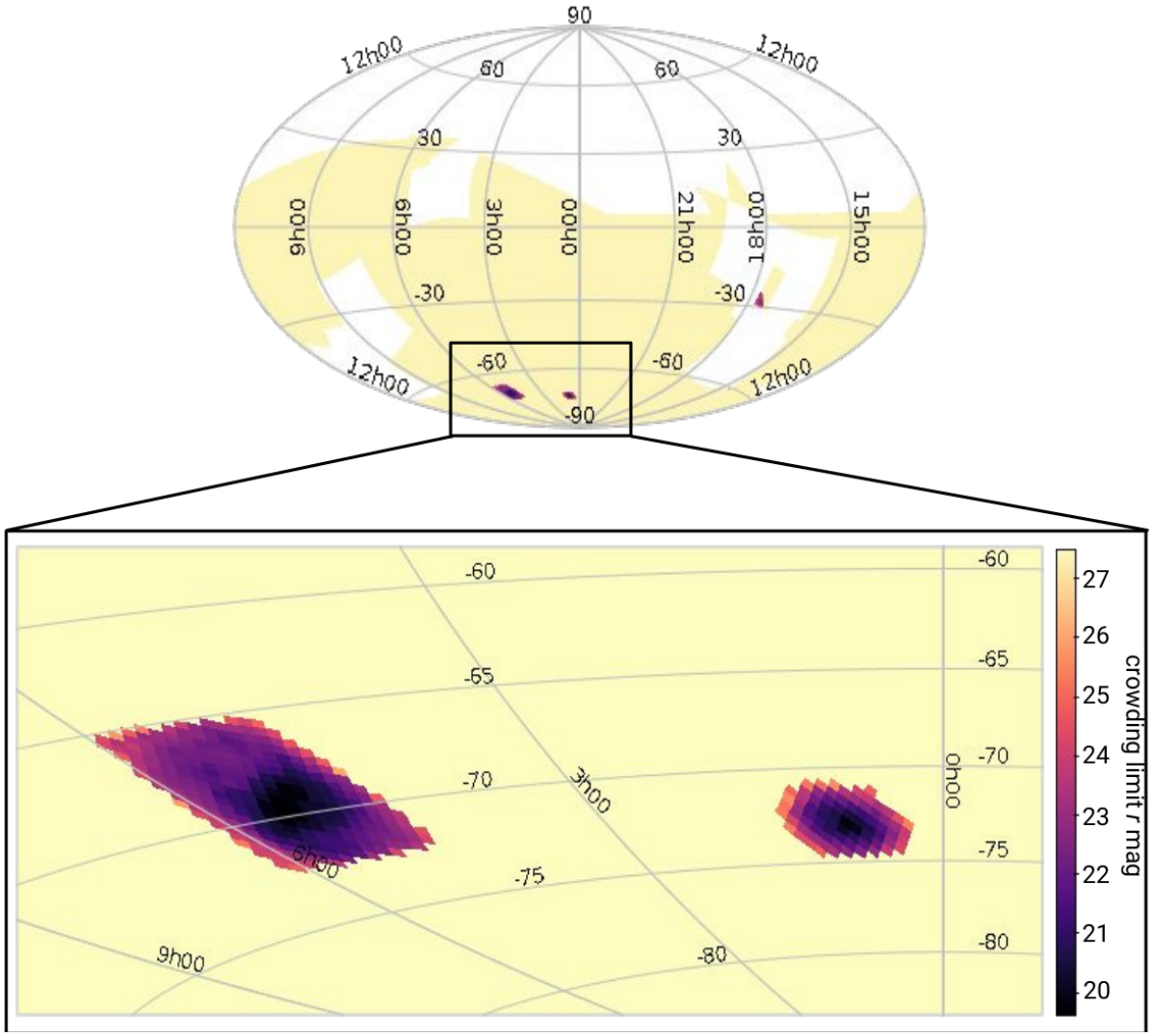


**Figure 5.10:** All sky representation of the MW simulation and the MCs. The pixel areas are color-coded according to expected crowding limit in the $r$-band. The analysis is still on-going for the regions in white. In the zoomed region around MCs we can see that the expected crowding limit reaches $r_{\rm crowd}$=20 mag in the very central regions.

computed luminosity function of faint stars to return the magnitude level $r_{\rm crowd}$ at which photometric errors due to crowding are larger than a given threshold (set to 0.1 mag, in our case). A seeing of 0.6 arcsec was assumed. This analysis is still ongoing for the MW disk and bulge. Results for the LMC and SMC main bodies are ready and and can be appreciated in Figure 5.10.

In the very central regions of the MCs, the actual limiting magnitude is predicted to be around 20 mag in the $r$-band. By looking at the CMDs of the Clouds shown in Figure 5.11, we expect that even in the most crowded regions LSST will be able to resolve a large fraction of the stellar populations of the MCs, including the Red Clump and part of the Main Sequence. We can also see that the Milky Way foreground contamination will not mix with the TP-AGB population in the $g-r$ vs. $r$ diagram, especially for the redder source.

The present catalogues for the MCs do not include the post-AGB stars, but they will be included in the next run together with the latest version of TP-AGB models calibrated in the SMC.

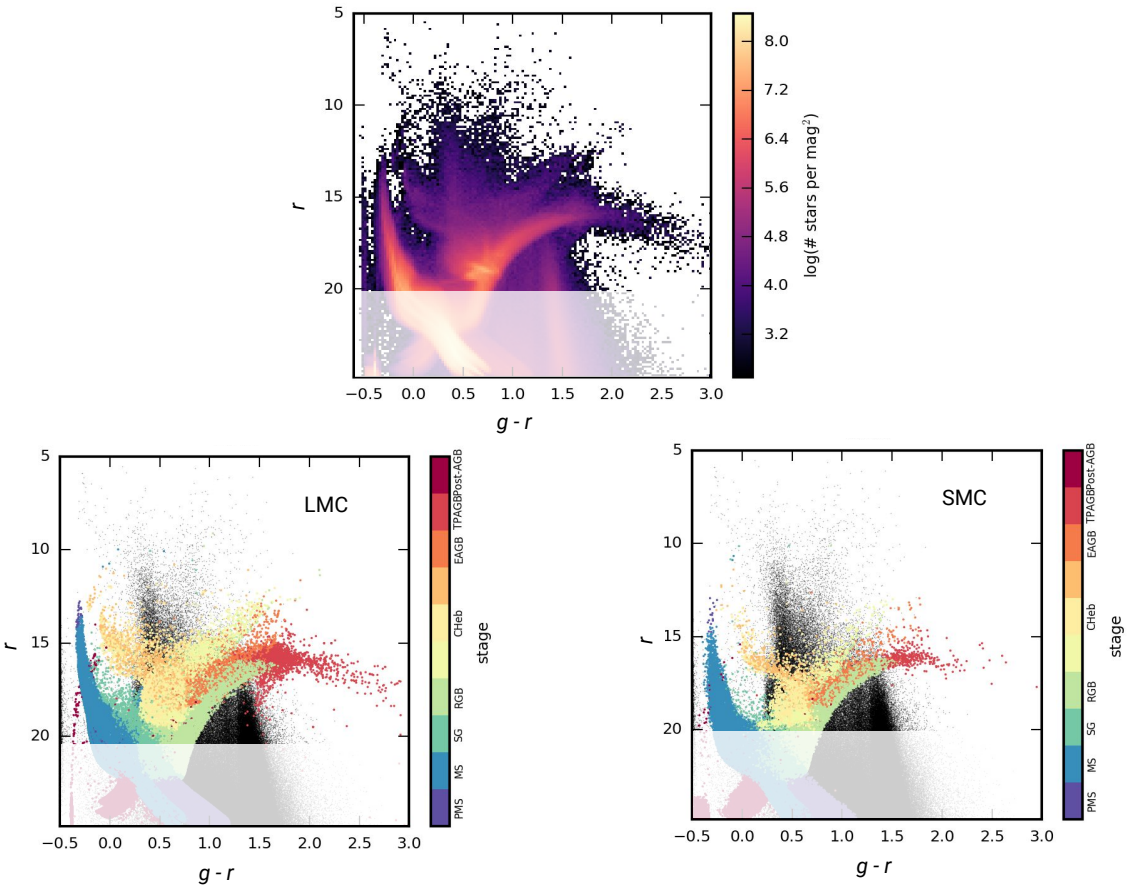


**Figure 5.11:** Top panel: $g - r$ vs. $r$ Hess diagram of the Magellanic Clouds and the Milky Way. Bottom panels: $g - r$ vs. $r$ CMDs of the LMC and SMC with stars colour-coded according to their evolutionary stage. The Milky Way foreground is shown with black dots in the background to show the MCs populations.

These synthetic catalogues will be available to the community through the NOAO Data Lab (`https://datalab.noao.edu/`) and will contain the photometry in the LSST and Gaia filters, the sky coordinates, all the relevant stellar parameters (mass, luminosity, effective temperature, surface composition etc.) and the kinematic information (proper motions, radial velocities) for the MW stars.

The project indeed aims to simulate all stellar types and properties that will be relevant in future LSST catalogues, including the time-series information. We are currently working on implementing the results of Trabucchi et al., (in prep.) to add the information on the periods for Long Period Variables. We are also improving the description of binary populations (P. Dal Tio et al., in prep.).

## 5.4 Preliminary results for Local Dwarf galaxies

This section presents a preliminary comparison between our calibrated models and the resolved populations of AGB stars observed in dwarf galaxies mainly in the Local Group. The identification of AGB stars in such systems has been carried out within the DUSTiNGS (DUST in Nearby Galaxies with Spitzer) program by Martha Boyer. A HST follow-up for six of these galaxies allowed to photometrically distinguish the population of C-rich and O-rich AGB stars. I simulated two galaxies of these samples using the SFHs derived from HST data by Weisz et al. (2014) and the best-fitting model S_35 for the SMC. A discussion of some preliminary results is given in Section 5.4.2.

### 5.4.1 Observations of DUSTiNGs galaxies

The DUSTiNGS imaging survey observed 50 nearby dwarf galaxies in the [3.6] and [4.5] *Spitzer* filters with the aim of identifying dust-producing AGB stars and massive stars (Boyer et al., 2015c). A total of 526 dusty variable AGB stars have been identified. The stars corresponds to the so-called extreme AGB stars and their [3.6]-[4.5] colour is redder than 0.1 mag (Boyer et al., 2015b). Studying the AGB population of these galaxies is important to address some open questions mainly related to the metallicity dependence of the dust production. The metallicity of the DUSTiNGS galaxies is in the range $-2.7 <$ [Fe/H] $< -1.1$ and a large fraction of the identified AGB stars are in the systems with very low metallicity (111 in galaxies with [Fe/H] $< -1.5$ and 12 in galaxies with [Fe/H] $< -2.0$). The inclusion of these AGB populations in the on-going calibration of TP-AGB models would expand the metallicity range covered. However, the AGB catalogues are not complete, most targets suffer from crowding effects and the classification is not as accurate as in the Magellanic Clouds, making a detailed calibration a non trivial task. With respect to AGB classification, a recent follow-up of six DUSTiNGS targets has been carried out with the WFC3/IR on the Hubble Space Telescope. Boyer et al. (2017) used a combination of filters (F127M, F139M, and F153M) that are able to distinguish the C-rich stars from the O-rich stars. Even if a a comparison between the predicted and observed number counts is not straightforward, the results of this work can be used to investigate the performance of the TP-AGB models calibrated in the SMC in terms of C/M ratio and circumstellar dust prescriptions.

The use of the HST WFC3/IR medium-band filters to distinguish C- and M-stars has been demonstrated by Boyer et al. (2013) in a field of the M31 disk. As shown in Figure 5.12 the filters F127M, F139M, and F153M fall the $H_2O$ and CN+$C_2$ features at 1.2–1.5 $\mu$m. The net separation between the two spectral types results in a minimal cross-contamination when C-stars and M-stars are identified. Indeed, by using the predicted colours of C-rich (Aringer et al., 2009), O-rich stars and K-giants (Aringer et al., 2016),

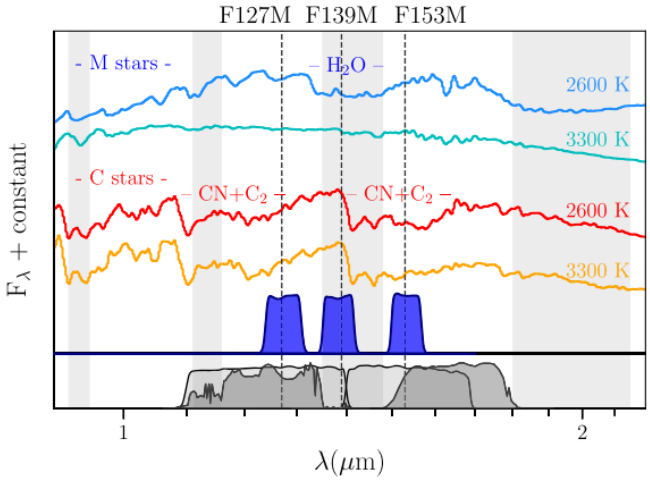


**Figure 5.12:** WFC3/IR medium-band filters that sample the water feature in M-stars and the CN+C2 feature in C-stars. Model spectra from Aringer et al. (2009, 2016) are shown, in addition to the 2MASS filters J and H (dark grey) and the WFC3/IR F125W and F160W filters (light gray). Figure from Boyer et al. (2017).

Boyer et al. (2013, 2017) showed that C- and M-type stars are clearly distinguishable in the F127M - F139M vs. F139M - F153M CCD (see Fig. 5.13). The picture is somewhat complicated by the effects of the circumstellar dust, that need to taken into account as most of the DUSTiNGS AGB stars are severely obscured.

The HST follow-up includes six star-forming DUSTiNGS galaxies, namely NGC 147, IC 10, Pegasus dIrr, Sextans B, Sextans A, and Sag DIG. The number of identified AGB stars in these objects increased by a factor of 2. Interestingly, 26 dusty M-stars have been identified and most of them are hosted in IC10.

The identification and classification of AGB stars is fully described by Boyer et al. (2017). Here, I mention the relevant aspects of the classification as some of the criteria will be used to select the AGB stars in the synthetic catalogues. They started by selecting all stars brighter than the Tip of the RGB in the F153M filter. This subsample does not contain the dustiest AGB stars that are fainter than the Tip of the RGB due to the circumstellar dust extinction. From this subsample, C-rich stars and M-stars can be identified on the basis of their location in the F127M - F139M vs. F139M - F153M CCD following the lines reported in Figure 5.13. However, Boyer et al. (2017) found that the data are slightly redder than both C- and O-rich models. This discrepancy does not affect the classification of C-stars, whereas the O-rich AGB sample can be contaminated by K-giants. However, the O-rich AGB stars can be separated using the position of the knee shown Figure 5.13. To recover the dustiest AGB stars, they used the *Spitzer* photometry. The [3.6]–[4.5] colour is used as a proxy for dust excess. They compare the colour of a source with the mean colour of the stars within 1 mag bin in the [4.5] filter and they marked the source as dusty-AGB if this excess is larger than $4\sigma$. Finally, if the candidate dusty-AGB sources are brighter than the Tip of the RGB in the [3.6] filter, they are included in the final catalogue.

### 5.4.2 Modelling DUSTiNGS galaxies

I selected as first objects to be simulated IC10, which is the most massive galaxy in the sample, and Sextans A, one of the most metal-poor. The Star Formation History of 40 Local Group dwarf galaxies has been recently derived by Weisz et al. (2014) through a CMD fitting technique applied to archival HST photometry. The HST photometry do not

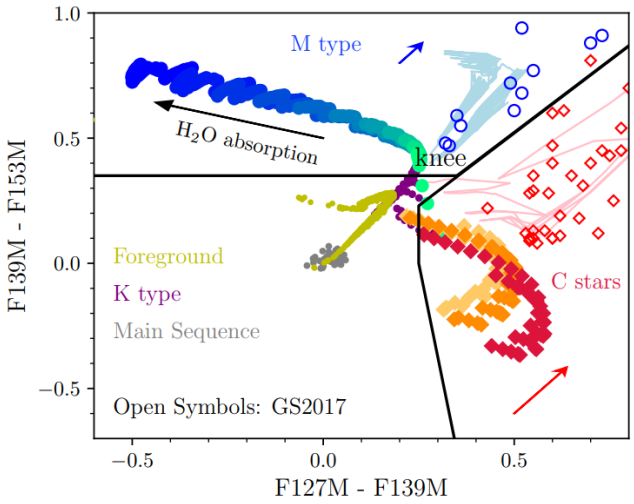


**Figure 5.13:** HST F127M - F139M vs. F139M - F153M CCD showing the sequence of C-star models by Aringer et al. (2009) with orange/red filled diamonds and the sequence of M/K-star models from Aringer et al. (2016) with purple (K-giants), cyan/blue (M-stars) filled circles. Simulated foreground stars from a TRILEGAL realisation are shown in yellow, in addition to a sample of main sequence stars of IC10 (grey dots). The black lines mark the separation between M- and C-stars. Dusty M- and C- stars in the LMC from Groenewegen and Sloan (2018a) are shown with open circles and diamonds, respectively. TRILEGAL isochrones computed with the TP-AGB tracks described in Marigo et al. (2017) are also shown for O-rich (blue) and C-rich (red) stars. Figure from Boyer et al. (2017)

reach the oldest MS turn-off point, but even if this is crucial to obtain a robust estimate of the ages they showed that their derivation is accurate enough when compared to the results obtained with deeper CMDs. The SFHs of IC10 and Sextans A (Weisz, priv. comm.) are shown in Figure. 5.14.

In the TRILEGAL simulations I adopted the distance and the $A_V$-extinction values as reported in Weisz et al. (2014) and Boyer et al. (2017). The extinction of Sextans A is $A_V = 0.12$ mag, whereas IC10 has a higher extinction, $A_V = 2.33$ mag. The distance values are 0.77 and 1.46 Mpc for IC10 and Sextans A respectively. The adopted total stellar mass in stars are $\approx 83$ and $22 \cdot 10^6$ $M_\odot$for IC10 and Sextans A.

The input prescriptions for the TP-AGB models are the same as the best-fitting model S_35 and the same dust bolometric corrections are adopted.

The AGB stars in the simulations are selected according to their evolutionary stage and to be brighter than the Tip of the RGB, but given the criteria adopted by Boyer et al. (2017) I also include the dustiest C-rich stars that are fainter then Tip of the RGB in the F153M filter. The O-rich and C-rich stars are identified with the predicted C/O ratio.

The results of the simulations are compared to the observations in Figure 5.15.

Our models confirm the net separation between C-rich and O-rich stars in both galaxies. There is a fairly good agreement in the location of the sequences also for the K-giants. Since the galaxy regions analysed by Weisz et al. (2014) and Boyer et al. (2017) are not the same, a direct comparison with the predicted stars counts and the observed ones cannot be performed. However, it is possible to compare the C/M ratio. It is worth recalling that, a slight shift in the division line between M- and K-type giants strongly affects the C/M ratio. As for the IC10, the predicted C/O ratio is slightly higher but satisfactorily similar to the observed one. The C/M ratio predicted for the AGB population of Sextans A is much lower than the observed one. Besides the already mentioned caveats, i.e. different galaxy regions sampled and the uncertain M-/K-stars separation, the low number statistic of Sextans A could also play a role. In addition, these preliminary TRILEGAL

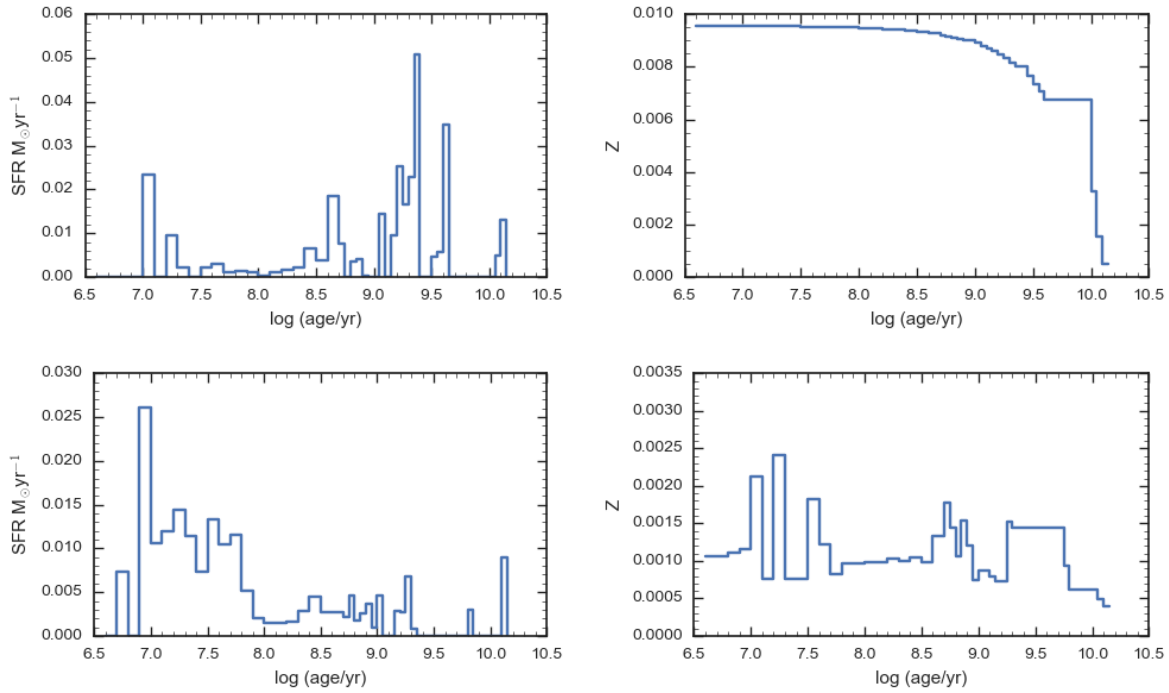


**Figure 5.14:** SFR(t) and AMR of IC10 and Sextans A as derived by Weisz et al. (2014).

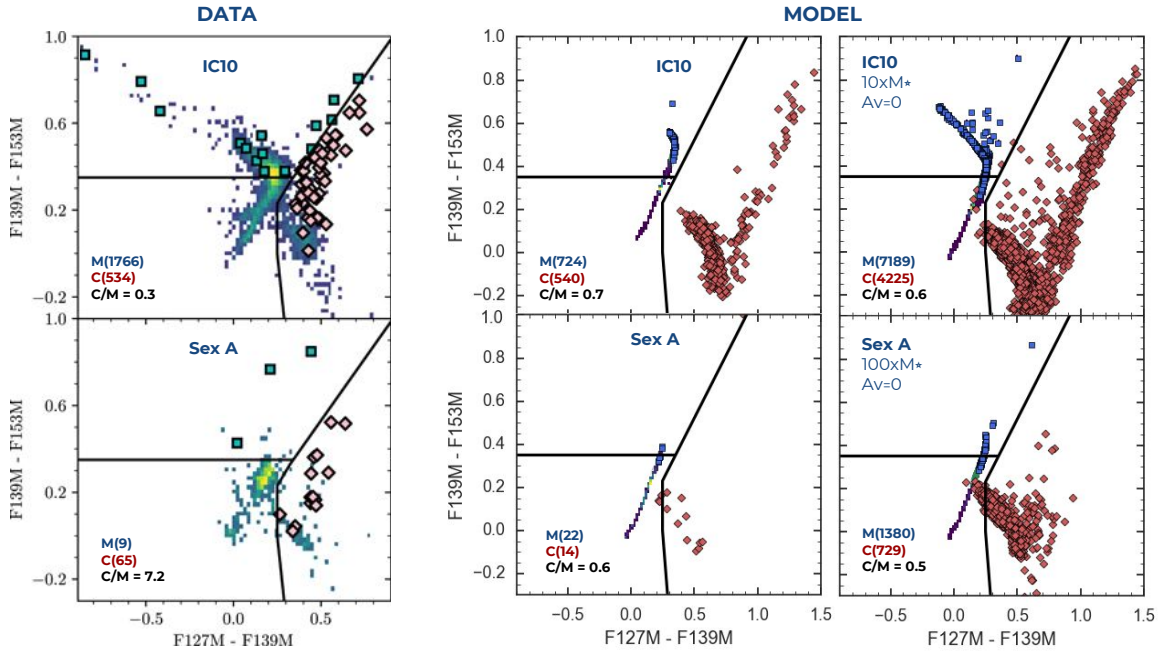


**Figure 5.15:** Left panel: HST CCD for IC10 and Sextans A reproduced from Boyer et al. (2017). The solid lines mark the adopted criteria to identify AGB stars and to separate C-rich and O-rich stars. Cyan squares and pink diamonds mark the dusty O- and C-rich stars, respectively, identified through their *Spitzer* colours. Middle and right panels: `TRILEGAL`simulations of IC10 and Sextans A. Blue squares and red diamonds identify the O-rich stars and C-rich stars, that are selected according to the predicted C/O ratio. The number of M- and C-stars in addition to the C/M ratio are indicated. The details of the simulations are explained in the text.

simulations do not account for incompleteness due to crowding and photometric errors. It also evident that the simulations do not predicted O-rich stars bluer than F127M - F139M in both galaxies. This can be the result of the applied dust bolometric corrections or can be due to the derived SFH. Indeed, from Figure 5.14 one can notice the for both galaxies, there is a minimum in the rate of star formation around $\log(t/yr) \approx 8$, i.e. 0.1 Gyr, more marked for IC10, and around $\log(t/yr) \approx 9$, i.e. 1 Gyr. In addition, the star formation rate between $\log(t/yr) \approx 9.5 - 9.6$ and $\approx 10$ is essentially zero. These age ranges corresponds to the ages of the more massive O-rich stars and to the low-mass C-rich and O-rich stars.

To investigate the effect of the SFH, I calculated a `TRILEGAL` simulation using a constant SFR for both galaxies. The AMR used is from Weisz et al. (2014). For both simulations I also set the extinction to zero and I increase the total mass in stars of a factor of 10 and 100 for IC10 and Sextans A respectively. The results are shown in the right panel of Figure 5.14. First, the sequence of O-rich stars now extends to bluer colours and a few massive O-rich stars populate the region close to the separation line from C-stars, i.e. F127M - F139M $\gtrsim 0.2$ and F139M - F153M $\gtrsim 0.5$. In addition, synthetic C-stars now appear in the region F127M - F139M $\approx 0.3 - 0.8$ and F139M - F153M $\approx 0.0 - 0.5$. The same considerations are true for Sextans A.

As for the sequence of synthetic C-rich stars, the reddest sources show F127M - F139M colours redder than the observations. By testing different dust mixtures and different tables of dust bolometric corrections such trend does not show any variations. The tests clearly show that prior to infer any possible conclusion about the performance of TP-AGB models in these systems, it is necessary to assess the accuracy of the SFH and more importantly the comparison between observed AGB stars and models should be performed using a SFH representative of the observed TP-AGB population. Once these issues are addressed, it will be possible to use these observations to put quantitative constraints on TP-AGB models and circumstellar dust models.

# Chapter 6

# Conclusions and Future Perspectives

The purpose of this Thesis is to provide a physically-sound calibration of the TP-AGB uncertain processes of mass-loss and third dredge-up. In the context of the ERC-STARKEY project, this task is accomplished using a global calibration method that relies on the the integration of the state-of-the art theoretical components, accounting for the complex physics of AGB stars, and accurate observations of AGB stars in the Small Magellanic Cloud.

A crucial ingredient of the calibration is the spatially-resolved star formation history of the SMC galaxy, which was initially derived by Rubele et al. (2015) using the deep near infrared photometry of the VMC survey. The SFH recovery was based on the CMD-reconstruction method applied to the stellar populations below the Tip of the RGB. The final outcomes of the method are the best-fitting values of star formation rate, age-metallicity relation, distance and extinction for more than one hundred regions across the SMC. However, a careful analysis of the solutions revealed non negligible discrepancies between the observations and best-fitting models, which would have hampered the accuracy of the TP-AGB calibration. For this reason, at the beginning of my PhD work I investigate the possible causes of such shortcomings, which were identified in a likely offset of the $Y$-band photometry of VMC and in the use of an earlier version of the `PARSEC` evolutionary tracks. To handle the above issues we act at various levels, first adopting the latest version of the stellar evolution models and improving the SFH technique, and then re-deriving the SFH of the SMC, including additional VMC regions (Rubele et al., 2018). The best-fitting solutions of the new SFH recovery give a robust description of the SMC stellar populations below the tip of the RGB, thus providing a more reliable starting point for the TP-AGB calibration.

The second fundamental dataset for this work consists of the catalogues that contain the complete census of AGB stars in the SMC (Boyer et al., 2011; Srinivasan et al., 2016). These observations are based on the infrared photometry of 2MASS and *Spitzer* and allowed the authors to identify and classify the AGB population in three main classes: i) O-rich stars, ii) C-rich stars, and iii) extreme-AGB stars.

Taking advantage of the AGB classification and the space-resolved SFH of the SMC, I performed detailed simulations of the AGB population of the SMC using the `TRILEGAL` code (Girardi et al., 2005). `TRILEGAL` includes all the necessary ingredients to convert model quantities in observational properties, i.e. the synthetic photometry in the relevant passbands. In particular the bolometric corrections for the cool giant stars are calculated from the stellar atmosphere models of Aringer et al. (2009) for C-stars and Aringer et al. (2016) for O-rich stars. The reprocessing of the radiation due to the circumstellar dust in mass-losing stars is taken into account using a revised version of the approach of Marigo et al. (2008). One of the main improvements is the calculation of the carbon

dust condensation factor using fitting relations derived from the same set of dynamical models of C-stars used to predict the mass-loss in the dust-driven regime (Mattsson et al., 2010; Eriksson et al., 2014). The TP-AGB tracks are computed with the COLIBRI code (Marigo et al., 2013). A key feature of COLIBRI is the fast computation of large grids of TP-AGB stellar models for several combinations of input prescriptions, mainly related to the mass-loss and the 3DU. The computational agility does not compromise the level of physical accuracy in the treatment of the envelope and atmospheric structures. Main points of strength refer to the on-the-fly solution of the equation of state for 500 atoms and 300 molecules, together with the gas opacities, and the integration of complete nuclear networks (relevant for the HBB and the pulse-driven nucleosynthesis). Importantly, most of the details of the TP-AGB evolutionary tracks are also maintained in the TRILEGAL isochrones that are the backbone of the population synthesis simulations (Marigo et al., 2017).

Given the uncertainties on the theoretical side, we adopt the mass-loss and third dredge-up as main free parameters . For both processes various prescriptions are tested along the calibration cycle. The final goal is to reproduce the observed number counts and the luminosity functions in the $K_{\rm s}$-band for the entire AGB star sample, as well as for the three AGB star subclasses at the same time.

Starting from the TP-AGB evolutionary tracks calibrated by Rosenfield et al. (2016), a first series of models is computed in the light of the discrepancies identified between observations and predictions. These models are constructed to explore the effect of the mass-loss and the impact of its efficiency on the population of O-rich, C-rich and extreme AGB stars. All TP-AGB models include a prescription for the "pre-dust" phase and specific mass-loss prescriptions for the dust-driven wind according to the chemical type of the stars. A novelty applies to the C-star class for which a mass-loss recipe based on the results of dynamical atmospheres for pulsating C-stars (Mattsson et al., 2010; Eriksson et al., 2014) is implemented.

The best-fitting model of this first series is able to match our requirements and give an excellent reproduction of the infrared CMDs of the SMC. The input prescription for the "pre-dust" mass-loss rate follows the Cranmer and Saar (2011) formalism and the results confirm the importance of the pre-dust mass-loss for low-mass, low-metallicity O-rich stars (Rosenfield et al., 2014, 2016). The Bloecker (1995) formalism for O-rich stars is coupled with the results of dynamical models for C-stars (Mattsson et al., 2010; Eriksson et al., 2014). The best-fitting model has a very high mass-loss efficiency ($\eta = 0.06$) for the O-rich stars. These models predict a maximum initial mass for the C-star formation which is around 2.6 $M_{\odot}$ for $Z_{\rm i} = 0.004$.

Given the extreme assumptions of this set of model, in particular the high efficiency of dust-driven winds in O-rich stars, and the heterogeneous predictions of the 3DU properties described in the literature , a second series of models is computed to explore the effect of the efficiency and the onset of the 3DU, in combination with a reduced efficiency of mass loss for O-rich stars. From this extensive study – more than 20 sets of TP-AGB tracks are computed – we derive important indications on the efficiency of the 3DU in the most massive C-rich stars. The 3DU parametrisation originally implemented in COLIBRI is based on the formalism suggested by Karakas et al. (2002) to reproduce the results of their full TP-AGB models. In that formalism the efficiency $\lambda$ is quite high and reaches values close to unity in all models with $M_{\rm i} \gtrsim 3M_{\odot}$. In the second series of models we relax the prescription by Karakas et al. (2002) and introduce a new parametrisation. The new formalism, inspired from the results of complete TP-AGB models (e.g. Ritter et al., 2018; Cristallo et al., 2015; Ventura and D'Antona, 2009; Herwig, 2004), keeps the necessary flexibility, through the adoption of free parameters, to perform our calibration.

The behaviour of $\lambda$ during the TP-AGB evolution of a given star is such that the initial increase of $\lambda$, as a consequence of the strengthening of the thermal pulses, is followed by a decrease due to the reduction of the envelope mass, until the 3DU is eventually quenched.

We vary the free parameters of the new 3DU formalism until we single out a second best-fitting model that performs as well as the first one in terms of the photometric properties, but it is in better agreement with the semi-empirical IFMRs. Indeed, the mass-loss efficiency for O-rich stars is lower, i.e. $\eta = 0.03$, and the efficiency of the 3DU of the more massive TP-AGB stars, i.e. $M_{\rm i} \gtrsim 3\ M_{\odot}$is significantly lower with respect to Karakas et al. (2002). The predicted range of initial masses of stars able to become C-rich is comparable to that of the first best-fitting model, but very different from the starting model in which C-stars cover larger initial masses ($M_{\rm i} \gtrsim 3M_{\odot}$). Interestingly, the present results are in line with the maximum initial mass for C-stars as derived from Magellanic Clouds' star clusters.

Using the synthetic simulations of this second best-fitting model, I present a characterisation of the AGB population in the SMC in terms of stellar parameters. The predicted mass-loss rates for O-rich and C-rich stars are in agreement with mass-loss rates estimates derived from spectral energy distributions of SMC stars (Nanni et al., 2018; Groenewegen and Sloan, 2018b; Goldman et al., 2018). An additional interesting result that emerges from this work is the photometric hint for the dependence of the mixing-length parameter on the luminosity. The comparison between the observed and synthetic sequences of RSG and AGB revealed a shift towards the red in the $J-K_{\rm s}$ colour that depends on the luminosity. To correct this discrepancy we compute a set of TP-AGB tracks in which the mixing length parameter increases with the luminosity. The comparison of the colour distributions of AGB stars in the SMC shows a remarkable improvement, which is also supported by a better reproduction of the slope of the fundamental-mode pulsators in the period-luminosity sequences of long period variables.

The calibrated models will be publicly available in the form of stellar isochrones and will be eventually included in population syntheses models. Although the present calibration involves TP-AGB models of SMC metallicities ($0.001 \lesssim Z \lesssim 0.004$), complete set of TP-AGB tracks are computed for all metallicities present in the original `PARSEC` v1.2S database, spanning the range $0.0001 < Z < 0.06$ ($-2.2 <$ [Fe/H] $< +0.7$). Extended `PARSEC+COLIBRI` isochrones derived from these tracks will be available from our web interfaces[1], for over 50 different photometric systems including major photometric surveys and instruments (e.g. 2MASS, SDSS, Spitzer, AKARI, HST/ACS, HST/WFC3, WISE, VISTA, Gaia, TESS), and future datasets (e.g. JWST, LSST, Euclid).

In the final part of my PhD thesis I discuss the synthetic AGB population for additional nearby galaxies. The first work applies to the LMC (Trabucchi et al., 2017). My contribution is to provide the LMC simulations in the Gaia and 2MASS photometric passbands. These simulations, based on the TP-AGB tracks calibrated in the SMC, guide the interpretation of a new observational diagram that combines the optical and infrared Wesenheit indexes. Such diagram is an excellent tool to distinguish the evolutionary stages of the evolved population of the LMC, in addition to discriminate the initial stellar masses and the chemical types. As a Junior member of the LSST "Stars, Milky Way and Local Volume Science Collaboration" I produce synthetic catalogues of the Magellanic Clouds in the Gaia and LSST filters. The simulations include `COLIBRI` TP-AGB tracks and will be available to the community to help in the mini-surveys observing strategy. Finally, I present some preliminary results about the simulations of AGB populations in Local Group dwarf galaxies, in particular for a few galaxies observed by the *Spitzer* DUSTiNGS program, in which C-rich and O-rich stars were photometrically

[1] `http://starkey.astro.unipd.it/cmd` and `http://stev.oapd.inaf.it/cmd`

classified using medium-band HST filters (Boyer et al., 2017). By using the SFH derived by Weisz et al. (2014) I simulate two of the six galaxies studied by Boyer et al. (2017), namely IC10, the most massive, and Sextans A, one of the more metal-poor. The models confirm the net separation between C-rich and O-rich stars in the HST CCD as proposed by Boyer et al. (2017). However, further steps need to be undertaken in a follow-up work, namely to address some non-trivial crowding effects, and to account for the different areas sampled by the HST archival photometry – from which the SFH has been derived –, and the Spitzer/HST photometry used to identify AGB stars.

As demonstrated for the SMC, a reliable calibration of TP-AGB models is feasible, provided detailed information of the SFH and AGB classification is available. Keeping this point in mind, I plan to extend the calibration of our TP-AGB models to the other nearby systems. The next object will be the Large Magellanic Cloud for which the same kind of data for the AGB stars as in the SMC are already available (Boyer et al., 2011; Riebel et al., 2010). The derivation of the space-resolved SFH based on the VMC photometry is currently underway.

The calibration carried out in this Thesis relies essentially on photometric data. However, additional observational constraints are available, i.e. pulsation periods, dust mass-loss rates, expansion velocities of dusty envelopes, that can be included in the calibration procedure. The results of linear pulsation models from Trabucchi et al. (2017, and in prep.) are being implemented in `TRILEGAL` to be routinely used in the population synthesis simulations. This is an important step-forward since precise measurements of pulsation periods are available for the AGB populations of the Magellanic Clouds and the quality and quantity of the data will greatly improve with future observing facilities as LSST.

I also plan to investigate further the case of a luminosity-dependent mixing length parameter. Additional interesting studies may be performed on the *Gaia* long period variables. We plan to extend the analysis to the SMC and Sagittarius, using the new diagram described in Lebzelter et al. (2018), and to investigate possible metallicity-dependant effects. As for the LSST simulations, the calibrated TP-AGB models will be included in the next simulations run together with the revised version of dust bolometric corrections based on Marigo et al. (2008). Finally, we will focus our analysis on the DUSTiNGS galaxies. By properly considering these systems, we will be able to push the TP-AGB calibration down to very low metallicities.

# Bibliography


Alcock, C., Axelrod, T. S., Bennett, D. P., Cook, K. H., Park, H. S., Griest, K., Perlmutter, S., Stubbs, C. W., Freeman, K. C., and Peterson, B. A. (1992). The search for massive compact halo objects with a (semi) robotic telescope. In Filippenko, A. V., editor, *Robotic Telescopes in the 1990s*, volume 34 of *Astronomical Society of the Pacific Conference Series*, pages 193–202.

Alongi, M., Bertelli, G., Bressan, A., and Chiosi, C. (1991). Effects of envelope overshoot on stellar models. *A&A*, 244:95–106.

Aringer, B., Girardi, L., Nowotny, W., Marigo, P., and Bressan, A. (2016). Synthetic photometry for M and K giants and stellar evolution: hydrostatic dust-free model atmospheres and chemical abundances. *MNRAS*, 457:3611–3628.

Aringer, B., Girardi, L., Nowotny, W., Marigo, P., and Lederer, M. T. (2009). Synthetic photometry for carbon rich giants. I. Hydrostatic dust-free models. *A&A*, 503:913–928.

Badnell, N. R., Bautista, M. A., Butler, K., Delahaye, F., Mendoza, C., Palmeri, P., Zeippen, C. J., and Seaton, M. J. (2005). Updated opacities from the Opacity Project. *MNRAS*, 360:458–464.

Bedding, T. R. and Zijlstra, A. A. (1998). HIPPARCOS Period-Luminosity Relations for Mira and Semiregular variables. *ApJ*, 506:L47–L50.

Bedijn, P. J. (1988). Pulsation, mass loss, and evolution of upper asymptotic giant branch stars. *A&A*, 205:105–124.

Bloecker, T. (1995). Stellar evolution of low and intermediate-mass stars. I. Mass loss on the AGB and its consequences for stellar evolution. *A&A*, 297:727.

Bonatto, C., Bica, E., and Santos, Jr., J. F. C. (2005). Spatial dependence of 2MASS luminosity and mass functions in the old open cluster NGC 188. *A&A*, 433:917–929.

Boothroyd, A. I. and Sackmann, I.-J. (1988). Low-Mass Stars. III. Low-Mass Stars with Steady Mass Loss: Up to the Asymptotic Giant Branch and through the Final Thermal Pulses. *ApJ*, 328:653.

Boyer, M. L., Girardi, L., Marigo, P., Williams, B. F., Aringer, B., Nowotny, W., Rosenfield, P., Dorman, C. E., Guhathakurta, P., Dalcanton, J. J., Melbourne, J. L., Olsen, K. A. G., and Weisz, D. R. (2013). Is There a Metallicity Ceiling to Form Carbon Stars?—A Novel Technique Reveals a Scarcity of C stars in the Inner M31 Disk. *ApJ*, 774:83.

Boyer, M. L., McDonald, I., Srinivasan, S., Zijlstra, A., van Loon, J. T., Olsen, K. A. G., and Sonneborn, G. (2015a). Identification of a Class of Low-mass Asymptotic Giant Branch Stars Struggling to Become Carbon Stars in the Magellanic Clouds. *ApJ*, 810:116.

Boyer, M. L., McQuinn, K. B. W., Barmby, P., Bonanos, A. Z., Gehrz, R. D., Gordon, K. D., Groenewegen, M. A. T., Lagadec, E., Lennon, D., Marengo, M., McDonald, I., Meixner, M., Skillman, E., Sloan, G. C., Sonneborn, G., van Loon, J. T., and Zijlstra, A. (2015b). An Infrared Census of DUST in Nearby Galaxies with Spitzer (DUSTiNGS). II. Discovery of Metal-poor Dusty AGB Stars. *ApJ*, 800:51.

Boyer, M. L., McQuinn, K. B. W., Barmby, P., Bonanos, A. Z., Gehrz, R. D., Gordon, K. D., Groenewegen, M. A. T., Lagadec, E., Lennon, D., Marengo, M., Meixner, M., Skillman, E., Sloan, G. C., Sonneborn, G., van Loon, J. T., and Zijlstra, A. (2015c). An Infrared Census of Dust in nearby Galaxies with Spitzer (DUSTiNGS). I. Overview. *ApJS*, 216:10.

Boyer, M. L., McQuinn, K. B. W., Groenewegen, M. A. T., Zijlstra, A. A., Whitelock, P. A., van Loon, J. T., Sonneborn, G., Sloan, G. C., Skillman, E. D., Meixner, M., McDonald, I., Jones, O. C., Javadi, A., Gehrz, R. D., Britavskiy, N., and Bonanos, A. Z. (2017). An Infrared Census of DUST in Nearby Galaxies with Spitzer (DUSTiNGS). IV. Discovery of High-redshift AGB Analogs. *ApJ*, 851:152.

Boyer, M. L., Srinivasan, S., van Loon, J. T., McDonald, I., Meixner, M., Zaritsky, D., Gordon, K. D., Kemper, F., Babler, B., Block, M., Bracker, S., Engelbracht, C. W., Hora, J., Indebetouw, R., Meade, M., Misselt, K., Robitaille, T., Sewiło, M., Shiao, B., and Whitney, B. (2011). Surveying the Agents of Galaxy Evolution in the Tidally Stripped, Low Metallicity Small Magellanic Cloud (SAGE-SMC). II. Cool Evolved Stars. *AJ*, 142:103.

Brandt, T. D. and Huang, C. X. (2015). Rotating Stellar Models Can Account for the Extended Main-sequence Turnoffs in Intermediate-age Clusters. *ApJ*, 807:25.

Bressan, A., Fagotto, F., Bertelli, G., and Chiosi, C. (1993). Evolutionary sequences of stellar models with new radiative opacities. II - Z = 0.02. *A&AS*, 100:647–664.

Bressan, A., Girardi, L., Marigo, P., Rosenfield, P., and Tang, J. (2015). Uncertainties in Stellar Evolution Models: Convective Overshoot. In Miglio, A., Eggenberger, P., Girardi, L., and Montalbán, J., editors, *Asteroseismology of Stellar Populations in the Milky Way*, volume 39 of *Astrophysics and Space Science Proceedings*, page 25.

Bressan, A., Marigo, P., Girardi, L., Nanni, A., and Rubele, S. (2013). Red Giant evolution and specific problems. In *European Physical Journal Web of Conferences*, volume 43 of *European Physical Journal Web of Conferences*, page 03001.

Bressan, A., Marigo, P., Girardi, L., Salasnich, B., Dal Cero, C., Rubele, S., and Nanni, A. (2012). PARSEC: stellar tracks and isochrones with the PAdova and TRieste Stellar Evolution Code. *MNRAS*, 427:127–145.

Caffau, E., Ludwig, H.-G., Steffen, M., Freytag, B., and Bonifacio, P. (2011). Solar Chemical Abundances Determined with a CO5BOLD 3D Model Atmosphere. *Sol. Phys.*, 268:255–269.

Castelli, F. and Kurucz, R. L. (2003). New Grids of ATLAS9 Model Atmospheres. In Piskunov, N., Weiss, W. W., and Gray, D. F., editors, *Modelling of Stellar Atmospheres*, volume 210 of *IAU Symposium*, page A20.

Catelan, M. and Smith, H. A. (2015). *Pulsating Stars*.

Chabrier, G. (2001). The Galactic Disk Mass Budget. I. Stellar Mass Function and Density. *ApJ*, 554:1274–1281.

Chen, Y., Bressan, A., Girardi, L., Marigo, P., Kong, X., and Lanza, A. (2015). PARSEC evolutionary tracks of massive stars up to 350 $M_{odot}$ at metallicities $0.0001 \leq Z \leq 0.04$. *MNRAS*, 452:1068–1080.

Chen, Y., Girardi, L., Bressan, A., Marigo, P., Barbieri, M., and Kong, X. (2014). Improving PARSEC models for very low mass stars. *MNRAS*, 444:2525–2543.

Cioni, M.-R., Loup, C., Habing, H. J., Fouqué, P., Bertin, E., Deul, E., Egret, D., Alard, C., de Batz, B., Borsenberger, J., Dennefeld, M., Epchtein, N., Forveille, T., Garzón, F., Hron, J., Kimeswenger, S., Lacombe, F., Le Bertre, T., Mamon, G. A., Omont, A., Paturel, G., Persi, P., Robin, A., Rouan, D., Simon, G., Tiphène, D., Vauglin, I., and Wagner, S. (2000). The DENIS Point Source Catalogue towards the Magellanic Clouds. *A&AS*, 144:235–245.

Cioni, M.-R. L., Clementini, G., Girardi, L., Guandalini, R., Gullieuszik, M., Miszalski, B., Moretti, M.-I., Ripepi, V., Rubele, S., Bagheri, G., Bekki, K., Cross, N., de Blok, W. J. G., de Grijs, R., Emerson, J. P., Evans, C. J., Gibson, B., Gonzales-Solares, E., Groenewegen, M. A. T., Irwin, M., Ivanov, V. D., Lewis, J., Marconi, M., Marquette, J.-B., Mastropietro, C., Moore, B., Napiwotzki, R., Naylor, T., Oliveira, J. M., Read, M., Sutorius, E., van Loon, J. T., Wilkinson, M. I., and Wood, P. R. (2011). The VMC survey. I. Strategy and first data. *A&A*, 527:A116.

Cioni, M.-R. L., Girardi, L., Marigo, P., and Habing, H. J. (2006). AGB stars in the Magellanic Clouds. II. The rate of star formation across the LMC. *A&A*, 448:77–91.

Cioni, M.-R. L. and Habing, H. J. (2003). AGB stars in the Magellanic Clouds. I. The C/M ratio. *A&A*, 402:133–140.

Correnti, M., Goudfrooij, P., Bellini, A., Kalirai, J. S., and Puzia, T. H. (2017). Dissecting the extended main-sequence turn-off of the young star cluster NGC 1850. *MNRAS*, 467:3628–3641.

Correnti, M., Goudfrooij, P., Kalirai, J. S., Girardi, L., Puzia, T. H., and Kerber, L. (2014). New Clues to the Cause of Extended Main-Sequence Turnoffs in Intermediate-age Star Clusters in the Magellanic Clouds. *ApJ*, 793:121.

Cranmer, S. R. and Saar, S. H. (2011). Testing a Predictive Theoretical Model for the Mass Loss Rates of Cool Stars. *ApJ*, 741:54.

Cristallo, S., Piersanti, L., Straniero, O., Gallino, R., Domínguez, I., Abia, C., Di Rico, G., Quintini, M., and Bisterzo, S. (2011). Evolution, Nucleosynthesis, and Yields of Low-mass Asymptotic Giant Branch Stars at Different Metallicities. II. The FRUITY Database. *ApJS*, 197:17.

Cristallo, S., Straniero, O., Piersanti, L., and Gobrecht, D. (2015). Evolution, Nucleosynthesis, and Yields of AGB Stars at Different Metallicities. III. Intermediate-mass Models, Revised Low-mass Models, and the ph-FRUITY Interface. *ApJS*, 219:40.

Cummings, J. D., Kalirai, J. S., Tremblay, P.-E., Ramirez-Ruiz, E., and Choi, J. (2018). The White Dwarf Initial-Final Mass Relation for Progenitor Stars From 0.85 to 7.5 $M_{\odot}$. *ArXiv e-prints*.

Cutri, R. M., Skrutskie, M. F., van Dyk, S., Beichman, C. A., Carpenter, J. M., Chester, T., Cambresy, L., Evans, T., Fowler, J., Gizis, J., Howard, E., Huchra, J., Jarrett, T., Kopan, E. L., Kirkpatrick, J. D., Light, R. M., Marsh, K. A., McCallon, H., Schneider, S., Stiening, R., Sykes, M., Weinberg, M., Wheaton, W. A., Wheelock, S., and Zacarias, N. (2003). *2MASS All Sky Catalog of point sources.*

Dalcanton, J. J., Williams, B. F., Melbourne, J. L., Girardi, L., Dolphin, A., Rosenfield, P. A., Boyer, M. L., de Jong, R. S., Gilbert, K., Marigo, P., Olsen, K., Seth, A. C., and Skillman, E. (2012). Resolved near-infrared stellar populations in nearby galaxies. *The Astrophysical Journal Supplement Series*, 198(1):6.

Dalcanton, J. J., Williams, B. F., Seth, A. C., Dolphin, A., Holtzman, J., Rosema, K., Skillman, E. D., Cole, A., Girardi, L., Gogarten, S. M., Karachentsev, I. D., Olsen, K., Weisz, D., Christensen, C., Freeman, K., Gilbert, K., Gallart, C., Harris, J., Hodge, P., de Jong, R. S., Karachentseva, V., Mateo, M., Stetson, P. B., Tavarez, M., Zaritsky, D., Governato, F., and Quinn, T. (2009). The ACS Nearby Galaxy Survey Treasury. *ApJS*, 183:67–108.

Davies, B., Kudritzki, R.-P., Gazak, Z., Plez, B., Bergemann, M., Evans, C., and Patrick, L. (2015). Red Supergiants as Cosmic Abundance Probes: The Magellanic Clouds. *ApJ*, 806:21.

Dell'Agli, F., García-Hernández, D. A., Ventura, P., Schneider, R., Di Criscienzo, M., and Rossi, C. (2015). AGB stars in the SMC: evolution and dust properties based on Spitzer observations. *MNRAS*, 454:4235–4249.

Dolphin, A. E. (2002). Numerical methods of star formation history measurement and applications to seven dwarf spheroidals. *MNRAS*, 332:91–108.

El-Badry, K., Rix, H.-W., and Weisz, D. R. (2018). An Empirical Measurement of the Initial–Final Mass Relation with Gaia White Dwarfs. *ApJ*, 860:L17.

Eriksson, K., Nowotny, W., Höfner, S., Aringer, B., and Wachter, A. (2014). Synthetic photometry for carbon-rich giants. IV. An extensive grid of dynamic atmosphere and wind models. *A&A*, 566:A95.

Fishlock, C. K., Karakas, A. I., Lugaro, M., and Yong, D. (2014). Evolution and Nucleosynthesis of Asymptotic Giant Branch Stellar Models of Low Metallicity. *ApJ*, 797:44.

Frogel, J. A., Mould, J., and Blanco, V. M. (1990). The asymptotic giant branch of Magellanic Cloud clusters. *ApJ*, 352:96–122.

Gaia Collaboration, Brown, A. G. A., Vallenari, A., Prusti, T., de Bruijne, J. H. J., Babusiaux, C., Bailer-Jones, C. A. L., Biermann, M., Evans, D. W., Eyer, L., and et al. (2018). Gaia Data Release 2. Summary of the contents and survey properties. *A&A*, 616:A1.

Girardi, L., Bertelli, G., Bressan, A., Chiosi, C., Groenewegen, M. A. T., Marigo, P., Salasnich, B., and Weiss, A. (2002). Theoretical isochrones in several photometric systems. I. Johnson-Cousins-Glass, HST/WFPC2, HST/NICMOS, Washington, and ESO Imaging Survey filter sets. *A&A*, 391:195–212.

Girardi, L., Bressan, A., Bertelli, G., and Chiosi, C. (2000). Evolutionary tracks and isochrones for low- and intermediate-mass stars: From 0.15 to 7 $M_{sun}$, and from Z=0.0004 to 0.03. *A&AS*, 141:371–383.

Girardi, L., Groenewegen, M. A. T., Hatziminaoglou, E., and da Costa, L. (2005). Star counts in the Galaxy. Simulating from very deep to very shallow photometric surveys with the TRILEGAL code. *A&A*, 436:895–915.

Girardi, L. and Marigo, P. (2007). Towards Simulating the Photometry, Chemistry, Mass Loss and Pulsational Properties of AGB Star Populations in Resolved Galaxies. In Kerschbaum, F., Charbonnel, C., and Wing, R. F., editors, *Why Galaxies Care About AGB Stars: Their Importance as Actors and Probes*, volume 378 of *Astronomical Society of the Pacific Conference Series*, page 20.

Girardi, L., Marigo, P., Bressan, A., and Rosenfield, P. (2013). The Insidious Boosting of Thermally Pulsing Asymptotic Giant Branch Stars in Intermediate-age Magellanic Cloud Clusters. *ApJ*, 777:142.

Girardi, L., Rubele, S., and Kerber, L. (2009). Discovery of two distinct red clumps in NGC 419: a rare snapshot of a cluster at the onset of degeneracy. *MNRAS*, 394:L74–L78.

Girardi, L., Williams, B. F., Gilbert, K. M., Rosenfield, P., Dalcanton, J. J., Marigo, P., Boyer, M. L., Dolphin, A., Weisz, D. R., Melbourne, J., Olsen, K. A. G., Seth, A. C., and Skillman, E. (2010). The ACS Nearby Galaxy Survey Treasury. IX. Constraining Asymptotic Giant Branch Evolution with Old Metal-poor Galaxies. *ApJ*, 724:1030–1043.

Glatt, K., Grebel, E. K., Sabbi, E., Gallagher, III, J. S., Nota, A., Sirianni, M., Clementini, G., Tosi, M., Harbeck, D., Koch, A., Kayser, A., and Da Costa, G. (2008). Age Determination of Six Intermediate-Age Small Magellanic Cloud Star Clusters with HST/ACS. *AJ*, 136:1703–1727.

Goldman, S. R., van Loon, J. T., Gómez, J. F., Green, J. A., Zijlstra, A. A., Nanni, A., Imai, H., Whitelock, P. A., Groenewegen, M. A. T., and Oliveira, J. M. (2018). A dearth of OH/IR stars in the Small Magellanic Cloud. *MNRAS*, 473:3835–3853.

Gordon, K. D., Meixner, M., Meade, M. R., Whitney, B., Engelbracht, C., Bot, C., Boyer, M. L., Lawton, B., Sewiło, M., Babler, B., Bernard, J.-P., Bracker, S., Block, M., Blum, R., Bolatto, A., Bonanos, A., Harris, J., Hora, J. L., Indebetouw, R., Misselt, K., Reach, W., Shiao, B., Tielens, X., Carlson, L., Churchwell, E., Clayton, G. C., Chen, C.-H. R., Cohen, M., Fukui, Y., Gorjian, V., Hony, S., Israel, F. P., Kawamura, A., Kemper, F., Leroy, A., Li, A., Madden, S., Marble, A. R., McDonald, I., Mizuno, A., Mizuno, N., Muller, E., Oliveira, J. M., Olsen, K., Onishi, T., Paladini, R., Paradis, D., Points, S., Robitaille, T., Rubin, D., Sandstrom, K., Sato, S., Shibai, H., Simon, J. D., Smith, L. J., Srinivasan, S., Vijh, U., Van Dyk, S., van Loon, J. T., and Zaritsky, D. (2011). Surveying the Agents of Galaxy Evolution in the Tidally Stripped, Low Metallicity Small Magellanic Cloud (SAGE-SMC). I. Overview. *AJ*, 142:102.

Goudfrooij, P., Girardi, L., and Correnti, M. (2017). Extended Main-sequence Turn-offs in Intermediate-age Star Clusters: Stellar Rotation Diminishes, but Does Not Eliminate, Age Spreads. *ApJ*, 846:22.

Goudfrooij, P., Girardi, L., Kozhurina-Platais, V., Kalirai, J. S., Platais, I., Puzia, T. H., Correnti, M., Bressan, A., Chandar, R., Kerber, L., Marigo, P., and Rubele, S. (2014). Extended Main Sequence Turnoffs in Intermediate-age Star Clusters: A Correlation between Turnoff Width and Early Escape Velocity. *ApJ*, 797:35.

Groenewegen, M. A. T. (2002). Carbon stars in the Local Group. *ArXiv Astrophysics e-prints*.

Groenewegen, M. A. T. (2006). The mid- and far-infrared colours of AGB and post-AGB stars. *A&A*, 448:181–187.

Groenewegen, M. A. T. (2012). An extension of the DUSTY radiative transfer code and an application to OH 26.5 and TT Cygni. *A&A*, 543:A36.

Groenewegen, M. A. T. and de Jong, T. (1993). Synthetic AGB evolution. I - A new model. *A&A*, 267:410–432.

Groenewegen, M. A. T. and Sloan, G. C. (2018a). Luminosities and mass-loss rates of Local Group AGB stars and red supergiants. *A&A*, 609:A114.

Groenewegen, M. A. T. and Sloan, G. C. (2018b). Luminosities and mass-loss rates of Local Group AGB stars and red supergiants. *A&A*, 609:A114.

Habing, H. J. and Olofsson, H., editors (2004). *Asymptotic Giant Branch Stars*. Springer: Astron. Astrophys. Libr.

Harris, J. and Zaritsky, D. (2002). StarFISH: A Robust Synthetic Color-Magnitude Diagram Package. In Lejeune, T. and Fernandes, J., editors, *Observed HR Diagrams and Stellar Evolution*, volume 274 of *Astronomical Society of the Pacific Conference Series*, page 600.

Harris, J. and Zaritsky, D. (2004). The Star Formation History of the Small Magellanic Cloud. *AJ*, 127:1531–1544.

Harris, J. and Zaritsky, D. (2009). The Star Formation History of the Large Magellanic Cloud. *AJ*, 138:1243–1260.

Herwig, F. (2000). The evolution of AGB stars with convective overshoot. *A&A*, 360:952–968.

Herwig, F. (2004). Evolution and Yields of Extremely Metal-poor Intermediate-Mass Stars. *ApJS*, 155:651–666.

Herwig, F. (2005). Evolution of Asymptotic Giant Branch Stars. *ARA&A*, 43:435–479.

Herwig, F., Bloecker, T., Schoenberner, D., and El Eid, M. (1997). Stellar evolution of low and intermediate-mass stars. IV. Hydrodynamically-based overshoot and nucleosynthesis in AGB stars. *A&A*, 324:L81–L84.

Hill, V. (1999). Abundances of cool supergiants in the SMC young cluster NGC 330. *A&A*, 345:430–438.

Höfner, S. and Olofsson, H. (2018). Mass loss of stars on the asymptotic giant branch. Mechanisms, models and measurements. *A&A Rev.*, 26:1.

Ita, Y., Tanabé, T., Matsunaga, N., Nakajima, Y., Nagashima, C., Nagayama, T., Kato, D., Kurita, M., Nagata, T., Sato, S., Tamura, M., Nakaya, H., and Nakada, Y. (2002). Pulsation at the tip of the first giant branch? *MNRAS*, 337:L31–L34.

Ita, Y., Tanabé, T., Matsunaga, N., Nakajima, Y., Nagashima, C., Nagayama, T., Kato, D., Kurita, M., Nagata, T., Sato, S., Tamura, M., Nakaya, H., and Nakada, Y. (2004). Variable stars in the Magellanic Clouds: results from OGLE and SIRIUS. *MNRAS*, 347:720–728.

Ivezic, Z., Nenkova, M., and Elitzur, M. (1999). User Manual for DUSTY. *ArXiv Astrophysics e-prints*.

Kalirai, J. S., Marigo, P., and Tremblay, P.-E. (2014). The Core Mass Growth and Stellar Lifetime of Thermally Pulsing Asymptotic Giant Branch Stars. *ApJ*, 782:17.

Karakas, A. I. (2010). Updated stellar yields from asymptotic giant branch models. *MNRAS*, 403:1413–1425.

Karakas, A. I. and Lattanzio, J. C. (2014). The Dawes Review 2: Nucleosynthesis and Stellar Yields of Low- and Intermediate-Mass Single Stars. *PASA*, 31:30.

Karakas, A. I., Lattanzio, J. C., and Pols, O. R. (2002). Parameterising the Third Dredge-up in Asymptotic Giant Branch Stars. *PASA*, 19:515–526.

Karakas, A. I., Lugaro, M., Carlos, M., Cseh, B., Kamath, D., and García-Hernández, D. A. (2018). Heavy-element yields and abundances of asymptotic giant branch models with a Small Magellanic Cloud metallicity. *MNRAS*, 477:421–437.

Kiss, L. L. and Bedding, T. R. (2003). Red variables in the OGLE-II data base - I. Pulsations and period-luminosity relations below the tip of the red giant branch of the Large Magellanic Cloud. *MNRAS*, 343:L79–L83.

Komatsu, E., Smith, K. M., Dunkley, J., Bennett, C. L., Gold, B., Hinshaw, G., Jarosik, N., Larson, D., Nolta, M. R., Page, L., Spergel, D. N., Halpern, M., Hill, R. S., Kogut, A., Limon, M., Meyer, S. S., Odegard, N., Tucker, G. S., Weiland, J. L., Wollack, E., and Wright, E. L. (2011). Seven-year Wilkinson Microwave Anisotropy Probe (WMAP) Observations: Cosmological Interpretation. *ApJS*, 192:18.

Kroupa, P. (2001). On the variation of the initial mass function. *MNRAS*, 322:231–246.

Lançon, A. and Wood, P. R. (2000). A library of 0.5 to 2.5 mu m spectra of luminous cool stars. *A&AS*, 146:217–249.

Lattanzio, J. C. and Wood, P. R. (2003). Evolution, Nucleosynthesis, and Pulsation of AGB Stars. In *Asymptotic giant branch stars*, page 23.

Lebzelter, T., Mowlavi, N., Marigo, P., Pastorelli, G., Trabucchi, M., Wood, P. R., and Lecoeur-Taïbi, I. (2018). A new method to identify subclasses among AGB stars using Gaia and 2MASS photometry. *A&A*, 616:L13.

Ludwig, H.-G., Freytag, B., and Steffen, M. (1999). A calibration of the mixing-length for solar-type stars based on hydrodynamical simulations. I. Methodical aspects and results for solar metallicity. *A&A*, 346:111–124.

Magic, Z., Weiss, A., and Asplund, M. (2015). The Stagger-grid: A grid of 3D stellar atmosphere models. III. The relation to mixing length convection theory. *A&A*, 573:A89.

Maraston, C. (2005). Evolutionary population synthesis: models, analysis of the ingredients and application to high-z galaxies. *MNRAS*, 362:799–825.

Marigo, P. (2015). Calibrating the Role of TP-AGB Stars in the Cosmic Matter Cycle. In Kerschbaum, F., Wing, R. F., and Hron, J., editors, *Why Galaxies Care about AGB Stars III: A Closer Look in Space and Time*, volume 497 of *Astronomical Society of the Pacific Conference Series*, page 229.

Marigo, P. and Aringer, B. (2009). Low-temperature gas opacity. ÆSOPUS: a versatile and quick computational tool. *A&A*, 508:1539–1569.

Marigo, P., Bressan, A., Nanni, A., Girardi, L., and Pumo, M. L. (2013). Evolution of thermally pulsing asymptotic giant branch stars - I. The COLIBRI code. *MNRAS*, 434:488–526.

Marigo, P. and Girardi, L. (2007). Evolution of asymptotic giant branch stars. I. Updated synthetic TP-AGB models and their basic calibration. *A&A*, 469:239–263.

Marigo, P., Girardi, L., and Bressan, A. (1999). The third dredge-up and the carbon star luminosity functions in the Magellanic Clouds. *A&A*, 344:123–142.

Marigo, P., Girardi, L., Bressan, A., Groenewegen, M. A. T., Silva, L., and Granato, G. L. (2008). Evolution of asymptotic giant branch stars. II. Optical to far-infrared isochrones with improved TP-AGB models. *A&A*, 482:883–905.

Marigo, P., Girardi, L., Bressan, A., Rosenfield, P., Aringer, B., Chen, Y., Dussin, M., Nanni, A., Pastorelli, G., Rodrigues, T. S., Trabucchi, M., Bladh, S., Dalcanton, J., Groenewegen, M. A. T., Montalbán, J., and Wood, P. R. (2017). A New Generation of PARSEC-COLIBRI Stellar Isochrones Including the TP-AGB Phase. *ApJ*, 835:77.

Marigo, P., Girardi, L., and Chiosi, C. (2003). The red tail of carbon stars in the LMC: Models meet 2MASS and DENIS observations. *A&A*, 403:225–237.

Mattsson, L., Wahlin, R., and Höfner, S. (2010). Dust driven mass loss from carbon stars as a function of stellar parameters . I. A grid of solar-metallicity wind models. *A&A*, 509:A14.

McQuinn, K. B. W., Skillman, E. D., Dalcanton, J. J., Dolphin, A. E., Holtzman, J., Weisz, D. R., and Williams, B. F. (2011). Observational Constraints on Red and Blue Helium Burning Sequences. *ApJ*, 740:48.

Melbourne, J., Williams, B. F., Dalcanton, J. J., Rosenfield, P., Girardi, L., Marigo, P., Weisz, D., Dolphin, A., Boyer, M. L., Olsen, K., Skillman, E., and Seth, A. C. (2012). The Contribution of TP-AGB and RHeB Stars to the Near-IR Luminosity of Local Galaxies: Implications for Stellar Mass Measurements of High-redshift Galaxies. *ApJ*, 748:47.

Milone, A. P., Bedin, L. R., Piotto, G., and Anderson, J. (2009). Multiple stellar populations in Magellanic Cloud clusters. I. An ordinary feature for intermediate age globulars in the LMC? *A&A*, 497:755–771.

Mowlavi, N., Lecoeur-Taïbi, I., Lebzelter, T., Rimoldini, L., Lorenz, D., Audard, M., De Ridder, J., Eyer, L., Guy, L. P., Holl, B., Jevardat de Fombelle, G., Marchal, O., Nienartowicz, K., Regibo, S., Roelens, M., and Sarro, L. M. (2018). Gaia Data Release 2: The first Gaia catalogue of long-period variable candidates. *ArXiv e-prints*.

Nanni, A., Bressan, A., Marigo, P., and Girardi, L. (2013). Evolution of thermally pulsing asymptotic giant branch stars - II. Dust production at varying metallicity. *MNRAS*, 434:2390–2417.

Nanni, A., Marigo, P., Girardi, L., Rubele, S., Bressan, A., Groenewegen, M. A. T., Pastorelli, G., and Aringer, B. (2018). Estimating the dust production rate of carbon stars in the Small Magellanic Cloud. *MNRAS*, 473:5492–5513.

Nanni, A., Marigo, P., Groenewegen, M. A. T., Aringer, B., Girardi, L., Pastorelli, G., Bressan, A., and Bladh, S. (2016). Constraining dust properties in circumstellar envelopes of C-stars in the Small Magellanic Cloud: optical constants and grain size of carbon dust. *MNRAS*, 462:1215–1237.

Nicholls, C. P., Wood, P. R., Cioni, M. R. L., and Soszyński, I. (2009). Long Secondary Periods in variable red giants. *MNRAS*, 399:2063–2078.

Nikolaev, S. and Weinberg, M. D. (2000). Stellar Populations in the Large Magellanic Cloud from 2MASS. *ApJ*, 542:804–818.

Nowotny, W., Höfner, S., and Aringer, B. (2010). Line formation in AGB atmospheres including velocity effects. Molecular line profile variations of long period variables. *A&A*, 514:A35.

Olsen, K. A. G., Blum, R. D., and Rigaut, F. (2003). Stellar Crowding and the Science Case for Extremely Large Telescopes. *AJ*, 126:452–471.

Reimers, D. (1975). Circumstellar absorption lines and mass loss from red giants. *Memoires of the Societe Royale des Sciences de Liege*, 8:369–382.

Reiter, M., Marengo, M., Hora, J. L., and Fazio, G. G. (2015). A Spitzer/IRAC characterization of Galactic AGB and RSG stars. *MNRAS*, 447:3909–3923.

Renzini, A. and Buzzoni, A. (1986). Global properties of stellar populations and the spectral evolution of galaxies. In Chiosi, C. and Renzini, A., editors, *Spectral Evolution of Galaxies*, volume 122 of *Astrophysics and Space Science Library*, pages 195–231.

Riebel, D., Meixner, M., Fraser, O., Srinivasan, S., Cook, K., and Vijh, U. (2010). Infrared Period-Luminosity Relations of Evolved Variable Stars in the Large Magellanic Cloud. *ApJ*, 723:1195–1209.

Ritter, C., Herwig, F., Jones, S., Pignatari, M., Fryer, C., and Hirschi, R. (2018). NuGrid stellar data set - II. Stellar yields from H to Bi for stellar models with $M_{ZAMS}$ = 1-25 $M_{\odot}$ and Z = 0.0001-0.02. *MNRAS*, 480:538–571.

Rosenfield, P., Marigo, P., Girardi, L., Dalcanton, J. J., Bressan, A., Gullieuszik, M., Weisz, D., Williams, B. F., Dolphin, A., and Aringer, B. (2014). Evolution of Thermally Pulsing Asymptotic Giant Branch Stars. IV. Constraining Mass loss and Lifetimes of Low Mass, Low Metallicity AGB Stars. *ApJ*, 790:22.

Rosenfield, P., Marigo, P., Girardi, L., Dalcanton, J. J., Bressan, A., Williams, B. F., and Dolphin, A. (2016). Evolution of Thermally Pulsing Asymptotic Giant Branch Stars. V. Constraining the Mass Loss and Lifetimes of Intermediate-mass, Low-metallicity AGB Stars. *ApJ*, 822:73.

Rubele, S., Girardi, L., Kerber, L., Cioni, M.-R. L., Piatti, A. E., Zaggia, S., Bekki, K., Bressan, A., Clementini, G., de Grijs, R., Emerson, J. P., Groenewegen, M. A. T., Ivanov, V. D., Marconi, M., Marigo, P., Moretti, M.-I., Ripepi, V., Subramanian, S., Tatton, B. L., and van Loon, J. T. (2015). The VMC survey - XIV. First results on the look-back time star formation rate tomography of the Small Magellanic Cloud. *MNRAS*, 449:639–661.

Rubele, S., Kerber, L., Girardi, L., Cioni, M.-R., Marigo, P., Zaggia, S., Bekki, K., de Grijs, R., Emerson, J., Groenewegen, M. A. T., Gullieuszik, M., Ivanov, V., Miszalski, B., Oliveira, J. M., Tatton, B., and van Loon, J. T. (2012). The VMC survey. IV. The LMC star formation history and disk geometry from four VMC tiles. *A&A*, 537:A106.

Rubele, S., Pastorelli, G., Girardi, L., Cioni, M.-R. L., Zaggia, S., Marigo, P., Bekki, K., Bressan, A., Clementini, G., de Grijs, R., Emerson, J., Groenewegen, M. A. T., Ivanov, V. D., Muraveva, T., Nanni, A., Oliveira, J. M., Ripepi, V., Sun, N.-C., and van Loon, J. T. (2018). The VMC survey - XXXI: The spatially resolved star formation history of the main body of the Small Magellanic Cloud. *MNRAS*, 478:5017–5036.

Ruffle, P. M. E., Kemper, F., Jones, O. C., Sloan, G. C., Kraemer, K. E., Woods, P. M., Boyer, M. L., Srinivasan, S., Antoniou, V., Lagadec, E., Matsuura, M., McDonald, I., Oliveira, J. M., Sargent, B. A., Sewiło, M., Szczerba, R., van Loon, J. T., Volk, K., and Zijlstra, A. A. (2015). Spitzer infrared spectrograph point source classification in the Small Magellanic Cloud. *MNRAS*, 451:3504–3536.

Schöier, F. L. and Olofsson, H. (2001). Models of circumstellar molecular radio line emission. Mass loss rates for a sample of bright carbon stars. *A&A*, 368:969–993.

Schröder, K.-P. and Cuntz, M. (2005). A New Version of Reimers' Law of Mass Loss Based on a Physical Approach. *ApJ*, 630:L73–L76.

Seaton, M. J. (2005). Opacity Project data on CD for mean opacities and radiative accelerations. *MNRAS*, 362:L1–L3.

Skrutskie, M. F., Cutri, R. M., Stiening, R., Weinberg, M. D., Schneider, S., Carpenter, J. M., Beichman, C., Capps, R., Chester, T., Elias, J., Huchra, J., Liebert, J., Lonsdale, C., Monet, D. G., Price, S., Seitzer, P., Jarrett, T., Kirkpatrick, J. D., Gizis, J. E., Howard, E., Evans, T., Fowler, J., Fullmer, L., Hurt, R., Light, R., Kopan, E. L., Marsh, K. A., McCallon, H. L., Tam, R., Van Dyk, S., and Wheelock, S. (2006). The Two Micron All Sky Survey (2MASS). *AJ*, 131:1163–1183.

Soszynski, I., Dziembowski, W. A., Udalski, A., Kubiak, M., Szymanski, M. K., Pietrzynski, G., Wyrzykowski, L., Szewczyk, O., and Ulaczyk, K. (2007). The Optical Gravitational Lensing Experiment. Period–Luminosity Relations of Variable Red Giant Stars. *Acta Astron.*, 57:201–225.

Soszyński, I., Udalski, A., Kubiak, M., Szymański, M., Pietrzyński, G., Zebruń, K., Szewczyk, O., and Wyrzykowski, L. (2004). The Optical Gravitational Lensing Experiment. Small Amplitude Variable Red Giants in the Magellanic Clouds. *Acta Astron.*, 54:129–152.

Soszyński, I., Udalski, A., Szymański, M. K., Kubiak, M., Pietrzyński, G., Wyrzykowski, Ł., Szewczyk, O., Ulaczyk, K., and Poleski, R. (2009). The Optical Gravitational Lensing Experiment. The OGLE-III Catalog of Variable Stars. IV. Long-Period Variables in the Large Magellanic Cloud. *Acta Astron.*, 59:239–253.

Soszyński, I., Udalski, A., Szymański, M. K., Kubiak, M., Pietrzyński, G., Wyrzykowski, Ł., Ulaczyk, K., Poleski, R., Kozłowski, S., and Pietrukowicz, P. (2011). The Optical Gravitational Lensing Experiment. The OGLE-III Catalog of Variable Stars. XIII. Long-Period Variables in the Small Magellanic Cloud. *Acta Astron.*, 61:217–230.

Srinivasan, S., Boyer, M. L., Kemper, F., Meixner, M., Sargent, B. A., and Riebel, D. (2016). The evolved-star dust budget of the Small Magellanic Cloud: the critical role of a few key players. *MNRAS*, 457:2814–2838.

Stancliffe, R. J., Izzard, R. G., and Tout, C. A. (2005). Third dredge-up in low-mass stars: solving the Large Magellanic Cloud carbon star mystery. *MNRAS*, 356:L1–L5.

Stancliffe, R. J., Tout, C. A., and Pols, O. R. (2004). Deep dredge-up in intermediate-mass thermally pulsing asymptotic giant branch stars. *MNRAS*, 352:984–992.

Straniero, O., Chieffi, A., Limongi, M., Busso, M., Gallino, R., and Arlandini, C. (1997). Evolution and Nucleosynthesis in Low-Mass Asymptotic Giant Branch Stars. I. Formation of Population I Carbon Stars. *ApJ*, 478:332–339.

Straniero, O., Gallino, R., and Cristallo, S. (2006). s process in low-mass asymptotic giant branch stars. *Nuclear Physics A*, 777:311–339.

Tang, J., Bressan, A., Rosenfield, P., Slemer, A., Marigo, P., Girardi, L., and Bianchi, L. (2014). New PARSEC evolutionary tracks of massive stars at low metallicity: testing canonical stellar evolution in nearby star-forming dwarf galaxies. *MNRAS*, 445:4287–4305.

Tayar, J., Somers, G., Pinsonneault, M. H., Stello, D., Mints, A., Johnson, J. A., Zamora, O., García-Hernández, D. A., Maraston, C., Serenelli, A., Allende Prieto, C., Bastien, F. A., Basu, S., Bird, J. C., Cohen, R. E., Cunha, K., Elsworth, Y., García, R. A., Girardi, L., Hekker, S., Holtzman, J., Huber, D., Mathur, S., Mészáros, S., Mosser, B., Shetrone, M., Silva Aguirre, V., Stassun, K., Stringfellow, G. S., Zasowski, G., and Roman-Lopes, A. (2017). The Correlation between Mixing Length and Metallicity on the Giant Branch: Implications for Ages in the Gaia Era. *ApJ*, 840:17.

Trabucchi, M., Wood, P. R., Montalbán, J., Marigo, P., Pastorelli, G., and Girardi, L. (2017). A New Interpretation of the Period-Luminosity Sequences of Long-period Variables. *ApJ*, 847:139.

Trampedach, R., Stein, R. F., Christensen-Dalsgaard, J., Nordlund, Å., and Asplund, M. (2014). Improvements to stellar structure models, based on a grid of 3D convection simulations - II. Calibrating the mixing-length formulation. *MNRAS*, 445:4366–4384.

Udalski, A., Szymański, M., Kaluzny, J., Kubiak, M., and Mateo, M. (1992). The Optical Gravitational Lensing Experiment. *Acta Astron.*, 42:253–284.

van der Marel, R. P. and Cioni, M.-R. L. (2001). Magellanic Cloud Structure from Near-Infrared Surveys. I. The Viewing Angles of the Large Magellanic Cloud. *AJ*, 122:1807–1826.

Vassiliadis, E. and Wood, P. R. (1993). Evolution of low- and intermediate-mass stars to the end of the asymptotic giant branch with mass loss. *ApJ*, 413:641–657.

Ventura, P. and D'Antona, F. (2009). Massive AGB models of low metallicity: the implications for the self-enrichment scenario in metal-poor globular clusters. *A&A*, 499:835–846.

Wagenhuber, J. and Groenewegen, M. A. T. (1998). New input data for synthetic AGB evolution. *A&A*, 340:183–195.

Weiss, A. and Ferguson, J. W. (2009). New asymptotic giant branch models for a range of metallicities. *A&A*, 508:1343–1358.

Weisz, D. R., Dolphin, A. E., Skillman, E. D., Holtzman, J., Gilbert, K. M., Dalcanton, J. J., and Williams, B. F. (2014). The Star Formation Histories of Local Group Dwarf Galaxies. I. Hubble Space Telescope/Wide Field Planetary Camera 2 Observations. *ApJ*, 789:147.

Whitelock, P. A., Feast, M. W., van Loon, J. T., and Zijlstra, A. A. (2003). Obscured asymptotic giant branch variables in the Large Magellanic Cloud and the period-luminosity relation. *MNRAS*, 342:86–104.

Willson, L. A. (2000). Mass Loss From Cool Stars: Impact on the Evolution of Stars and Stellar Populations. *ARA&A*, 38:573–611.

Winters, J. M., Le Bertre, T., Jeong, K. S., Nyman, L.-Å., and Epchtein, N. (2003). Mass-loss from dusty, low outflow-velocity AGB stars. I. Wind structure and mass-loss rates. *A&A*, 409:715–735.

Wood, P. R. (2000). Variable Red Giants in the LMC: Pulsating Stars and Binaries? *PASA*, 17:18–21.

Wood, P. R. (2015). The pulsation modes, masses and evolution of luminous red giants. *MNRAS*, 448:3829–3843.

Wood, P. R., Alcock, C., Allsman, R. A., Alves, D., Axelrod, T. S., Becker, A. C., Bennett, D. P., Cook, K. H., Drake, A. J., Freeman, K. C., Griest, K., King, L. J., Lehner, M. J., Marshall, S. L., Minniti, D., Peterson, B. A., Pratt, M. R., Quinn, P. J., Stubbs, C. W., Sutherland, W., Tomaney, A., Vandehei, T., and Welch, D. L. (1999). MACHO observations of LMC red giants: Mira and semi-regular pulsators, and contact and semi-detached binaries. In Le Bertre, T., Lebre, A., and Waelkens, C., editors, *Asymptotic Giant Branch Stars*, volume 191 of *IAU Symposium*, page 151.

Wood, P. R. and Sebo, K. M. (1996). On the pulsation mode of Mira variables: evidence from the Large Magellanic Cloud. *MNRAS*, 282:958–964.

Zaritsky, D., Harris, J., and Thompson, I. (1997). A digital photometric survey of the magellanic clouds: First results from one million stars. *AJ*, 114:1002–1013.